UNIVERSITÀ
DEGLI STUDI
DI PADOVA

Head Office: Università degli Studi di Padova

Department of Geosciences

Ph.D. COURSE IN GEOSCIENCES

XXXIV SERIES

GEODYNAMIC AND SEISMOLOGICAL MODELLING OF THE CENTRAL-WESTERN MEDITERRANEAN MID-LATE CENOZOIC DYNAMICS AND STRUCTURE

Thesis written with the financial contribution of the

ERC StG 758199 NEWTON.

Coordinator: Prof. Claudia AGNINI

Supervisor: Prof. Manuele FACCENDA

Co-Supervisor: Dr. Brandon Paul VANDERBEEK

Ph.D. student: Rosalia LO BUE

Abstract

The Central-Western Mediterranean is one of the most complex tectonic settings on Earth. The articulate lithospheric structure currently observed in the region is the result of manifold tectonic processes that have occurred since the Mid-Late Cenozoic. Despite its shallow tectonic evolution has been relatively well constrained by a wealth of geological and geophysical data, several uncertainties persist about the recent mantle dynamics and the mechanisms that led to the present-day surface morphology and deep slab geometry. This Thesis attempt to reproduce the recent large-scale evolution of the Central-Western Mediterranean and the associated strain-induced upper mantle fabrics and seismic anisotropy adopting a strategy that combines geodynamic and seismological numerical modelling techniques. We explore a wide range of models and evaluate the modelling results by comparing seismological synthetics and the predicted tectonic evolution with geophysical and geological observations. The good correlation between modelled and observed slab morphology and seismic anisotropy patterns poses new important constraints on the tectonic evolution of the study area, explaining the major tectonic events proposed in the literature (e.g., the rotation of the Sardinian-Corsican block and the opening of back-arc basins related to the retreat of the Ionian trench, the lateral tearing and breakoff of oceanic slabs, etc..) that have contributed to shaping the Central-Western Mediterranean. The research activities demonstrate that this methodology can capture to a first order the overall evolution and the current geological scenario of the study region, thus representing a powerful tool to investigate mantle dynamics. Furthermore, geodynamic models were exploited to test the capabilities and limitations of P- and S-waves anisotropic inversions, showing that inverting for seismic anisotropy allows to avoid notable imaging artefacts and, consequently, errors in the interpretation of the tomographic results.

Sommario

Il Mediterraneo Centro-Occidentale è uno degli ambienti tettonici più attivi della Terra. Il suo attuale assetto geologico è frutto di complessi processi di subduzione e collisione che hanno caratterizzato questa regione fin dal medio-tardo Cenozoico. Le caratteristiche strutturali uniche del Mediterraneo lo hanno reso una della aree più studiate al mondo e sebbene la sua recente evoluzione tettonica sia stata in parte ben vincolata da una grande quantità di dati geologici e geofisici, persistono tuttora alcune incertezze sui meccanismi che hanno portato alla sua attuale geomorfologia superficiale e alla geometria degli slab subdotti. In questa Tesi sono state combinate alcune tecniche di modellazione numerica geodinamica e sismologica per riprodurre l'evoluzione geodinamica del Mediterraneo Centro-Occidentale negli ultimi 30 milioni di anni. Una vasta gamma di modelli numerici sono stati prodotti e analizzati attraverso un confronto con esperimenti sintetici sismologici e osservazioni geologiche e geofisiche della regione. La buona correlazione tra i modelli numerici e i dati reali ha posto importanti vincoli sulla sua recente evoluzione, riuscendo a spiegare i principali eventi tettonici già proposti in letteratura (es. la rotazione del blocco sardo-corso, la forma arcuata della catena appenninica, la frammentazione delle porzioni litosferiche subdotte, ecc.) dandone una lettura sia geodinamica che sismologica. Le attività di ricerca hanno dimostrato come questa metodologia può rappresentare uno strumento fondamentale per lo studio di ambienti geodinamici complessi. Inoltre, i modelli geodinamici sono stati utilizzati come casi di studio sintetici per testare le capacità e i limiti di tecniche di inversioni anisotropiche delle onde P ed S, dimostrando che considerare l'anisotropia nelle inversioni tomografiche consente di evitare notevoli artefatti di imaging ed errori nell'interpretazione dei risultati tomografici.

Contents

List of Figures

List of Tables

To my father

Chapter 1

INTRODUCTION

The Central-Western Mediterranean (CWM) is one of the most active tectonic setting on Earth (Figure 1.1). Large mountain ranges (e.g., Pyrenees, Alps, Apennines, Dinarides, Hellenides), back-arc extensional basins (e.g., Alborean, Algerian, Liguro-Provençal and Tyrrhenian basins), active volcanoes (e.g., Vesuvius, Vulcano, Etna, Stromboli) and violent earthquakes are the present-day expression of manifold tectonic processes that have occurred since the Cenozoic.

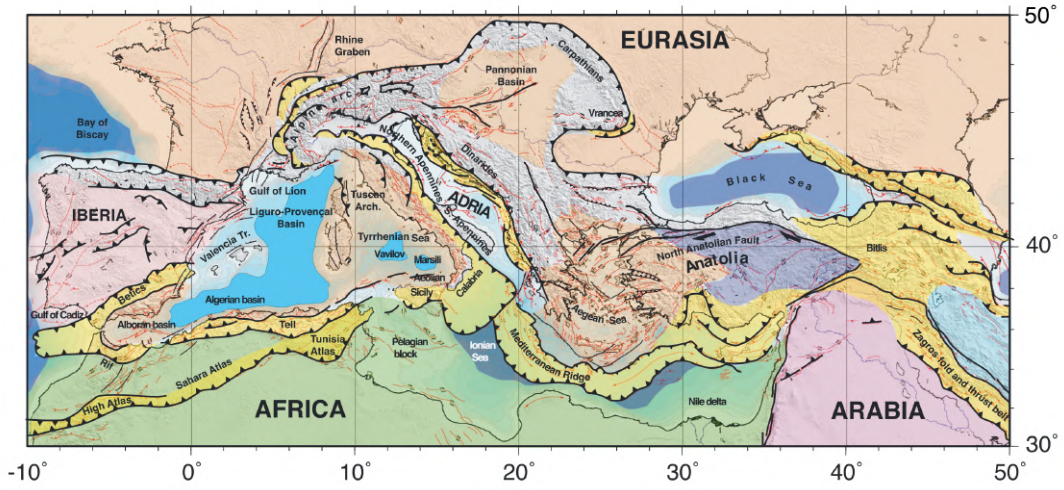

Figure 1.1: *Tectonic setting of the entire Mediterranean region from Faccenna et al. (2014) showing the main structures, mountain ranges, subduction zones, back-arc basins, etc.*

The primary ingredients of these long-term evolutionary processes were the slow convergence between the African and Eurasian plates and the presence of several different microplates in the Tethyan realm that produced intermittent phases of subduction and collision (Carminati et al., 2012; Faccenna et al., 2014). Specifically, over the last 30 Myr this region was characterized by the collision of the Adria microplate with the Eurasia plate along the Alpine-Dinaric system and by the retreat of two massive trenches originally located in the area of the current Balearic islands and South of France (e.g., Carminati et al., 2012; Faccenna et al., 2014; Faccenna et al., 2007; Faccenna et al., 2004; Funiciello & Faccenna, 2010; Jolivet et al., 2008; Jolivet et al., 2006; Jolivet et al., 2009; Lonergan & White, 1997; Mauffret et al., 2004; Platt & Vissers, 1989; Romagny et al., 2020; Rosenbaum et al., 2002b; Van Hinsbergen et al., 2020; Van Hinsbergen et al., 2014; Vignaroli et al., 2008). The Ionian trench migrated to the South-East leading to the formation of the Calabria-Peloritan Arc (South Italy) and the Apenninic chain. The Alboran trench retreated toward the South-West forming the Gibraltar arc, the Betic Cordillera (South Spain), and the Rif chain (North Morocco).

The coexistence of these different geodynamic processes has shaped the complex lithospheric structure currently observed in the region. The very low convergence rate between these two continental plates (Dewey et al., 1989; Jolivet & Faccenna, 2000; Ward, 1994) has created the conditions to preserve the geological remains of these past tectonic events on the surface. These singular footprints made the Mediterranean a real open-air laboratory to study a wide range of geodynamic processes and improved our understanding of the Earth's internal structure, mantle dynamics and the interaction between surface tectono-magmatic processes and deep mantle convection patterns.

Over the past decades, seismological observations allowed to indirectly explore the Earth's interior, yielding increasingly detailed constraints on mantle dynamics and structure. In particular, tomographic methods (e.g., P-, S- and surface-wave tomography) yield three-dimensional wave velocity models that are commonly used to infer present-day distributions in physical and chemical properties affecting seismic-wave propagation such as density, temperature, melt fraction and volatile content. Positive seismic wave velocity anomalies are commonly interpreted as cold lithosphere subducted at asthenospheric depths and beyond, while the presence of negative velocity anomalies is explained with mantle portions that are either hotter and/or volatile-rich and/or partially molten (e.g., Aki et al., 1977; Bijwaard et al., 1998; Dziewonski et al., 1977; Fukao & Obayashi, 2013; Fukao et al., 1992; Fukao et al., 2001; Grand et al., 1997; Obayashi & Fukao, 1997; Romanowicz, 2021; Simmons et al., 2010; Spakman & Nolet, 1988; Spakman, 1991; Van der Hilst et al., 1997; Van der Hist et al., 1991; Van der Meer et al., 2018; Zhao et al., 2009; Zhao et al., 1992).

From the early 1990s, many different tomographic models (e.g., Bezada et al., 2013; Gutscher et al., 2002; Piromallo & Morelli, 2003; Spakman, 1991; Spakman et al., 1993; Spakman & Wortel, 2004; Van der Meer et al., 2018; Wortel & Spakman, 2000; Wortel et al., 2009) have illuminated the mantle structure in the Mediterranean revealing the complex and multiform slabs geometry under this region (Figure 1.2). Several positive velocities anomalies interpreted as subducted lithospheric portions have been found below active and fossil subduction margins in the Alboran, Kabylides, Calabria-Apennine, Alpine, Dinarides and Hellenic areas (Bezada et al., 2013; Gutscher et al., 2002; Piromallo & Morelli, 2003; Spakman, 1991; Spakman et al., 1993; Spakman & Wortel, 2004; Van der Meer et al., 2018; Wortel & Spakman, 2000; Wortel et al., 2009). In the same studies, broad low velocity anomalies are imaged in the mantle portions surrounding the slab, which can only be partly

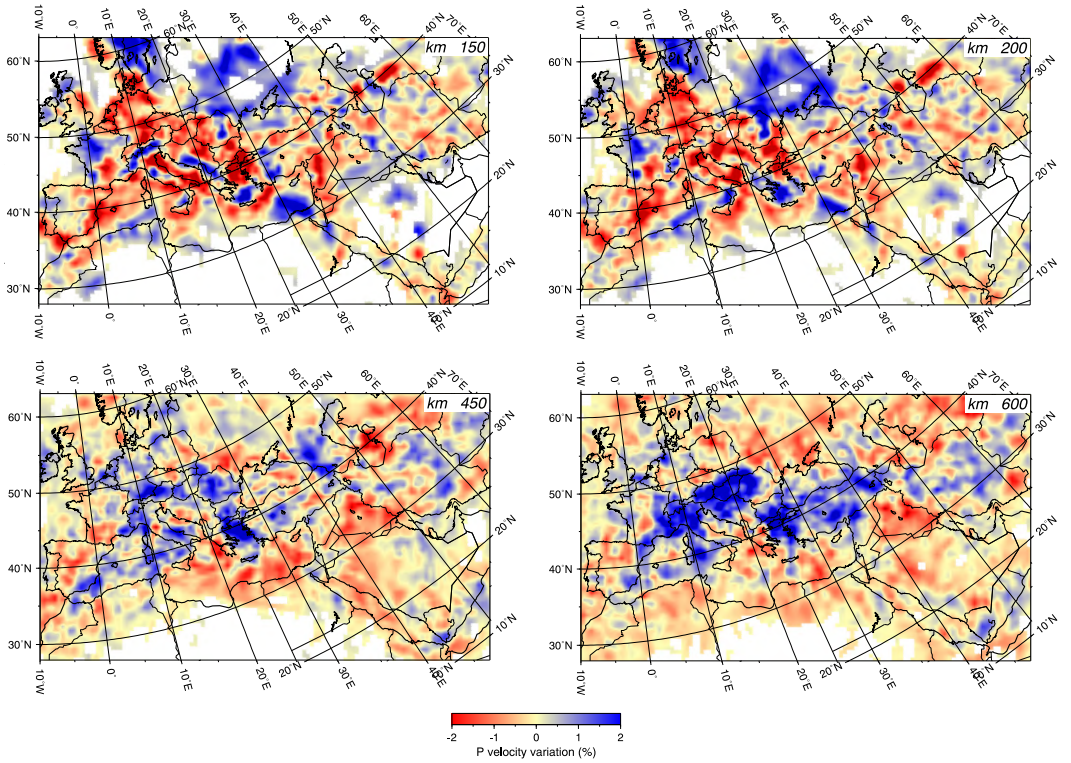

Figure 1.2: *The tomographic model of Piromallo and Morelli (2003) showing the average Vp perturbation at 150, 200, 450 and 600 km depth in the Entire Mediterranean region (courtesy of Andrea Morelli).*

explained with the opening of back-arc basins and related upwelling of hot mantle at lithospheric depths and/or partial melting.

Despite the abundance of geological and geophysical data in the Central-Western Mediterranean region there are still some aspects of its geodynamic history that have not yet been fully elucidated concerning (a) the mechanisms that led to the present-day surface and deep slab geometry, (b) the development and evolution of the episodes of slab tearing and segmentation along northern Africa and the western Adria plate margins, and (c) the relations between mantle dynamics and plate surface and deep kinematics. These uncertainties can be partly addressed by measuring seismic anisotropy, which bears information about the recent dynamics of hot mantle portions, and by exploiting geodynamic modelling.

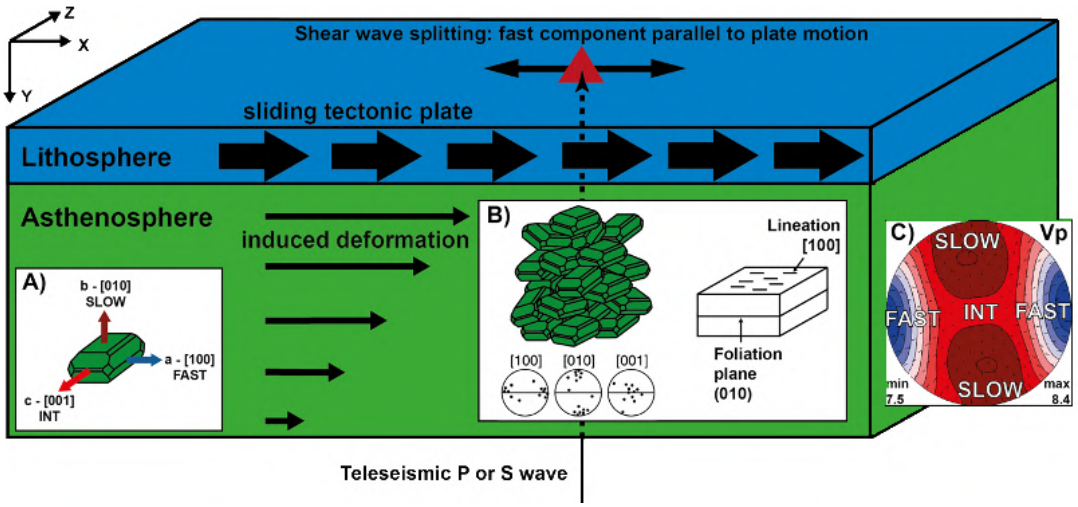

Figure 1.3: *Cartoon sketch of the relationship between horizontal mantle flow induced by a sliding tectonic plate and the resulting macroscopic seismic anisotropy due to A-type olivine fabric. a) Olivine crystal with the relative seismic wave velocities associated with its crystallographic axes (a-[100] fast, b-[010] slow, c-[001] intermediate); b) An aggregate of olivine crystals aligned according to the deformation flow (the A-type fabric is characterized by the fast axis of anisotropy parallel to the horizontal flow direction and by the slow axis normal to the shear plane); c) Pole projection of P-wave velocity varying as a function of the propagation direction for an A-type olivine fabric generated with D-REX. Picture made by Manuele Faccenda.*

Ultramafic rocks of the Earth's upper mantle (above 400 km) are often seismically anisotropic (Burgos et al., 2014; Karato et al., 2008). This is because they are composed by mechanically anisotropic minerals (Figure 1.3), mostly olivine, that under differential stress, and at high pressure and temperature conditions, tend to develop a lattice/crystal preferred orientation (LPO/CPO) which depends on several deformation mechanisms, including plastic deformation, dynamic recrystallization and grain-boundary sliding (Bystricky et al., 2000; Jung, 2017; Kaminski et al., 2004; Lee et al., 2002; Nicolas & Christensen, 1987; Park & Levin, 2002; Zhang et al., 2000).

Seismic anisotropy is the directional dependence of seismic wave velocities. Another phenomenon associated with seismic anisotropy is shear wave splitting (SWS), whereby shear waves splits into two orthogonally polarized components that travel at different speeds. The time delay between the fast and slow components and the polarization direction of the fast component provide information about the strength and orientation of the anisotropic

mantle fabrics (Kaminski & Ribe, 2002; Karato et al., 2008; Long & Becker, 2010; Long & Silver, 2009; Nicolas & Christensen, 1987; Savage, 1999). This direct link between mantle deformation and macroscopic seismic anisotropy can provide important constraints on the mantle flow pattern, dynamics and tectonics (Hess, 1964; Ismaıl & Mainprice, 1998; Jung & Karato, 2001; Jung et al., 2006; Karato, 2008; Karato et al., 2008; Long, 2013; Long & Silver, 2008, 2009; Mainprice et al., 2007; Nicolas & Christensen, 1987; Savage, 1999; Silver, 1996; Skemer & Hansen, 2016; Smith et al., 2001; Tommasi & Vauchez, 2015; Zhao et al., 2016), and, in particular, it may help to reconstruct the recent mantle flow patterns in the Mediterranean region.

Despite its potential importance, investigating the dynamics of the Earth's interior from seismic anisotropy is typically not simple. Firstly, laboratory experiments indicate that the strain-induced LPO patterns vary as a function of the deformation history, temperature, deviatoric stress and water content conditions (Karato et al., 2008). Secondly, an additional anisotropic source can be generated by the preferred orientation of structures such as faults, tabular intrusions, gas or fluid-filled cracks, and layered media with different elastic properties (shape preferred orientation; SPO). It follows that the extrapolation of the mantle flow from seismic anisotropy and SKS splitting studies is neither unique nor always warranted, especially at subduction zones where complex and non-steady-state 3D flow patterns may establish.

Significant directional variations in seismic velocities due to anisotropic fabrics can additionally contaminate tomographic models with apparent thermo-petrological anomalies. Several studies have indeed shown that neglecting the presence of seismic anisotropy in tomographic models, which is a common assumption, can introduce notable imaging artefacts and, consequently, errors in the interpretation of the tomographic results (Bezada et al., 2016; Blackman & Kendall, 1997; Blackman et al., 1996; Kendall, 1994; Lloyd

& Van Der Lee, 2008; Menke, 2015; Sobolev et al., 1999; VanderBeek & Faccenda, 2021). This is a poor assumption considering that tomographic models are used to constrain geodynamic simulations and infer mantle flow and structure (Becker & Boschi, 2002; Faccenna & Becker, 2010; Simmons et al., 2006; Wang & Becker, 2019).

Recently, VanderBeek and Faccenda (2021) and Wang and Zhao (2021) have independently developed a methodology to invert for P-wave isotropic (mean velocity) and anisotropic (magnitude of hexagonal anisotropy, azimuth and dip of the symmetry axis) parameters. When tested on a relatively simple 3D geodynamic model of subduction that includes elastic anisotropy (Figure 1.4a), VanderBeek and Faccenda (2021) found that unaccounted for seismic anisotropy (isotropic approximation) or allowing for only azimuthal variations in seismic velocity (i.e., no dipping fabrics) generates strong imaging artifacts in the tomographic results (Figure 1.4b).

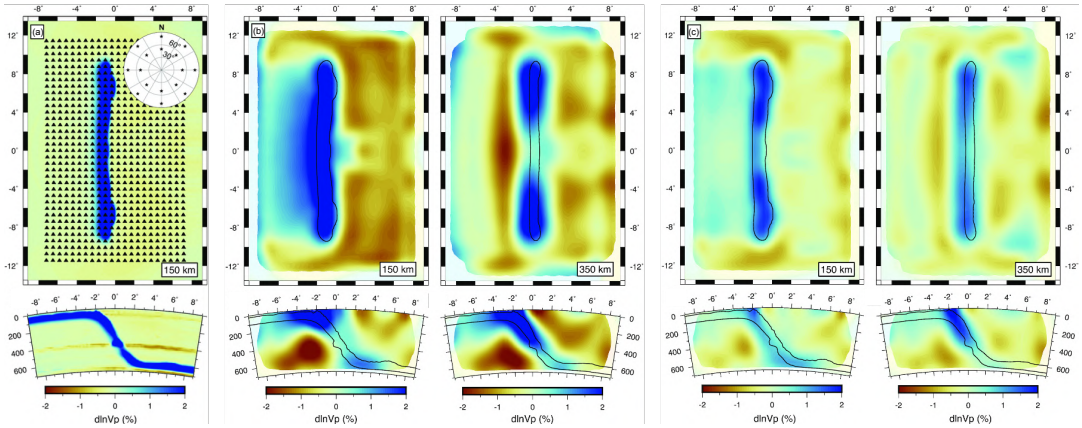

Figure 1.4: *Teleseismic P-wave tomographic reconstructions of subduction simulations from VanderBeek and Faccenda (2021). a) Isotropic model structure with inset displays distribution of synthetic events and triangles showing locations of seismic stations. b) Isotropic inversion of anisotropic data. Velocity perturbations are plotted at 150 km and 350 km depth. East–west cross-sections are plotted at 0° N (left) and 4°30 S (right). Unaccounted for anisotropic structure generates significant distortions in slab geometry and several strong low-velocity anomalies. Interpretations of such features could lead to erroneous inferences on subduction dynamics. c) Isotropic structure recovered from anisotropic inversion that includes symmetry axis azimuth and elevation. Velocity perturbations are plotted as in b. When anisotropic parameters are included in the inversion, all major artifacts are strongly minimized.*

In contrast, this new inversion strategy yields a much more accurate reconstruction of the upper mantle isotropic and anisotropic structures with artifacts strongly minimized (Figure 1.4c). From these tests it follows that inverting for seismic anisotropy can provide new insights into the 3D upper mantle structure and dynamics.

Geodynamic modelling is another fundamental tool for investigating the Earth's internal structure and dynamics. The reason is mainly due to the fact that it "compensates" for the unavailability of the data needed to constrain the evolution of geological processes over time (Gerya, 2019). Most of geodynamics processes in fact occur at timescales and depths that cannot be observed directly (Figure 1.5), therefore theoretical and experimental methods traditionally used are unable to explain the exact nature of these processes (Gerya, 2019; Zhao et al., 2009). Furthermore, the direct measurements of physical parameters (stress, strain, composition, temperature, pressure, etc.) are limited to few rock samples, while numerical models allow to know their distribution anywhere in the computational domain. The principle is simple, many geodynamic problems can be translated into mathematical models, usually a set of partial differential equations and boundary and/or initial conditions defined in a specific computational domain (Ismail-Zadeh & Tackley, 2010; Van Zelst et al., 2021; Zhao et al., 2009). These numerical models are able to quantitatively predict the evolution of the crust and mantle that slowly deform over geological time (Ismail-Zadeh & Tackley, 2010), and in this context the numerical model becomes essential for understanding the long-term and deep evolution of a

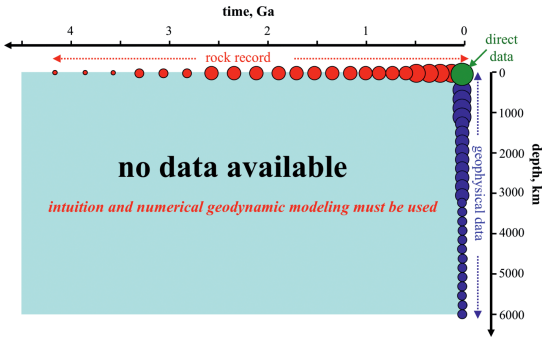

Figure 1.5: *Time-depth diagram showing the availability of data for constraining geodynamic evolution of the Earth from Gerya (2019).*

wide range of geological processes, such as subduction, collision, slab break-off, mantle convection etc.

The rapid development of computational power has particularly favored 3D numerical modelling allowing to explore the real three-dimensional nature of the mantle flow field close to subduction zone (for an interesting review see Jadamec, 2016). This led new insight into slab-driven 3D mantle flow, mantle upwelling at slab edges and upper mantle deformation (Capitanio et al., 2011; Capitanio & Faccenda, 2012; Di Giuseppe et al., 2008; Faccenda & Capitanio, 2013; Funiciello & Faccenna, 2010; Holt et al., 2015; Jadamec & Billen, 2010; Liu & Stegman, 2012; Menant et al., 2016; Paczkowski et al., 2014; Piromallo et al., 2006; Rodríguez-González et al., 2014; Sharples et al., 2014; Stegman et al., 2006; Van Dinther et al., 2010; Zhong & Gurnis, 1996). The ability of 3D models to capture three-dimensional flow patterns in subduction systems has directed many studies to address the anisotropic signature that likely results from mantle flow activated around subducting slabs (Becker & Faccenna, 2009; Faccenda & Capitanio, 2012, 2013; Jadamec & Billen, 2012; Jadamec & Billen, 2010; Long, 2013).

A previous study by Long et al. (2007) has combined flow fields computed from a range of 2D numerical subduction zone models with assumptions about the relationship between the orientation of the maximum finite strain axis and the resulting anisotropy to predict shear wave splitting. This allowed the authors to evaluate how the observable shear wave splitting is affected by different model parameters influencing the finite strain distribution in the mantle wedge. However, dynamic recrystallization was neglected and therefore the magnitude of the calculated anisotropy for large strains was likely underestimated (Ribe, 1992).

Subsequent studies used more realistic models of LPO development based on dynamic recrystallization and plastic deformation. These models have been combined with instantaneous mantle flow solutions to investigate the strain-induced anisotropy of the upper-mantle (Becker et al., 2008; Becker et al., 2006b; Lassak et al., 2006; Miller & Becker, 2012). However, these studies assume time-independent, steady-state flow dynamics. This approximation is effective in global intra-oceanic contexts (e.g., Pacific and Atlantic oceans) where plate motions and shallow mantle flow remained stable over the past 43 Ma (Becker et al., 2003; Faccenna et al., 2013) but it may not be valid near moving mid-ocean ridges and retreating trenches (Heuret & Lallemand, 2005; Masalu, 2007). An important contribution was offered by Faccenda and Capitanio (2012, 2013) that have extended this methodology to account for the non-steady-state evolution typical of many subduction zones, yielding mantle fabrics that are physically consistent with the deformation history.

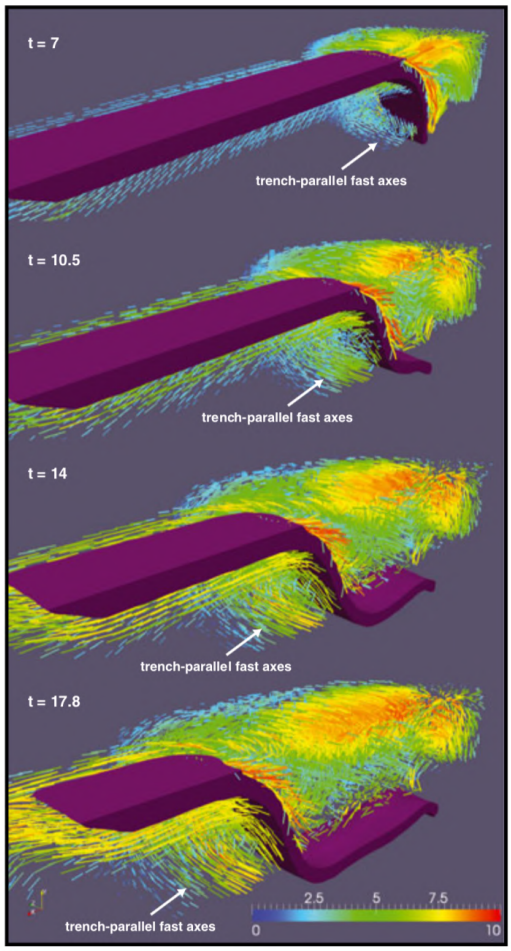

Figure 1.6: *Snapshots of the evolution of a 3D Earth-like subduction model and computed mantle fabric from Faccenda and Capitanio (2012). The purple surface is the contour of the density field around the plate. The length and color of each bar are proportional to the amount of anisotropy. Time is in Ma. In its evolution, the slab sinks through the mantle, rolls back and lies over the 660 km discontinuity. The anisotropy in the sub-slab region increases with subduction and is characterized by two domains, the shallower with trench-perpendicular fast axes and the deeper with trench-parallel anisotropy.*

Modelling the upper mantle seismic anisotropy for 3D numerical models of Earth-like self-consistent subduction, Faccenda and Capitanio (2013) found that a strong upper mantle fabric develops around the retreating slab with a magnitude of the anisotropy proportional to the amount of subduction and independent of the subduction rate. They identified two types of anisotropic domains that control the SKS splitting patterns in the modelled sub-slab mantle (Figure 1.6): the shallower with trench-perpendicular fast axes generated by the subducting plate advance and the deeper with trench-parallel anisotropy due to trench-parallel extension associated with slab retreat. Their results showed that the upper mantle dynamics can be inferred by comparing predictions of numerical flow models with seismic measurements. Furthermore, this new methodology can be applied to any geodynamic setting.

This has paved the way for more recent studies that have applied a numerical approach similar to Faccenda and Capitanio (2012, 2013) to real tectonic settings. Hu et al. (2017) presented a model for the South America Cenozoic subduction history using a geodynamic simulation constrained by both past plate reconstructions and present mantle seismic structures. Then they used the resulting mantle flow to generate synthetic seismic anisotropy datasets that is subsequently compared with SWS measurements and surface wave anisotropy, bringing new insights on the origin of seismic anisotropy in South America. A similar methodology was used by Zhou et al. (2018) to constrain the origin of the complex anisotropy pattern in the Western United States. Confal et al. (2018) modelled the 3-D geodynamics of the Eastern Mediterranean and Anatolian subduction systems, the strain-induced LPO in the upper mantle and seismic wave propagation reproducing to a first order the time-dependent 3D patterns of mantle convection and a resulting seismic anisotropy consistent with measured observations. These studies suggest that by combining geodynamic and seismological simulations it is possible

to predict the relations between upper mantle flow and SKS splitting patterns and reproduce to a first order the overall geodynamic evolution of a given study area.

In this Thesis, the main goal is to investigate the tectonic evolution of the Central-Western Mediterranean convergent margin during the Mid-Late Cenozoic. Its subduction and collision dynamics, over the past 30 million years, involved manifold processes at the micro and macro scale and modelling the complex multi-scale mechanisms that have contributed to shaping the complex lithospheric structure of the region should require a multidisciplinary approach. Here, I use a strategy that combines geodynamic and seismological numerical modelling techniques similar to Confal et al. (2018), Faccenda and Capitanio (2012, 2013), Hu et al. (2017), and Zhou et al. (2018) has been adopted. The research activities attempt to reproduce the articulated structure of the upper mantle beneath this region and provide important geodynamic and seismological constraints on the processes that contributed in shaping the Central-Western Mediterranean. Furthermore, the geodynamic models were exploited as synthetic case studies which were fundamental for testing the capabilities and limitations of P- and S-wave imaging techniques, and that will be likely useful to improve in the future tomographic models of the Earth's mantle.

The objectives of this Thesis are addressed in three different research chapters, which have been published or are in preparation for publication as independent articles and therefore have their own abstract, introduction, method, results, discussion and conclusion. After an overview of the governing equations and the methods presented in the Chapter 2, the body of this Thesis consists of the following chapters:

- **Chapter 3: The Role of Adria Plate Lithospheric Structures on the Recent Dynamics of the Central Mediterranean Region**

  We combine geodynamic and seismological numerical modelling techniques to reproduce and constrain the Mid-Late Cenozoic evolution of the Central Mediterranean region. In the numerical models, calibrated specifically for the Central Mediterranean subduction zone, structural heterogeneities within the Adria plate (a thin continental lithosphere in the modelled Umbria-Marche region and a stiffer continental promontory in its central portion corresponding to the Abruzzo-Laziale platform as suggested by Lucente et al., 2006) have been included. We explore a wide range of models and evaluate the modelling results by comparing seismological synthetics (Rayleigh and P-wave anisotropy, SKS splitting and isotropic anomalies) and the predicted tectonic evolution with geophysical and geological observations. We found that, although the opening of back-arc extensional basins in response to the retreat of the Ionian slab is a common feature in all models, lithospheric heterogeneities within the Adria plate profoundly impact on the segmentation of the subducting slab and are fundamental for the development of key tectonic features such as a prolonged eastward retreat of the Ionian plate and the formation of a slab window below the modelled Central Apennines. This bring new insights into the complex structure of the upper mantle beneath the region confirming that the main geological and geophysical observables in the Central Mediterranean can be directly linked to the recent dynamics of the Ionian slab and Adria plate.

- **Chapter 4: Tomographic image interpretation and Central-Western Mediterranean-like upper mantle dynamics from coupled seismological and geodynamic modelling approach**

  We extended the modelling methodology of Lo Bue et al. (2021) to simulate the geodynamic evolution over ∼20-30 Myr of a model showing similar features to those currently observed in the Central-Western Mediterranean region (e.g., detached or stagnating slabs, slab windows, etc). After comparing the model with SKS splitting observations in order to quantify the discrepancies with the true Central-Western Mediterranean, we use the elastic tensors predicted for the modeled configuration to perform 3D P-wave anisotropic tomography by inverting synthetic P-wave delay times as in VanderBeek and Faccenda (2021). Using the geodynamic model as benchmark, we evaluate the capabilities of seismic tomography to recover a complex subduction environment in different conditions, such as poorly coverage and bad data quality that are common to many real tectonic settings. Despite the non-ideal source and receiver distributions, our results show that the anisotropic P-wave tomography allows to well recover to a first order isotropic structures and anisotropic patterns. However, we observed that, especially in poorly covered areas, the magnitude of anisotropy appears generally underestimated. In the light of future developments, our study suggests that by combining micro- and macro-scale geodynamic simulations and seismological modelling of seismic anisotropy it will be possible to reproduce, at least to a first order, the tectonic evolution of real study regions thus providing fundamental constraints on the processes that have contributed in shaping their current geological scenario.

- **Chapter 5: Imaging upper mantle anisotropy with teleseismic S-wave delays: Insights from tomographic reconstructions of subduction simulations**

  We evaluate the bias introduced when ignoring for seismic anisotropy (isotropic assumption) in shear wave tomographic models. We model the teleseismic shear wavefield through a geodynamic model of subduction that includes elastic anisotropy predicted from micromechanical models of polymineralic aggregates advected through the simulated flow field. The influence on the imaging results of the chosen coordinates system in which S-wave arrival times are measured (e.g., radial versus transverse) is addressed. It's found that the isotropic imaging assumption introduces notable artefacts in the recovered velocity models and, consequently, lead to erroneous inferences regarding mantle dynamics. We observe that when S-wave travel-times are measured in the direction of wave polarisation, the apparent anisotropic shear velocity can be approximated using sinusoidal functions of period π and 2π. The sinusoidal approximation allows us to use ray-based methods to predict S-wave travel-times through anisotropic models. We show that this parameterisation can be used to invert S-wave travel-times for the orientation and strength of anisotropy analogously to the anisotropic P-wave travel-time tomography by VanderBeek and Faccenda (2021), and that artifacts are strongly minimized.

This thesis concludes with a final Chapter 6 where the main goals achieved and possible future perspectives are discussed.

Chapter 2

METHODOLOGY

In the present Thesis, I adopt a methodological approach that combines geodynamic and seismological numerical modelling techniques to simulate the multi-scale mechanisms that have characterized the complex Central-Western Mediterranean convergent margin during the Mid-Late Cenozoic.

The method integrates:

- macro-scale geodynamic modelling of the Central-Western Mediterranean subduction system;
- micro-scale simulations of strain-induced upper mantle fabrics;
- seismological synthetics (isotropic P-wave anomalies, P-wave anisotropy, SKS splitting, Rayleigh wave azimuthal anisotropy and P- and S-wave anisotropic tomography).

In this chapter, after an overview of the equations that govern the thermo-mechanical evolution and the rheology of the Earth's crust and mantle, I describe the numerical software used in the different research activities.

2.1 Macro-scale geodynamic modelling

2.1.1 Governing Equations

Over a geological time scale (i.e., on the order of thousands or millions of years), the Earth's crust and mantle rocks behave like slowly creeping fluids. Accordingly, the concepts of fluid dynamics can be applied to model the Earth's interior and its dynamics. In geophysical fluid dynamics, the equations that govern the thermo-mechanical evolution of the Earth's crust and mantle are derived from physical conservation laws of mass, momentum and energy. These conservation equations are usually formulated as partial differential equations (PDEs) which impose relations between the unknowns variables (i.e., velocity, pressure, and temperature) and their partial derivatives with respect to space and time (Van Zelst et al., 2021). Their solution requires the integration of constitutive relations describing the material properties such as the density and the deformation behaviour under applied stresses (Section 2.1.3 and 2.1.4).

The three conservation equations of mass, momentum and energy can be simplified on the basis of a number of different approximations that are commonly used in geodynamics (see Gassmöller et al., 2020; Schubert et al., 2001; Van Zelst et al., 2021). At sufficiently long timescales, the Earth's mantle can be treated as an incompressible highly viscous medium and the Boussinesq approximations can be adopted (McKenzie et al., 1974). Based on these assumptions, the three equations are briefly described below (for further details please refer to Gerya, 2019).

Earth materials can be considered as a continuous geological media. This implies that, on a macroscopic scale, the material is continuously distributed and completely fills the space it occupies not containing mass-free voids or gaps (e.g., cracks and pores are considered to be filled by fluids/air) (Gerya, 2019; Van Zelst et al., 2021). Displacement in a continuous medium must

proceed without creating voids, i.e., if some rocks are displaced from a certain area other rocks must come into this area and substitute the displaced fragment (Gerya, 2019). This type of continuous behaviour is formalized in the continuity equation, which describes the conservation of mass during the displacement of a continuous medium. This implies that within a fixed volume, local changes in mass must be accompanied by an equal net influx or outflux of mass. These changes are caused by compaction or dilation of material, i.e., a change in density. This usually happens as a response to a change in external conditions (such as a change in temperature or pressure) or due to phase transitions or chemical reactions (Van Zelst et al., 2021). For incompressible media (i.e, when there are no large lateral variations in pressure and temperature and no phase transformations inducing volume changes (Gerya, 2019)), the continuity equation is

$$\nabla \cdot \overrightarrow{u} = 0 \tag{2.1}$$

where $\overrightarrow{u}$ is the velocity (m/s) and $\nabla\cdot$ denotes the divergence operator.

The deformation of a continuous medium is the result of the balance of internal and external forces acting on this medium. The equation of motion that relates forces and deformation is the so-called momentum equation, which describes the conservation of momentum for a continuous medium in the gravitational field. In highly viscous continuous media, the conservation of momentum and the link between forces and deformation can be accurately described by the Stokes equation for slow flow:

$$-\nabla P + \nabla \cdot \tau = -\rho \overrightarrow{g} \tag{2.2}$$

where P,τ, ρ and g are the pressure (Pa), deviatoric stress tensor (Pa), density (kg/m^3) and gravitational acceleration ($g_x = g_z = 0, g_y = 9.81\ ms^{-2}$)

respectively.

In geodynamic processes the heat transport plays a crucial role and is often intrinsically coupled to material deformation (e.g., in the convection of the mantle, subduction etc..). The equation that describes the balance of heat in a continuum and relates temperature changes due to heat generation, advection and conduction is the heat conservation equation:

$$\rho C_p \frac{DT}{Dt} = -\nabla \cdot \overrightarrow{q} + H \tag{2.3}$$

where D/Dt is the material time derivative and ρ, Cp,T and q are the density (kg/m^3), specific heat capacity (J/kg/K), temperature (K) and heat flux (W/m^2), respectively. The heat flux $q(W/m^2)$ is related to the temperature gradient $\frac{\partial T}{\partial x}(K/m)$ according to the Fourier's law of heat conduction:

$$q = -k\frac{\partial T}{\partial x} \tag{2.4}$$

where $k(W/m/K)$ is the thermal conductivity and may depend on P, T, composition and structure of the material. The heat source term H (W/m^3) accounts for radiogenic (i.e., due to the decay of radioactive elements that are present in rocks), adiabatic (i.e., due to changes in pressure) and shear heating (i.e., related to dissipation of the mechanical energy during irreversible non-elastic deformation).

2.1.2 Numerical Method

Many geodynamic problems can be described by mathematical models that are able to quantitatively predict the evolution of the crust and mantle that slowly deform over geological time (Ismail-Zadeh & Tackley, 2010), and in this context the numerical modelling becomes essential for understanding the long-term and deep evolution of a wide range of geodynamics processes.

From a mathematical point of view, by using the three physical principles of the conservation of mass, momentum, and energy, as well as the related chemical laws, the real geodynamic problem can be translated into a mathematical model, usually a set of partial differential equations (PDEs) and boundary and/or initial conditions defined in a specific computational domain (Ismail-Zadeh & Tackley, 2010; Van Zelst et al., 2021; Zhao et al., 2009). Two principal methods are used for solving PDEs: analytical and numerical. Since the non linear nature of crustal and mantle rheologies and their coupling to multi-component systems, it is very difficult to find analytical solutions to solve these equations and, alternatively, discretization and numerical methods are used to find approximate solutions (Gerya, 2019; Ismail-Zadeh & Tackley, 2010; Van Zelst et al., 2021; Zhao et al., 2009; Zhong et al., 2007).

The most popular numerical approaches used in geodynamic modelling are finite difference (FDM), finite element (FEM) and finite volume (FVM) methods. These methods convert the partial differential equations that are used to describe the dynamics of the Earth's interior into a system of linear or non-linear equations that can be solved by matrix algebra techniques. The equations are discretized and solved on a numerical grid (or numerical mesh) made up of a finite number of points that represents the distribution of field variables in space (and time). Each method has its pros and cons, the preference is often determined by the developer's attitude, for example the code used in this Thesis uses the finite difference method (Patankar, 2018). This method is relatively simple to implement and defines the values of the model parameters at the nodes of a grid and approximates the spatial and temporal derivatives at a point by calculating the incremental ratio with respect to the values assumed by the model in the adjacent nodes.

For example, the first derivative of gravity potential by x-coordinate can be computed by using finite differences as follows

$$\frac{\partial \phi}{\partial x} \approx \frac{\Delta \phi}{\Delta x} = \frac{\phi_2 - \phi_1}{x_2 - x_1} \tag{2.5}$$

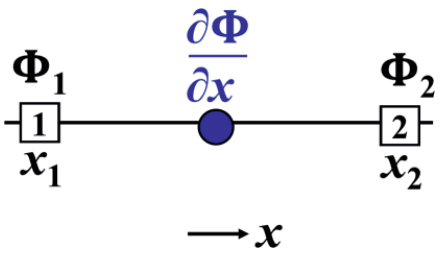

Figure 2.1: *1D numerical grid for computing the first-order derivative of the gravity potential* $\frac{\partial \phi}{\partial x}$ *using FDM from Gerya (2019).*

where $\Delta\phi = \phi_2 - \phi_1$ and $\Delta x = x_2 - x_1$ are the differences in gravity potential u and x-coordinate respectively between points 1 and 2 (Gerya, 2019). The distance Δx regulates the accuracy of the calculation, the smaller the distance the more accurate the solution. Similarly, higher-order derivatives can be calculated.

Grid points can be Eulerian, if they have steady positions or Lagrangian, if they move according to the local flow. An Eulerian grid does not deform with deformation of the medium and this simplifies the numerical formulation. However, a great disadvantage of using an Eulerian grid is the necessity to account for advective terms in time-dependent PDEs, which often causes numerical problems (e.g., numerical diffusion). For a Lagrangian grid it is the contrary, it deforms with the deformation of the medium producing numerical problems while the absence of advective terms in the PDEs is an advantage. The use of either depends on the partial differential equations to be solved and on the type of physical processes to be modeled, although it is often advantageous to use a combination of Eulerian and Lagrangian grids (Gerya, 2019; Zhong et al., 2007).

The discretisation process results in a linear system of equations with its size being the number of unknowns:

$$A * x = b \tag{2.6}$$

where A is a $n * n$ sparse matrix with the coefficients, x is a $n * 1$ vector with the unknowns, typically consisting of velocity components, pressure, and temperature on the grid, and b is a $n * 1$ with the known terms. Such systems typically contain thousands, millions and even billions of linear equations and the methods for solving these large system of equations are subdivided into iterative (e.g., Jacobi, Gauss-Siedel iteration schemes) and direct (e.g., Gaussian, Gauss-Jordan elimination) methods.

Direct methods are used in the case of linear algebraic equations and are systematic procedures based on algebraic elimination. Direct solvers do not require an initial guess, the solution is accurate and no iterations are needed. However, they are computationally expensive and therefore can be used only for 1D and 2D (or small 3D) problems. To solve large 3D problems, iterative solvers are commonly used due to their low memory consumption and relatively small amount of operations. The solution is obtained asymptotically by an iterative procedure. A trial solution is assumed and substituted into the system of equations to determine the mismatch, and an improved solution is obtained from the mismatch data, until a convergent result is achieved (Ismail-Zadeh & Tackley, 2010). However, the accuracy of the solution may be low and convergence may be slow because of large differences in matrix coefficients (high condition number) and residuals at wavelength longer than grid spacing.

Otherwise, higher accuracy and faster convergence can be achieved by using a multigrid method (Fedorenko, 1964; Wesseling, 1995), where the same equations are solved in parallel on several grids (typically with different resolution) and information is exchanged between these grids. A series of coarser grids are constructed by interpolating residuals and field variables from finer

to coarser levels (restriction operation) while computed corrections are interpolated back from coarser to finer levels (prolongation operation). The iterations are then applied to these grids (smoothing), to find corrections at different wavelengths for the correct solution on the finer grid. The corrections are then interpolated again on finer grids (extension). Multigrid approach is widely used in 3D numerical modelling of mantle convection and plate tectonic processes (e.g., Tackley, 2000, 2008) as well as the code I3MG used in this thesis (Gerya, 2019).

In geodynamic modelling, special care must be taken when solving the advection equation, which describes the change in spatial distribution of physical properties over time due to deformation. For a scalar function (A) at an Eulerian point, this equation is written as follows:

$$\frac{\partial A}{\partial t} = -\overrightarrow{v} \cdot grad(A) \tag{2.7}$$

As previously stated, solving this equation in an Eulerian reference frame produces numerical diffusion. To advect field variables describing the physical properties of the medium, I3MG uses the Marker-in-Cell (MIC) technique, that combine the use of Lagrangian advecting points (markers, tracers or particles) with an immobile, Eulerian grid (Christensen, 1982; Gerya, 2019; Schmeling, 1987; Weinberg & Schmeling, 1992; Woidt, 1978). At the beginning of the simulation, properties are distributed on a large amount of Lagrangian points that are advected according to a given/computed velocity field. The advected material properties (e.g., density) are then interpolated from the displaced Lagrangian points to the Eulerian grid. The process is repeated at each timestep. To speed-up the heavy computational load of the 3D models, most of the routines included in I3MG are parallelized using a shared-memory architecture (OpenMP). The software is run on the NEWTON project cluster located in our department which includes the full-shared

memory machine SuperDome Flex 8s (224 interconnected cores).

2.1.3 Rheological Model

Earth's crust and mantle can experience several different (visco-elasto-plastic) deformation mechanisms in relation to stress, strain rates and P-T conditions. Elastic deformation is reversible and has a significant effect for small strains and relatively low stresses applied at a relatively short time scale ($< 10^4$ years). On geological time scales ($> 10^5$ years), typical of the subduction zones, the Earth's mantle behaves basically like an highly viscous fluid, therefore, the elastic response of the lithosphere and mantle can be neglected and only the viscous or visco-plastic rheology is considered (Billen, 2008). Both viscous deformation and plastic yielding are irreversible.

In this Thesis, the mantle mechanical behaviour is modelled using a visco-plastic rheology based on deformation invariants (Ranalli, 1995).

The major mechanism of viscous deformation at high temperature ($> 0.3 - 0.5\ T_{melting}$) and for long lasting mechanical stresses is the solid-state creep, the ability of crystalline substances to deform irreversibly under applied deviatoric stresses. The two major types of high-T creep are diffusion creep and dislocation creep. Diffusion creep is the process of diffusion of atoms through the interior (Herring-Nabarro creep) and along the boundaries (Coble creep) of crystalline grains subjected to stresses that leads to bulk rock deformation. It is typically dominant at relatively low stresses and grain sizes. At higher stresses and large grain sizes, dislocation creep is dominant and is the result of the migration of dislocations (linear defects in the crystal lattice structure) along specific planes through the interior of crystals.

Both diffusion and dislocation creep rheologies are given by the following flow law (Arrhenius-type equation) which relates the second invariant of the

deviatoric stress τ_{II} and the strain rate $\dot{\varepsilon}$ (Karato & Wu, 1993):

$$\dot{\varepsilon}_{II} = A\left(\frac{\tau_{II}}{\mu}\right)^{n}\left(\frac{b}{d}\right)^{m} exp\left(-\frac{E+PV}{RT}\right) \tag{2.8}$$

where P is pressure (Pa), T is temperature (K), R is the gas constant (8.314 J/(K mol)), d is grain size (mm), μ is the shear modulus (Pa) and A, n, m, E and V are experimentally determined rheological parameters: A is the pre-exponential factor (s^{-1}), n is the stress exponent ($n = 1$ in the case of diffusion creep and $n > 1$ in the case of dislocation creep), m is the grain size exponent (m=2-3 for diffusion creep and m=0 for dislocation creep), E is the activation energy (J/mol) and V is the activation volume (m^3/mol).

The equation 2.8 can be reformulate in terms of an effective viscosity ($\eta_{disl,diff}$) written as a function of the second invariant of the deviatoric stress τ_{II} or strain rate $\dot{\varepsilon}_{II}$:

$$\eta_{disl,diff} = \frac{\tau_{II}}{2\dot{\varepsilon}_{II}} \tag{2.9}$$

At low $T < 0.5\ T_{melting}$ and high deviatoric stresses (> 0.1 GPa) , typical of the lithosphere, the dominant creep mechanism is the Peierls mechanism, a temperature-dependent mode of plastic deformation. Rheological flow law for Peierls creep is commonly represented as (Katayama & Karato, 2008):

$$\eta_{peierls} = 0.5A\tau_{II}^{-1} exp\left\{\frac{E+PV}{RT}\left[1-\left(\frac{\tau_{II}}{\sigma_{Peierls}}\right)^{p}\right]^{q}\right\}. \tag{2.10}$$

where $\sigma_{Peierls}, A, E, V, p$ and q are experimentally determined parameters: $\sigma_{Peierls}$ is the Peierls stress (GPa) that limits the strength of the material, A is a material constant for Peierls creep (Pa^2s), E is the activation energy (J/mol) and V is the activation volume (m^3/mol), the exponents p and q depend on the shape and geometry of obstacles that limit the dislocation motion. According to microscopic models, p and q should have the following range

$0 < p \leq 1$, $1 \leq q \leq 2$ (Kocks et al., 1975), in this thesis we use $p = 1$ and $q = 2$ as experimentally determined by (Katayama & Karato, 2008).

The resulting ductile viscosity is given by the harmonic average of the combined dislocation, diffusion and Peierls creep mechanisms:

$$\eta_{ductile} = \left(\frac{1}{\eta_{disl}} + \frac{1}{\eta_{diff}} + \frac{1}{\eta_{peierls}} \right)^{-1} \tag{2.11}$$

The brittle behaviour of rocks is known in continuum mechanics as plastic deformation, which occurs when an absolute shear stress limit τ_y of the medium is reached. A pseudo-plastic viscosity is then computed as:

$$\eta_{pl} = \frac{\tau_y}{2\dot{\varepsilon}_{II}} \tag{2.12}$$

τ_y is determined with a plastic Drucker–Prager criterion (Ranalli, 1995):

$$\tau_y = C_{DP} + \mu P \tag{2.13}$$

where $C_{DP} = C\cos\phi = 1MPa$ is the cohesion, $\mu = \sin\phi$ is the friction coefficient and ϕ is the friction angle and P is total pressure. In our models, to model strain-induced brittle weakening, the initial friction coefficient is linearly decreased upon reaching a final lower value when the accumulated plastic strain is 0.1.

Finally, the effective viscosity is given by:

$$\eta_{eff} = min(\eta_{ductile}, \eta_{pl}) \tag{2.14}$$

Parameter values used in this study are defined in the table 3.1.

2.1.4 Petrological Model

The stable mineralogy and physical properties for the mantle used in our geodynamic models are those computed with the Gibbs free energy minimization program PERPLE_X (Connolly, 2005) and tested by Mishin et al. (2008) for a pyrolytic mantle composition. The Gibbs free energy minimization approach (e.g., Connolly & Kerrick, 1987; De Capitani & Brown, 1987; Dorogokupets et al., 1988; Karpov et al., 1976), by using thermodynamic databases, derives thermodynamic potentials and other physical properties of minerals as a function of P-T conditions via standard thermodynamic relations. This approach favors a more realistic modelling of the mantle (e.g., taking into account changes of rock density and thermal properties during the evolution of different geodynamic processes), and for this reason it has been used on so-called coupled petrological-thermomechanical numerical geodynamic models (e.g., Gerya, 2019; Gerya et al., 2006; Gerya et al., 2004; Mishin et al., 2008; Tackley, 2008).

One of the main effect of taking thermodynamic databases into account is the incorporation of solid-state phase transitions, with uncertainties on mineral thermodynamic properties that increase with depth. These transitions are associated with significant changes in mantle density and seismic wave speeds (Turcotte & Schubert, 2014), and affect the dynamics of mantle convection due to (a) density changes and (b) latent heating (Christensen & Yuen, 1985; Richter, 1973; Schubert et al., 1975; Tackley, 1993; Zhong & Gurnis, 1994). In our numerical models, the only major phase transition is the olivine-spinel occurring at about 410 km depth (the spinel-perovskite reaction at 670 km depth does not affect at all the model evolution that is confined in the upper mantle and transition zone). Although the slab has a more depleted composition, it has been demonstrated that the density anomalies of a harzburgitic mantle are similar to those of a pyrolitic composition (Faccenda

& Dal Zilio, 2017). This confirms what was found by the study of Nakagawa et al. (2009), which showed that even at global scale when using phase assemblages with different major oxides abundance and computed with the same software (PERPLE_X) the mantle convection patterns do not change substantially.

2.1.5 Petrological-Thermo-Mechanical macro scale geodynamic modelling - software I3MG

The software used in this Thesis to create 3D petrological-thermo-mechanical models is I3MG (Gerya, 2019). This code numerically solve the governing equations defined in the previous sections in a 3D Cartesian geometry and is based on staggered[1] finite differences and marker-in-cell techniques combined with iterative multigrid solvers. A detailed explanation of how the code works can be found in Gerya (2019). Here we will only give a brief overview of the main steps of the algorithm.

Firstly, the code simultaneously solves the momentum and continuity equations to obtain values for velocity that are present in both equations and pressure. The temperature equation is only solved later because it requires adiabatic and shear heating values which are calculated from the velocity, pressure, stress, and strain rate fields. Lastly, the code discretizes the advection equation as it requires a velocity field. Physical properties are transported through a 3D staggered Eulerian grid by Lagrangian markers, driven by a velocity field interpolated from the Eulerian grid. Physical parameters such as temperature, pressure, stresses, strain rates and velocities (advection) are recomputed at every timestep. The main steps of the algorithm are as follows:

[1] A staggered grid consists of several types of nodal points having different geometrical positions at which different variables are defined. These type of grids are convenient choice for thermomechanical numerical problems with variable viscosity when finite differences are used to solve the continuity, Stokes and temperature equations.

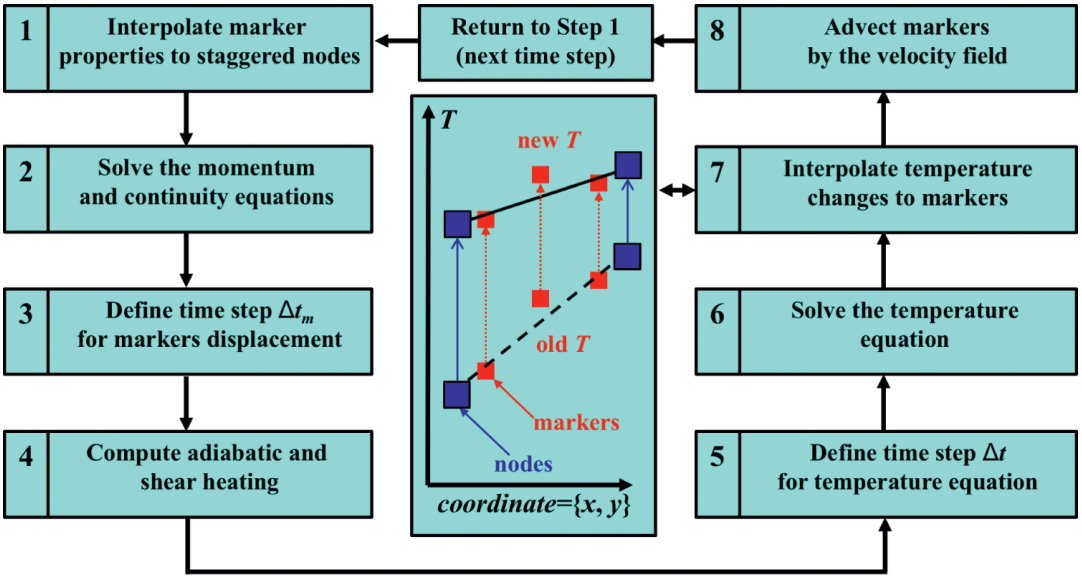

Figure 2.2: *Possible structure of a numerical thermomechanical viscous 2D code, which employs staggered finite differences and marker-in-cell technique (SFD-MIC) to solve the momentum, continuity and temperature equations taken from Gerya (2019)*

(1) Interpolate marker proprieties to staggered nodes. The code calculates the scalar physical properties ($\eta_m, \rho_m, \alpha_m, C_{pm}, k_m$, etc.) for each marker and interpolates these properties from the markers to various Eulerian nodes and applies boundary conditions for the nodal temperatures interpolated from markers.

(2) Solve the momentum and continuity equations. It discretizes the 3D Stokes and the incompressible 3D continuity equations using a multigrid approach.

(3) Define an appropriate displacement time step Δ_t for markers based on the velocity field computed in Step 2.

(4) Compute the shear and adiabatic heating terms H_s and H_a at the Eulerian nodes.

(5) Define a suitable time step Δ_t for the 3D temperature equation.

(6) Discretize the 3D temperature equation in a Lagrangian formulation.

(7) Interpolate the calculated nodal temperature changes from the Eulerian nodes to the markers and calculate new marker temperatures (T_m) taking into account physical diffusion on a subgrid (marker) level.

(8) Advect markers by velocity field. The code uses a fourth-order in space, first-order in time classical Runge-Kutta scheme combined with continuity-based velocity interpolation to advect all markers throughout the mesh according to the globally calculated velocity field v. Return to Step 1 to perform the next time step.

2.1.6 Initial configuration of 3D models - software geomIO

Performing 3D geodynamic numerical simulations requires accurate and realistic initial configurations. A powerful tool that allows us to build a very detailed initial model is the MATLAB toolbox geomIO (Bauville & Baumann, 2019). This software constructs 3D geometries from 2D drawings realized in a vector-graphics editor (i.e. Inkscape) and adds a temperature and compositional distribution to the model. Hence, it is possible to create a 3D regional numerical model starting from a 2D map of the region of interest.

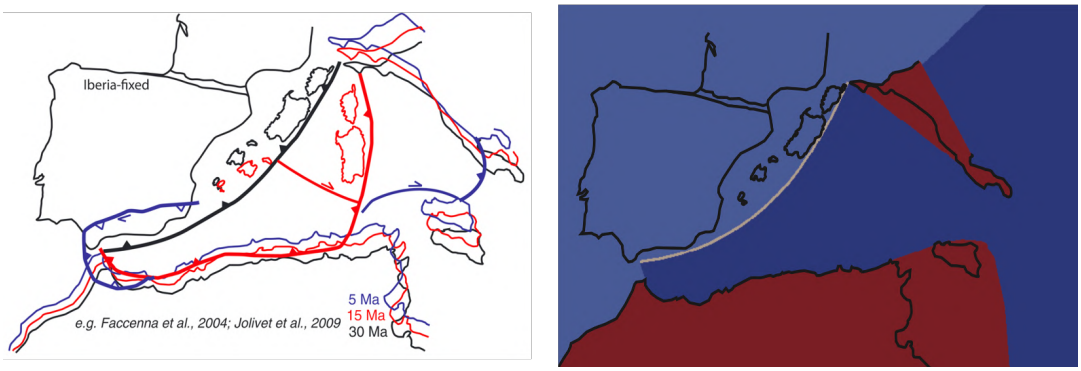

Figure 2.3: *Example of initial setup of the Mediterranean region realized using the MATLAB toolbox geomIO. The initial model consists of two continental plates (Africa and Adria; red), an overriding plate (Eurasia; light blue) and a subduting oceanic plate (Ionian Ocean; blue) according to a paleogeographic reconstruction at 30 Ma proposed by Faccenna et al. (2014), Jolivet et al. (2009), and Van Hinsbergen et al. (2014).*

In this Thesis, we use geomIO to build realistic initial numerical models representing the tectonic configuration of the Central-Western Mediterranean 30 million years ago. We use the graphic software Inkscape to draw 2D maps of the main tectonic plates that characterized the Mediterranean region 30 Ma based on tectonic and paleogeographic reconstructions present in the literature (Faccenna et al., 2014; Lucente et al., 2006; Lucente & Speranza, 2001; Romagny et al., 2020; Van Hinsbergen et al., 2014). Then, we create the 3D initial temperature and compositional model using the MATLAB toolbox geomIO (Bauville & Baumann, 2019) setting the initial lithosphere temperature distribution of each geological plate according to the half-space cooling model (Turcotte & Schubert, 2014), while the underlying asthenosphere is characterized by a constant adiabatic temperature gradient of $0.5 K km^{-1}$. The detailed model of the region generated with geomIO is then imported on I3MG to define a realistic initial setup of the petrological-thermo-mechanical models.

2.2 Seismological Modelling

2.2.1 Seismic Anisotropy in the Upper Mantle

Seismic anisotropy is an intrinsic property of elastic materials that causes a variation in the seismic wave velocities as a function of their propagation and/or polarization directions (Crampin, 1981; Hansen et al., 2021; Long & Becker, 2010). Mathematically, anisotropy is described by the elastic stiffness tensor, C_{ijkl}, which relates stress σ_{ij} and strain ϵ_{kl} in a continuous media (the general Hooke's law):

$$\sigma_{ij} = C_{ijkl}\epsilon_{kl} \tag{2.15}$$

The elastic tensor C_{ijkl} is a 4th order stiffness tensor represented by a matrix of 81 elastic parameters. If all components of the tensor are known,

a complete description of the seismic anisotropy can be calculated for any elastic medium. The elastic properties of geological media are often characterized by a symmetry that reduces the number of the stiffness tensor components, in fact media with higher symmetry require fewer parameters for their description. For the most general case (triclinic symmetry class), 21 independent elastic moduli are needed to describe the medium, but the Earth's mantle can be further approximated with hexagonal symmetry, which requires only 5 independent elastic constants. This approximation allows to reduce the necessary number of parameters for the description of seismic anisotropy. One way to describe seismic anisotropy in an elastic medium is in terms of radial (or transverse isotropy) or azimuthal anisotropy. The first refers to a difference in propagation velocity between horizontally and vertically polarized waves (Long & Becker, 2010), and is defined as the squared ratio of the horizontally polarized S-wave velocity to the vertically polarized S-wave velocity, $(\frac{V_{sh}}{V_{sv}})^2$ (Hansen et al., 2021). The latter indicates a directional dependence of wave velocity with azimuth. These two anisotropy descriptors provide valuable insight into anisotropic fields that reflect dynamic processes within the Earth, including upper mantle flow directions (e.g., radial anisotropy helps to differentiate between horizontal and vertical mantle flow while azimuthal anisotropy may provide information on the direction of horizontal mantle flow).

In the mantle, seismic anisotropy is caused mainly by the non-random distribution of crystallographic orientation of intrinsically anisotropic minerals, called lattice-preferred orientation (LPO), or crystallographic-preferred orientation (CPO) or simply fabric (Kaminski & Ribe, 2001; Karato et al., 2008; Nicolas & Christensen, 1987; Wenk, 2016; Zhang & Karato, 1995). LPO reflects the deformation processes to which a rock has been subjected. Therefore, if the relationship between LPO and the anisotropic field is known, then

observation of seismic anisotropy can provide constrains on mantle dynamics, mantle flow pattern and tectonics (Hansen et al., 2021; Jung, 2017; Jung & Karato, 2001; Jung et al., 2006; Karato et al., 2008; Long, 2013; Long & Silver, 2008; Nicolas & Christensen, 1987; Savage, 1999).

The development of crystal aggregates LPO in the upper mantle depends on several deformation mechanisms, including plastic deformation and dynamic recrystallization (Bystricky et al., 2000; Kaminski et al., 2004; Lee et al., 2002; Nicolas & Christensen, 1987; Zhang et al., 2000).

Laboratory experiments on single crystals have shown that plastic deformation occurs heterogeneously due to crystalline slip. Slip is characterized by a slip plane (plane on which slip occurs) and a slip direction (direction along which slip occurs), together they form a slip system. Slip system is identified by Miller indices (hkl)[uvw] where (hkl) indicates the plane and [uvw] the orientation. Plastic deformation take places by the propagation of a slip front (Orowan, 1934; Polanyi, 1934; Taylor, 1934), that is a line (not necessarily a straight line) that separates the region of a crystal that has already slipped from the undeformed one (Karato, 2008). This line is called a dislocation. The orientation and magnitude of a dislocation is characterized by the Burgers vector. This vector is parallel to the slip direction.

As previously stated, dislocation creep is the most important mechanism for producing LPO in Earth's interior. It produces crystal rotation and preferential alignment of crystal (CPO), with the easy-slip plane oriented in the direction of flow. This means that knowing which slip system is active allows to infer the flow direction. However, there are generally several slip systems in a mineral active at different temperatures and the dominant slip system can change when the physical/chemical conditions of deformation change (Karato, 2008). These changes result in major changes in the nature of LPO. Consequently, it is necessary to know the dominant slip system under

a given physical and chemical condition to infer the geometry of the deformation from the seismic anisotropy.

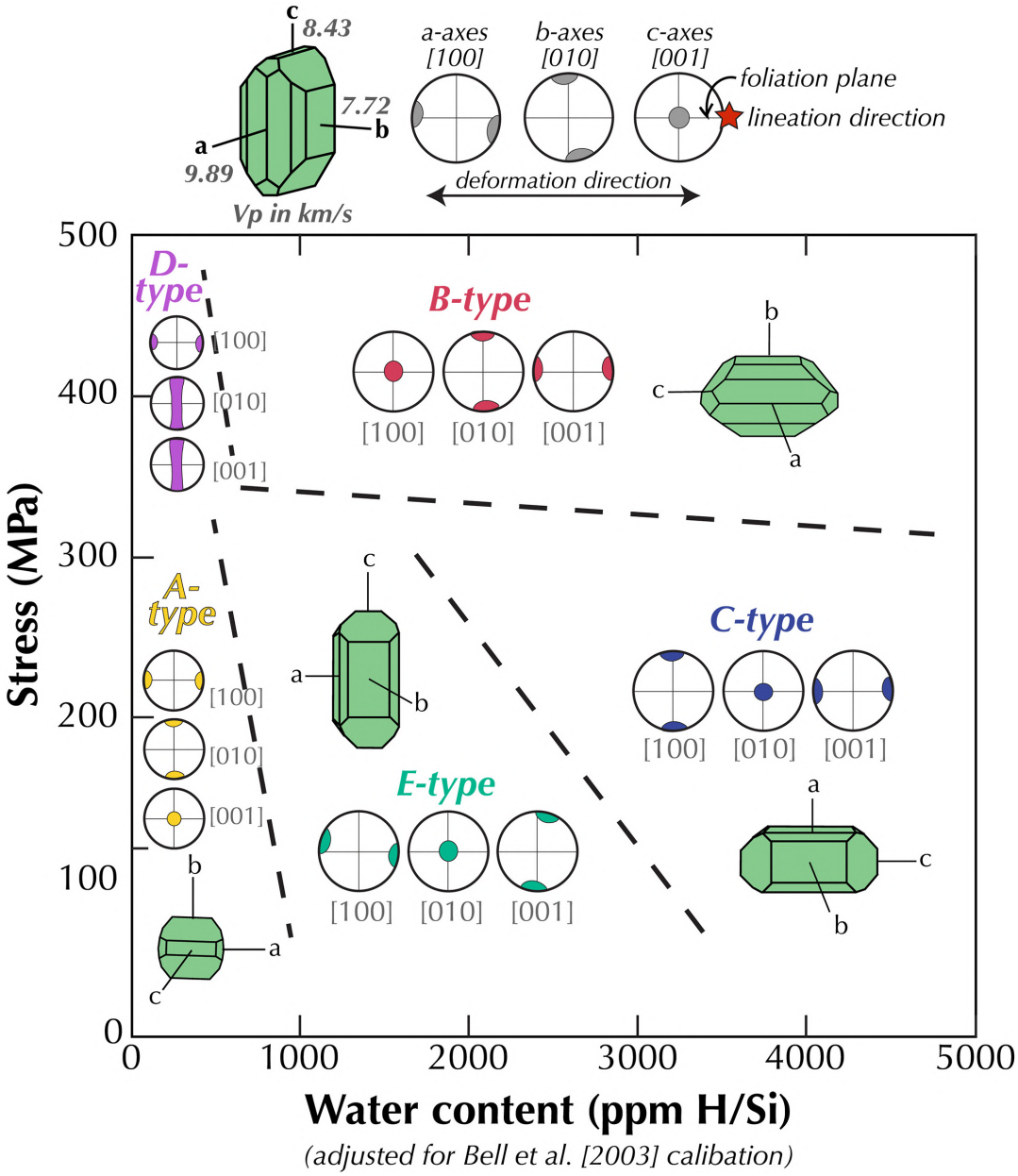

Figure 2.4: *Deformation fabrics of olivine as a function of water content and stress from Bernard et al. (2019).*

The major contribution to the upper mantle anisotropy is mainly due to the olivine LPO, as olivine is the most abundant mineral and has a large intrinsic single-crystal anisotropy (18% for shear waves; e.g., Mainprice et al., 2007). The way in which the three crystallographic axes of olivine (a-fast, b-slow, c-intermediate) align with respect to the shear direction is often

classified according to the types of LPO (e.g., A-, B-, C-, D-, and E-type, see Karato et al., 2008).

In recent decades, several laboratory experiments focusing on the relationship between LPO types and deformation conditions, indicated that olivine LPO patterns may vary as a function of the deformation history, temperature, deviatoric stress and water content conditions (Hansen et al., 2014; Jung & Karato, 2001; Jung et al., 2006; Karato et al., 2008; Katayama et al., 2004; Katayama & Karato, 2006). In figure 2.4, five types of olivine LPO are shown as a function of water content and stress (Bernard et al., 2019). For example, at relatively low stresses, high temperatures, and low water contents, A-type olivine fabric prevails (Karato et al., 2008), which result in an LPO pattern where the fast axes of individual olivine crystals tend to align in the direction of shear. While at relatively high stresses, low temperatures and in the presence of water, B-type fabric dominates and in this case the fast axes of olivine tend to align 90° away from the maximum shear direction in the shear plane (Jung & Karato, 2001; Long & Becker, 2010). Therefore, the relation between seismic anisotropy and flow geometry is mineral specific and also depends on the physical and chemical conditions (Karato, 2008). It follows that the extrapolation of the mantle flow from seismic anisotropy is not straightforward. It is also worth noting that some efforts have been made to explain the effect of anisotropy into rheology (Christensen, 1987; de Montserrat et al., 2021; Király et al., 2020). Király et al. (2020) suggest that anisotropic viscosity in the asthenosphere can significantly affect the motions of tectonic plates playing a critical role in upper mantle dynamics, however, for simplicity, this effect has not been considered here.

Micro-scale geodynamic modelling of strain-induced LPO development - software D-REX_M

The strain-induced LPO can be estimated using sophisticated numerical software that account for the basic macrophysics of the deformation mechanisms (Becker et al., 2003; Blackman & Kendall, 2002; Chastel et al., 1993; Dawson & Wenk, 2000; Kaminski et al., 2004; Tommasi, 1998; Wenk & Tomé, 1999). A software widely used to study the upper mantle strain-induced anisotropy in mantle convection models (Lassak et al., 2006; Miller & Becker, 2012) is D-REX (Kaminski et al., 2004). The original version of this code calculates the LPO of olivine-enstatite aggregates in steady-state convective flows by plastic deformation, dynamic recrystallization (by sub-grain rotation and grain-boundary migration), and grain-boundary sliding of small grains. A detailed explanation of the equations used in this code to calculate the LPO and related seismic anisotropy can be found in Browaeys and Chevrot (2004), Kaminski and Ribe (2001), Kaminski and Ribe (2002), and Kaminski et al. (2004).

In this Thesis, we use a modified version of D-REX (Kaminski et al., 2004), that in addition accounts for the non-steady-state evolution of geodynamic systems (Faccenda & Capitanio, 2012, 2013), for the LPO of transition zone and lower mantle aggregates and for elastic properties scaled by the local P-T conditions (Faccenda, 2014). This modified version, called D-REX_M, can be found inside the open source software package ECOMAN.

A large number of regularly spaced Lagrangian particles representing upper and transition zone mantle mineral aggregates is initially placed in the computational domain. Each particle consists of a number of randomly oriented crystals forming an isotropic upper mantle. For example, in the first 410 km of the upper mantle it is usually used a modal composition of 70%

olivine and 30% orthopyroxene aggregate to recreate an harzburgitic composition while in the transition zone mantle a more fertile, pyrolitic composition is employed (60% spinel and 40% majoritic garnet) (Faccenda, 2014).

These particles are then advected by means of the Eulerian velocity field obtained by the macro-flow simulations (section 2.1.5) with a fourth-order Runge-Kutta scheme. At each time-step, the orientations of these crystals change in response to gradients in the velocity field, generating LPO.

At the end of the simulation, an elastic tensor C_{ijkl} (2.15) is generated. It is calculated as a function of the crystals orientation, volume fraction, modal composition of the aggregate, single crystal elastic properties scaled by the local P-T conditions, and with a Voigt averaging scheme.

Synthetic SKS Splitting - software FSTRACK

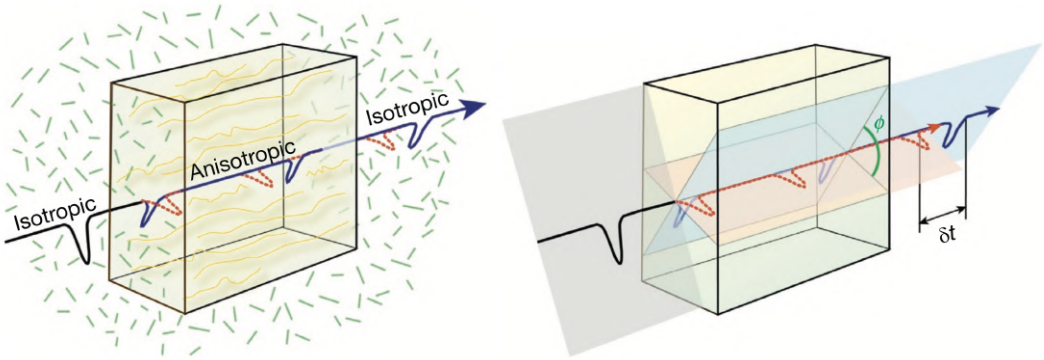

Figure 2.5: *Schematic diagram showing the shear wave splitting phenomenon. S-wave (in black) traverses an anisotropic medium and splits into a fast S wave (in blue) and a slow one (in red). The delay time δ_t gives information about the strength of anisotropy, the azimuth Φ about the geometry of the anisotropy. Figure from Maupin and Park (2015) (courtesy of Ed Garnero).*

A widely diffused method to detect seismic anisotropy is by measuring the splitting of seismic shear waves (SWS). When a shear wave travels through an anisotropic medium, it splits in two orthogonally polarized S waves travelling with different velocities (Babuska & Cara, 1991; Bowman & Ando, 1987; Savage, 1999). This phenomenon can be analyzed by measuring two parameters: the delay time δ_t between the arrival of the fast and

slow S waves and the polarization azimuth Φ of the fast wave (Figure 2.5). These splitting parameters yield constraints on the anisotropic structures of the Earth mantle and crust, the first is proportional to the thickness and the intrinsic anisotropy of the medium while the second contains information about the geometry of the anisotropic fabric.

The analysis of shear wave splitting is commonly applied to the SKS phases. When entering the liquid outer core, S-waves are converted into P waves and all source-side anisotropy is removed. At the core-mantle boundary (CMB) they are then converted in radially polarized SV waves. If along the raypath from the CMB to the surface they encounter an anisotropic medium, they are split and some signal is recorded on the transverse component (Sieminski et al., 2008; Silver & Chan, 1991). Numerical simulations have shown that SKS waves are mostly sensitive to anisotropic parameters at upper mantel depths (Sieminski et al., 2008). Hence, SKS splitting patterns are useful to constrain the receiver-side upper mantle fabrics.

In this Thesis, the synthetic SKS splitting is computed using the routines included in the software package FSTRACK (Becker et al., 2006b). We use the elastic tensors of the olivine-enstatite aggregates calculated from DREX_M (section 2.2.1) as input for FSTRACK. These routines calculate the SKS splitting parameters (polarization azimuth Φ and delay time δ_t) starting from the elastic tensors of the olivine-enstatite aggregates calculated from DREX_M. Synthetic seismograms are computed using the cross-correlation method developed by Menke and Levin (2003) through the following steps:

(1) A 2D grid of virtual seismic stations regularly spaced is constructed at the surface of the large-scale geodynamic model.

(2) Below each station and down to 400 km and after recovering the elastic tensors from each aggregate's stiffness matrix, the code builds a vertical stack of horizontal layers (minimum thickness of 25 km) where the

elastic tensor of each layer is radially averaged within a distance of 50 *km*. This is about the SKS waves Fresnel zone at 100 km depth (Monteiller & Chevrot, 2011). To avoid the formation of too many thin layers, the elastic tensors are averaged into one single matrix when the vertical distance between two or more particles is less than 25km.

(3) Next, assuming an incident plane wave (5° for typical SKS arrivals) into the mantle over a range of frequencies from 0 to 25 Hz, it computes a pulse seismogram via inverse Fourier transform using the method of (Kennett, 2009) with anisotropic extensions (Booth & Crampin, 1983; Chapman & Shearer, 1989).

(4) The resulting synthetic seismograms in the SKS band (3.3–10 s) are then constructed applying band-pass filters from 0.1 to 0.3 Hz that represent the typical frequency band for SKS waves (Faccenda & Capitanio, 2012, 2013).

(5) Finally, the SKS splitting parameters are determined by applying the cross-correlation method of Menke and Levin (2003) and, due to dependence of splitting parameters on back azimuth (Becker et al., 2006b), by averaging all the fast azimuths and delay times at each station measured by rotating the vertical stack of elastic tensors by 5° intervals around the vertical y-axis.

2.2.2 P- and S-waves Anisotropic tomography

In chapters 4 and 5 of this Thesis, geodynamic models were exploited as synthetic case studies to test the capabilities and limitations of P- and S-wave anisotropic imaging techniques to accurately capture subduction zone structure. Here, the methodology proposed by VanderBeek and Faccenda (2021) for imaging upper mantle anisotropy with teleseismic P-wave delays is briefly

described. For the part concerning S-waves Anisotropic tomography, please refer to chapter 5, where the method is fully explained.

VanderBeek and Faccenda (2021) presented a new strategy for the inversion of teleseismic P-wave delays for upper mantle isotropic velocity and arbitrarily oriented hexagonal anisotropy. P-wave tomography requires the prediction of ray paths and P-wave traveltimes. To address this issue the method employs the shortest path algorithm (Moser, 1991) inside the main study volume and the TauP method (Buland & Chapman, 1983) outside assuming a 1D earth model.

It is well established that the Earth's mantle can be approximated with hexagonal symmetry (Becker et al., 2006a). This approximation allows to describe the directional dependence of P-wave velocity with a periodic function of 2α and 4α where α is the angle between the symmetry axes and the wave propagation direction (Backus, 1965; Thomsen, 1986). Considering that in the mantle 4α is an order of magnitude smaller than 2α, P-wave velocity can be further simplified as:

$$v = \overline{v}[1 \pm f\cos(2\alpha)] \tag{2.16}$$

where $\overline{v}$ is isotropic velocity and f is the fractional magnitude of the velocity variations whose sign indicates whether the symmetry axis is the fast or the slow one. Its value is fixed throughout the inversion. Since $\cos(2\alpha)$ is equal to the dot product of the ray directional vector and the anisotropic symmetry axis vector, the eq. 2.16 can be expanded as:

$$v = \overline{v}[1 \pm f(2[\cos(\theta)\cos(\gamma)\cos(\phi-\psi) + \sin(\theta)\sin(\gamma)]^2 - 1)] \tag{2.17}$$

where θ and γ are the ray and symmetry axis elevation and ϕ and ψ are the ray and symmetry axis azimuth, respectively.

The parameterization proposed by VanderBeek and Faccenda (2021), although not linear, has the advantage of separating variables that control the orientation and magnitude of azimuthal anisotropy from the variable that controls dip. This allows of using a purely isotropic starting model from which estimating in a first step azimuthal anisotropy, and subsequently dip anisotropy. Alternative methods exist for for azimuthal and dip anisotropy inversions, but require anisotropic starting models already close to the final solution (Munzarová et al., 2018).

By introducing three anisotropic terms,

$$A = (n_1^2 - n_2^2) \tag{2.18}$$

$$B = 2n_1n_2 \tag{2.19}$$

$$C = n_3 \tag{2.20}$$

where n is the symmetry axis vector, the eq. 2.17 can be rewrote in terms of slowness u as follows

$$\begin{aligned} u = \overline{u}[1 \pm ([A\cos(2\phi) + B\sin(2\phi)]\cos^2(\theta) - G\sin^2(\theta) - C^2\cos(2\theta) \\ + \sqrt{2}C[s_1(G+A)^{1/2}\cos(\phi) + s_2(G-A)^{1/2}\sin(\phi)]\sin(2\theta))]^{-1} \end{aligned} \tag{2.21}$$

where $G = \sqrt{A^2 + B^2}$ and $s_1 = sign(n_1)$, $s_2 = sign(n_2)$ to avoid sign ambiguity. One can recover the spherical anisotropic parameters of equation 2.17 as $f = G + C^2$, $\psi = \arctan[B/(G+A)]$ and $\gamma = \arctan[C/G^{1/2}]$.

Next, the partial derivatives of the travel time with respect to slowness and the three anisotropic parameters are calculated from equation 2.21. A system of equations is obtained which is solved using the LSQR approach (Paige & Saunders, 1982). Given the high number of unknowns (i.e. $4 \times$ #*nodes*), regularization through damping and smoothing factors is required to solve the ill-posed problem.

Chapter 3

The Role of Adria Plate Lithospheric Structures on the Recent Dynamics of the Central Mediterranean Region

R. Lo Bue[1], M. Faccenda[1], and J. Yang[1]

This manuscript is published as: "Lo Bue, R., Faccenda, M., & Yang, J. (2021). The Role of Adria Plate Lithospheric Structures on the Recent Dynamics of the Central Mediterranean Region. Journal of Geophysical Research: Solid Earth, 126(10), e2021JB022377". MF conceived the study. RLB performed and analyzed all the numerical experiments, and wrote the first draft of the manuscript. JY contributed to the preparation of the initial setup and implementation of the rheological model. All the authors contributed equally to the discussion of the results and to the conclusions of this study.

[1]Dipartimento di Geoscienze, Università di Padova, Padova, Italy

Abstract

The Tertiary tectonic evolution of the Central Mediterranean has been relatively well constrained by abundant geological data. Yet, several uncertainties persist about the mechanisms that led to the present-day surface morphology and deep slab geometry. Here, we combine geodynamic and seismological numerical modeling techniques to reproduce the recent large-scale evolution of the Central Mediterranean and the associated strain-induced upper mantle fabrics and seismic anisotropy. 3D thermo-mechanical subduction models were designed and calibrated according to paleogeographic-tectonic reconstructions and seismological observations available in the literature. It is found that, although the opening of back-arc extensional basins in response to the retreat of the Ionian slab is a common feature in all models, structural heterogeneities within the Adria plate and/or the geometry of its Tyrrhenian passive margin profoundly impact on the segmentation of the subducting slab and the amount of Ionian trench retreat. More, in general, this study highlights the importance of coupling geodynamic and seismological modeling to better constrain the tectonic evolution of complex convergent margins such as the Central Mediterranean.

Plain Language Summary

The Central Mediterranean represents one of the most complex subduction zones on Earth. Its recent tectonic evolution is linked to the motion of three main plates (Africa, Adria, and Europe) and to the opening of the Liguro-Provençal and Thyrrenian basins. However, the mechanisms that led to the present-day surface and deep morphology of the region remain unclear. Here, we present a new approach, which can reduce these uncertainties by combining geodynamic and seismological numerical modeling techniques.

Our study confirms that the main geological and geophysical observables in the Central Mediterranean are likely linked to the recent dynamics of the Tyrrhenian slab and the Adria plate. In addition, we show that structural heterogeneities within the Adria plate play an important role in the formation of a wide slab window below the Central Apennines, in the retreat of the Northern Apennines and the Ionian trenches till the present-day position, and in the curvature of the Apennines chain.

Key Points:

- Geodynamic and seismological modeling methods are combined to reproduce the recent evolution of the Central Mediterranean
- The influence on trench shape and slab tears of structural heterogeneities within the Adria plate is addressed
- Geodynamic models are validated against seismic anisotropy observations

3.1 Introduction

In the geodynamic context of the slow convergence between the African and Eurasian plates, the Central Mediterranean region has been involved in a complex subduction process that over the last 30 Myr was characterized by the rapid retreat of the Ionian trench, the opening of back-arc extensional basins (i.e., Liguro-Provençal, Algerian, and Tyrrhenian basins) and episodes of slab lateral tearing, segmentation, and break-off (Carminati et al., 2012; Faccenna et al., 2014; Faccenna et al., 2007; Faccenna et al., 2004; Jolivet et al., 2006; Jolivet et al., 2009; Mauffret et al., 2004; Rosenbaum et al., 2002b; Van Hinsbergen et al., 2014). Although the shallow tectonic evolution has been

relatively well constrained by a wealth of geological data, several uncertainties persist about the recent mantle dynamics of this region and the interaction between surface tectono-magmatic processes and deep mantle convection patterns. Analog and/or numerical modeling of 3D mantle flow evolution specifically designed for the Mediterranean could provide important clarifications about these processes. However, given the high complexity of the Mediterranean tectonic setting, few research groups have attempted to reproduce its evolution.

On the one hand, analog models of a single subducting and rolling back slab have been able to address and reproduce some of the key aspects of the Central Mediterranean history such as (a) the initiation of the subduction process, (b) the subduction dynamics and their relationships with plate kinematics, (c) the episodicity of back-arc extension, and finally (d) the role played by slab-induced mantle circulation (Aster et al., 2012; Guillaume et al., 2010; Guillaume et al., 2013). On the other hand, 3D numerical models have highlighted the importance of considering appropriate plate geometries and lateral buoyancy variations to reproduce the recent dynamics of the Central-Western Mediterranean and Alpine regions (Kaus et al., 2020; Lo Bue & Faccenda, 2019; Magni et al., 2014).

Among the aspects of the Central Mediterranean geodynamic history that have not yet been fully clarified, there are (a) the development and evolution of the episodes of slab tearing and segmentation along northern Africa and the western Adria plate margins, and (b) the relations between mantle dynamics and plate surface and deep kinematics. The latter can be estimated by measuring seismic anisotropy generated by strain-induced lattice/crystal preferred orientation (LPO/CPO) of intrinsically anisotropic minerals, which is thought to be the primary source of seismic anisotropy (Park & Levin, 2002). As there is a direct link between upper mantle deformation and macroscopic seismic anisotropy, a quantitative analysis of the seismic anisotropy

may help to reconstruct the recent upper mantle flow patterns.

Laboratory experiments indicate that the strain-induced LPO patterns vary as a function of the deformation history, temperature, deviatoric stress, and water content conditions (Karato et al., 2008). It follows that the extrapolation of the mantle flow from seismic anisotropy is neither simple nor always warranted, especially at subduction zones where complex and non-steady-state 3D flow patterns may establish. A promising approach that helps to reduce the number of plausible models that can explain a given anisotropy data set is to compare seismic measurements with predictions of numerical and experimental flow models (Long et al., 2007). Traditional numerical modeling studies of mantle fabrics and the associated anisotropy assume time-independent, steady-state flow dynamics (Becker et al., 2006b). This method is effective in global intra-oceanic contexts (e.g., Pacific and Atlantic oceans) where plate motions and shallow mantle flow remained stable over the past 43 Ma (Faccenna et al., 2013). Recently, Faccenda and Capitanio (2012, 2013) have extended this methodology to account for the non-steady-state evolution typical of many subduction zones, yielding mantle fabrics that are physically consistent with the deformation history. Hu et al. (2017), Zhou et al. (2018) and Confal et al. (2018) applied a similar modeling approach to real tectonic settings, such as the South America, the North America, and the eastern Mediterranean subduction systems, respectively.

In this study, we first briefly review the Central Mediterranean tectonic evolution and the seismological data available for the region. Subsequently, we show the results of applying the modeling methodology of Faccenda and Capitanio (2012, 2013) to the Central Mediterranean convergent margin. The modeling results are then evaluated and discussed by comparing seismological synthetics (SKS splitting, Rayleigh and P-wave anisotropy, and isotropic

anomalies) and the predicted tectonic evolution with geophysical and geological observations. Throughout the study, we use "Ma" to indicate geological time before present, and "Myr" when referring to the elapsed time after the start of the model.

3.1.1 Tectonic Evolution of the Region

The tectonic evolution of the entire Mediterranean region in the Mid-Late Cenozoic is connected with the relative motion of three main plates (Africa, Adria, and Europe) and in its central portion is dominated by the collision between the Adria and Eurasian plates along the Alps. Two oceanic trenches flanked the Alpine collision: the Liguro-Provençal/Tyrrhenian trench on the western side (object of this study) and the Hellenic trench on the eastern side. The presence of an unknown number of smaller continental blocks and oceanic basins in the Tethyan realm produced intermittent phases of subduction and collision that led to the currently observed complex geological setting (Carminati et al., 2012; Faccenna et al., 2014).

Before ∼30–35 Ma, the underthrusting of the European continental lithosphere below Apulia-Adria induced the formation of the Alps. After ∼30–35 Ma, when the subduction rate of the Ionian ocean overcame the Africa-Eurasia convergence rate, the tectonic regime along the oceanic trenches switched from compressional to extensional. The evolution of this later tectonic stage (Figure 3.1a) can be summarized in several episodes of slab roll-back and opening of back-arc basins (Carminati et al., 2012; Dewey et al., 1989; Faccenna et al., 2014; Faccenna et al., 2007; Faccenna et al., 2004; Gueguen et al., 1998; Jolivet et al., 2009; Malinverno & Ryan, 1986; Rosenbaum et al., 2002a; Wortel & Spakman, 2000).

Several widely accepted tectonic reconstructions indicate that at ∼35–30 Ma an incipient Ionian slab was already present in the upper mantle below

the Corsica-Sardinia continental block, which may have triggered the subsequent "spontaneous" evolution of the subduction system (Faccenna et al., 2014; Faccenna et al., 2001). In the first stage of back-arc extension, from ∼32-30 Ma to ∼16-15 Ma, Corsica and Sardinia were separated from the European mainland by a ∼40° clockwise rotation, leading to the opening of the Liguro-Provençal basin (Faccenna et al., 2014; Faccenna et al., 1997; Gattacceca & Speranza, 2002; Rollet et al., 2002; Rosenbaum et al., 2002b). The collision between the Corsica-Sardinia microplate with the western margin of Adria caused the formation of the Apennines (Patacca et al., 1990).

The second major stage of trench retreat, from ∼15 Ma to the present-day, led to the opening of the Tyrrhenian Sea basin. The first period of extension was characterized by continental lithosphere thinning in the northern Tyrrhenian Sea, and by trench retreat in the western part of the southern Tyrrhenian Sea. In the latest Messinian (6–5 Ma), the ultrafast roll-back rate of the narrow Ionian slab toward the southeast induced the opening of the southern Tyrrhenian Sea basin and the formation of new oceanic lithosphere. This happened in two distinct episodes with the formation of the Vavilov Basin (4–3 Ma) and, further to the east, of the Marsili Basin (2–1 Ma) surrounded by the currently active Aeolian island arc (Faccenna et al., 2007).

3.1.2 Isotropic Seismic Tomographies

Since the late 1990s, seismic tomographic methods have revealed several positive velocities anomalies interpreted as subducted lithospheric portions lying below the Alboran, Kabylides, and Calabria-Apennine areas Bezada et al. (2013), Gutscher et al. (2002), Piromallo and Morelli (2003), Spakman (1991), Spakman et al. (1993), Spakman and Wortel (2004), Van der Meer et al. (2018), Wortel and Spakman (2000), and Wortel et al. (2009).

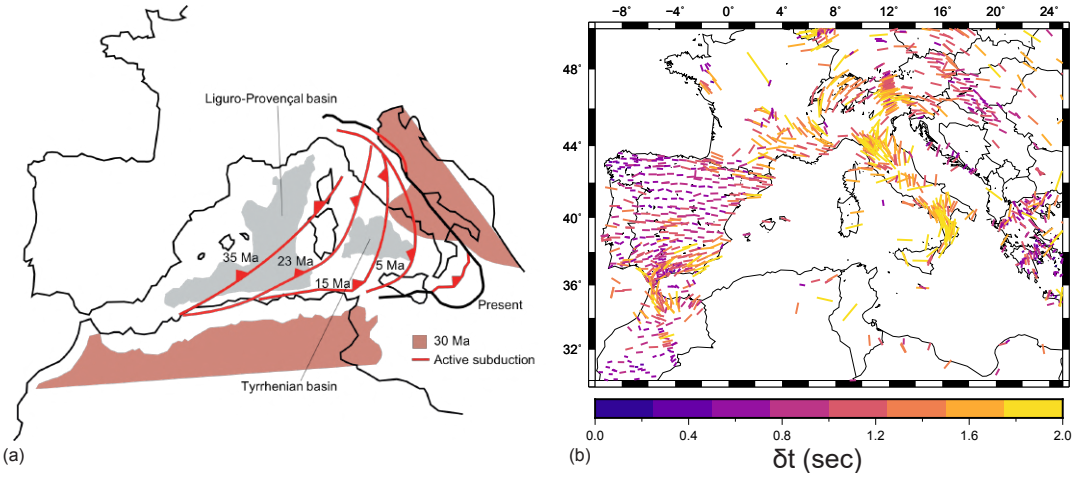

Figure 3.1: *(a) Evolution of the Central Mediterranean region in the last 30 Ma (adapted from Faccenna et al. (2014), Lucente et al. (2006), Lucente and Speranza (2001), and Van Hinsbergen et al. (2014)). Red lines indicate active subduction at different age stages, while the black thick line is the present-day frontal thrust. The brown region illustrates the geometry of the Africa and Adria continental plates, excluding the thin margins, at 30 Ma (adapted from Lucente et al. (2006), Lucente and Speranza (2001), and Van Hinsbergen et al. (2014)). (b) SKS-splitting data in the Central-Western Mediterranean (Becker et al., 2012) and references therein updated as of December 06, 2020; (http://www-udc.ig.utexas.edu/external/becker/sksdata.html). The bars show the orientation of the SKS fast component and their length and color coding is proportional to the delay time.*

A dominant feature in P-wave tomographic models is a broad high velocity anomaly associated with the North Apenninic-Calabrian slab (Amato et al., 1993; Lucente et al., 1999; Piromallo & Morelli, 2003; Selvaggi & Chiarabba, 1995; Spakman et al., 1993; Spakman & Wortel, 2004; Van der Meer et al., 2018).

To the south, the narrow Calabria slab appears to broaden at the base of the upper mantle and to stagnate in the mantle transition zone of the Central Mediterranean (Neri et al., 2009; Spakman & Wortel, 2004). A similar result was obtained by Giacomuzzi et al. (2012) using a tomographic inversion based on analysis of relative residuals of S-wave arrivals from teleseismic events, and by Scarfì et al. (2018), who detected a narrowing of the subduction system caused by horizontal tearing affecting both the sides of the slab.

Neri et al. (2012) analyzed different geophysical data sets (gravity anomalies, seismic tomographic structure, and seismicity within the crust and uppermost mantle) and proposed that the slab is still continuous beneath the central part of the Calabrian arc, whereas detachment has already occurred beneath the arc edges (beneath northern Calabria and northeastern Sicily). Presti et al. (2019) suggested that clear necking of the foundering slab has already occurred (at a depth of 150 km), slab detachment has not happened yet but appears to be geologically close, implying the imminent end of the subduction process in the Central Mediterranean.

Further north along the Apenninic chain, several seismic tomography studies associated high-velocity anomalies to the subducted Ionian ocean and western margin of the Adria plate (Benoit et al., 2011; Giacomuzzi et al., 2012; Kästle et al., 2018; Koulakov et al., 2009; Lucente et al., 1999; Piromallo & Morelli, 2003; Rosenbaum et al., 2008; Spakman & Wortel, 2004; Van der Meer et al., 2018; Zhao et al., 2016). The same studies indicate that the high-velocity anomalies found below the Calabrian arc and the Northern Apennines appear to be laterally continuous below 250 km depth. At shallower depths, instead, a slow velocity anomaly is found below central Italy, which is associated with the presence of a slab window.

The vertical continuity and lateral extent of the slab beneath the northern Apennines are debated. Based on early tomographic models showing no apparent connection between the Adriatic plate and the subducted lithosphere, Spakman (1990) and Spakman et al. (1993) interpreted the northern Apennines deep anomaly as a detached slab under the entire Apennines resulting from the lateral migration of a slab tear from north to south. Conversely, the subsequent regional mantle models of Piromallo and Morelli (1997, 2003) exhibit local evidence for a continuous slab beneath Tuscany, at the same location where Spakman et al. (1993) found a small slab gap only

about 50 km wide. Other teleseismic tomography studies of the Italian peninsula do not reveal any significant gap in the subducted lithosphere below the northern Apennines, and suggest the presence of a slab window below the central-southern Apennines and in between the two high-velocity bodies in the northern Apennines and Calabrian regions (Amato et al., 1993; Lucente et al., 1999). Following these results, Lucente and Speranza (2001), proposed an evolution of the Apennines arc-trench system strongly influenced by the irregular shape of the Adria continental margin colliding with the trench. According to this study, the cessation of subduction and the detachment of the slab beneath central Italy was possibly caused by the presence of a thick continental lithosphere promontory of the Adria plate. However, more recent studies suggest that the northern Apennines slab reaches a depth of only ∼150-300 km Giacomuzzi et al. (2012) and Spakman and Wortel (2004).

El-Sharkawy et al. (2020) used Rayleigh wave tomography to image the entire Mediterranean upper mantle down to about 300 km. Although Rayleigh wave tomographies are characterized by a low lateral resolution and are affected by vertical smearing (strictly speaking, also teleseismic body wave tomographies of the upper mantle bear the same problem), they provide a useful source of information about the structure of shallower mantle layers that supplement those derived from body wave models. The El-Sharkawy et al. (2020)'s model highlights that the Calabrian slab is vertically continuous in the area beneath Calabria and easternmost Sicily but detached beneath the southern Apennines and the northern Sicily. In particular, a low-velocity anomaly extending from 70 km down to about 250 km depth is detected beneath the Central Apennines, which supports the presence of the Central Apennines Slab Gap. Below 250 km depth, a high-velocity anomaly is detected below the central Apennines, which can be related to the top edge of the north-westward dipping Calabrian Slab. Further north, the high-velocity anomaly appears to extend down to only 250 km depth beneath the

Northern Apennines.

3.1.3 Seismic anisotropy

Seismic anisotropy is widespread in the Mediterranean and it shows a complex pattern that likely has some relations with the recent (20–30 Ma) tectonic evolution of this region (Buontempo et al., 2008; Lucente et al., 2006; Schmid et al., 2004). Measurements of shear wave splitting of core-refracted (mainly SKS and SKKS, herein referred for simplicity to just SKS) waves in the Central Mediterranean is characterized by average delay times of around 1–2 s, suggesting the presence of well-developed upper mantle fabrics and strong seismic anisotropy. The SKS fast azimuths have a preferential trend of NNW-SSE (i.e., trench parallel) along the Apenninic belt, which is turning to a more NS orientation over the Apennines foreland (Baccheschi et al., 2007; Civello & Margheriti, 2004; Lucente & Margheriti, 2008; Lucente et al., 2006; Margheriti et al., 2003; Petrescu et al., 2020; Plomerová et al., 2006; Salimbeni et al., 2013) (Figure 3.1b). The trench-parallel anisotropy appears to be in contrast with the trench-perpendicular P-wave fast directions found by Hua et al. (2017), in correspondence of the isotropic high-velocity anomaly imaged beneath the Northern Apennines as described in Section 3.1.2. Moving westward over the Tyrrhenian basin, SKS delay times increase and the fast azimuths, parallel to the stretching direction of the back-arc basin, have been related to back-arc extension (Faccenna et al., 2014; Jolivet et al., 2009; Lucente et al., 2006). More in general, EW-oriented fast directions running parallel to the opening trajectory of the Liguro-Provençal and Tyrrhenian basins are observed in the Central Mediterranean by both SKS and Rayleigh waves (Zhu & Tromp, 2013). Beneath the central Apennines, instead, smaller delay times have been interpreted as being due to a larger vertical component of shear and related steeply oriented fast axes (Lucente & Margheriti, 2008).

The presence of trench-perpendicular SKS fast azimuths has been related to either subduction windows or to toroidal mantle flow patterns at the edge of slabs. An example of the latter feature can be found in the Sicily channel where SKS fast axes turn to NS and then EW in the Tyrrhenian Sea (Baccheschi et al., 2007; Civello & Margheriti, 2004).

3.2 Methods

In this section, we describe the numerical methods used to generate subduction-induced mantle flow patterns and to calculate strain-induced mantle fabrics and synthetic seismic anisotropy.

3.2.1 Mechanical numerical modelling

3D petrological-thermo-mechanical models of subduction have been carried out with I3MG that is based on the finite difference method (FDM) combined with a marker-in-cell (MIC) technique (Gerya, 2019). The physical properties are defined on and advected by Lagrangian markers. A staggered Eulerian grid is defined to solve the equations of conservation of mass (Equation 3.1), momentum (Equation 3.2), and energy (Equation 3.3):

$$\nabla \cdot \overrightarrow{u} = 0 \tag{3.1}$$

$$-\nabla P + \nabla \cdot \tau = -\rho \overrightarrow{g} \tag{3.2}$$

$$\rho C_p \frac{DT}{Dt} = -\nabla \cdot \overrightarrow{q} + H \tag{3.3}$$

where D/Dt is the material time derivative and $\overrightarrow{u}, P, \tau, \rho, C_p, \overrightarrow{g}, T, \overrightarrow{q}$ are the velocity, pressure, deviatoric stress, density, heat capacity, gravitational acceleration ($g_x = g_z = 0, g_y = 9.81\ ms^{-2}$), temperature and heat flux, respectively. The heat source term H accounts for radiogenic, adiabatic and shear heating.

The stable mineralogy and physical properties for the mantle used in our models are those computed with PERPLE_X (Connolly, 2005) and tested by Mishin et al. (2008) for a pyrolytic mantle composition. One of the main effect of taking thermodynamic databases into account is the incorporation of solid-state phase transitions, with uncertainties on mineral thermodynamic properties that increase with depth. These transitions are associated with significant changes in mantle density and seismic wave speeds (Turcotte & Schubert, 2014), and affect the dynamics of mantle convection due to (1) density changes and (2) latent heating (Christensen & Yuen, 1985; Richter, 1973; Schubert et al., 1975; Tackley, 1993; Zhong & Gurnis, 1994). In our numerical models the only major phase transitions is the olivine-spinel occurring at about at 410 km depth (the spinel-perovskite reaction at 670 km depth does not affect at all the model evolution that confined in the upper mantle and transition zone). Although the slab has a more depleted composition, it has been demonstrated that the density anomalies of a harzburgitic mantle are similar to those of a pyrolitic composition (Faccenda & Dal Zilio, 2017). This confirms what found by the study of Nakagawa et al. (2009), which showed that even at global scale when using phase assemblages with different major oxides abundance and computed with the same software (PERPLE_X) the mantle convection patterns do not change substantially.

The numerical domain is a cartesian box defined by the $(x - y - z)$ coordinates ($2600 \times 700 \times 1800\ km$) discretized with ($261 \times 101 \times 181$ nodes), with y being the vertical direction. Velocity boundary conditions are free slip everywhere. We focus on modeling self-consistent subduction driven by internal buoyancy forces (no kinematic conditions are prescribed). A constant temperature of 273 K is applied at the top boundary, while a constant incoming heat flux of 2 mW/m^2 is imposed at the bottom boundary. The side boundaries are insulating.

Table 3.1: *Physical properties of rocks used in this study.*

Property	Symbol	Value	Unit
Diffusion Creep (Karato & Wu, 1993)			
Pre-exponential factor	A	$8.7 \cdot 10^{15}$	s^{-1}
Activation energy	E	300	$kJmol^{-1}$
Activation volume	V	4.5	cm^3mol^{-1}
Stress exponent	n	1	-
Grain-size exponent	m	2.5	-
Burger vector	b	0.5	nm
Grain size	d	1	mm
Dislocation Creep (Karato & Wu, 1993)			
Pre-exponential factor	A	$3.5 \cdot 10^{22}$	s^{-1}
Activation energy	E	540	$kJmol^{-1}$
Activation volume	V	17	cm^3mol^{-1}
Stress exponent	n	3.5	-
Grain-size exponent	m	0	-
Peierls Creep (Katayama & Karato, 2008)			
Pre-exponential factor	A	$10^{7.8}$	Pa^2s
Activation energy	E	532	$kJmol^{-1}$
Activation volume	V	12	cm^3mol^{-1}
Peierls stress	$\sigma_{Peierls}$	9.1	GPa
Exponent	p,q	1, 2	-,-

$R = 8.313\ Jmol^{-1}K^{-1}$ is the gas constant, while μ = 80 GPa is the shear modulus.

The mantle mechanical behaviour is modelled using a visco-plastic rheology based on deformation invariants (Ranalli, 1995). The effective viscosity is given by the harmonic average of the combined dislocation, diffusion and Peierls creep mechanisms (parameters and physical meaning are defined in Table 3.1):

$$\eta_{ductile} = \left(\frac{1}{\eta_{disl}} + \frac{1}{\eta_{diff}} + \frac{1}{\eta_{peierls}} \right)^{-1} \tag{3.4}$$

where the dislocation and diffusion creep are given by (Karato & Wu, 1993):

$$\dot{\varepsilon}_{II} = A \left(\frac{\tau_{II}}{\mu}\right)^{n} \left(\frac{b}{d}\right)^{m} exp\left(- \frac{E + PV}{RT} \right) \tag{3.5}$$

$$\eta = \frac{\tau_{II}}{2\dot{\varepsilon}_{II}} \tag{3.6}$$

where the flow laws are written as a function of the second invariant of the deviatoric stress τ_{II} or strain rate $\dot{\varepsilon}_{II}$. At elevated stresses ($> 0.1GPa$) typical of low-T conditions creep is accommodated via the Peierls mechanism as (Katayama & Karato, 2008):

$$\eta_{peierls} = 0.5 A \tau_{II}^{-1} exp\left\{ \frac{E + PV}{RT} \left[1 - \left(\frac{\tau_{II}}{\sigma_{Peierls}} \right)^{p} \right]^{q} \right\}. \tag{3.7}$$

A pseudo-plastic viscosity is computed as:

$$\eta_{pl} = \frac{\tau_{y}}{2\dot{\varepsilon}_{II}} \tag{3.8}$$

Finally, the effective viscosity is given by:

$$\eta_{eff} = min(\eta_{ductile}, \eta_{pl}) \tag{3.9}$$

The plastic strength τ_y is determined with a plastic Drucker–Prager criterion Ranalli (1995):

$$\tau_y = C_{DP} + \mu P \tag{3.10}$$

where $C_{DP} = C\cos\phi = 1MPa$ is the cohesion, $\mu = \sin\phi$ is the friction coefficient and ϕ is the friction angle. To model strain-induced brittle weakening, the initial friction coefficient is linearly decreased upon reaching a final lower value when the accumulated plastic strain is 0.1. The lower and upper cutoff of the viscosity are set to 10^{18} and 10^{24} $Pa\,s$.

The geometry of the Central Mediterranean was drawn according to the paleogeographic and tectonic reconstructions at ~30 Ma proposed by Lucente and Speranza (2001), Lucente et al. (2006), Faccenna et al. (2014) and Van Hinsbergen et al. (2014). The 3D initial temperature and compositional (crust vs. mantle) fields were created with the MATLAB toolbox geomIO (Bauville & Baumann, 2019) and then imported on I3MG to define the initial setup of the petrological-thermo-mechanical model.

The initial numerical model (Figure 3.2) consists of a subducting oceanic plate that represents the Ionian Ocean, two lateral continental blocks corresponding to the Adria and Africa plates, and an overriding plate that corresponds to the Iberia and European plates. To initiate subduction self-consistently, (a) a wide slab is located from Gibraltar to Corsica dipping 40° and extending down to 300 km in the upper mantle, (b) a rheologically weak zone has been inserted on the slab top surface to lubricate the initial contact between the overriding and the subducting plates (constant viscosity of 10^{18} $Pa\,s$ and constant density of 3200 kg/m^3), and (c) the overriding plate in between the trench and the European plate is composed of a young lithospheric portion that offers little resistance to slab roll-back and trench retreat. The 300 km long slab is needed to trigger slab roll-back self-consistently, and it might

be representative of a more recent stage of the Central Mediterranean history rather than the 30 Ma assumed here. In some models, the Adria plate structure, located in the current Apenninic area, is characterized by the presence of a stiffer continental promontory in its central portion and of a thin continental lithosphere in the Umbria-Marche region (Calcagnile & Panza, 1980; Geiss, 1987; Lucente et al., 2006; Lucente & Speranza, 2001; Maino et al., 2013; Miller & Piana Agostinetti, 2012; Panza et al., 2003). The African plate consists of a slightly thinner margin on its eastern side toward the Ionian ocean (Arab et al., 2020). The initial lithosphere temperature distribution has been determined according to the half-space cooling equation (Turcotte & Schubert, 2014), while the underlying asthenosphere is characterized by a constant adiabatic temperature gradient of 0.5 Kkm^{-1}. The continental plates (Africa, Africa eastern margin, Iberia, Adria, and Adria promontory) are set to be 150 Myr, the western-northern portion of Adria is 90 Myr old to replicate a thin continental lithosphere, the young portion of the upper plate is 1 Myr to facilitate the trench retreat (we justify the young age by assuming a well-developed continental rifting system North of the Balearics and Corsica-Sardinia block). The subducting oceanic plate is 80 Myr old (which is representative of the thermal structure of the Piemonte-Ligurian oceanic lithosphere 30 Ma ago; Van Hinsbergen et al. (2014)), while the slab in the mantle has an age of 70 Myr to model partial heating up by surrounding mantle. The density is calculated using the thermodynamic databases except in some models where for the crust of the continental promontory we use a constant value of 2700 kg/m^3. Otherwise, the continental crust density is computed as being that of the mantle minus 400 kg/m^3, except for the Adria thin margin where we subtract 200 kg/m^3 to model a less buoyant continental lithosphere. A detailed description of the crust and lithospheric mantle thicknesses together with other information for each plate can be found in Table 3.2.

Table 3.2: *Rheological parameters, effective thickness and age of the different plates for the Reference Model CM. For all the other models we only indicate the differences with respect to Model CM.* ρ_{mantle} *is the mantle density from the thermodynamic databases. The viscosity of the weakzone is constant* (10^{18} *Pas). The employed low friction coefficients for crustal material ensure lubrication at the plates contact and one-sided, terrestrial-like subduction geometry Gerya et al. (2008).*

Plate Name	Effective Thickness [km]		Friction coefficent [-]		Density [kg/m^3]
MODEL CM					
Lithosphere	*Crust*	*Mantle*	*Initial*	*Final*	
Eurasia (150 Myr)	20		0.020	0.005	$\rho_{mantle} - 400$
		60	0.600	0.400	ρ_{mantle}
Africa W (150 Myr)	40		0.020	0.005	$\rho_{mantle} - 400$
		60	0.600	0.400	ρ_{mantle}
Africa E (150 Myr)	25		0.020	0.005	$\rho_{mantle} - 400$
		65	0.600	0.400	ρ_{mantle}
Adria Promontory (150 Myr)	40		0.600	0.400	2700
		50	0.600	0.400	ρ_{mantle}
Adria thin margin (90 Myr)	15		0.020	0.005	$\rho_{mantle} - 200$
		70	0.600	0.400	ρ_{mantle}
Ionian Ocean (90 Myr)	10		0.020	0.005	ρ_{mantle}
		80	0.600	0.400	ρ_{mantle}
Upperplate (1 Myr)	10		0.010	0.010	ρ_{mantle}
		80	0.600	0.400	ρ_{mantle}
Weakzone (70 Myr)	20	-	-	-	3200
MODEL A					
Adria thin margin is absent					
MODEL B					
Adria promontory is absent					
MODEL C-F1-F2					
Adria promontory and Adria thin margin are absent					
MODEL D1					
Adria Promontory crust	"	"	"	"	$\rho_{mantle} - 500$
MODEL D2					
Adria Promontory crust	"	"	"	"	$\rho_{mantle} - 400$
MODEL D3					
Adria Promontory crust	"	"	"	"	$\rho_{mantle} - 300$
MODEL D4					
Adria thin margin crust	"	"	"	"	$\rho_{mantle} - 400$
MODEL E					
Adria Promontory crust	"	"	0.020	0.005	"

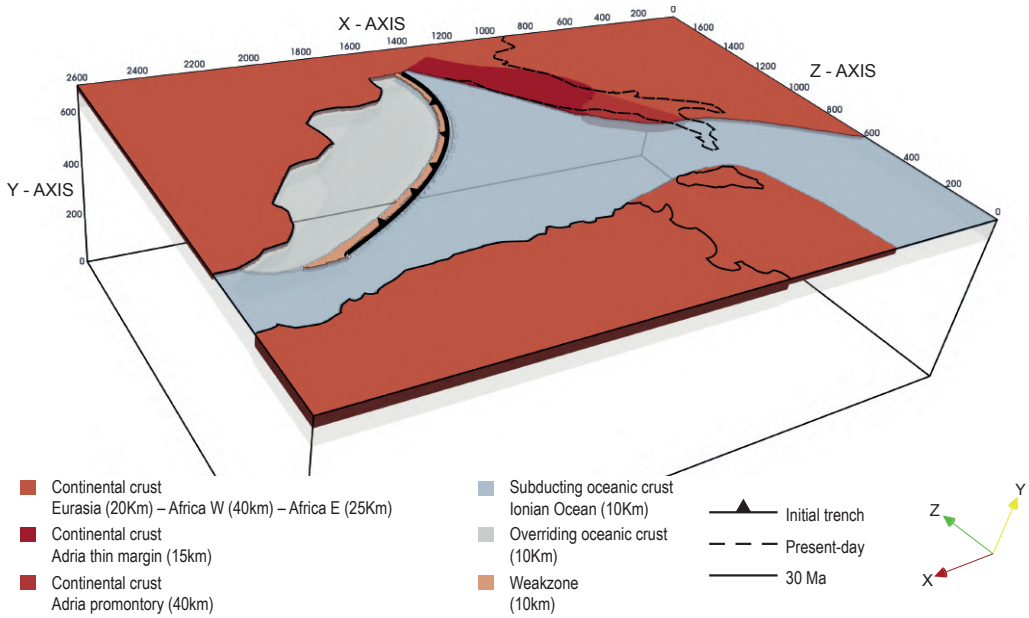

Figure 3.2: *Initial model setup for the reference Model CM. It consists of a subducting oceanic plate (Ionian Ocean; light blue), two lateral continental blocks (Adria and Africa; orange), an overriding plate (Iberia and Europe: orange; thin upper plate: light gray) drawn according to paleogeographic reconstructions at 30 Ma proposed by Faccenna et al. (2014) and Van Hinsbergen et al. (2014). The Adria plate is characterized by the presence of a stiffer continental promontory (dark orange) and a thin continental margin (red) as proposed by Lucente et al. (2006) and Lucente and Speranza (2001). A wide slab is located from Gibraltar to Corsica extending down to 300 km. The solid black line indicates the coastlines at 30 Ma (Van Hinsbergen et al., 2014), while the dashed black line the present-day coastlines of peninsular Italy.*

3.2.2 Strain-induced LPO

The development of crystal aggregates LPO in the upper mantle depends on several deformation mechanisms, including plastic deformation, dynamic recrystallization (by sub-grain rotation and grain-boundary migration), and grain-boundary sliding (Kaminski et al., 2004). Here, we use a modified version of D-REX (Kaminski et al., 2004), that incorporates these deformation mechanisms to compute the LPO and accounts for the non-steady-state evolution of geodynamic systems (Faccenda & Capitanio, 2013).

Lagrangian particles representing upper and transition zone mantle mineral aggregates are regularly distributed throughout the computational domain (25 km reciprocal distance along the three directions, for a total of

209,664 aggregates). Each particle consists of 1,024 randomly oriented crystals forming an initially isotropic upper mantle with harzburgitic composition (70% olivine and 30% orthopyroxene modal abundance) and transition zone mantle with a more fertile, pyrolitic composition (60% spinel and 40% majoritic garnet) (Faccenda, 2014). These particles are then advected by means of the Eulerian velocity field obtained by the macro-flow modeling. At each time step, the orientations of these crystals change in response to gradients in the velocity field, generating LPO. We only compute the strain-induced fabrics in the upper mantle (from the Moho to the 410 km discontinuity) as SKS splitting parameters are mostly sensitive to this mantle layer (Sieminski et al., 2008). The upper mantle fabrics are reset and transformed to isotropic transition zone mantle aggregates upon crossing the Olivine-Spinel phase transition, and vice versa. Crystal aggregates of the transition zone are always assumed to be seismically isotropic (i.e., random crystal orientation). We use the same dimensionless crystallographic parameters as in Rappisi and Faccenda (2019) with the nucleation rate $\lambda^* = 5$, the grain-boundary-mobility $M^* = 1$ and the threshold volume fraction $\chi^* = 0.9$. When compared to previously published parameters calibrated with laboratory experiments (e.g., Boneh et al., 2015; Faccenda & Capitanio, 2013; Kaminski et al., 2004), the low M^* and high χ^* yield weaker fabrics and smaller amounts of seismic anisotropy that are more consistent with seismological observations.

3.2.3 SKS Splitting

The synthetic SKS splitting is calculated using routines included in the software package FSTRACK (Becker et al., 2006b). The code first obtains a pulse seismogram via inverse Fourier transform using the method of Kennett (2009) with anisotropic extensions (Booth & Crampin, 1983; Chapman & Shearer, 1989) by computing the harmonic response of a horizontal layer stack to an

incident plane wave (5° for typical SKS arrivals) over a range of frequencies (0–25 Hz). Synthetic seismograms in the SKS band (3.3–10 s) are then constructed applying band-pass filters from 0.1 to 0.3 Hz. Successively, the splitting is determined with the cross-correlation method of Menke and Levin (2003). A 2D grid of virtual seismic stations regularly spaced is constructed in the model. After recovering the elastic tensors from each aggregate's stiffness matrix, we build below each station and down to 400 km a vertical stack of horizontal layers (minimum thickness of 25 km) where the elastic tensor of each layer is radially averaged within a distance of 50 km. The SKS splitting parameters of each seismic station are obtained by averaging all the fast azimuths and delay times measured by rotating the vertical stack of elastic tensors by 5° intervals around the y-axis.

3.2.4 P-wave anisotropy and S-wave azimuthal anisotropy

P-wave anisotropy is computed for each crystal aggregate as $Vp_{anis}(\%) = (Vp_{max} - Vp_{min})/(Vp_{max} + Vp_{min}) * 200$, where Vp_{max} and Vp_{min} are the max. and min. P-wave velocities evaluated for different incidence angles and azimuths. Another precious source of information is represented by the azimuthal anisotropy of Rayleigh waves, which however has a low lateral resolution. To roughly simulate this effect, we have interpolated the elastic tensors of crystal aggregates to a grid with node spacing of 100 x 25 x 100 km. The fast azimuth ϕ and magnitude G of the S-wave azimuthal anisotropy are then computed as, respectively:

$$\phi = 0.5 \cdot \tan^{-1}(G_s/G_c) \tag{3.11}$$

$$G = \sqrt{G_c^2 + G_s^2} \tag{3.12}$$

where $G_c = (C_{55} - C_{44})/2$, $G_s = C_{45}$ and C_{55}, C_{44}, C_{45} are the elastic tensor moduli.

3.3 Results

3.3.1 Reference Model CM

In this section, we describe in detail the tectonic evolution of the Reference Model CM. This model, among the several ones that have been tested as a function of the rheological parameters and of the plates structural/geometrical characteristics, is capable of reproducing the main geological and geophysical observations of the Central Mediterranean given the intrinsic model limitations. The influence of the imposed structural heterogeneities and rheological parameters are discussed in the next section.

The Reference Model CM is characterized by the presence of structural heterogeneities in the Adria continental plate, that is, a thinned margin in its northern portion and a stiffer promontory in its center as proposed by Lucente and Speranza (2001) and Lucente et al. (2006) (Figure 3.2). In this model, the subduction, driven solely by the slab negative buoyancy, initiates through progressive bending and roll-back of the oceanic plate, and causes a homogeneous stretching of the overriding lithosphere (Figure 3.3, Supplementary Movie S1). The Ionian slab and trench rapidly migrate southeastward with episodes of slab lateral tearing, segmentation, and break-off when a continental margin enters the trench.

Specifically, the western part of the trench reaches the African continent in ∼4.5 Myr. When the trench impacts with the African margin, part of the continental lithosphere subducts and reaches the depth of ∼150 km, and at ∼6.4 Myr slab tearing occurs at the transition between the oceanic lithosphere and the more buoyant continental lithosphere (Figure 3.3a). Lithosphere tearing subsequently propagates eastward along the African passive margin, favoring slab rollback toward the east.

At ∼7-8Myr (Figure 3.3b) the north-eastern portion of the trench progressively collides with the thin north-western margin of the Adria plate and the

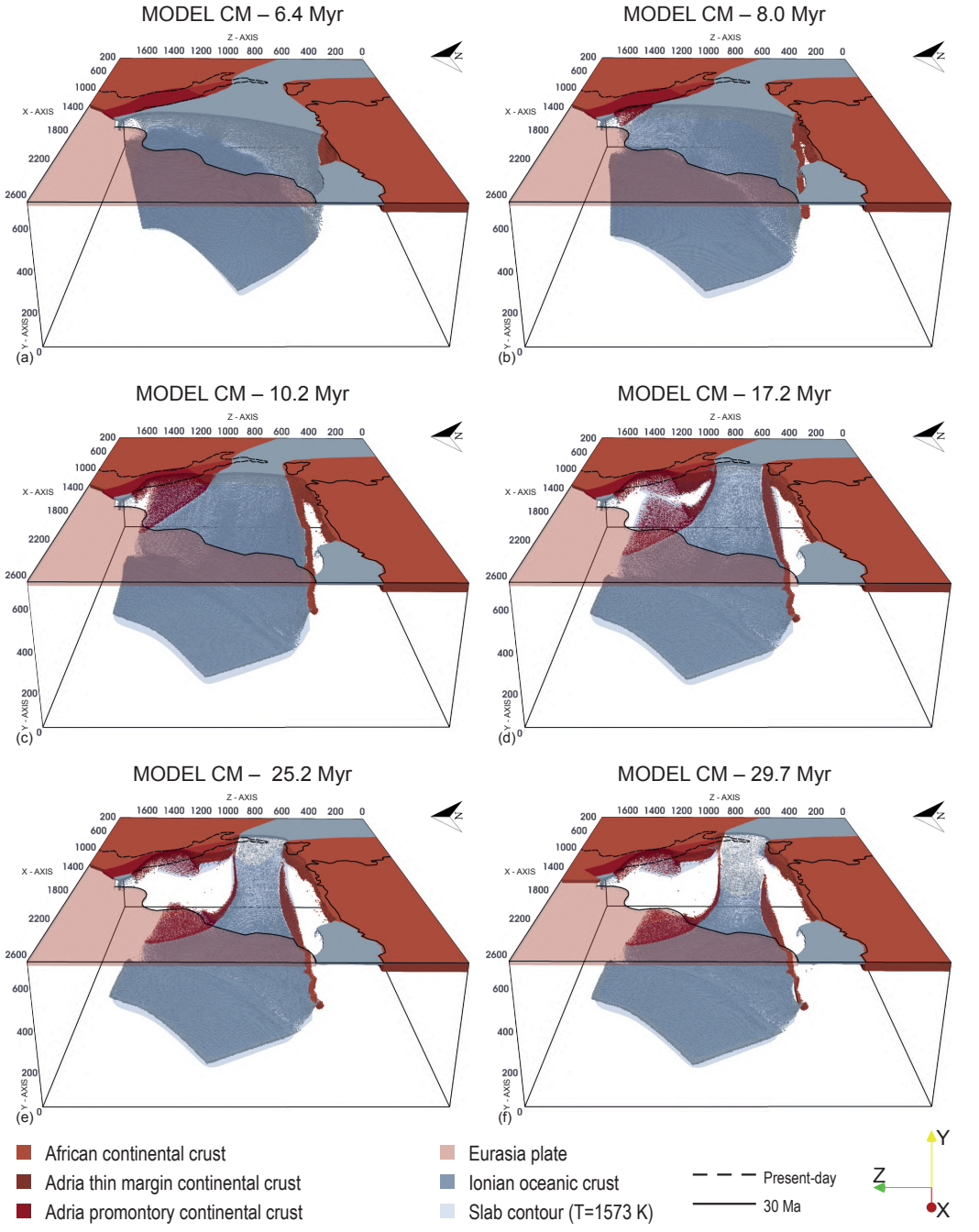

Figure 3.3: *Snapshots of the Reference Model CM evolution. In light gray, the subducted slab (contour at T=1,573 K) below ∼120 km depth. The Eurasian plate was opacified in the $1600 < x < 2600$ km range for a better visualization of the subducted slab. The solid black line indicates the coastlines at 30 Ma (Van Hinsbergen et al., 2014), while the dashed black line indicates the present-day coastlines of peninsular Italy.*

subsequent continental crust subduction induces (a) along-trench buoyancy variations resulting in a progressive curvature of the trench and (b) tearing of the slab north-eastern edge along the oceanic-continental lithosphere boundary (Figure 3.3c). After ∼10 Myr, the trench reaches Central Adria with partial subduction of the stiffer continental promontory. At the same time, the subducting slab has already reached the lower boundary of the model and stagnates horizontally in the mantle transition zone.

Between ∼15 Myr and ∼16 Myr, slab break-off occurs beneath the Adria promontory. The rupture rapidly propagates laterally, allowing, in only a few million years, the formation of a wide slab window that breaks the single arc geometry and creating two separated arcs (Figure 3.3d). The slab northern segment retreats east-ward until it breaks at a depth between 150 and 200 km (∼18 Myr), while the remaining Ionian slab becomes narrower and continues to migrate south-eastward.

After ∼25-30 Myr (Figure 3.3e and f), slab remnants are found in model areas corresponding to the present-day northern Apennines and southern Tyrrhenian sea. The northern slab segment is hanging down to ∼150 km depth and extends deeper from ∼400 km down to about ∼660 km depth. The southern slab segment instead extends continuously from the surface down to the mantle transition zone although incipient detachment is observed in the eastern African margin.

3.3.2 Comparison between the Reference Model CM and other models

Here, we want to evaluate the influence on trench shape and on the occurrence and timing of slab tears (e.g., Mason et al., 2010) of the structural heterogeneities within the Adria plate. We explore a wide range of models (Table 2) where, with respect to the Reference Model CM, we varied the geometry of the Adria plate and the buoyancy and stiffness of the Adria promontory and Adria thin margin crust. Unfortunately, the past extent of the Adria plate and the geometry of its passive margins are quite uncertain, mostly because the latter are now subducted. As a consequence, in the literature there appears to be consensus on the Mid-to-Late Cenozoic kinematic evolution of the Ionian subduction margin, while few studies have attempted to reconstruct the distribution of oceanic and continental portions of the Adria plate, and thus the geometry of its margins. For this reason, here we have tested different potential margin geometries and plate configurations (homogeneous vs. heterogeneous plate, straight vs. curved passive margin), partly following those suggested in the literature (Faccenna et al., 2014; Lucente & Speranza, 2001; Van Hinsbergen et al., 2014), and partly hypothesizing some potential geometries like those depicted in Figure 3.6.

As expected, the initial subduction dynamics of all models are similar to that of Model CM: the initial slab sinks through the mantle and retreats to the south-east. When the trench impacts with the African margin, lateral slab tearing favors subsequent eastward rollback. Important differences among models occur when the trench reaches the Adria continental margin.

When the thin continental margin in the northern Adria plate is absent (Model A), the eastward migration of the northern Ionian trench is hindered and slab tearing below the Adria promontory occurs ∼3 Myr later than in the Model CM (∼19 Myr). Over the next few millions of years, the tear

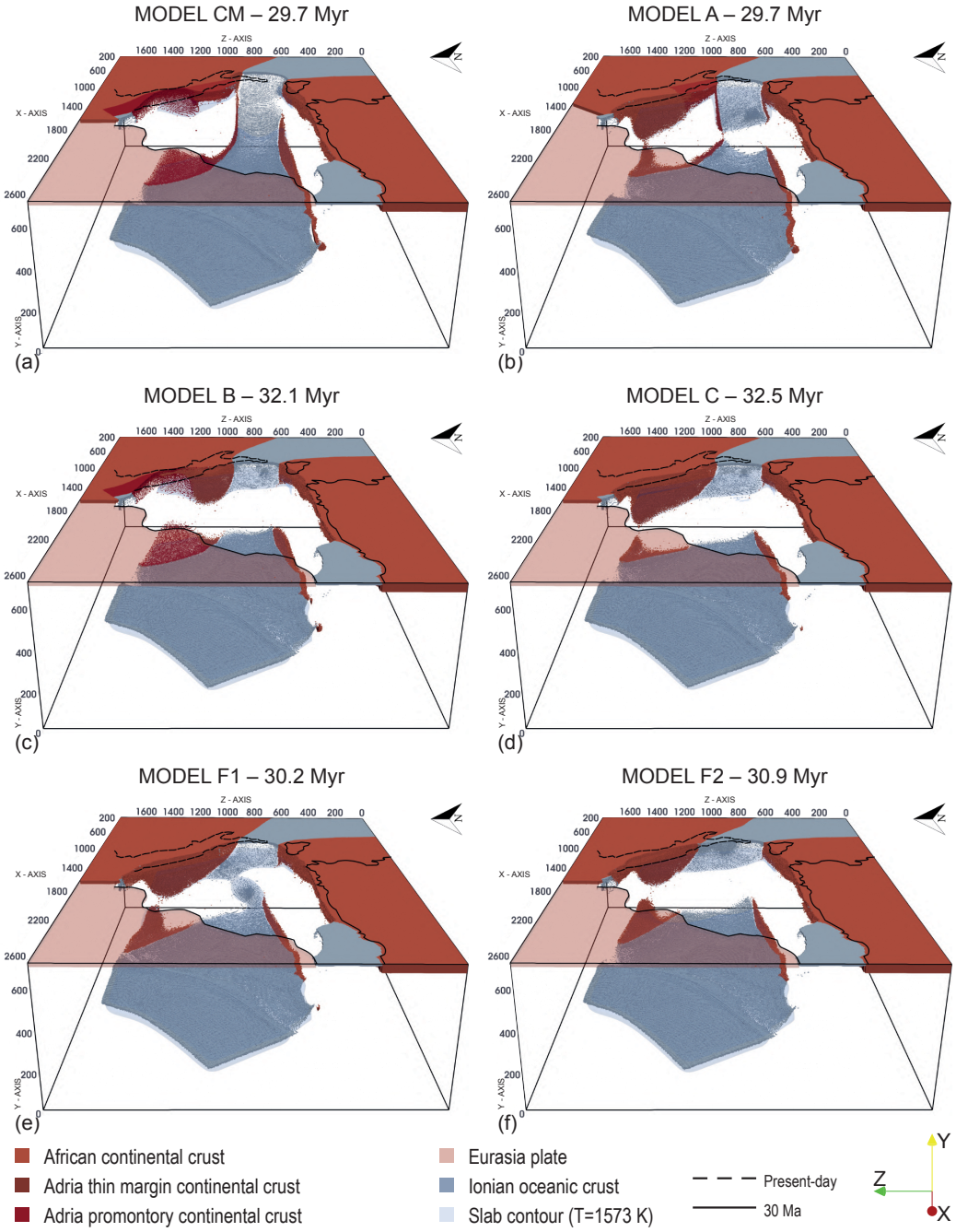

Figure 3.4: *Snapshot at ∼30Myr of: (a) Model CM, (b) Model A, (c) Model B, (d) Model C, (e) Model F1 and (f) Model F2. Color-coding and coastlines as in Figure 3.3*

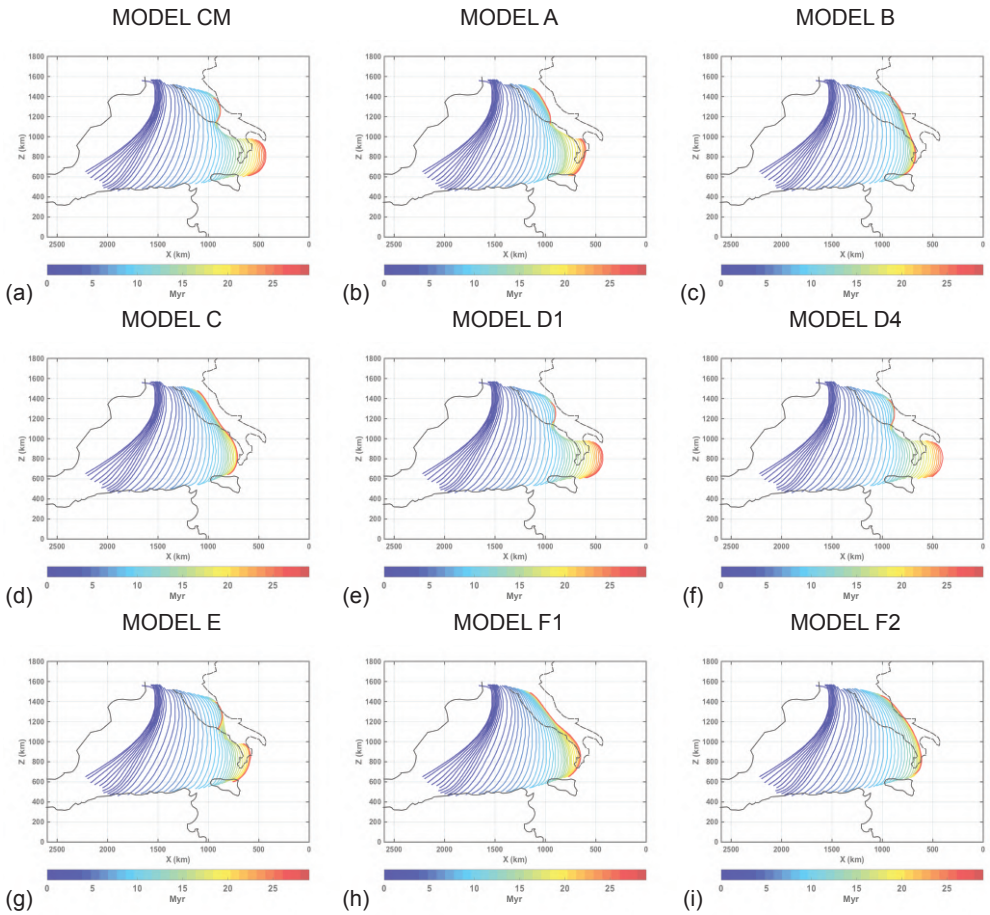

Figure 3.5: *Top view of the trench position evolution up to 30 Myr for: (a) Model CM, (b) Model A, (c) Model B, (d) Model C, (e) Model D1, (f) Model D4, (g) Model E, (h) Model F1 and (i) Model F2. The color bar indicates the time in million years. In models CM, B, D1, D4, E and F2 the northern section of the trench retreats till the Adriatic Sea in ∼30 Myr. The retreat of the Ionian slab till the present-day position in the Calabro-Peloritan region is reproduced in models CM, D1, D4. Coastlines as in Figure 3.2*

spreads laterally forming a wide slab window (Supplementary Figure 3.10b) and leading to complete slab detachment at ∼30 Myr (Figure 3.4b) with slab remnants down to ∼350 km depth. This results in a lower amount of retreat of the northern Ionian trench, whose final shape appears linear and not arcuate as in Model CM (Figure 3.5a, 3.5b and Supplementary Figure 3.11b, 3.11c).

When the Adria promontory is not included (Model B), the central slab window and the consequent double arc geometry are not generated. At ∼20

Myr the northern part of the trench is curved and has reached the same position as Model CM (Figure 3.5a and 3.5c). The Ionian slab totally breaks off between ~24 and ~25 Myr (Supplementary Figure 3.10c), resulting in a smaller amount of trench retreat to the south when compared to Model CM (Figure 3.5a, 3.5c and Supplementary Figure 3.11b, 3.11d). At ~30 Myr, we find remains of hanging subducted lithosphere only in the central part of the Adria plate (Figure 3.4c).

When both the stiff continental promontory and the thin continental margin are removed (Model C), a tear occurs at ~21 Myr in the slab central portion and again quickly spreads toward its edges. At ~23 Myr, the southern edge of the slab breaks at a depth between 150 and 200 km (Supplementary Figure 3.10d), while the remaining northern slab breaks at a depth of ~300 km at ~30 Myr (Figure 3.4d). The final position of the trench is equal to Model A in the northern part and equal to Model B in the southern part (Figure 3.5b–3.5d and Supplementary Figure 3.11c–3.11e).

The continental crust is much more buoyant with a density of ~2,700–3,000 kg/m3, compared to 3,300 kg/m3 for the mantle. Here, we further test the influence of the density of the promontory continental crust in models D1, D2, and D3, which is 500, 400, and 300 kg/m3, respectively, lighter than the mantle. This density is higher than that in Model CM where it was set constant and equal to 2,700 kg/m3. The models evolution remains very similar to Model CM, and a wide slab window develops leading to the formation of two separate arcs after the subduction of the denser continental promontory. At ~30 Myr the shape and position of the two trenches of these three models are very similar to Model CM (Figure 3.5a and 3.5e). An analogous result was obtained for Model D4, where a more buoyant Adria thin continental margin is tested by decreasing the continental crust by 200 kg/m3 (i.e., $\rho_{crust} = \rho_{mantle} - 400\ kg/m^3$) relative to that of Model CM (Figure 3.5a and 3.5f). In general, the influence of continental crust density of different

Adria plate domains is minor and exerts negligible effects on the final model evolution.

In Model E, we have instead inserted a less rigid promontory, whose initial and final friction coefficients are set equal to those of the Adria plate (0.020 and 0.005). Although the overall evolution of the subduction is similar to that of the Model CM, the timing of slab break-off is different. At ∼25 Myr, total slab detachment has already occurred in both the northern and southern slabs, that is, at least 5 million years earlier than the Model CM. This causes a minor retreat of the southern trench (Figure 3.5a, 3.5g and Supplementary Figure 3.11b, 3.11f).

Finally, we tested two models (models F1 and F2) with a homogeneous Adria plate (without lateral heterogeneities). In these models, the initial geometry of the Adria plate is simpler than in Model CM (Figure 3.6). Model F1 shows a westward convex geometry of the Adria plate western margin (Figure 3.6a), which is instead straight in Model F2 (Figure 3.6b). In Model F1, the evolution of the Ionian slab in the mantle is well reproduced (Supplementary Movie S2), with the formation of the wide slab window under the central part of Adria (Supplementary Figure 3.10e). At ∼30 Myr the northern slab is broken at a depth of about 200 km while the southern slab is still continuous (Figure 3.4e). Compared to the Model CM, however, the retreat of the two trenches is smaller. Furthermore, the trench arcuate shape observed in Model CM is not recreated (Figure 3.5a, 3.5h and Supplementary Figure 3.11b, 3.11g). The evolution of Model F2 is instead similar to that of Model B. When the Adria plate passive margin enters the trench, the slab breaks off completely without developing the slab window and the two separate arcs (Supplementary Figure 3.10f). At ∼30 Myr, we find remains of subducted lithosphere only in the central part of the Adria plate (Figure 3.4f). Also, in this case, the final shape of the trench is linear (Figure 3.5i and Supplementary Figure 3.11h).

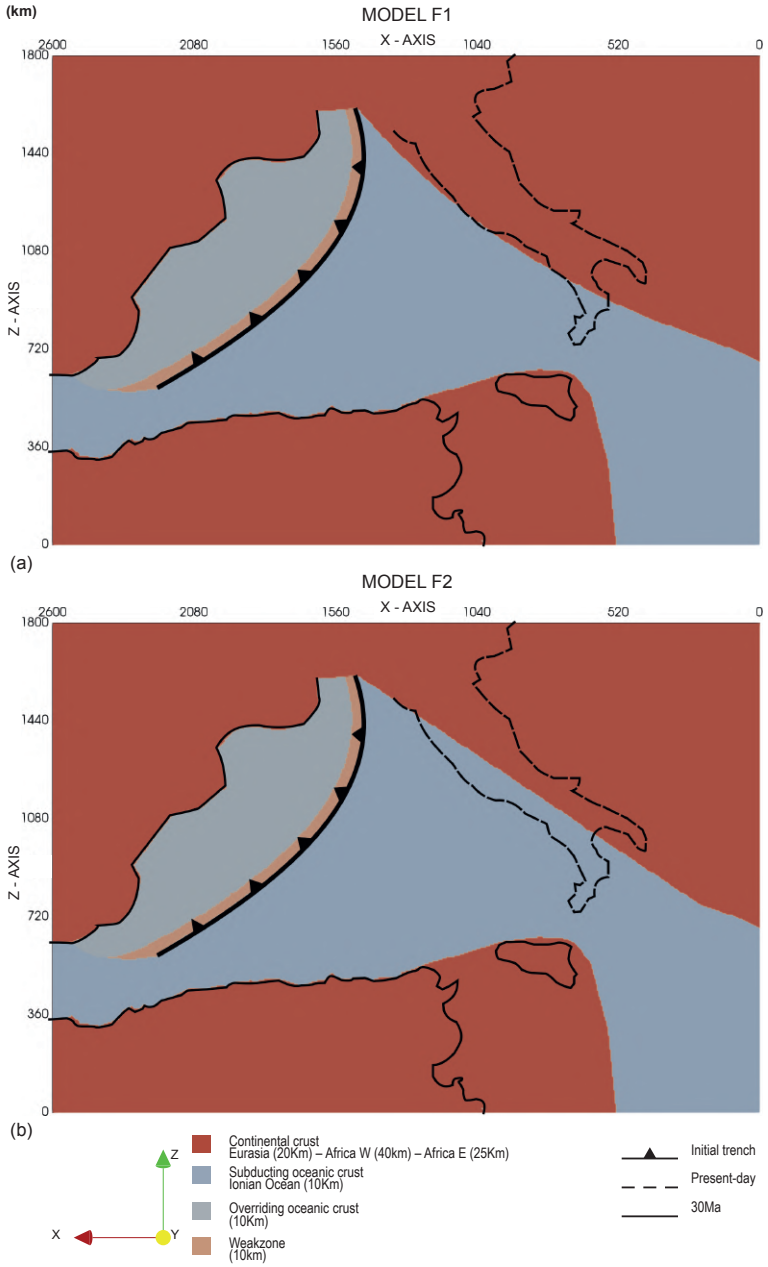

Figure 3.6: *Top view of the initial model setup for the models with a homogeneous Adria plate (without structural heterogeneities): (a) Model F1 and (b) Model F2). Coastlines as in Figure 3.2*

.

3.3.3 Upper mantle flow, LPO and synthetic seismic anisotropy

The mantle flow induced by slab subduction for Model CM is characterized by the presence of poloidal and toroidal components (Supplementary Movie

S1)). The initial slab subduction is associated with a dominant poloidal asthenospheric flow and mantle upwelling in the mantle wedge. At the same time, slab rollback is accommodated by return flow from the sub-slab region toward the mantle wedge around the slab edges and, at later stages, through the newly formed slab window.

The evolution of the subduction margin produces strong upper mantle fabrics in the area surrounding the retreating slab to a depth of 410 km and considerable amount of seismic anisotropy. In the supra-slab upper mantle, the general trend of the fast azimuths is trench-perpendicular, while the sub-slab mantle is characterized by trench-parallel extension and anisotropy (Faccenda & Capitanio, 2012, 2013) (Figures 3.7, 3.8 and Supplementary Figure 3.11). In areas characterized by slab break-off/lateral tearing and vertical flow such as around the modeled Northern Apennines and Calabrian arc, the shear wave anisotropy is relatively small due to the dipping fast axes of olivine crystals at shallow mantle depths (to which SKS phases are mostly sensitive). Synthetic SKS splitting measurements (Figure 3.7 and Supplementary Figure 3.11b) indicate that the fast shear wave component orients perpendicular to the past trench positions in the back-arc region. This results in a smoothly rotating direction pattern, with a dominance of NW directions in the north turning progressively toward EW. The back-arc region is characterized by very high delay times ($\delta t = 2 - 3.4s$), which reduce closer to the trench ($\delta t < 1.5s$) and orient parallel to it in the fore arc region. Around the slab edges, the teleseismic fast shear wave component traces the underlying return flow ($\delta t = 1 - 2s$) with a circular pattern surrounding the southern and the norther trenches. The P-wave and Rayleigh wave fast azimuths are consistent with those of the SKS-splitting data (Figure 3.8). Around the region corresponding to the northern Apennines there is significant change in P-wave and SKS anisotropic patterns between ~20 and ~30 Myr (Figure

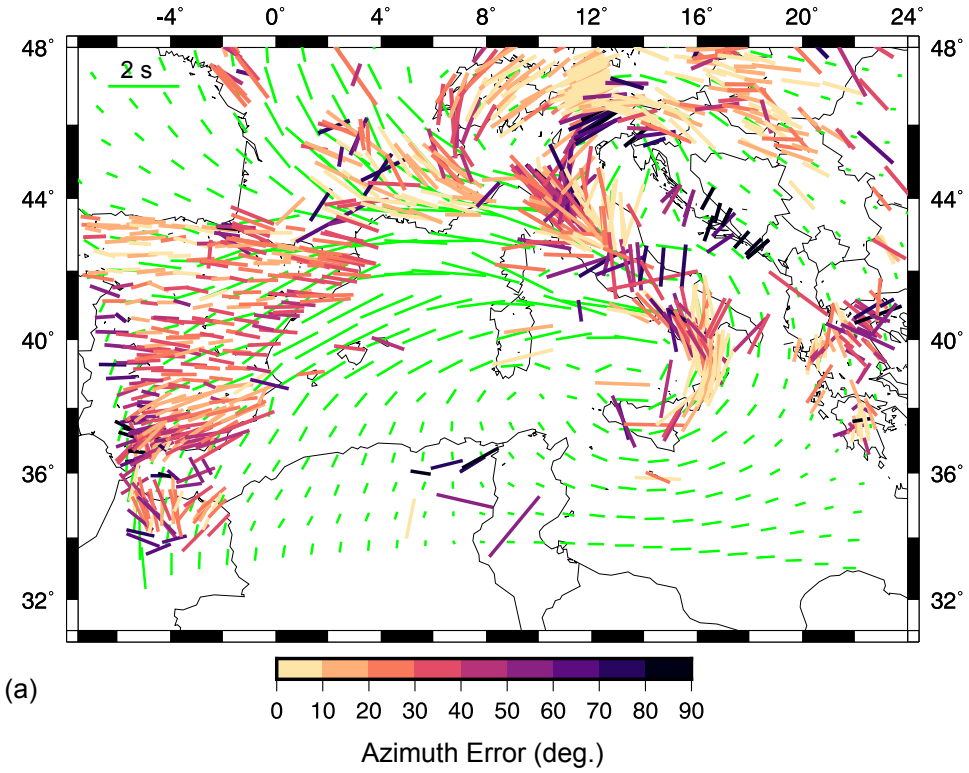

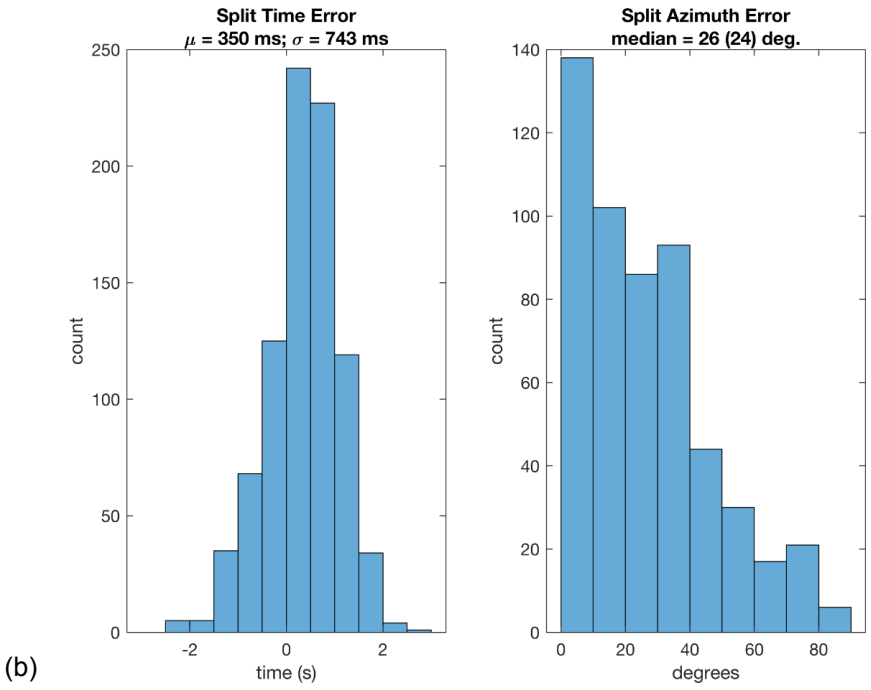

Figure 3.7: *(a) SKS-splitting measurements in the Central-Western Mediterranean (Becker et al., 2012) color-coded by the error in the orientation compared with synthetic SKS splitting measurements for Model CM at ∼20My (green bars). The EW green bar in the upper left corner indicates 2 sec. (b) Split time error and split azimuth error histograms.*

3.9). At earlier stages, strong and trench-parallel P-wave and SKS anisotropy results from the retreating western Adria margin (Figure 3.9c and 3.9e). At later stages, however, the trench-parallel SKS fast azimuths are substantially reduced and the P-wave fast directions at 130 km depth turn to trench-perpendicular dipping toward the sinking and detached Ionian slab (Figure 3.9d and 3.9f). This is because the detached Ionian slab induces a downward and radially converging mass flux (Figure 3.9a and 3.9b) in the shallow upper mantle that progressively re-orients the fast axis of the olivine crystals from ∼NW to ∼NE (Figure 3.9g and 3.9h; Vp pole figures).The change in fast axis dip from sub-horizontal to SW dipping is responsible for the decrease in SKS splitting δ_t (Figure 3.9g and 3.9h; S-wave anisotropy pole figures).

The mantle flow evolution of the other models (A, B, C, D1, D2, D3, D4, E, F1 [Supplementary Movie S2], and F2) is similar to Model CM, where lithospheric deformation and asthenospheric flow are controlled by the slab roll-back and poloidal and toroidal components of mantle circulation are both active. An important difference occurs in the models where a shallow slab window does not form (B, C, F1, and F2). In this case, the return flow entering the window is not established and a larger toroidal flow component around the edges of the wider slab is observed.

We also calculated the synthetic SKS splitting parameters for models A, B, C, E, F1, and F2 (Supplementary Figures 3.11c– 3.11h and 3.12). In the bark-arc region, SKS splitting patterns of these models are quite similar to those of Model CM, with a fast shear wave component aligned trench-perpendicular and showing an anticlockwise rotating pattern. Substantial differences are found in regions near the trench affected by the slab break-off and lateral tearing. In the models A, B, C, E, F1, and F2, the clockwise pattern of the fast azimuths surrounding the southern trench is characterized by shorter delay times ($\delta t < 1s$) due to a lower amount of trench retreat (Figure 3.5b–3.5d,

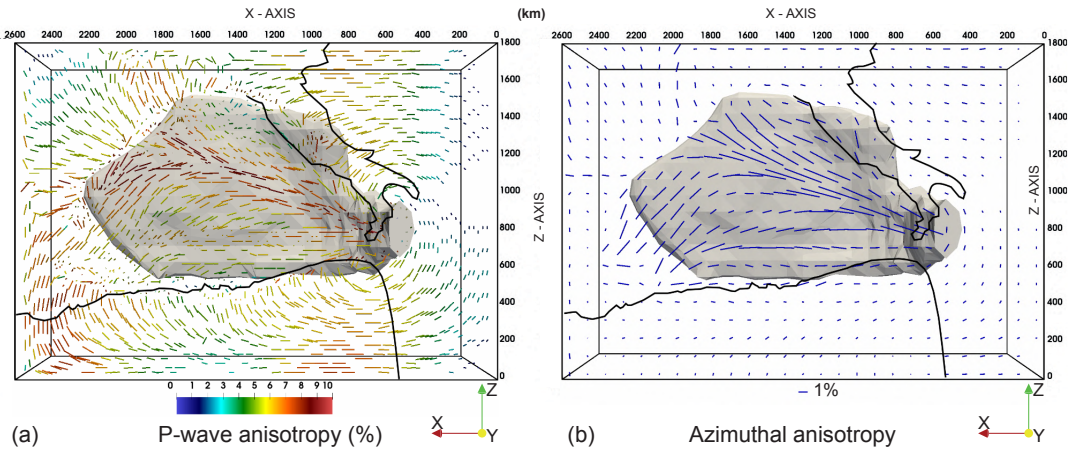

Figure 3.8: *Top-view of the Reference Model CM at ∼30 Myr showing (a) Vp_{anis} for selected aggregates at a depth of 150 km, with the length and color of each bar proportional to the amount of anisotropy and the direction indicating the direction of Vp_{max}; (b) the S-wave azimuthal anisotropy at a depth of 140 km with the orientation and length of the blue bars representing the fast azimuth Φ and magnitude G of azimuthal anisotropy, respectively. The EW blue bar outside the domain indicates 1% of azimuthal anisotropy. The grey surface shows the material with P- (left) and S-wave (right) isotropic velocity anomaly $\geq$ 1% with respect to the depth-averages velocities below 140 km depth, and corresponds to the Ionian slab. The coastlines of Africa at 30 Ma and the present-day coastlines of peninsular Italy are indicated in black for reference.*

3.5g–3.5i and Supplementary Figures 3.11c–3.11h, 3.12). Conversely, in models A, C, F1, and F2 (Supplementary Figures 3.11c, 3.11e, 3.11g, 3.11h and 3.12), the circular pattern surrounding the northern trench is well highlighted by the higher delay times ($\delta t = 1 - 1.5s$). This reflects the strong toroidal flow establishing around the rectilinear slab present at shallow depths along the entire Adria plate. Furthermore, in models B, C, F1, and F2 (Supplementary Figures 3.11d, 3.11e, 3.11g, 3.11h and 3.12), differences emerge in the Adria central portion where the fast axes orient parallel to the trench as the absence of the slab window does not produce any return flow through it.

3.4 Discussion

3.4.1 Data and model limitations

The direct application of numerical modeling to natural cases is affected by the modeling assumptions and limitations. For example, in our large-scale geodynamic models, the relative position of the plates slightly differs from the present-day one. This is because we used an initial configuration defined at ~30 Ma according to the paleogeographic and tectonic reconstructions from Faccenna et al. (2014), Lucente et al. (2006), Lucente and Speranza (2001), and Van Hinsbergen et al. (2014), and we have not applied a convergence rate between the plates (self-consistent subduction). As such, the African continent never reaches its current position. It is worth noting though that we mainly focus on the subduction system and its effect on mantle flow and anisotropy patterns. An initial geometry defined at ~30 Ma should not have a strong impact on mantle flow directions and splitting parameters since the slow Africa-Europe plates convergence has not caused a drastic change in plates position over this time span.

The model domain is defined in Cartesian coordinates, which could cause discrepancies when comparing our synthetic observations with the real measurements (e.g., Figure 3.7). Furthermore, tectonic reconstructions show that at ~30 Ma, an incipient slab (150 km), located from Gibraltar to Corsica, was already subducted in the upper mantle (Faccenna et al., 2014; Van Hinsbergen et al., 2014). However, to trigger a "spontaneous" subduction system, the trench has been initially positioned further south with the slab extending to a depth of 300 km to model a more developed subduction and increase the slab negative buoyancy. This could cause a difference in rates of Ionian slab retreat at the model early stage when compared to those reported in the literature.

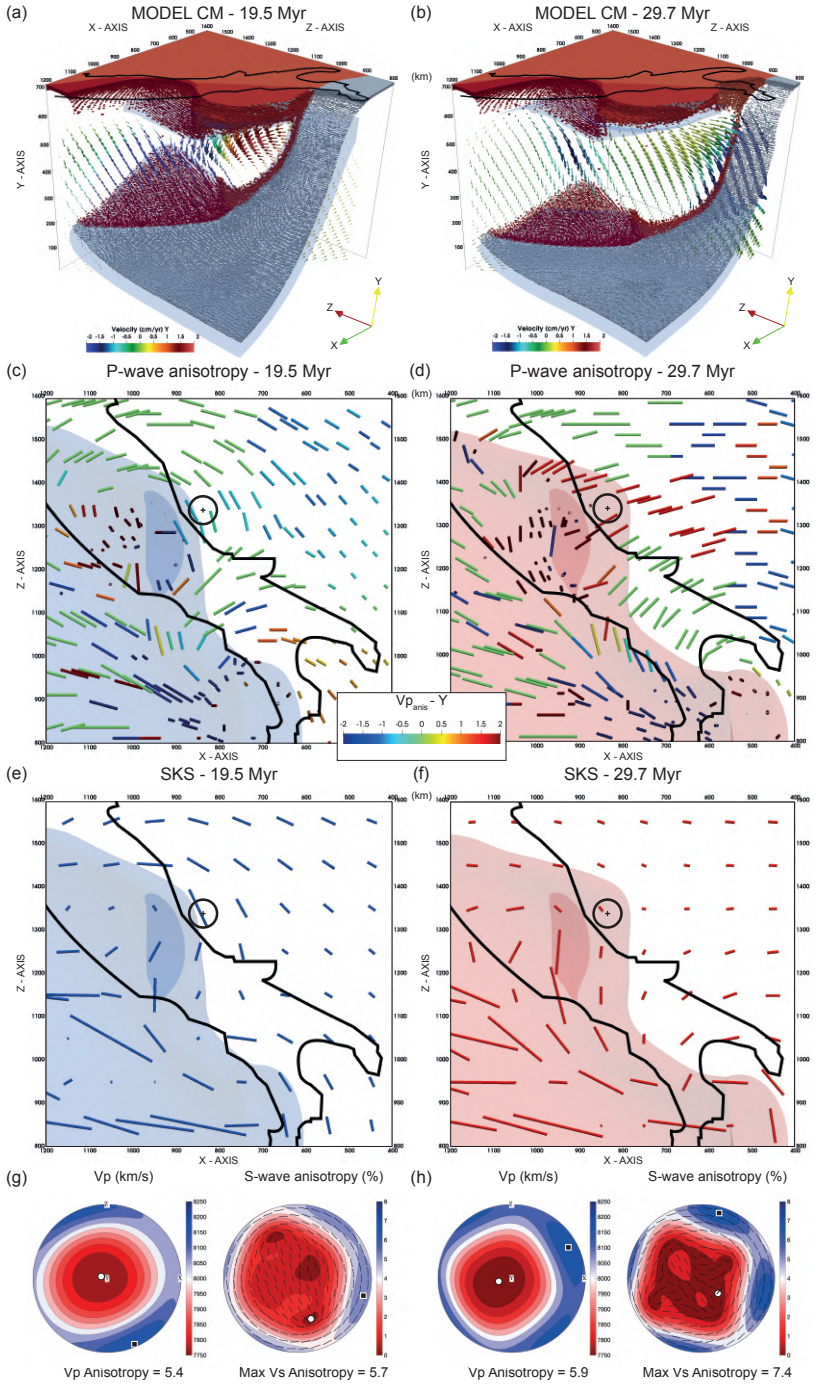

Figure 3.9: *Compositional field and seismic anisotropy in the reference Model CM at ∼20 Myr (left column) and ∼30 Myr (right column). First row is the compositional field cropped around the region corresponding to the Apenninic belt with a vertical slice of the velocity field crossing the Apennines. The arrows length is proportional to the velocity magnitude, and are color-coded according to the velocity vertical (Y) component. Second row is the P-wave anisotropy at 137.5 km depth. The bars length is proportional to the Vp_{anis} magnitude, and are color-coded according to the Vp_{anis} vertical (Y) component. Third row is the SKS splitting. The transparent blue and red volumes denote the lithosphere deeper (lighter) or shallower (darker) than 200 km depth. Fourth row shows the pole projections P-wave velocity (m/s) and $Vs_{anis} = (Vs_1 - Vs_2)/(Vs_1 + Vs_2) * 200$ as a function of the propagation direction for a mantle crystal aggregates representative of the northern Apennines area ($X = 837.5\ km$, $Y = 137.5\ km$, $Z = 1337.5\ km$; shown by the circled cross in panels c,d,e,f). The bars in the Vs_{anis} plot indicate the polarization direction of the Vs_1 component. The black square and white circle indicate, respectively, max. and min. values.*

The Central Mediterranean dynamics has been likely affected by the presence of multiple subducting slabs rather than a single one as in our models. Numerical and analog models with multiple subductions demonstrated that the number and geometry of interacting slabs strongly affect the overall force balance, and that interactions through the mantle can exert a primary control on the geometry and kinematics of subduction (Holt et al., 2018; Holt et al., 2017; Jagoutz et al., 2015; Luth et al., 2013; Peral et al., 2020). In addition, it remains difficult if not impossible to evaluate the role of other structural heterogeneities (i.e., oceanic transform faults) and geometrical complexities that might have been potentially present within the subducted Ionian plate and eastern Adria margin and that have not been considered here.

It is important to point out that validation of geodynamic models through comparison of the seismological synthetics with observations is limited by (a) uncertainties concerning the seismological data sets and related to the fact that, for example, a good azimuthally coverage is needed to properly describe the back-azimuthal dependency of the SKS splitting parameters, (b) lack of anisotropy data in oceanic regions and certain continental areas (i.e., Central Apennines), and (c) ignoring other sources of seismic anisotropy in our models. The latter include fossil LPO fabrics in the crust and mantle of the subducted and overriding lithosphere, and preferentially aligned compositional heterogeneities and fluid-filled cracks. About crustal fabrics, we note that SKS and SKKS waves have a wide lateral sensitivity (the Fresnel zone is typically on the order to 100 km or more in the upper mantle), and the role of the few tens of km thick subducted continental crust on seismic anisotropy of long-wavelength waves is likely minor. Little is known about the mantle fossil anisotropy which might be present in the Ionian-Adria lithosphere, but we note that it would be quite a coincidence the situation where the orientation of the rotated (i.e., subducted) fabrics is consistent with the

systematic along-strike orientation of the SKS fast azimuths along the mountain belts with a very complex arcuate geometry. As an example, Petrescu et al. (2020) carried out Fresnel analysis of the SKS splitting data with trench-parallel patterns along Alps and placed the source of anisotropy at asthenospheric depths. The anisotropy produced by fluid-filled, 10 km thick crustal faults in the Apennines is typically small ($<$ 0.1 sec in average; Baccheschi et al., 2016), while Faccenda et al. (2019) have demonstrated that extrinsic anisotropy due compositional heterogeneities is negligible. Hence, we believe that strain-induced LPO fabrics in the recently deforming hot mantle should explain most of the observations in the area.

Modeling of strain-induced LPO in upper mantle rocks has also some limitations related to the incomplete knowledge of the relative contribution of the different creep mechanisms as a function of the local P-T conditions, and to the employed numerical approach (for a recent review of this topic, see Hansen et al., 2021).

Despite these limitations, we find a good correspondence between the modeled and observed surface and deep isotropic structures, and seismic anisotropy patterns. This might indicate that our numerical geodynamic models are able to capture the first order of the overall evolution and the current geological scenario of the Central Mediterranean. In particular, the models reproduce several episodes of slab lateral tearing and break-off that have been proposed according to geological and seismological data.

3.4.2 Comparison with seismic tomography models

A common feature of all of our synthetic models is a high-velocity body (Figure 3.8) arranged horizontally over the 660 km discontinuity. This high-velocity anomaly is a prominent feature in P-wave tomographic models (Amato et al., 1993; Lucente et al., 1999; Piromallo & Morelli, 2003; Selvaggi &

Chiarabba, 1995; Spakman et al., 1993; Spakman & Wortel, 2004; Van der Meer et al., 2018) and it has been interpreted as the Ionian slab lying and broadening at the base of the upper mantle.

The slab remnants found in the later stages of Model CM under the regions corresponding to the Northern Apennines and Calabrian arc are consistent with (a) the observed intermediate and deep seismicity (Chiarabba et al., 2005), and (b) the two pronounced high-speed surface anomalies separated by a slow velocity anomaly (Central Apennines Slab Gap) detected by seismic tomography models. A high-velocity anomaly is detected at 250 km and deeper below the entire Apenninic belt that can be related to subducted Ionian oceanic lithosphere. The portion of the slab under the northern Apennines extends down to 150 km depth and from ∼200 km down to about 660 km depth (Figures 3.3d and 3.9a). This is consistent with recent tomographic studies (El-Sharkawy et al., 2020; Giacomuzzi et al., 2012; Spakman & Wortel, 2004) suggesting that the Northern Apennines slab reaches a depth of only 150–300 km. The vertical width of the slab gap increases with time, such that top portion of the detached slab is at 400 km depth at ∼30 Myr (Figures 3.3f, 3.4a and 3.9b). The northern section of the modeled trench retreats westward and already at ∼20 Myr resembles the arcuate shape of the present-day northern Apennines extending from the western Po Plain to the Adriatic Sea. Toward the south, the modeled Ionian slab reaches its present-day position in the Calabro-Peloritan region again at ∼20 Myr (Figure 3.5a). According to Model CM (Figures 3.3f and 3.4a), the Calabrian slab is continuous from the surface up to a depth of 660 km beneath the northern and central Calabria but the detachment has already occurred beneath north eastern Sicily (El-Sharkawy et al., 2020; Giacomuzzi et al., 2012; Neri et al., 2012; Presti et al., 2019; Scarfì et al., 2018). Thus, the modeled structures of Model CM at ∼20 Myr appear to be quite compatible with the present-day surface and deeper configuration (Figure 3.9, left column). This is in agreement with the fact that

our initial model geometry characterized by a deeper slab than what reconstructed at ∼30 Ma by Faccenna et al. (2014) and Van Hinsbergen et al. (2014) is likely representative of a more a recent stage of the Ionian subduction.

A substantially similar evolution was obtained for the models A, D1, D2, D3, D4, E, and F1 (Figure 3.4b and 3.4e), although with a minor retreat of the trenches in the models A, E, and F1 (Figure 3.5b, 3.5g, 3.5h and Supplementary Figures 3.11c, 3.11f, 3.11g). This implies that continental crust thickness and strength, rather than its density contrast with respect to the mantle (models D1, D2, D3, and D4), play a major role in defining the modeled final configuration.

Results inconsistent with tomography observations were instead obtained for the models B, C, and F2, where the absence of the stiffer Adria promontory causes the complete break-off of the Ionian slab (Figure 3.4c, 3.4d, and 3.4f). In Model B, we find hanging subducted lithosphere only below the central Apennines, which is in contrast with seismic tomographies supporting the presence of a slab gap (Figure 3.4c). In models C and F2, a hanging slab is found under the entire Apenninic chain (Figure 3.4d and 3.4f). Moreover, the absence of a thin continental margin in the northern Adria plate (models A, C, F1, and F2) hinders the western retreat of the northern trench and the formation of an arcuated trench similar to that observed along the Apenninic chain (Figure 3.5b, 3.5d, 3.5h, 3.5i and Supplementary Figure 3.11c, 3.11e, 3.11g, 3.11h). It is important to mention that including a free surface condition near the top boundary could affect the final geometry of the model in the continental areas, as portions of the continental crust entering the trench could be thrusted over the foreland, shifting the trench more eastward (Faccenda et al., 2009).

In synthesis, our geodynamics experiments highlighted that the initial subduction dynamics of all models are similar and important differences in terms of rollback rates, trench shape, and occurrence and timing of slab tears

occur in the final stages of their evolution when the Adria continental margin enters the trench. In particular, our results show that:

1. The presence of a thin continental lithosphere (models CM, B, D1, D2, D3, D4, and E) favors the curvature of the Northern Apennines trench and its retreat till the Adriatic Sea, which suggests that the arched shape of the northern Apennines is a consequence of deep processes occurring inside the Earth, that is, the lateral flexion of the subducting Adriatic plate (Lucente & Speranza, 2001);

2. The development of a slab window below the Central Apennines and double arcs geometry, as shown by seismic tomographies, occurs in the models where a stiffer continental promontory in central Italy is inserted (models CM, A, D1, D2, D3, D4, and E) and/or the Thyrrenian passive margin of the Adria plate is curved (Model F1);

3. The presence of both structural heterogeneities within the Adria plate (promontory and thin margin) helps the retreat of the Ionian slab till the present-day position in the Calabro-Peloritan region.

3.4.3 Comparison with observed seismic anisotropy

Figure 3.7 shows a comparison between predicted and observed (by Becker et al., 2012) SKS splitting measurements in terms of azimuth and time errors. More in detail, panel "a" shows the observed measurements color-coded by the error in the orientation compared with synthetic predicted from Model CM at ∼20 My (green bars). The general pattern of the synthetic 3D anisotropy calculations matches the observed data in the whole study region with an average misfit angle of about 26°, but lower values are found in the Calabrian arc (0-10°), southern France (0-20°) and eastern Alps (0-10°), although the mantle flow in the latter area could be affected by its proximity to

the model edges. In contrast, a significant mismatch between predicted and observed fast azimuths is found in the Dinaric Alps and Central Apennines where the predictions mainly exhibit a trench-parallel preferential direction with an average angle rotated by 90° with respect to the observations. These discrepancies could arise from the fact that in this study we have ignored the presence of the Alpine and Dinaric slabs. In fact, the Adria microplate is subducting on both the western and eastern margins, which may cause a strong interaction between the two subduction zones (Király et al., 2018) that has not been considered in our models. The comparison between observed and predicted data is also limited by the fact that some areas are not covered by real measurements as in the case of the Tyrrhenian Sea, the Ionian Sea, and partly in the Central Apennines.

Bearing in mind these discrepancies, our results (Figures 3.7–3.9 and Supplementary Figure 3.11) reveal the dominant role of subduction-induced mantle flow in generating the observed seismic anisotropy and shear wave splitting. Moving from West to East, three main areas characterized by different anisotropy patterns are identified.

Around the area corresponding to the Liguro-Provençal basin the synthetic SKS splitting, P-wave anisotropy, and Rayleigh wave azimuthal anisotropy measurements exhibit a smooth $\sim 90°$ rotation, with a dominance of NW orientation in the north (southern France) turning progressively toward EW in the Corsica-Sardinia block. We confirm the interpretation proposed by (Lucente et al., 2006) that relates this feature to the formation of the Liguro-Provençal basin and to the clockwise rotation of the Corsica-Sardinia block.

In the modeled Tyrrhenian domain, the fast shear wave component orients parallel to the stretching direction of the back-arc basin, which is consistent with the observations (Jolivet et al., 2009; Lucente et al., 2006). However, delay times are higher $(\delta t = 2 - 3.4s)$ due to the thick and homogeneous anisotropic layer with sub-horizontal fast axis extending down to the base

of the upper mantle. This might indicate that either dislocation creep is active down to only 200–250 km (Karato & Wu, 1993) or that mantle fabrics are weaker than those modeled.

Beneath the Apennines, the pattern of observed SKS fast axes abruptly changes orientation and becomes parallel to the mountain chain, following its curvature from NW-SE in the north, to a more NS orientation along the Apennines foreland and to NE-SW in the farther south Calabria. Along the northern Apennines (Figure 3.9), the trench-perpendicular P-wave anisotropy measured by (Hua et al., 2017) could be interpreted with the presence of a large gap in the sinking Ionian slab as in the latest stages of Model CM (Figure 3.9b and 3.9d). At earlier stages of Model CM, instead, that is, during or right after slab detachment, the SKS-splitting delay times are more consistent with the observations, but the P-wave fast azimuths are trench-parallel (Figure 3.9a, 3.9c and 3.9e). Because of the striking difference between these two patterns, it follows that a more detailed characterization of the seismic anisotropy in the northern Apennines could provide useful information to determine whether the slab is continuous or not in the upper mantle. In the Sicily channel, smaller-scale features show trench-perpendicular SKS azimuths at the western corner of the Calabrian slab, where SKS fast axes turn to NS and then EW in the Tyrrhenian Sea. According to our models, these patterns reflect the retreat of the Adria-Ionian trenches and related trench-parallel extension in the sub-slab mantle, and toroidal flow around the Calabria slab Civello and Margheriti (2004), Faccenna et al. (2014), and Faccenna et al. (2007), Jolivet et al. (2009). In our reference Model CM, the SKS fast azimuths are somewhat trench-perpendicular beneath Central Adria as a result of the mantle flowing through the slab window. However, the scarcity of splitting data in this region does not allow to safely infer the mantle flow at depth and compare our results with the few available observations.

3.5 Conclusions and outlook

We combined macro-scale geodynamic modeling with micro-scale simulations of strain-induced upper mantle fabrics and seismological synthetics to reproduce and constrain the tectonic evolution of the Central Mediterranean over the last ∼20–30 Myr. Starting from different tectonic scenarios, we have employed 3D thermo-mechanical simulations to test the role of lithospheric structural heterogeneities and certain rheological parameters on the self-consistent model evolution. After calculating the upper mantle elastic properties as a function of the strain history and local P-T conditions, the model results were then validated by comparing seismological synthetics (isotropic P-wave anomalies, P-wave anisotropy, SKS splitting, and Rayleigh azimuthal anisotropy) and major tectonic features (i.e., slab and trench geometry) with observations.

Our modeling results bring new insights into the complex structure of the upper mantle beneath the region confirming that the main geological and geophysical observables in the Central Mediterranean can be directly linked to the recent dynamics of the Ionian slab and Adria plate. Furthermore, our results suggest that lateral variations in lithosphere thickness and stiffness can substantially influence the tectonic history of a natural environment. We show that the presence of structural heterogeneities within the Adria plate as imaged by, for example, Miller and Piana Agostinetti (2012) and Panza et al. (2003), and/or the geometry of its Tyrrhenian passive margin plays a fundamental role on:

1. The curvature of the Northern Apenninic trench and its retreat to the Adriatic Sea. This is favored by the presence of the thin continental lithosphere in the northern Adria plate that is prone to subduction.

2. The development of a slab window below the Central Apennines separating two high-velocity anomalies as shown by seismic tomographies.

A good fit between predicted and observed slab morphology was obtained for the models where a thick continental promontory lithosphere is inserted inside the Adria plate. In these scenarios, slab break-off occurs beneath the area corresponding to the Central Apennines and is favored when the thick promontory is bounded by lithospheric portions (the thin continental margin in the North and the oceanic Ionian plate in the South) that tend to subduct and retreat eastward. This rupture rapidly propagates laterally, allowing, in only a few million years, the formation of two separated arcs, the northern Apennines and the Calabrian arcs. Results inconsistent with tomography observations were instead obtained for the models where the absence of the stiffer Adria promontory results in the complete break-off of the Ionian slab.

3. The retreat of the Ionian slab till the present-day position in the Calabro-Peloritan region in models when both structural heterogeneities were present.

Despite some discrepancies due to the imposed model geometry and some limitations in the methods, the good correlation between predicted and observed slab morphology and seismic anisotropy patterns pose new important constraints on the recent evolution of the study area. Our geodynamic models explain the rotation of the Sardinian-Corsican block, the opening of the Liguro-Provençal and Tyrrhenian basins, the retreat of the Apennines and Ionic trenches until their present-day position. In particular, this work offers valuable constraints on the hypothesized break-off of the slab beneath the Central Apennines widely debated in the literature, giving a combined geodynamic and seismological reading. Our study demonstrates that this type of combined simulation is able to capture a first order of the overall evolution and the current geological situation of the region providing an overview on the processes that have led to the opening of the Central Mediterranean.

To obtain a better comparison between the synthetic and observed data and to limit the model uncertainties, we envisage that future numerical studies should attempt to (a) improve the model geometry by considering the Earth's sphericity and the Africa-Eurasia plates convergence, (b) account for the presence of the Alpine and Dinaric slabs that likely affect the mantle flow below the Adria plate surrounding regions, and (c) perform further seismological synthetics, such as P-wave anisotropic tomographic inversions (e.g., VanderBeek & Faccenda, 2021). At the same time, more abundant and high-quality seismological measurements could provide more constraints on the upper mantle structure and flow dynamics. For example, at present, it is not yet clear whether the northern Apenninic slab is continuous down to the transition zone or not. Furthermore, SKS splitting in some specific areas such as the Central-Southern Apennines are sparse, such that there it is not possible to infer whether the shallow upper mantle is flowing through the Central Apennines Slab Gap as a result of the recent retreat of the nearby Calabrian and Northern Apennines slabs. Similarly, P-wave and S-wave anisotropic tomography models of the entire Mediterranean region would likely help in better constraining the recent dynamics and deep structure of this region. However, a single P-wave anisotropic tomography for the Alpine region (Hua et al., 2017) has been produced so far Hua et al. (2017), which is unexpected given the good azimuthal coverage of the area (e.g., Piromallo & Morelli, 2003).

Acknowledgments

This study is supported by the ERC StG 758199 NEWTON. Open Access Funding provided by Università degli Studi di Padova within the CRUI-CARE Agreement.

Data Availability Statement

T. Gerya provided the I3MG code used for the subduction modeling. This code is available on Figshare. B. P. VanderBeek created the map in Figure 1b using the software GMT. The modified version of the D-Rex code used for the fabric modeling, and the routines used to calculate SKS splitting parameters, P-wave and Rayleigh wave anisotropy can be found inside the ECOMAN software package. The MATLAB toolbox geomIO used to define the geometry of the model initial setup can be found at https://geomio.bitbucket.io/. Paraview was used for graphic visualization of the model output. Files for visualization in Paraview of the reference Model CM are available on Figshare. The map in Figure 1b is created with GMT 5.4.3 which is under a GNU Lesser General Public License. Data from real SKS splitting measurements were taken from sksdata (Becker et al., 2012). Reviews by Simone Pilia and Luca De Siena have substantially improved an earlier version of this article.

Supplementary Material

Supplementary Movie S1. Model CM evolution. Initial setup is shown in Figure 3.2. In blue the subducted slab (contour at T=1573 K) below 130 km depth. The continental plates of Adria, Africa and Iberia and the oceanic plate were opacified for better visualization of the subducted slab. The arrows indicate the velocity field at ∼250Km depth, and their length is proportional to the velocity magnitude.

Supplementary Movie S2. Model F1 evolution. Initial setup is shown in Figure 3.6a. Color-coding as in Supplementary Movie S1.

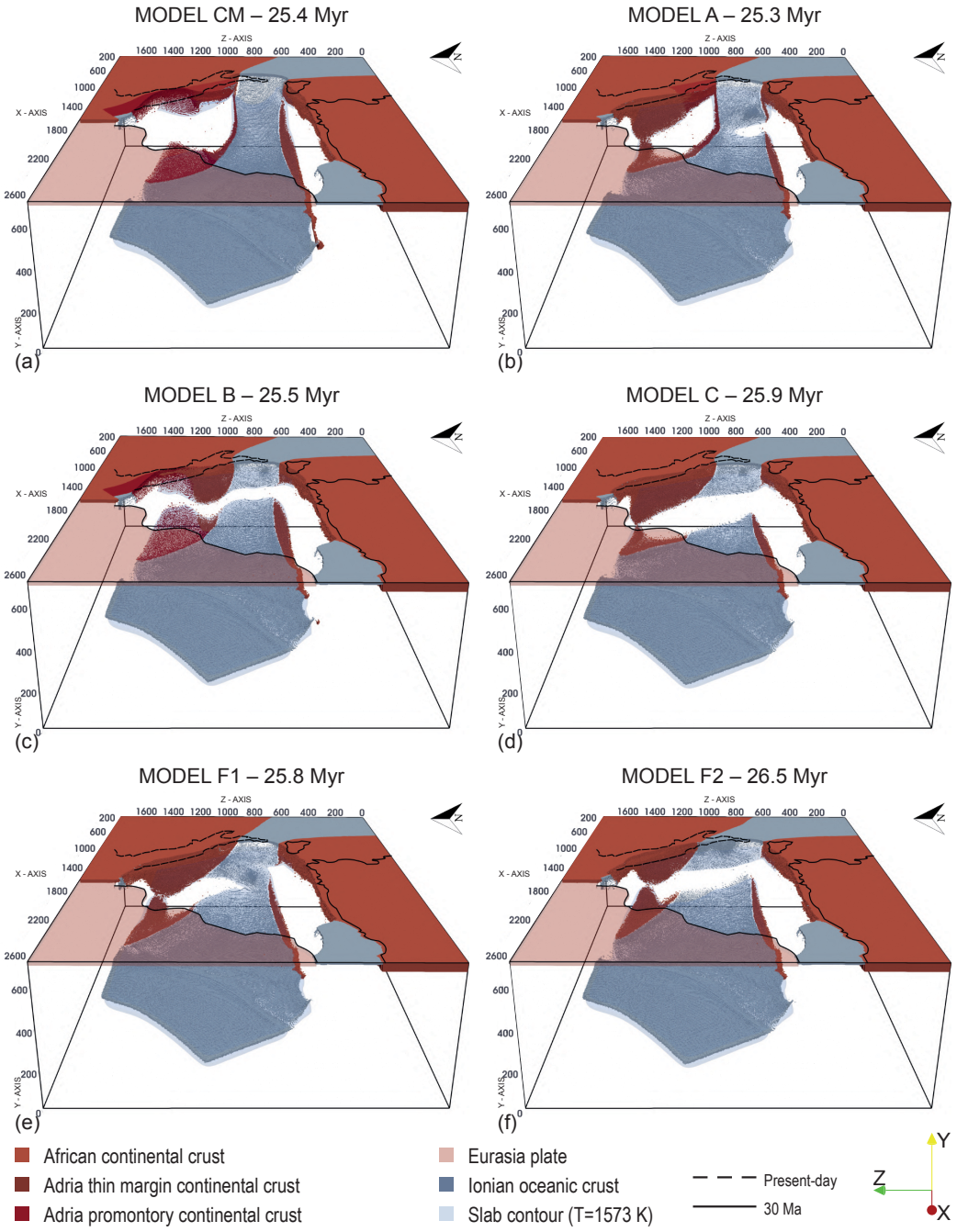

Figure 3.10: *Snapshot at 25Myr of: (a) Model CM, (b) Model A, (c) Model B and (d) Model C, (e) Model F1 and (f) Model F2. Color-coding and coastlines as in Fig. 3.3.*

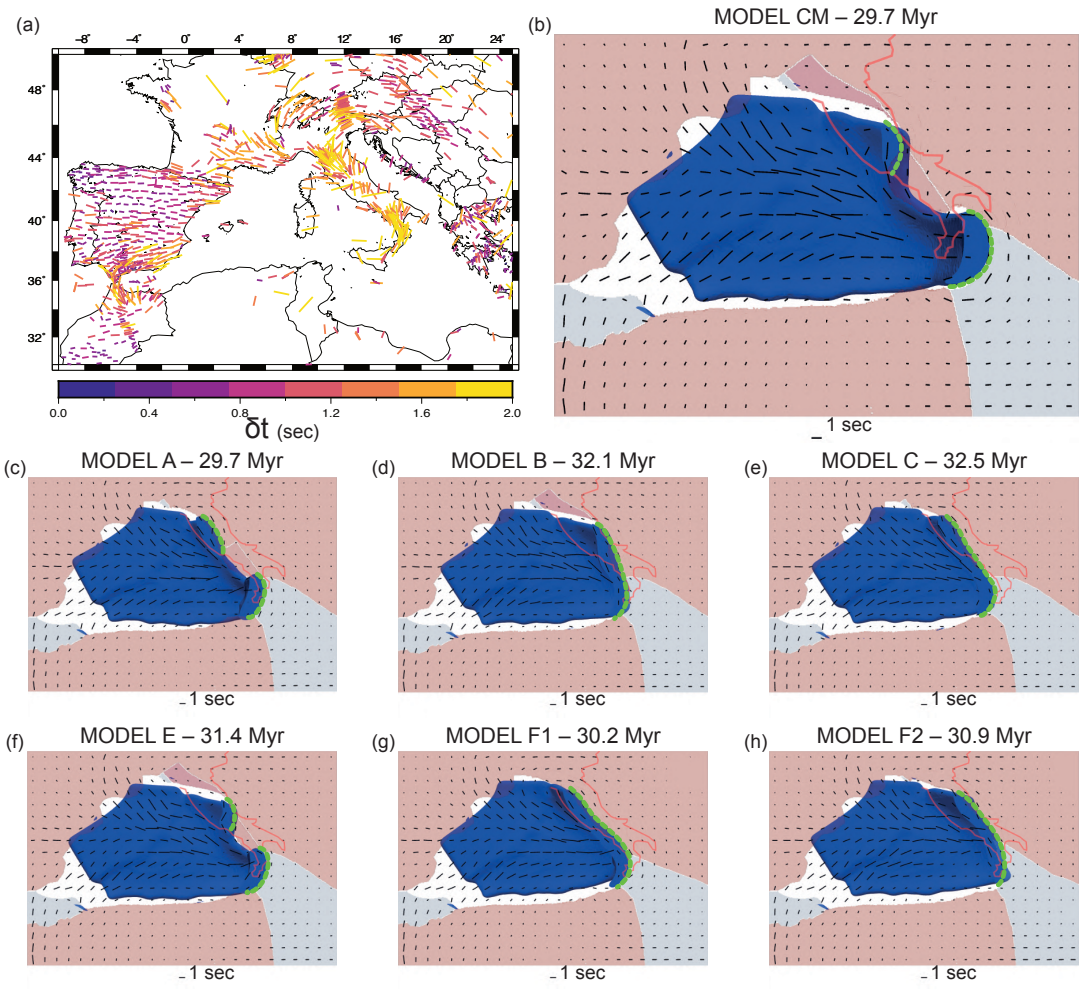

Figure 3.11: *(a) SKS-splitting measurements in the Central-Western Mediterranean (as in Fig. 1b) compared with synthetic SKS splitting measurements for: (b) Model CM, (c) Model A, (d) Model B, (e) Model C, (f) Model E, (g) Model F1 and (h) Model F2. The EW black bars outside the domain indicates 1 sec. The blue surface envelopes the subducted lithosphere (T < 1573 K) below 120 km depth. The present-day coastlines of peninsular Italy are indicated in red for reference. The green dashed thick line indicates the position of the active trenches.*

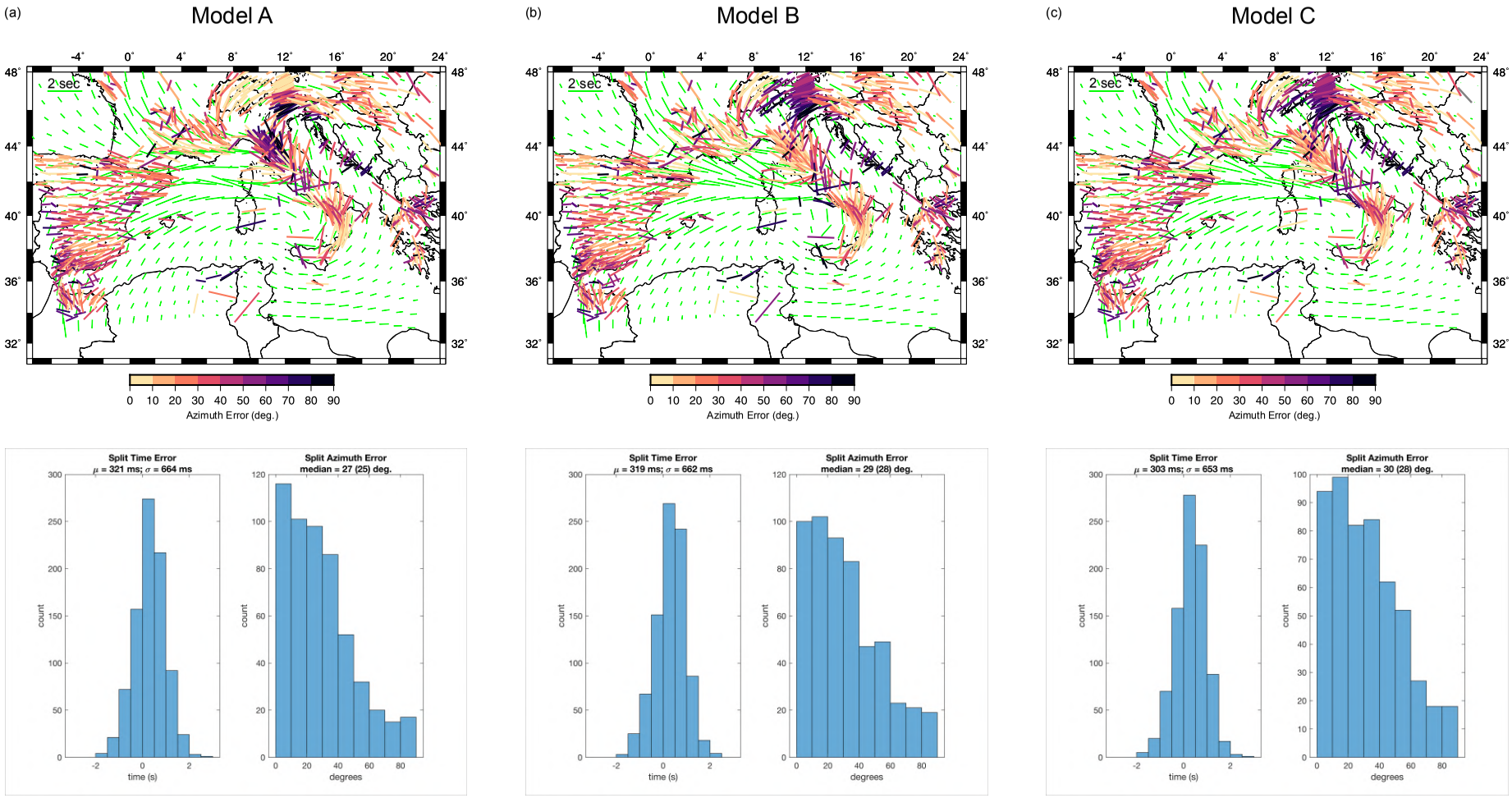

Figure 3.12: *On the top SKS-splitting measurements in the Central-Western Mediterranean (Becker et al., 2012) color-coded by the error in the orientation compared with synthetic SKS splitting measurements (green bars - the EW green bar in the upper left corner indicates 2 s) and on the bottom split time error and split azimuth error histograms for (a) Model A, (b) Model B and (C) Model C at ∼20 My.*

Chapter 4

TOMOGRAPHIC IMAGE INTERPRETATION AND CENTRAL-WESTERN MEDITERRANEAN-LIKE UPPER MANTLE DYNAMICS FROM COUPLED SEISMOLOGICAL AND GEODYNAMIC MODELLING APPROACH

R. Lo Bue[†,1], F. Rappisi[†,1], B. P. Vanderbeek[1] and M. Faccenda[1]

This manuscript is under review in Frontiers in Earth Science - Solid Earth Geophysics. All the authors conceived the study. RLB performed the geodynamic and seismological (i.e. strain-induced fabric estimation and SKS splitting calculations) numerical modelling. FR performed the seismological forward and P-wave tomography. RLB and FR wrote the first draft of the manuscript. BPV and MF supervised the findings of this work. All the authors contributed equally to the discussion of the results and to the conclusions of this study.

[†]indicates the first authors.
[1]Dipartimento di Geoscienze, Università di Padova, Padova, Italy

Abstract

The Central-Western Mediterranean (CWM) is one of the most complex tectonic setting on Earth. Episodes of slab rollback, break-off and tearing, the opening of back-arc extensional basins (i.e., Liguro-Provençal, Alborean, Algerian and Tyrrhenian basins), the presence of large mountain ranges, active volcanoes and violent earthquakes have made the Mediterranean an ideal environment to study a wide range of geodynamic processes and an important target for seismological studies (e.g, seismic tomography). Here we build a geodynamic model which, although it does not reproduce its exact tectonic structure (e.g., due to the limits of the numerical method, approximations in the initial setup, etc), presents multiple and geometrically complex subduction systems analogous to those found in the CWM. The tectonic evolution of this model is estimated with petrological-thermo-mechanical 3D simulations, then, we dynamically compute the upper mantle fabrics and seismic anisotropy as a function of the strain history and local P-T conditions. After comparing the model with SKS splitting observations in order to quantify the discrepancies with the true Central-Western Mediterranean, we use the elastic tensors predicted for the modeled configuration to perform 3D P-wave anisotropic tomography by inverting synthetic P-wave delay times. Using the geodynamic model as reference, we evaluate the capabilities of a recently developed seismic tomography technique to recover the isotropic anomalies and anisotropy patterns related to a complex subduction environment in different conditions, such as poor data coverage and bad data quality. We observe that, although P-wave tomography still remains a powerful tool to investigate the upper mantle, the reliability of the retrieved structures strongly depends on data quality and data density. Furthermore, the recovered anisotropic patterns are consistent with those of the target model, but in general an underestimation of the anisotropy magnitude in the upper mantle

is observed. In the light of future developments, our study suggests that by combining micro- and macro-scale geodynamic simulations and seismological modelling of seismic anisotropy it will be possible to reproduce, at least to a first order, the tectonic evolution of real study regions (e.g., the Mediterranean) thus providing fundamental constraints on the processes that have contributed in shaping their current geological scenario.

4.1 Introduction

Since the early 1990s numerous seismological studies have been carried out to image the Earth's upper mantle and seismic tomography proved to be a fundamental tool for constraining the past and present-day mantle dynamics and structure (Liu & Gu, 2012; Rawlinson et al., 2014; Romanowicz, 2021; Van der Meer et al., 2018). Tomographic methods (e.g. P-, S- and surface-wave tomography) yield wave velocity models that are commonly used to infer distributions in physical and chemical properties affecting seismic-wave propagation such as density, temperature, melt fraction and volatile content.

At the same time, petrophysical analysis of exhumed rock samples and micromechanical laboratory experiments (Blackman & Kendall, 2002; Faccenda, 2014; Kaminski et al., 2004; Karato et al., 2008; Long & Becker, 2010; Ribe, 1989; Savage, 1999; Skemer & Hansen, 2016) have shown that the development of mineral and compositional fabrics mainly associated with rock deformation can create significant directional variations in seismic velocities known as seismic anisotropy. Although the presence of seismic anisotropy in Earth's upper mantle is well-established, scientists have often assumed the Earth's interior as seismically isotropic. This approximation certainly simplifies the computational approach but at the same time it can introduce notable imaging artefacts and, consequently, errors in the interpretation of the tomographic results (Bezada et al., 2016; Blackman & Kendall, 1997; Blackman et

al., 1996; Kendall, 1994; Lloyd & Van Der Lee, 2008; Menke, 2015; Sobolev et al., 1999; VanderBeek & Faccenda, 2021).

Recently, VanderBeek and Faccenda (2021) and Wang and Zhao (2021), have independently developed a methodology to invert for P-wave isotropic (mean velocity) and anisotropic (magnitude of hexagonal anisotropy, azimuth and dip of the symmetry axis) parameters. When tested on a relatively simple, 3D geodynamic model of subduction, VanderBeek and Faccenda (2021) found that the new inversion technique produces a much more accurate reconstruction of the upper mantle isotropic and anisotropic structures. In contrast, ignoring for seismic anisotropy (isotropic approximation) or allowing for only azimuthal variations in seismic velocity (i.e., no dipping fabrics) generates strong imaging artifacts. From these tests it follows that taking into account seismic anisotropy can provide new insights into the 3D upper mantle structure and dynamics. Despite these encouraging results, it remains unclear whether isotropic and anisotropic structures of the Earth's mantle can be simultaneously recovered by P-wave anisotropic inversions in real and more complex tectonic settings.

Along with seismic imaging techniques, over the last decades numerical geodynamic modelling became an essential approach for understanding the long-term and deep evolution of a wide range of geological processes, which otherwise would remain unconstrained due to the lack of geological data (Gerya, 2019). Owing to the development of increasingly high performance computers and more advanced numerical techniques, it is nowadays possible to simulate the multiscale tectonic evolution of 3D complex settings for 10s or 100s of millions of years (Van Zelst et al., 2021). However, despite being a powerful tool, numerical modelling is also affected by several limitations that could potentially bias the final output, such as uncertainties in the employed initial model geometry, physical parameters (mainly viscosity), chemical compositions, and limited computational power.

In order to test the limitations of the tomographic and numerical modelling methods, a promising approach is combining micro- and macro-scale geodynamic modelling simulations of mantle flow to predict mantle isotropic and anisotropic structures and then perform seismological synthetics (Confal et al., 2018; Faccenda & Capitanio, 2012, 2013; Hu et al., 2017; Lo Bue et al., 2021; Zhou et al., 2018). We decided to apply this combined methodology to the Central Western Mediterranean (CWM) region. In the last 20-30 million years, this area has experienced complex tectonic activity characterized by back-arc extension related to slab retreat in the Liguro-Provençal, Alborean, Algerian and Tyrrhenian basins and episodes of slab break-off, lateral tearing and interactions between slabs (Carminati et al., 1998; Carminati et al., 2012; Faccenna et al., 2014; Faccenna et al., 2007; Faccenna et al., 2004; Jolivet et al., 2008; Jolivet et al., 2006; Jolivet et al., 2009; Király et al., 2018; Lonergan & White, 1997; Mauffret et al., 2004; Platt & Vissers, 1989; Rosenbaum et al., 2002b; Spakman et al., 1988; Spakman & Wortel, 2004; Van Hinsbergen et al., 2020; Van Hinsbergen et al., 2014; Vignaroli et al., 2008; Wortel & Spakman, 2000) and a wealth of geological and geophysical data are available. Numerous tomographic models and geodynamic studies focusing on the CWM upper mantle are available, which can be used here to test the reliability of our approach.

We first extend the modelling methodology of Lo Bue et al. (2021) to create a geodynamic model that resemble observed slabs morphology and anisotropic mantle fabrics of the CWM. The geodynamic model is then exploited as synthetic case study to test the capabilities and limitations of P-waves isotropic and anisotropic inversions in recovering complex geological scenarios using the methodology of VanderBeek and Faccenda (2021).

In this work, we attempt to answer some fundamental questions. How well does P-wave anisotropic tomography recover the modeled isotropic and anisotropic structures? How reliable are the inferred anisotropic patterns

with respect to the upper mantle fabrics? Which are the main artefacts introduced in the tomographic image when neglecting seismic anisotropy? To which extent vertical smearing bias the inverted structures when only using teleseismic P-wave travel times?

4.2 Methodology

4.2.1 Geodynamic Numerical Modelling

We construct a 3D petrological-thermo-mechanical numerical model of the Central-Western Mediterranean convergent margin using I3MG (Gerya, 2019), which is based on the finite difference method (FDM) combined with a marker-in-cell (MIC) technique. The mass, momentum and energy conservation equations are solved on a staggered Eulerian grid while the physical properties are interpolated to the Lagrangian markers for advection. The Earth's mantle is treated as a highly viscous incompressible medium. Visco-plastic deformation is simulated by combining a Drucker-Prager yielding criterion with dislocation, diffusion and Peierls creep mechanisms.

In this paper we refer to our geodynamic model as Model CWM (Central Western Mediterranean Model). This model is an updated version of the Reference Model CM of Lo Bue et al. (2021). Here, the computational domain has been enlarged and has dimensions of 3700 x 700 x 2200 km (373 x 101 x 229 nodes) along the $x - y - z$ coordinates, with y being the vertical direction. As in Model CM, subduction modelling is self-consistent, driven only by internal buoyancy forces. Velocity boundary conditions are free slip everywhere. We impose a constant incoming heat flux of 2 mW/m^2 at the bottom boundary, while the top boundary is characterized by a constant temperature of 273 K. The side boundaries are insulating. The models account for frictional

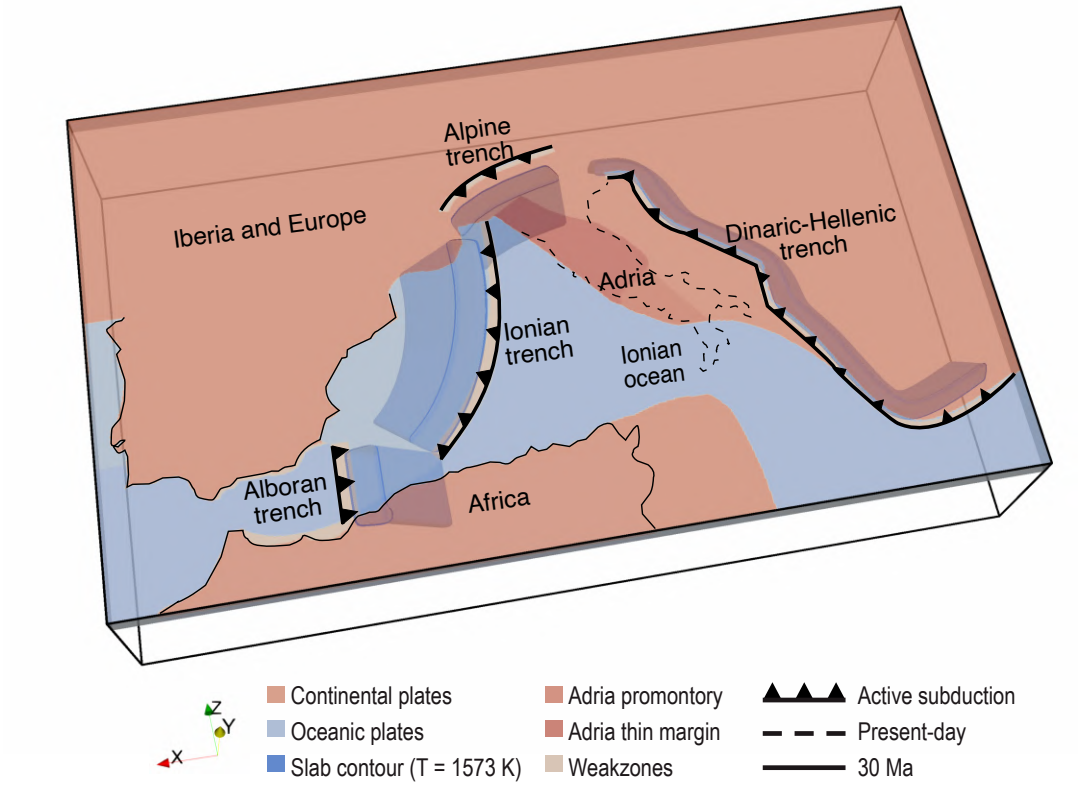

Figure 4.1: *Initial model setup for Model CWM. It consists of a subducting oceanic plate (Ionian Ocean;light blue) surrounded by lateral continental blocks (Adria, Africa, Iberia and Europe; salmon pink) drawn according to paleogeographic reconstructions at ∼30 Ma proposed by Faccenna et al. (2014), Romagny et al. (2020), and Van Hinsbergen et al. (2014). The Adria plate is characterized by the presence of a stiffer continental promontory (peach pink) and a thin continental margin (red) as proposed by Lo Bue et al. (2021), Lucente et al. (2006), and Lucente and Speranza (2001). Multiple subducting slabs are positioned according to the chosen reconstructions (i.e., Alboran and Ionian trenches as in Romagny et al. (2020); Alpine and Dinaric-Hellenic trenches as in Faccenna et al. (2014)) and taking into account the limitations imposed by numerical modelling. The solid black line indicates the coastlines at ∼30 Ma as in Van Hinsbergen et al. (2014), while the dashed black line the present-day coastlines of peninsular Italy. The plates are opacified for a better visualization of the subducted slab.*

and adiabatic heating, and for thermal and dynamic effects of phase changes (except that the medium is assumed to be incompressible).

We used the MATLAB toolbox geomIO (Bauville & Baumann, 2019) to create the 3D initial temperature and compositional fields. The tectonic plate geometry has been designed according to the paleogeographic and tectonic reconstructions at ∼30 Ma proposed by Faccenna et al. (2014), Lucente et al.

(2006), Lucente and Speranza (2001), Romagny et al. (2020), and Van Hinsbergen et al. (2014) although some simplifications were required due to limitations imposed by numerical modelling.

In the initial setup (Figure 4.1), a subducting oceanic plate, that represents the Ionian Ocean, is surrounded by lateral continental blocks corresponding to the Adria, Africa, Iberia and European plates. The position of the plates in the Oligocene-Miocene was adapted from a reconstruction of Van Hinsbergen et al. (2014). It is worth noting that, not having applied a convergence rate between the plates (self-consistent subduction), their relative position slightly differs from the present-day one. However, an initial geometry defined in the Oligocene-Miocene should not have a strong impact on mantle flow directions and splitting parameters as the slow Africa-Europe plates convergence has not caused a drastic change in plates position over this time span.

In Model CWM, we considered a more realistic paleo-tectonic configuration of the region, which is characterized by the presence of multiple subducting slabs rather than a single one as in Model CM.

Subduction in the Ionian plate occurs along two trenches as in Romagny et al. (2020). The longest one stretches from the Alps to the southeast of the Baleares and is associated with a slab dipping 40° NW and extending down to 300 km in the upper mantle. A second one is placed in the Alboran domain, where a slab with the same dipping angle but an opposite vergence extends down to 350 km in the upper mantle (Romagny et al., 2020). Throughout the manuscript we use "Ionian slab and Ionian trench" to indicate the former subduction zone and "Alboran slab and Alboran trench" when referring to the latter. It is worth noting that to trigger slab roll-back self-consistently, the Ionian trench has been positioned further south as in Lo Bue et al. (2021) and the initial depth of the Alboran and Ionian slabs has been increased compared to tectonic reconstructions. This could cause

a difference in rates of slabs retreat when compared to those reported in the literature and be representative of a more recent stage of the Central-Western Mediterranean history rather than the 30 Ma assumed here.

Two large collisional suture zones, are present in the continental Adria and European plates as in Faccenna et al. (2014). To the north, we find the Alpine trench with its characteristic arcuate shape and, to the east of the model, the Dinaric-Hellenic trench that extends from Eastern Alps to the southernmost tip of the Hellenic peninsula (Faccenna et al., 2014). In both trenches the slab dips almost vertically into the upper mantle to a depth of about 350 km to simulate locked collision zones. In this area slabs extended down to 350 km depth to model flow barriers due to the presence of subducted slab.

In the area of the model corresponding to the present-day Apenninic chain, we use the same initial configuration as in Lo Bue et al. (2021), characterized by lithospheric heterogeneities which are fundamental for the development of key tectonic features such as a prolonged eastward retreat of the Ionian plate and the formation of a slab window below the modelled central Apennines. The Adria plate consists of a thin continental lithosphere in the Umbria-Marche region and of a stiffer continental promontory in its central portion corresponding to the Abruzzo-Laziale platform (Calcagnile & Panza, 1980; Geiss, 1987; Lo Bue et al., 2021; Lucente et al., 2006; Lucente & Speranza, 2001; Maino et al., 2013; Miller & Piana Agostinetti, 2012; Panza et al., 2003). The African plate structure, nearby Sicily and the Sicilian Channel area, is characterized by a slightly thinner margin (Arab et al., 2020; Lo Bue et al., 2021).

The initial lithosphere thermal structure was modeled using the half-space cooling equation (Turcotte & Schubert, 2014), while the underlying asthenosphere consists of a 0.5 K/km constant adiabatic temperature gradient. The thermal age of the Ionian oceanic plate is 80 Myr, while that of the two slabs

is 70 Myr to simulate partial heating upon subduction. The age of the continental plates (Africa, Africa eastern margin, Iberia, Adria and Adria promontory) is 150 Myr while an age of 90 Myr was imposed for the thinned portion of Adria continental lithosphere. To activate a self-consistent subduction, the Ionian plate north of the two trenches is composed of a young lithospheric portion (1 Myr - the young age is justified by assuming a well-developed continental rifting system North of the Balearics and Corsica-Sardinia block). Furthermore, rheologically weak zones (constant viscosity of 10^{18} $Pa\,s$ and constant density of 3200 kg/m^3) have been inserted (i) on the slabs top surface to lubricate the initial contact between the overriding and the subducting plates, and (ii) around southwest Iberia and northwest Africa to facilitate the Alboran trench retreat (e.g., Chertova et al., 2014). The plates thermal structures and flow law parameters have been tuned to allow a self-consistently subduction and simultaneously to reproduce the main tectonic events as close as possible to the geological reconstructions. This may cause a too weak rheology and faster rates of mantle convection once self-sustained subduction has started due to the non-linear viscous behaviour of the mantle.

The density is computed using the thermodynamic databases generated with PERPLE_X (Connolly, 2005) and tested by Mishin et al. (2008) for a pyrolytic mantle composition. The continental crust density is calculated as being that of the mantle minus 400 kg/m^3, except for the Adria thin margin where we subtract 200 kg/m^3 to model a less buoyant continental lithosphere. Instead, for the crust of the Adria promontory we use a constant value of 2700 kg/m^3. More details about the physical parameters used in the geodynamic model can be found in Lo Bue et al. (2021).

4.2.2 Predicting mantle anisotropy and SKS splitting

The development of seismic anisotropy in the upper mantle is calculated using a modified version of D-Rex (Kaminski et al., 2004), which incorporates the deformation mechanisms inducing LPO (plastic deformation, dynamic recrystallization and grain-boundary sliding) and accounts for deformation history and non-steady-state evolution of geodynamic systems (Faccenda, 2014; Faccenda & Capitanio, 2013).

A large number of Lagrangian particles representing mineral aggregates are regularly distributed throughout the numerical domain (25 km reciprocal distance along the 3 directions, for a total of 364672 aggregates). Each particle consists of 1024 randomly oriented crystals, which results in an initially isotropic upper mantle. We use a harzburgitic upper mantle composition (70% olivine and 30% orthopyroxene modal abundance) and a more fertile pyrolitic mantle composition in the transition zone (60% spinel and 40% majoritic garnet) (Faccenda, 2014). The Eulerian velocity field obtained by the macro-flow simulation is then used to passively advect the particles and LPO is generated at each time step through the re-orientation of such particles in response to the gradients in the velocity field. Since SKS splitting parameters are mostly sensitive to the upper mantle (Sieminski et al., 2008), we only model the anisotropy from the Moho to the 410 km discontinuity. We use the same dimensionless crystallographic parameters as in (Rappisi & Faccenda, 2019) with the nucleation rate $\lambda = 5$, the grain-boundary-mobility $M = 1$ and the threshold volume fraction $\chi = 0.9$, which generate weaker fabrics and seismic anisotropy more consistent with the observations.

Synthetic SKS splitting parameters are computed using the software package FSTRACK (Becker, 2006). Through the stiffness matrix the code recovers the elastic tensors for each aggregate and then, below each station and down to 400 km, it builds a vertical stack of horizontal layers (minimum thickness

of 25 *km*) where the elastic tensor of each layer is radially averaged within a distance of 50 *km*. Next, assuming an incident plane wave (5° for typical SKS arrivals) into the mantle over a range of frequencies from 0 to 25 Hz, using the inverse Fourier transform, it computes a pulse seismogram that will be further filtered to construct SKS waves (i.e. from 0.1 to 0.3 *Hz*). Finally, by applying the cross-correlation method of Menke and Levin (2003) and averaging all the fast azimuths and delay times at each station measured by rotating the vertical stack of elastic tensors by 5° intervals around the y-axis, the SKS splitting parameters are determined. The software for computing mantle aggregates fabrics and SKS splitting can be found in the open source software package ECOMAN.

4.2.3 3-D P-wave Anisotropic Tomography

We use the anisotropic seismic imaging method by VanderBeek and Faccenda (2021), that solves for perturbations to P-wave slowness and three additional parameters that define the anisotropic magnitude, azimuth, and dip in a hexagonally symmetric medium. The tomographic algorithm does not require an anisotropic starting model which could potentially distort the results if not close enough to the true solution as in the case of the anisotropic imaging method of Munzarová et al. (2018). Additionally, changes in elevation and surface velocity are explicitly addressed in teleseismic imaging using 3D ray tracing through a user-defined 3D velocity model that incorporates elevation (Toomey et al., 1994).

Ray theoretical travel-times are estimated (i) with the shortest-path algorithm (Moser, 1991) through Model CWM described in the previous section using the mantle aggregates full elastic tensor at ∼21 Myr, and (ii) with the tau-p method (Crotwell et al., 1999) outside the study area using a 1D radial Earth velocity model. The geodynamic model was centered on 42°N 12.5°E

to match the main seismic structures with the real positions observed in current tomographic images.

Partial derivatives of the travel-times with respect to the model parameters are computed along the discretized ray paths. The LSQR method (Paige & Saunders, 1982) is used to solve the resulting linear system of equations relating changes in model parameters to changes in travel-times. To regularize the ill-posed inverse problem, damping and smoothing constraints are used. The choice of the regularization parameters that limit the norm of the model perturbational vector and enforce the Laplacian spatial smoothness of the model perturbations, thus controlling the length and the roughness of the solution vector relative to the length of the data residual vector, i.e. λ_d and λ_s respectively, is discussed in section 4.2.3.

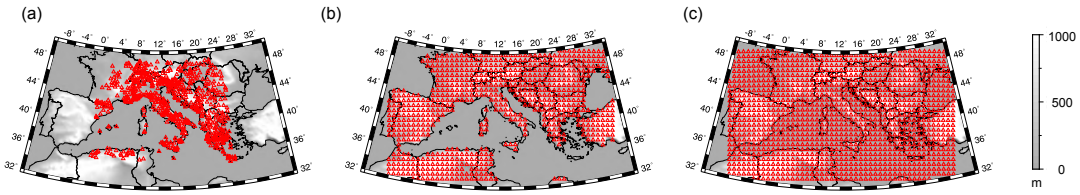

Figure 4.2: *Plot of the real land as in Rappisi et al. (2022) (a), ideal land (b) and ideal marine and land (c) station distribution.*

Starting model, discretization and regularization

We use a regular grid with uniform 10 km node spacing for the forward calculation of travel-times. The initial mantle velocity model is the isotropic 1D AK135 model (Kennett et al., 1995). We applied an Earth flattening transform (Müller, 1971) to account for Earth's curvature in our Cartesian model domain.

Perturbations to the three anisotropic parameters and the mean P-wave slowness (i.e. inverse of velocity, $u = 1/v$) are solved on a coarser regular grid with 40 km node spacing and then, at each iteration, linearly mapped

to the finer model used for travel-times calculation. Model CWM was considered down to 700 km depth, however, to limit the number of inversion parameters, anisotropic perturbations were restricted to the upper 400 km where there is the best ray crossing and mineral physics predicts mantle anisotropy to be most significant (Karato et al., 2008).

To resemble realistic conditions a first inversion was performed using delay times calculated through our Model CWM with the same distribution of sources (Supplementary Figure 4.12a) and receivers (Figure 4.2a), and the same regularization parameters as in the anisotropic tomography model of the Central Mediterranean by Rappisi et al. (2022) (Test 1). For this first test normally distributed errors with a standard deviation of 450 ms was added to the seismic data.

Next, several sets of inversions were run imposing a 1-sigma error of 125 ms applied to synthetic data and a smoothing-to-damping ratio (λ_s/λ_d) of 100 and damping values (λ_d) of 1,2,...9,10 with different synthetic datasets. For these sets of tests we used: (i) same sources (Supplementary Figure 4.12a) and station array as in Test 1 (Test2); (ii) an ideal on land receivers distribution (Figure 4.2b) (Test 3); (iii) an ideal marine and on land receivers distribution (Figure 4.2c) (Test 4). In the last two cases (Test 3 and 4) the receivers are equally spaced 75 km apart and the teleseismic events are placed at a distance from the center of the domain from a minimum of 35 ° up to a maximum of 110°, every 10° of azimuth (Supplementary Figure 4.12b), guaranteeing a perfectly homogeneous azimuthal events distribution, thus removing any bias associated with preferential sampling of certain back azimuths.

In addition we performed (iv) purely isotropic inversions in order to evaluate the effect of neglecting seismic anisotropy on the tomographic image (Test5), and (v) an inversion where the Model CWM is considered to be isotropic below 200 km to address vertical smearing of anisotropic structures (Test 6).

Table 4.1: *Inversions summary table. The type of inversion (isotropic/anisotropic), receivers distribution, true model, standard deviation of normally distributed data errors, damping and smoothing factors and relevant figures for each inversion are listed. In bold the λ_d corresponding to the preferred solution.*

	Type	**Receivers Distribution**	**True Model**	**Data error**	λ_d	λ_s/λ_d	**Figures**
Test 1	Anisotropic	Real land (Rappisi et al., 2022)	Anisotropic down to 400 km	450 ms	6	200	4.6e-h; 4.16c-d; 4.17e-h
Test 2	Anisotropic	Real land (Rappisi et al., 2022)	Anisotropic down to 400 km	125 ms	1,**2**,3,...,10	100	4.6i-l; 4.13a; 4.16a-f; 4.17i-l
Test 3	Anisotropic	Ideal Land	Anisotropic down to 400 km	125 ms	1,**2**,3,...,10	100	4.8a-d; 4.13c; 4.16g-h
Test 4	Anisotropic	Ideal Marine + Land	Anisotropic down to 400 km	125 ms	1,**2**,3,...,10	100	4.6m-p; 4.13b; 4.16i-j; 4.17m-p
Test 5	Isotropic	Ideal Marine + Land	Anisotropic down to 400 km	125 ms	1,**2**,3,...,10	1000	4.8a-d; 4.13d; 4.16k-l
Test 6	Anisotropic	Ideal Marine + Land	Anisotropic down to 200 km	125 ms	2	100	4.8e-h; 4.16m-n

We constructed L-curves (Aster et al., 2018) plotting the squared model norm ($|dm|^2$) as a function of the squared norm of the delay time residuals normalized by the estimated data uncertainty (χ^2) for different values of damping factor (λ_{du}) (Supplementary Figure 4.13). Ideal solutions are considered those near the corner of the L-curve where an increase in model norm does not result in an appreciable decrease in data residuals. For each test, convergence is usually reached before or at iteration 3.

Reliability of the tomographic results

To explore possible trade-offs between isotropic and anisotropic parameters, a synthetic inversion was aimed at reconstructing the isotropic component of model CWM. To test if velocity anomalies present in our preferred isotropic model could yield erroneous anisotropy, delays predicted through this model –not considering the anisotropic components– were inverted for both isotropic and anisotropic parameters. The result is showed in Figure 4.3. Isotropic anomalies were faithfully recovered with minimal anisotropic perturbations throughout the entire study area (generally $<$1%) with the exception of higher-magnitude anisotropic perturbations ($<$2%) in the Southern Tyrrhenian sea, Ionian sea and Sicilian Channel.

Permuted data test similar to Bijwaard et al. (1998), Rawlinson and Spakman (2016), and Spakman (1991) was performed in order to assess the model amplitude error as the anomaly amplitudes are interpreted in terms of geodynamic features and errors could potentially bring to wrong interpretations. The inverted dataset is the data vector of the last iteration of Test 2, randomly permuted. The "permuted dataset" can be considered noise that has the same average, standard deviation and distribution of the delay times "not permuted" used for Test 2. By permuting the data vector order, there is no more correlation between the delay times and the raypaths. The starting model is the tomography obtained at the last iteration of Test 2. This

choice allows to guarantee that the ray geometry of the permuted data test is comparable to that in Test 2. The result is showed in Figure 4.4. We do not observe regions with systematic anomaly patterns, on the contrary, random anomalies are recovered with delay time residual $\chi^2 \approx 8.8$ and the RMS amplitude variations $\approx 0.99\%$. This value is much bigger than the data residual observed for Test 2 (i.e. $\chi^2 \approx 0.95$; Supplementary Figure 4.13a) and for Test 3, 4 and 5 as well (i.e. $0.85 < \chi^2 < 3.6$; Supplementary Figure 4.13b-d). The random distribution of the retrieved anomalies and the low data fit obtained for the permuted data test compared with the higher data fit of the correlated (i.e. the data vector not permuted) data test suggest that the results of our tests (i.e. Test 1-6) are reliable.

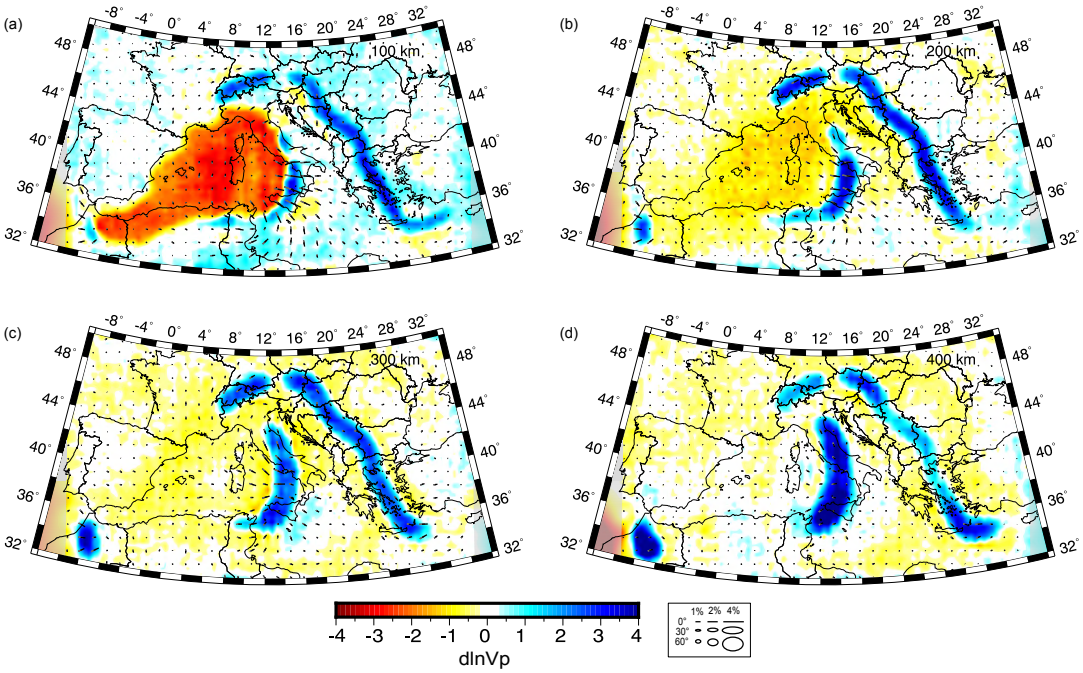

Figure 4.3: *Isotropic restoration synthetic test. Anisotropic inversion of purely isotropic synthetic data calculated through our model CWM, i.e., non taking into account the anisotropic patterns. While no anisotropic structures have been considered when performing the forward problem, the inversion does introduce some anisotropic perturbations. Anisotropy is represented by ellipse symbols where the major axis of the ellipse parallels the fast-direction and the minor axis scales linearly with the symmetry axis dip into the view plane such that fabrics parallel and normal to the cross-sections plot as lines and circles, respectively. Anisotropic perturbations were restricted to the upper 400 km. See legend. Areas of poor data coverage are masked in grey.*

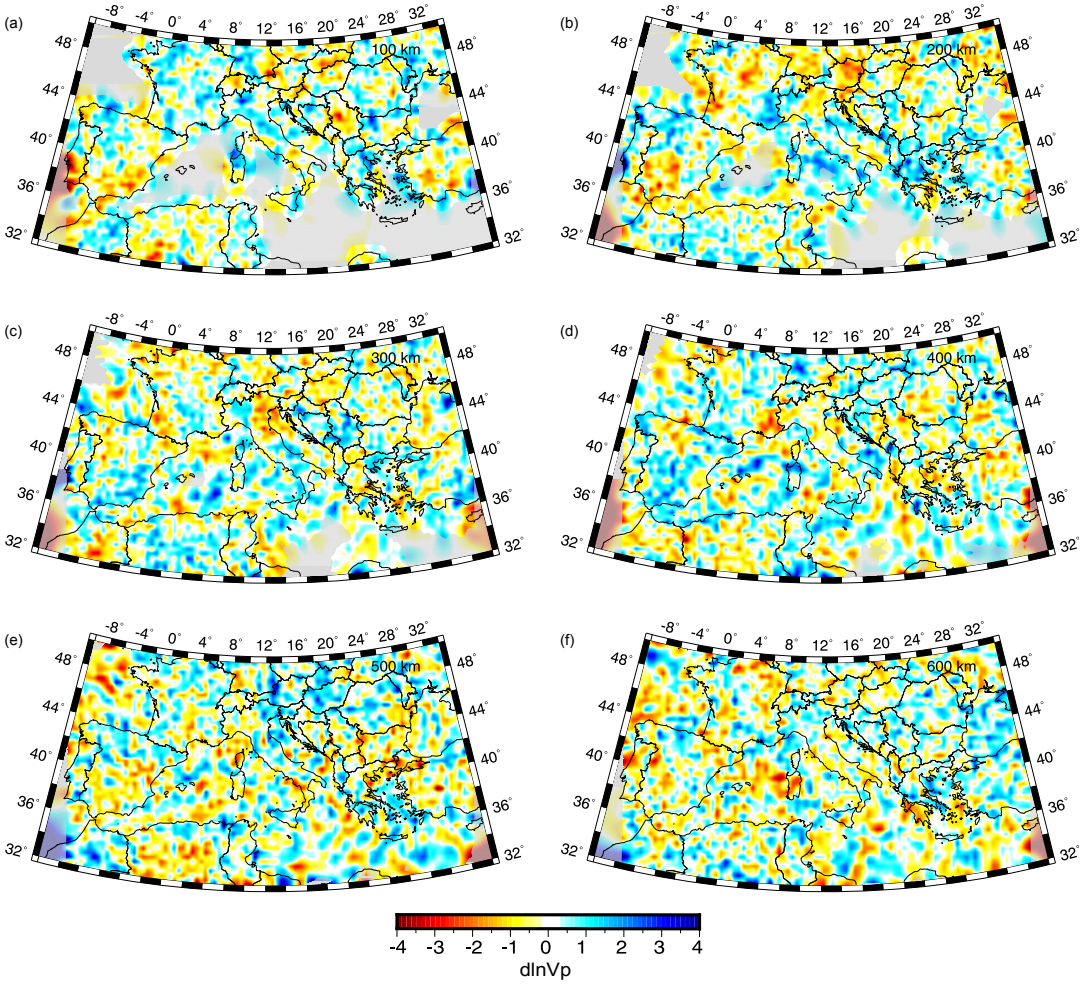

Figure 4.4: *Permuted data test. P-wave velocity anomalies obtained from the inversion of randomly permuted delay times.*

4.3 Results

4.3.1 Geodynamic evolution of the Central Western Mediterranean (Model CWM)

In this section the geodynamic evolution of Model CWM is addressed (Supplementary Movie S3). The following discussion focuses on a mere description of our geodynamic model evolution. Analogies and differences between Model CWM and the real tectonic evolution of the Central-Western Mediterranean region will be discussed in section 4.4.1. The Alpine and Dinaric slabs have been included in the Model CWM only to evaluate their influence in the mantle flow below the Adria plate surrounding regions, but they also

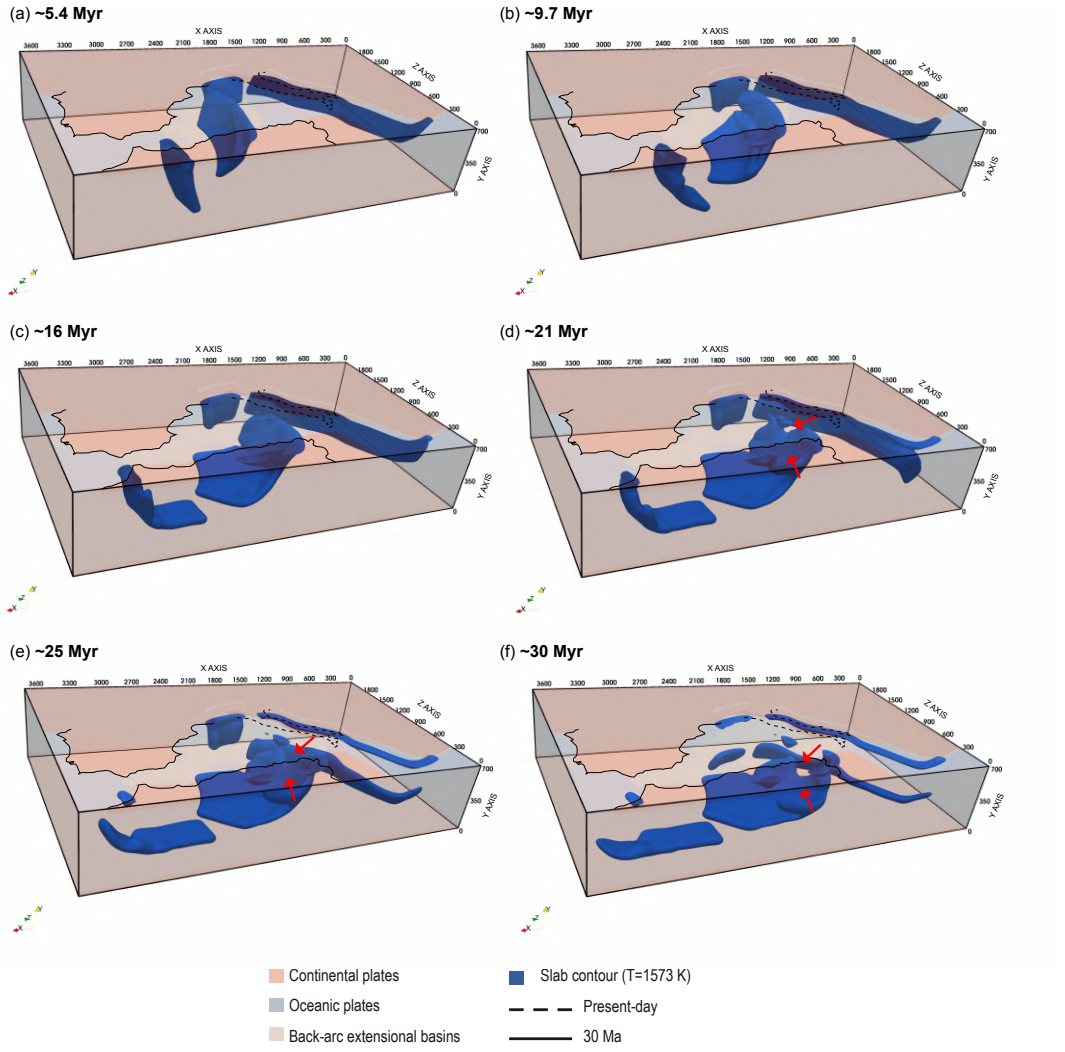

Figure 4.5: *Snapshots of the Model CWM geodynamic evolution. In blue the subducted slabs (contour at T=1573 K) below ∼100 km depth. The plates are partially transparent for a better visualization of the subducted slabs. The solid black line indicates the coastlines in the Oligocene-Miocene (Van Hinsbergen et al., 2014), while the dashed black line indicates the present-day coastlines of peninsular Italy. The red arrows indicate the two slab windows beneath the Central Apennines and the Africa continental plate.*

represent important targets to be recovered by our tomographic inversions. Their geodynamic evolution is characterized by further slab verticalization and final break-off.

The slabs negative buoyancy drives the evolution of the two active oceanic subductions. The oceanic plates progressively sink down to the the mantle transition zone and after bending start to rollback accompanied by a stretching of the overriding lithosphere. The Ionian slab migrates south-eastward while the Alboran slab south-westward. The rollback of the two slabs evolves

with episodes of lateral tearing, segmentation and break-off when trenches impact with a continental margin.

The tectonic evolution of the Ionian slab is similar to that of Model CM (Lo Bue et al., 2021). In a few million years ($\sim$ 4 Myr), the western part of the Ionian trench collides with the African plate inducing slab tearing along the passive margin and subduction of continental crust fragments. The tear propagates along the African margin, favouring the eastward slab rollback (Figure 4.5a). Subsequently, the northeastern edge of the trench reaches the thin northwestern Adria margin progressively causing subduction of the Adria continental crust, slab lateral tearing along the oceanic-continental lithosphere transition, and the formation of a curved trench due to the variations of buoyancy along it. Meanwhile, the Alboran slab rapidly rolls back westward, accommodated by lithosphere tearing along the African and Iberian margins (Figure 4.5a,b). In $\sim$10 Myr, both subducting slabs are already stagnating horizontally in the mantle transition zone at the bottom of the model.

After $\sim$16 Myr (Figure 4.5c), the Alboran slab reaches the area of the model corresponding to the current Gibraltar region, after which a very slow trench retreat is observed until the complete detachment at $\sim$23 Myr.

The late evolution of the Ionian slab is instead more complex and important differences occur compared to the Model CM (Lo Bue et al., 2021). When the Ionian trench reaches Central Adria, part of the stiffer continental promontory subducts causing slab break-off. As in Lo Bue et al. (2021), this rupture generates a large slab window that splits the Ionian slab in two separate slabs. Contrary to Lo Bue et al. (2021), here, this phenomenon also occurs on the side of the African continent. This leads to a final geometry of the Ionian slab characterized by the presence of two wide windows, one below the area corresponding to the current Central Apennines and one beneath the north-eastern African margin (Figure 4.5d).

After ∼20 Myr (Figure 4.5d,e,f), slab remnants are found in model areas corresponding to the present-day Northern Apennines, Southern Tyrrhenian sea, Alboran sea and Kabylides. At ∼20 Myr, the Ionian slab (portions beneath the Northern Apennines and south of the Tyrrhenian Sea - Supplementary Figure 4.14a) and the Alboran slab extend continuously from the surface down to the mantle transition zone.

At ∼ 25 Myr, the Northern Apenninic and Kabylides slabs hang down to ∼150 km depth (Supplementary Figure 4.14b). The first one extends further deeper from ∼180 km down to about ∼660 km depth while a horizontal segment of the Kabylides slab is still joined to the Ionian slab from ∼180 km down to about ∼300. The remaining portion of the Ionian slab (south of the Tyrrhenian Sea) instead extends continuously from the surface down to the mantle transition zone. The Alboran slab is already detached. At ∼ 30 Myr, the Calabrian slab appears still anchored to the surface (Supplementary Figure 4.14c) showing clear evidences of break-off. The model evolves with the complete detachment of all the slabs (Figure 4.5f).

4.3.2 Upper Mantle Flow, LPO, and Synthetic Seismic Anisotropy

The subduction and rollback of the Ionian and Alboran slabs in the Model CWM induces a complex flow in the surrounding mantle characterized by the presence of poloidal and toroidal components (Supplementary Movie S3). The initial sinking of the two slabs (i.e. Ionian and Alboran) generates a dominant poloidal flow component and mantle upwelling in the mantle wedge (i.e., arrows pointing downward or upward in correspondence of slabs and basins, respectively - Supplementary Movie S3). Subsequently, toroidal cells are also generated by slab rollback that forces the mantle to flow

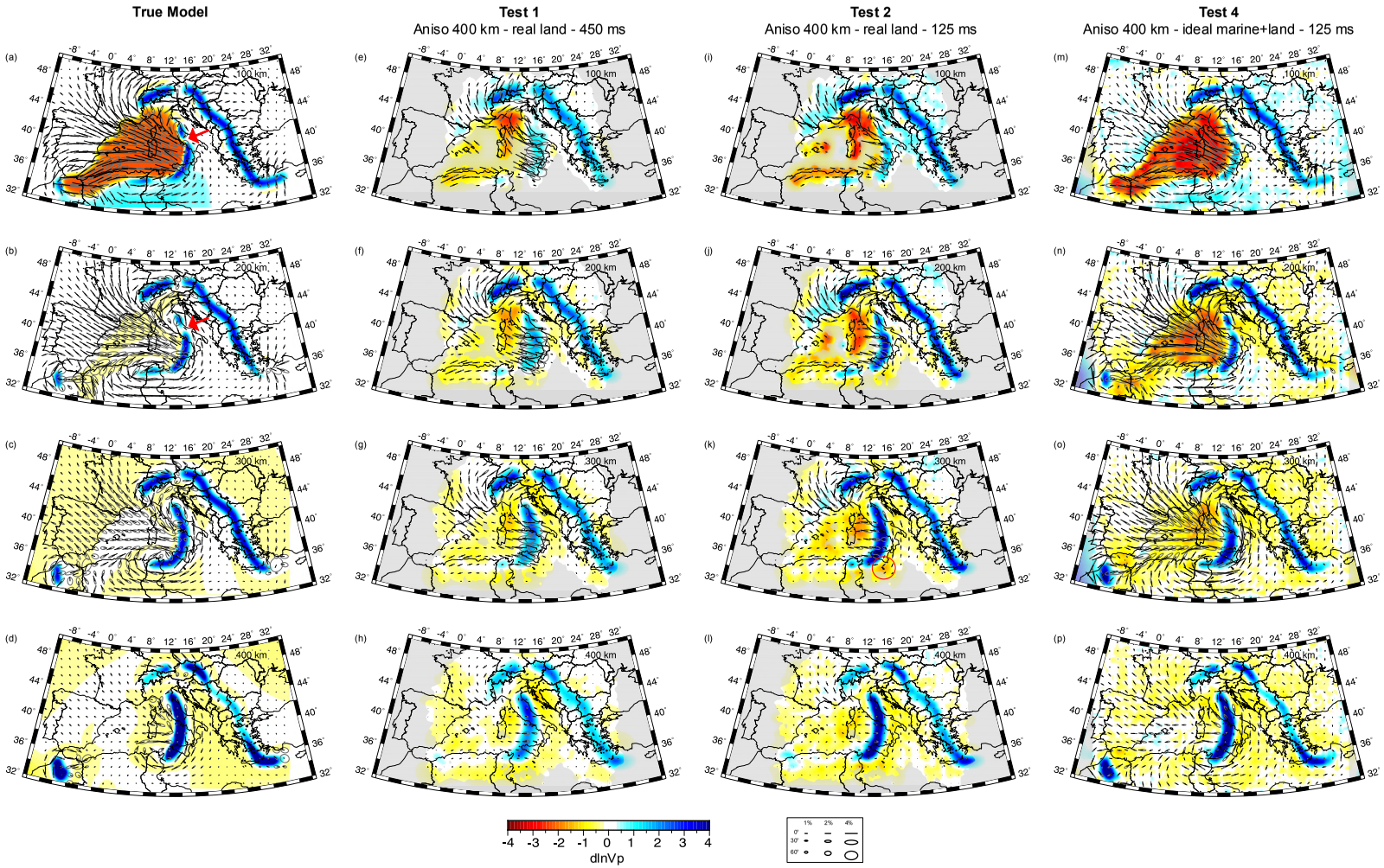

Figure 4.6: *True model and anisotropic tomography results. Depth slices are shown at 100 km, 200 km, 300 km and 400 km depth for the true model (a-d), the model resulting from Test 1 (e-h), Test 2 (i-l) and Test 4 (m-p). Isotropic anomalies are plotted with respect to the reference velocity model. We plot anisotropic fabrics as ellipses where the major axis of the ellipse parallels the fast-direction of anisotropy in the view plane and scales with the anisotropic magnitude while the minor axis scales linearly with the symmetry axis dip into the view plane. Thus, fabrics parallel and normal to the view plane plot as lines and circles, respectively; see legend. Areas of poor data coverage are masked in grey. The red arrows in panels a and b indicate the position of the slab window below the Central Apennines. The red circle in panel k indicates a low velocity artefact.*

circularly around the edges of the two slabs and through the slab windows that are formed at later stages.

Here, compared to Model CM (Lo Bue et al., 2021), the complexity of the mantle flow increases due to the presence of the multiple subducting slabs. We observe the mantle flowing mainly horizontally toward southeast and west directions in response to the horizontal motion of the Ionian and Alboran slabs, respectively. The Dinaric and Alpine slabs act as a barrier to the large toroidal flow patterns induced by the retreat of the Ionian plate found in Model CM of Lo Bue et al. (2021). As a result, the mantle flows parallel to the Dinaric slab in the region corresponding to the Adriatic sea and Dinarides, as well parallel to the Alpine slab. The strongest upper mantle fabrics are observed in the area surrounded by the Alboran and Ionian slabs, down to 400 km depth, while east of the Dinaric slab and in the eastern Ionian sea mainly isotropic structures are found (Figure 4.6a-d). This is because Model CWM only partially reproduces the retreat of the Aegean slab over the Cenozoic. Trench-perpendicular azimuths are observed in the supra-slab upper mantle, corresponding to the Tyrrhenian and Alboran basins. The sub-slab upper mantle portions (i.e. below Calabrian, Alboran and Alpine slabs) are instead characterized by the presence of trench-parallel fabrics. Near-horizontal fabrics are found in the area of the Ionian sea and in the continental European plate. More steeply dipping fabrics are instead observed in the Tyrrhenian sea, Alboran basin and Northern Italy in correspondence of the subducting slabs.

The upper mantle fabrics patterns are reflected in those of the synthetic SKS splitting measurements shown in Figure 4.7. In the back-arc regions, the fast azimuths orient parallel to the trajectory of the Ionian and Alboran trenches migration. The delay times in these regions are very high ($\delta t = 2 - 3.2s$), reflecting fabrics that are consistent within the entire upper mantle, and are reduced in the areas near the two trenches ($\delta t = 1 - 1.5s$) due to the

superposition of mantle domains with contrasting fabric patterns. In the fore arc regions, the teleseismic fast shear wave components align trench-parallel, while around the slabs edges, they form a circular pattern highlighting the underlying return flow ($\delta t = 1 - 1.5s$).

4.3.3 Anisotropic tomography inversions

Tomography results are shown in Figure 4.6 and 4.8, with additional maps at 500 km and 600 km depth in Supplementary Figure 4.16 and narrower colorscale limits (i.e. [-2% – +2%]) in Supplementary Figure 4.17.

Following the workflow described in section 4.2.3, we first inverted a set of time delays computed through Model CWM using the distribution of sources and receivers as in Rappisi et al. (2022) (see Supplementary Figure 4.12a and Figure 4.2a; Test 1). We added random errors with a standard deviation of 450 ms to the data (i.e. a value corresponding to the amount of error usually encountered in real case studies). This solution reproduces realistic study conditions to test the ability of our method in recovering the main isotropic and anisotropic structures of the target (Figure 4.6 e-h).

The marine areas of the Tyrrhenian, Adriatic, Ionian Sea and Strait of Sicily are poorly sampled, resulting in a general loss of fast and slow anomaly amplitude. Nevertheless, the main isotropic structures (i.e. the Alpine, Northern Apennines, Calabrian and Dinaric-Hellenic slabs) are well recovered. The Northern Apenninic and Calabrian slabs are imaged as a single weak fast anomaly stretching along the N-S direction, while in the geodynamic model a ∼150 km wide window is present at shallow depth, i.e ∼100-200 km beneath central Italy (Figures 4.5d, 4.14a and 4.6a-b).

Test 1 exhibits a ∼-2% low velocity artefact in correspondence of the northern Tyrrhenian basin and Corsica-Sardinia block at ∼200 km depth (Figure 4.6f), indicating some vertical smearing of the true low velocity structure

confined in the upper 100 km of the domain. Anisotropy patterns are well recovered where seismic ray coverage is relatively abundant, e.g., the near-horizontal circular pattern of P-wave fast azimuths around the Western Alps in Southern France. Trench perpendicular steeply dipping fabrics are imaged above the Calabrian slab in the Tyrrhenian Sea, while E-W oriented fabrics are found in the Northern African margin.

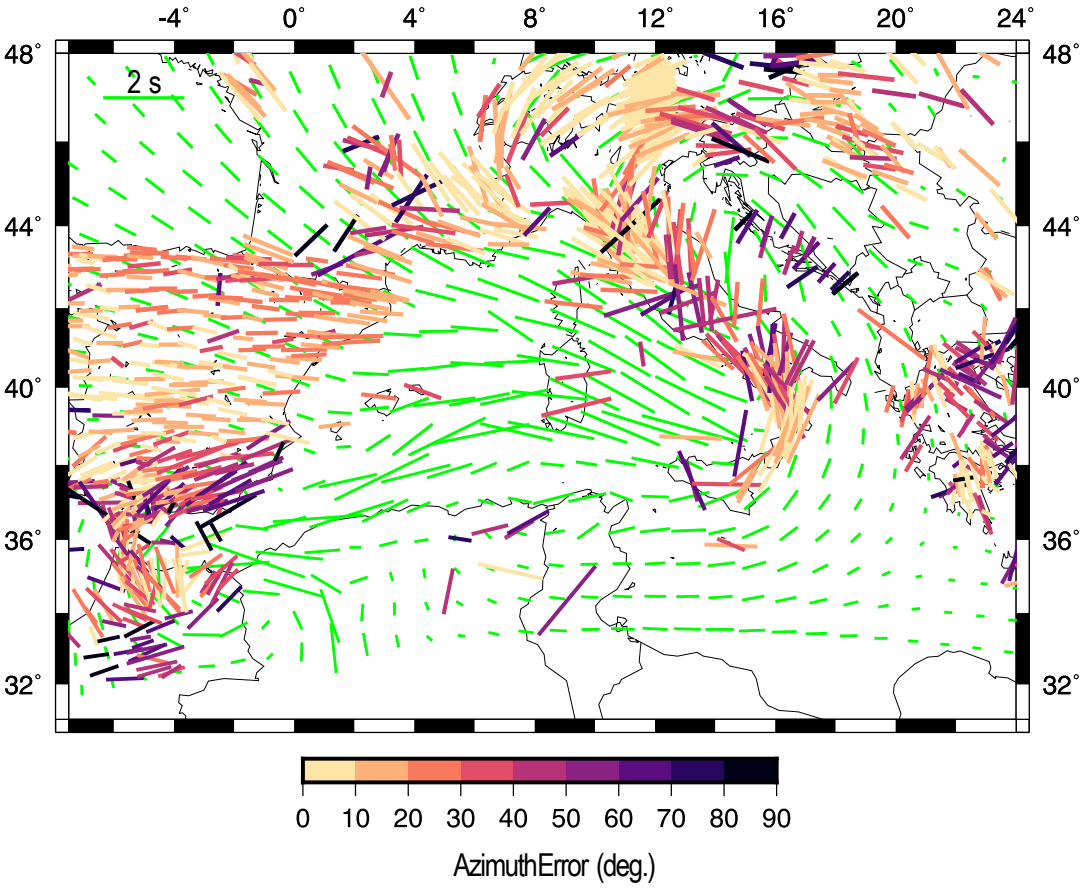

Figure 4.7: *SKS-splitting measurements in the Central-Western Mediterranean (Becker et al., 2012) color-coded by the angular misfit compared with synthetic SKS splitting measurements for Model CWM at ∼20 Myr (green bars). The EW green bar in the upper left corner indicates 2 s. Time-delay misfits are shown in Supplementary Figure 4.15a.*

The recovered isotropic and anisotropic structures from the model resulting from Test 2 (Figure 4.6i-l) indicate that a better quality dataset increases the probability of better retrieving the magnitude and sharpness of the true anomalies. However, at the same time new and increased in magnitude tomography artefacts are observed. For example, the low velocity artefact at

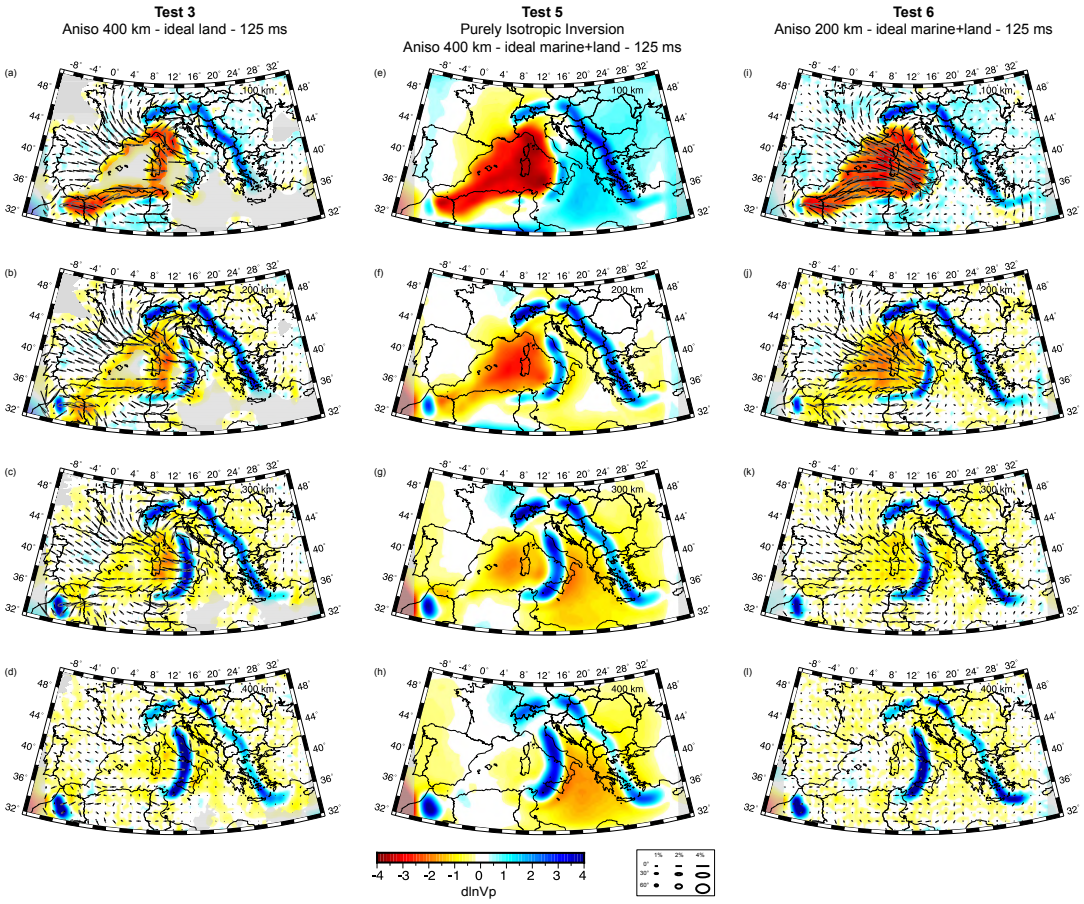

Figure 4.8: *Depth slices at 100 km, 200 km, 300 km and 400 km depth for the tomographic results from Test 3 (a-d), Test 5 (e-h) and Test 6 (i-j). Isotropic anomalies are plotted with respect to the starting model. Anisotropy is plotted using ellipses as described in Figure 4.6. Areas of poor data coverage are masked in grey.*

200 km depth (Figure 4.6j) in the Tyrrhenian sea, east of the Sardinia-Corsica block, is in Test 2 much stronger than it was in Test 1 (Figure 4.6f) with an increase in magnitude of ∼1%. And also, a new ∼100 km wide low velocity artefact (∼-2%) appears at 300 km depth south of Sicily (Figure 4.6k). High velocity artefacts already observed in Test 1, such as the one in Spain and west of the Alps, are in Test 2 much bigger (i.e. joined in a single broader anomaly) and slightly stronger in amplitude, covering the entire southern portion of France at 100 and 200 km depth (Figure 4.6i-j). Although the anisotropy patterns do not differ from the ones of Test 1, a reduction in their magnitude is observed above the Calabrian slab (i.e. in the Tyrrhenian Sea

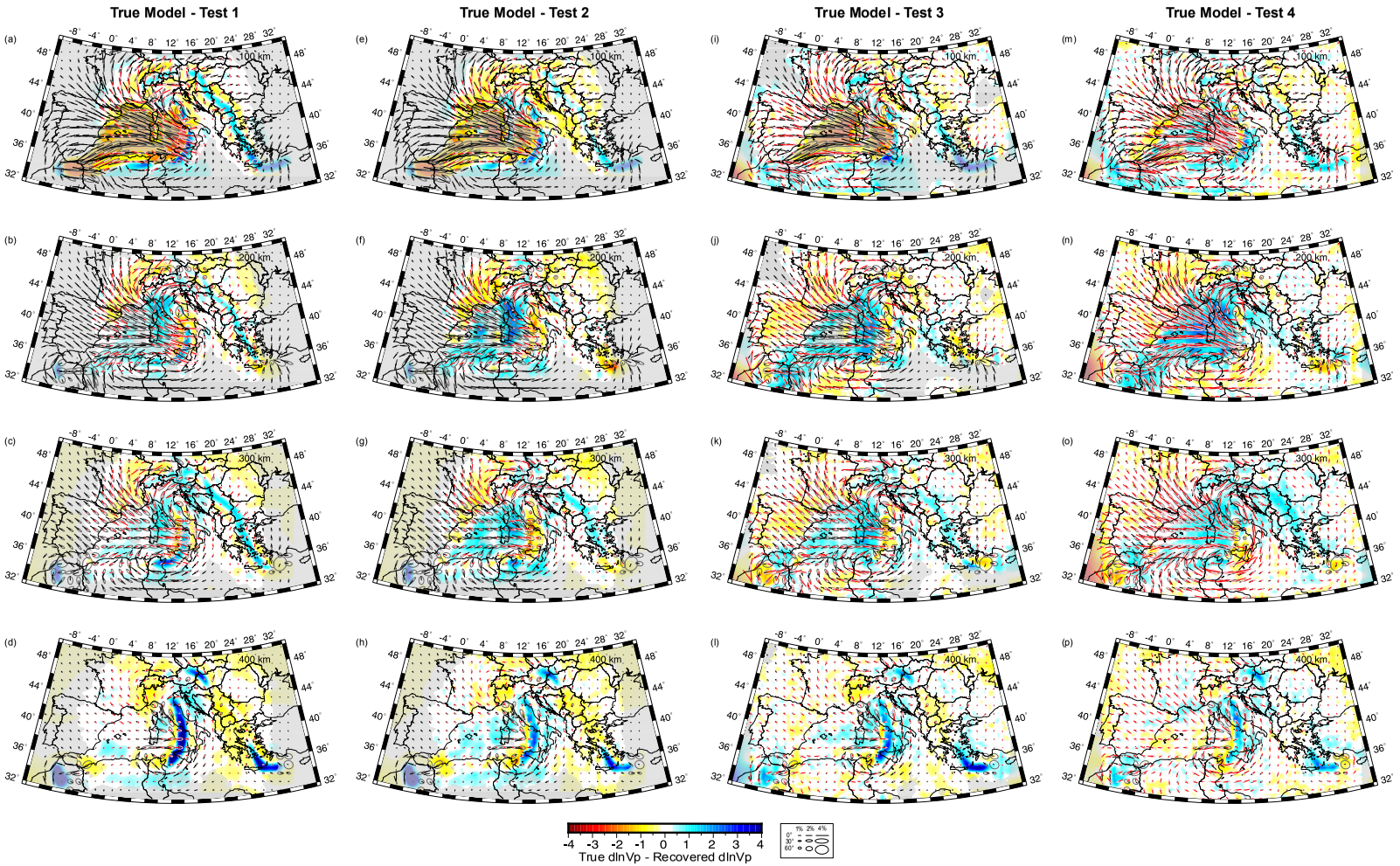

Figure 4.9: *Depth slices at 100 km, 200 km, 300 km and 400 km showing the differences between the true model and (a-d) Test 1, (e-h) Test 2, (i-l) Test 3 and (m-p) Test 4. Anisotropy is plotted using ellipses as described in Figure 4.6. Areas of poor data coverage are masked in grey.*

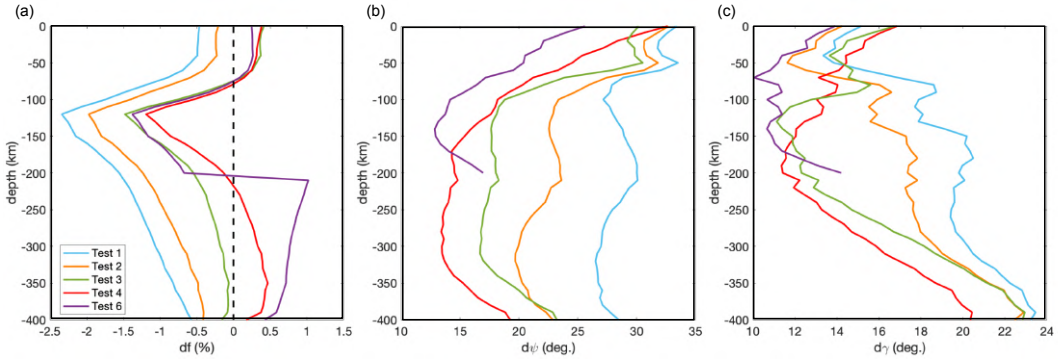

Figure 4.10: *Errors in recovered anisotropic parameters. Mean errors in the anisotropic (a) fraction, (b) azimuth, and (c) elevation as a function of depth are shown for Test 1 (blue line), Test 2 (orange line), Test 3 (green line), Test 4 (red line) and Test 6 (purple line).*

dipping fabrics). Probably due to the trade-off between isotropic and anisotropic components, it is worth noting that this reduction is associated with an increase in the magnitude of the isotropic fast anomaly.

In Test 4, with an ideal distribution of sources (Supplementary Figure 4.12b) and marine and land receivers (Figure 4.2c), the fast anomalies are better retrieved in terms of amplitude and spatial distribution (i.e. size and geographic position). However, many artefacts still persist, for example, at 100 km depth (Figure 4.6m) the Calabrian fast anomaly exhibits a weak magnitude (i.e., ∼1% vs. ∼3% in the true model). More importantly, at 200 km depth (Figure 4.6n) the slow velocity artefact located est of the Sardinia-Corsica block in the previous tests now affects the entire Liguro-Provençal and Tyrrhenian basins. Although the weak magnitude of the Calabrian fast anomaly, the gap between Northern Apennines and Calabrian slab is better retrieved at 100 and 200 km depth (Figure 4.6m, n) with respect to the previous Test 1 and Test 2. The Alboran fast anomaly is recovered as well and placed in the correct geographic position (Figure 4.6p). The high velocity artefact imaged in Test 2 beneath the southern France at shallow depth (100-200 km; Figure 4.6i-j), now disappears and the recovered model better resembles the target. The ideal station coverage also helps in retrieving anisotropic

patterns and magnitude at every depth slice, including the well sampled marine areas where the NW-SE fabrics are now recovered in the Tyrrhenian Sea. Similar results, i.e. about sensitivity of teleseismic P-wave tomography under different conditions, have been previously described (e.g., Lévěque et al. (1993), Rawlinson and Spakman (2016), and Spakman and Nolet (1988)).

Considering that placing marine receivers is a costly procedure, we also performed a set of inversions with an ideal distribution of on-land receivers only (Figure 4.2b). The result is shown in Figure 4.8a-d. The main effect of having reduced the number of receivers is the underestimation of anisotropy in poorly sampled areas. For example, the trench-parallel patterns bordering the eastern side of the Apenninic fast anomaly in Test 3 (Figure 4.8a-d) appears weaker than it is in the true model and in Test 4 (Figure 4.6a-d, 4.6m-p).

Figure 4.8 also shows the results of Test 5 and 6 performed, respectively, in isotropic approximation (Figure 4.8e-h; i.e. ignoring seismic anisotropy) or with a model that is anisotropic only in the top 200 km (Figure 4.8i-l). In both cases, we observe that the isotropic solution contains a number of fast anomaly features broadly consistent with the true model (Figure 4.6a-d). However, several slow velocity artefacts are imaged around and above the main slabs (i.e. Alpine and Calabrian slabs) especially when not considering seismic anisotropy (Figure 4.8e-h). Figure 4.8i-l indicate that seismic anisotropy is retrieved also at depths below 200 km where the true model is instead isotropic. This suggests that when only using teleseismic P-waves anisotropic structures are vertically smeared similarly to isotropic anomalies.

4.4 Discussion

4.4.1 How well does Model CWM fit seismological observations?

In this work we have extended the modelling methodology of Lo Bue et al. (2021) to build a structurally complex geodynamic model which was then exploited to test the capabilities of anisotropic P-wave seismic tomography to recover a Mediterranean-like subduction environment. With respect to Model CM of Lo Bue et al. (2021), the new geodynamic model CWM has been updated by using a different paleo-tectonic configuration characterized by the presence of additional subducting plates (i.e., Alboran, Alpine and Dinaric subduction zones).

Similarly to previous studies (Holt et al., 2018; Holt et al., 2017; Jagoutz et al., 2015; Király et al., 2018; Luth et al., 2013; Peral et al., 2020), here we notice that the presence of multiple subducting slabs influences the overall force balance, the geometry and kinematics of the subduction systems, as well as the mantle flow patterns. The inclusion of additional subduction zones has partly improved the prediction of the mantle dynamics leading to a better correspondence between the modeled and observed surface and deep isotropic structures, and seismic anisotropy patterns when compared to Model CM of Lo Bue et al. (2021). A quantitative comparison between predicted and observed SKS splitting measurements (Figure 4.7; Becker et al. (2012) database updated December 6, 2020) shows a moderate improvement in terms of the average misfit angle from $\sim 26^{\circ}$ in Model CM (Lo Bue et al., 2021) to $\sim 23^{\circ}$ in Model CWM (Supplementary Figure 4.15). In detail, the general pattern of the synthetic 3D anisotropy calculations matches the observed data with a relatively lower misfit angle in the model areas corresponding to the Iberian peninsula and the Apennines chain if compared to

the Model CM (Lo Bue et al., 2021). In the Dinaric Alps area the synthetic fast splitting directions are trench parallel. Here, the average angular misfit between predicted and observed fast azimuths remains high, but with slightly reduced values of about $70 - 80^{\circ}$ degrees, compared to 90° degrees of Lo Bue et al. (2021). Lastly, we acknowledge that split times are not particularly well-fit considering that the residual mean and standard deviation are 667 ms and 592 ms, respectively (Supplementary Figure 4.15). However, the magnitude of the average misfit of the whole model is mainly due to the broad mismatch found in the south of the Iberian Peninsula.

Uncertainties in the initial model geometry and in the modeled mantle rheology are likely responsible for the major discrepancies. Other sources of mismatch could be related to the modelling of the mantle textures, and to the presence of fossil fabrics within the oceanic and continental subducted lithosphere that have not been included here. Furthermore, the employed free slip boundary conditions prevent lateral mantle flow across the bottom and vertical boundaries. The large discrepancy in the area of the southern Iberian Peninsula may be partly due to the fact that the model does not account for the Cenozoic Eurasia-Africa convergence, and the relative position of the African plate has remained fixed since $\sim$30 Ma differing slightly from the present-day one. As such, the Alboran arc is positioned further south than its present-day position (under Morocco).

Although Model CWM is based on paleogeographic and tectonic reconstructions of the region in the Oligocene-Miocene (Faccenna et al., 2014; Lucente et al., 2006; Lucente & Speranza, 2001; Romagny et al., 2020; Van Hinsbergen et al., 2014), geometrical assumptions, that could potentially bias the final output, were required due to limitations imposed by numerical modelling.

First, the initial geometry and thermal ages of the subducting slabs were

partly simplified and this could strongly influence the comparison with seismological data. This could be the case of the Alps and Dinarides where a simplified initial portion of the subducted lithosphere was imposed to model flow barriers. We note that the detachment of Alpine slabs prior to collision is still debated in some areas, such as the Western Alps where Kästle et al. (2020) favor the interpretation of a recent European slab break-off, consistent with observations of strong exhumation and sedimentation that started around 2–7 Ma ago and is still ongoing (Escher & Beaumont, 1997; Fox et al., 2016; Kuhlemann, 2007; Nocquet et al., 2016). On the contrary, Zhao et al. (2016) document the lateral continuity of the European slab from the Western Alps to the Central Alps, and the downdip slab continuity beneath the Central Alps, ruling out the hypothesis of slab break-off to explain Cenozoic Alpine magmatism. The teleseismic P-wave tomography of Rappisi et al. (2022), referred as model ani-NEWTON21, exhibits a continuous slab beneath the Alps, divided into an Eastern, Central, and Western segment characterised by changes in dip. Similarly, the extent of the Dinaric slab at ∼30 Ma is largely debated. Post-collisional uplift and contemporaneous emplacement of igneous rocks (33-22 Ma) in the internal Dinarides may suggest either (i) "that the Oligocene-Miocene orogen-wide uplift was driven by post-break-off delamination of the Adriatic lithospheric mantle" (Balling et al., 2021), or (ii) verticalization of the Adria slab driven by slab pull and consequent upper plate extension, which is exactly what is modeled in our Model CWM. In conclusion, the available geophysical and geological data do not allow to discriminate between a model of post-collisional slab break-off and one of post-collisional slab verticalization (as modelled for the Alps and Dinarides in our Model CWM), as both would imply upper plate extension, uplift and magma emplacement (Faccenda et al., 2009; Faccenda et al., 2008).

Secondly, the tectonic reconstruction of Romagny et al. (2020) shows that ∼30 Ma the Mesozoic Tethyan lithosphere was consumed in two different

trenches located from the Alps to the southeast of the Baleares and in the Alboran domain, respectively. Two incipient slabs (∼150-200 km) were already subducted in the upper mantle. However, to trigger a "spontaneous" subduction system, the Ionian trench has been initially positioned further south with the slab extending to a depth of 300 km, while the Alboran one further west with a 350 km deep slab, in order to model a more developed subduction and increase the slab negative buoyancy. This could cause a difference in rates of Ionian and Alboran slabs retreat at the model early stage when compared to those reported in the literature. However, we note that in the reconstructions by Faccenna et al. (2014) and Romagny et al. (2020) the initial plate geometry at ∼23 Ma does not differ substantially from that at ∼35 Ma, and from our initial setup. This is likely related to the slow dynamics typical of incipient subduction systems.

Despite the modelling limitations, Model CWM reproduces several episodes of slab lateral tearing and break-off that have been proposed according to geological and seismological data. The model is partly able to recover the main features found in the seismic tomography models. After ∼20 Myr (Figure 4.5d,e,f and Supplementary Figure 4.14) subducted lithospheric portions are found below the areas corresponding to the Alboran, Kabylides and Calabria-Apennine region where seismic tomographic methods have revealed several positive velocities anomalies (Bezada et al., 2013; Gutscher et al., 2002; Piromallo & Morelli, 2003; Spakman, 1991; Spakman et al., 1993; Spakman & Wortel, 2004; Van der Meer et al., 2018; Wortel & Spakman, 2000; Wortel et al., 2009). For example, Model CWM retrieves (a) the high-velocity body arranged horizontally over the 660 km discontinuity interpreted as the Ionian slab lying and broadening at the base of the upper mantle by P-wave tomographic models (Amato et al., 1993; Lucente et al., 1999; Piromallo & Morelli, 2003; Selvaggi & Chiarabba, 1995; Spakman et al., 1993; Spakman & Wortel, 2004; Van der Meer et al., 2018); (b) the portion of the slab under the

Northern Apennines extending down to 150 km depth and from ∼180 km down to about 660 km depth (Supplementary Figure 4.14b) (El-Sharkawy et al., 2020; Giacomuzzi et al., 2012; Spakman & Wortel, 2004) and (c) the Calabrian slab continuous from the surface down to a depth of 660 km (El-Sharkawy et al., 2020; Giacomuzzi et al., 2012; Neri et al., 2012; Presti et al., 2019; Rappisi et al., 2022; Scarfì et al., 2018); (d) the portion of slab imaged under the north African margin of Algeria, hanging down to ∼150 km depth and from ∼200 km joining to the Calabrian slab (Supplementary Figure 4.14b) (Chertova et al., 2014; Van der Meer et al., 2018); (e) the presence of two wide windows in the Ionian slabs, one below the area corresponding to the present-day Central Apennines and one beneath the north-eastern African margin (Amato et al., 1993; Carminati et al., 1998; Faccenna et al., 2014; Faccenna et al., 2007; Lucente & Speranza, 2001; Magni et al., 2014; Piromallo & Morelli, 1997, 2003; Spakman & Wortel, 2004; Van der Meer et al., 2018).

On the contrary, the modeled Alboran slab, in addition to being in a wrong position (i.e. further south than its current position), possesses a morphology which is not entirely realistic. This is probably due to the imposed initially 350 km long slab and to the slab tearing occurring as soon as the trench interacts with the continental margins, thus preventing any arcuate shape of the margin. However, we note that the geometry and length of the Alboran slab in model CWM at 0 (initial conditions; Figure 4.1) and ∼20 Ma (Figure 4.5d) are similar to those obtained by Chertova et al. (2014) at -20 and 0 Ma (see Figure 8 and Figure 10 of Chertova et al. (2014)). The flat portion of our Alboran slab at ∼20 Ma (Figure 4.5) is consistent with the Spakman and Wortel (2004) model (as presented in Figure 3 of Chertova et al. (2014)).

4.4.2 How well does tomography recover the target model?

We performed seismological forward and inverse simulations by testing different types of data coverage and quality. To help the comparison between the different tests and evaluating their capabilities in recovering model CWM, Figure 4.9 shows the difference between the true model and the solution of Test 1, Test 2, Test 3 and Test 4, both in terms of isotropic and anisotropic structures (i.e. dlnVp = dlnVp true model - dlnVp tomography model). We observe that the average difference in retrieved isotropic velocity is in general low (∼[-1%,+1%]) and gradually decreases moving from Test 1 to Test 4. For example, Figure 4.9a-d shows maximum values of dlnVp of ∼3% for Test 1, i.e. in the Apenninic slab at 400 km depth (Figure 4.9d), that gradually decrease to ∼1% for Test 4. For Test 4 (i.e. test with perfect data coverage), higher values are observed in the western side of the model, with peaks of ∼ 1.5% in the Liguro-Provençal basin at 200 km depth (Figure 4.9n). True and recovered anisotropy patterns are plotted in black and red, respectively, showing high degree of matching both in terms of azimuth and dip. With few exceptions of sparse differences in dip angles, no particular areas of discrepancy are identified.

From our results it emerged that even with a non-ideal source-station coverage the recovery of isotropic structures and anisotropic patterns is quite good, although anisotropy magnitude is overall underestimated (especially in poorly sampled areas). This suggests that the amount of mantle anisotropy could be higher than that retrieved by tomographic models with commonly uneven source-receiver distributions. The consequences of the inhomogeneous distribution of seismicity and stations on ray coverage and on retrieved tomographic images is known in isotropic tomographic models (e.g., Antolik et al., 2003; Boschi & Dziewonski, 1999; Bozdağ et al., 2016; Dalton &

Ekström, 2006; Masters et al., 1996; Ruan et al., 2019). Here we show that similar problems are also found in anisotropic seismic tomographic models (e.g., causing underestimation of anisotropy magnitude). In addition, it emerged that tomographic images calculated from data with a scarce seismic coverage are potentially affected by the presence of anomalies placed in a wrong geographic position. This is the case of the Alboran slab that in Figure 4.6e-l appears shifted toward the east. This kind of artefacts could bring errors in the tomographic model interpretation when fast anomalies are present close to the boundaries of the sampled area. Increasing data quality (i.e., decreasing data error; Test 2) helps in better retrieving the magnitude of the isotropic and anisotropic structures, but at the same time leads to an increase in the magnitude and size of the artefacts in poorly sampled areas (Figure 4.6e-l). In addition, Figure 4.6m-p shows that ideal data coverage allows for a more accurate retrieval of anomaly magnitudes without increasing artefact amplitudes. However, we note that the higher number of receivers (e.g., in the Tyrrhenian and Liguro-Provençal basins) at 200 km depth amplifies the smearing of the upper low-velocity layer with respect to Test 3 where, on the contrary, the limited number of stations (i.e. limited rays) reduces this effect.

In the inversions where seismic anisotropy is ignored (Test 5), we observe that several slow anomalies appear in the tomographic sections (Figure 4.8e-h). This is especially evident in the area north of the Alps (Figure 4.8a) and below the Calabrian slab (i.e. in the Ionian Sea, Figure 4.8b-d). Considering that these anomalies are not present in the true model and indeed completely disappear in the anisotropic inversions (Figure 4.6), it follows that they are seismic artefacts due to the isotropic approximation.

Lastly, the test carried out on the model isotropic only from 200 km depth down (Test 6), showed that both the isotropic and anisotropic features are subjected to vertical smearing (4.8g,h). This should be taken into account when interpreting teleseismic P-wave anisotropic tomography.

In order to further characterize model differences between true and tomographic models, we have computed the average misfit values for fraction of anisotropy (df), azimuth and dip angles (i.e. $d\psi$ and $d\gamma$) with increasing depth (Figure 4.10a-c) with respect to the true values. We observe that the average solution gradually improves, better resembling the true model, with decreasing data error and improving data coverage. The higher values of misfit are in fact observed for the model obtained from the inversion performed with the bigger data error (i.e. 450 ms, Test 1) and the worst receiver distribution. This is true for both df and $d\psi$, while for $d\gamma$ is valid below $\sim$70 km depth (Figure 4.10c). For all models the average azimuthal misfit is highest in the upper 50 km (due to the poor ray coverage at these depths by teleseismic P-waves), below which it rapidly decreases and remains roughly constant with depth except for a slight increase toward the bottom of the anisotropic domain. In contrast, the dip angle average misfit gradually increases with depth. The misfit curves for Test 4 and Test 6 show similar shapes but with shifted absolute values in the upper 150 km. This indicates that the presence of deeper anisotropy (Test 4) associated with poor vertical resolution deteriorates the quality of the retrieved shallower structures.

4.5 Conclusion

We applied the modelling methodology of Lo Bue et al. (2021) to simulate the geodynamic evolution over $\sim$20-30 Myr of a model that presents similar characteristics to those currently observed in the Central-Western Mediterranean region (e.g., detached or stagnating slabs, slab windows, etc). To quantify similarities and discrepancies between the obtained geodynamic model and the current tectonic setting, the model results were verified by comparing seismological synthetics (isotropic P-wave anomalies, P-wave anisotropy and SKS splitting) and major tectonic features (i.e., slab and trench geometry)

with observations. This comparison confirms that, with respect to the previous study of Lo Bue et al. (2021), using a more complex initial geometry (i.e. including the Alboran, Alpine and Dinaric-Hellenic slabs) allows us to perform a step forward toward the better recovering of the mantle flow, overall evolution and current tectonic beneath this region. However, we note that model CWM is still far from reproducing the exact evolution and present-day tectonic setting of the area and further studies need to be performed in this direction. For example, next-level numerical studies should attempt to improve the model geometry by considering the Earth's sphericity and the Africa-Eurasia plates convergence.

Despite the several limitation of the numerical methods (e.g., Cartesian coordinates system, no plates convergence, no fossil LPO, fabrics within the lithosphere, free slip boundaries, no mantle in/outflow, etc..) and the assumptions necessary to start and drive the simulation self-consistently (e.g., initial slab depths, mantle rheology parameters, etc..), we observe that at $\sim$20 Myr model CWM exhibits interesting geological features resembling those found in the Central-Western Mediterranean (e.g., Calabrian slab continuous from the surface down to the base of the upper mantle, the presence of two wide windows in the Ionian slab, etc). For this reason, we used the modeled elastic properties at this stage (i.e. the elastic tensors at $\sim$20 Myr), to perform 3D P-wave anisotropic tomography using the approach proposed by Vander-Beek and Faccenda (2021). Using the geodynamic model as reference model, we evaluated the capabilities of seismic tomography to recover a complex subduction environment in different conditions, such as poor station coverage and bad data quality. From the seismological inversions and the comparison between purely isotropic and anisotropic solutions it emerges that (i) it is fundamental to invert for anisotropy to improve the reliability of the tomographic result and (ii) even a non-ideal source-station coverage allows

to recover isotropic structures and anisotropic patterns from teleseismic P-wave tomography. Anisotropy magnitude, although consistent with those of the synthetic target model, is overall underestimated in the upper mantle especially in poorly sampled areas. In light of this, it is recommended to increase the number of marine and land stations and improve the accuracy of teleseismic arrival time measurements. However, it should be noted that perfect coverage of receivers does not guarantee an ideal tomographic solution. For example, Test 4, despite being performed with receivers distributed over the entire study area, presents various imaging artefacts. Future steps aiming at recreating a "perfect coverage" should be characterized by a good ray sampling, thus to include seismic rays that cover different directions in order to guarantee an excellent resolution (e.g., not only teleseismic events). Furthermore, although the synthetic inversions confirm that the developed methodology for P-wave anisotropic tomography is capable of retrieving with a good approximation the modeled upper mantle structures, the employed geodynamic simulations do not account for compositional variations, presence of fluids/melt and lithospheric fossil fabrics that can affect the seismic properties of natural tectonic settings. The presence of these further complexities remains to be tested, and it will be considered in future studies.

The synthetic tomography results demonstrated that using a combination of geodynamic and seismological numerical modelling techniques could represent a powerful tool to investigate mantle dynamics. Although the modelling limitations, we obtained a 3D complex mantle structure that partly resemble some main characteristics of the actual present-day mantle in the Central-Western Mediterranean. This opens new perspectives towards the future possibility of creating models of the geodynamic evolution that can be constrained by the structure and mantle anisotropy obtained from P-travel

time anisotropic tomography. To better constrain the initial tectonic configuration, an interesting future development would be to formulate a fluid dynamic inverse problem to reproduce unknown mantle flow back in time from seismic tomographic observations of the mantle and reconstructions of past plate motions using variational data assimilation (Bunge et al., 2003). Adjoint modelling is in fact a great opportunity to produce realistic mantle retrodictions models. However, the development of testing of this methodology is still far from being applicable to complex 3D tectonic settings such as the Mediterranean. This technique has been successfully applied to reproduce the recent dynamics in the South America and North America subduction zones (Hu et al., 2017; Zhou et al., 2018), However, we believe that exhumation back in time of the slabs stagnating in the mantle transition zone is non-trivial when the plate convergence rate is quite small (basically, by inverting gravity there is not easy way to exhume back at the surface these slabs), which is one of the reason why we choose to model forward in time the Central-Western Mediterranean dynamics. Reuber and Simons (2020), although showing the potentials (and limitations) of this technique on quite simple 2D and static (not dynamic) model configurations, concluded that the method "needs to be thoroughly tried and tested on real-world examples". Adding mantle fabrics to improve the mantle flow retrodictions is an ongoing research activity in our group, that we hope to include in our models in the near future.

Acknowledgments

This study is supported by the ERC StG 758199 NEWTON. T. Gerya provided the I3MG code used for the subduction modelling. The modified version of the D-Rex code used for the fabric modelling, and the routines used to calculate SKS splitting parameters, P-wave and Rayleigh wave anisotropy can be found inside the ECOMAN. The MATLAB toolbox geomIO was used to define the geometry of the model initial setup. Paraview was used for graphic visualization of the model output. Tomographic maps were created using Generic Mapping Tools (Wessel et al., 2019) with colormaps developed by Crameri (2018a, 2018b). The manuscript was significantly improved thanks to the constructive feedback and comments from the editor, Wim Spakman and an anonymous reviewer.

Supplementary Material

Supplementary Movie

Supplementary Movie S3. Model CWM evolution. Initial setup is shown in Figure 4.1. In blue the subducted slab (contour at T=1573 K) below ∼100 km depth. The continental plates of Adria, Africa and Iberia and the oceanic plate were opacified for better visualization of the subducted slab. The arrows indicate the velocity field at ∼200Km depth, and their length is proportional to the velocity magnitude.

Supplementary Figures

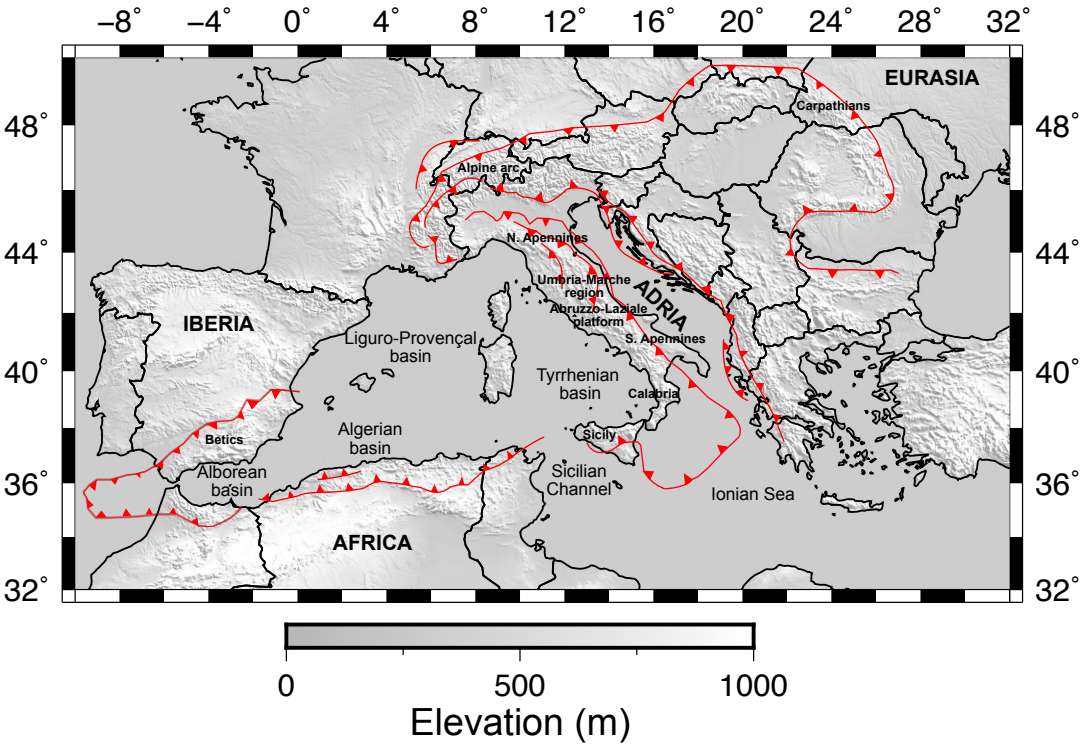

Figure 4.11: *Tectonic setting of the entire Mediterranean region adapted from Faccenna et al. (2014) showing the main structures, mountain ranges, subduction zones, back-arc basins, etc.*

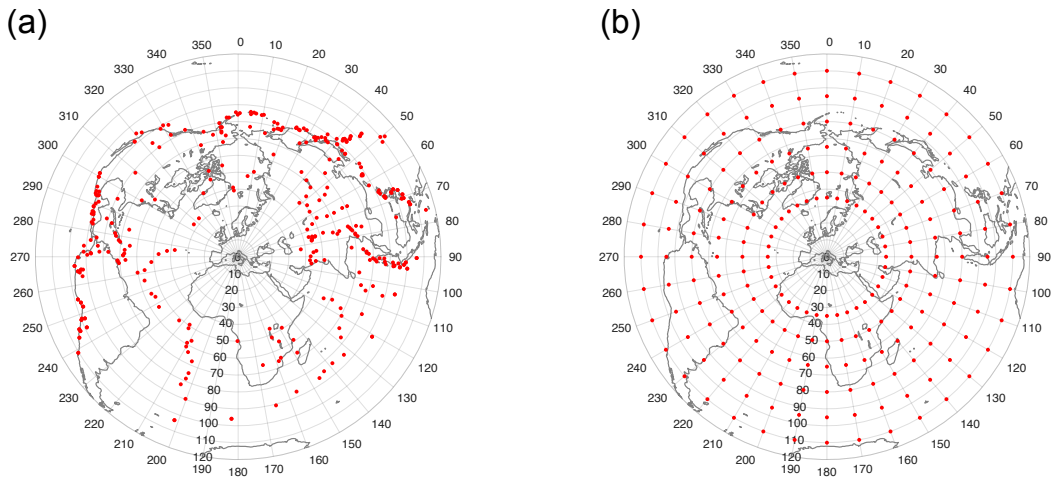

Figure 4.12: *Events distribution for (a) Test 1, 2 and (b) for Test 3, 4, 5 and 6.*

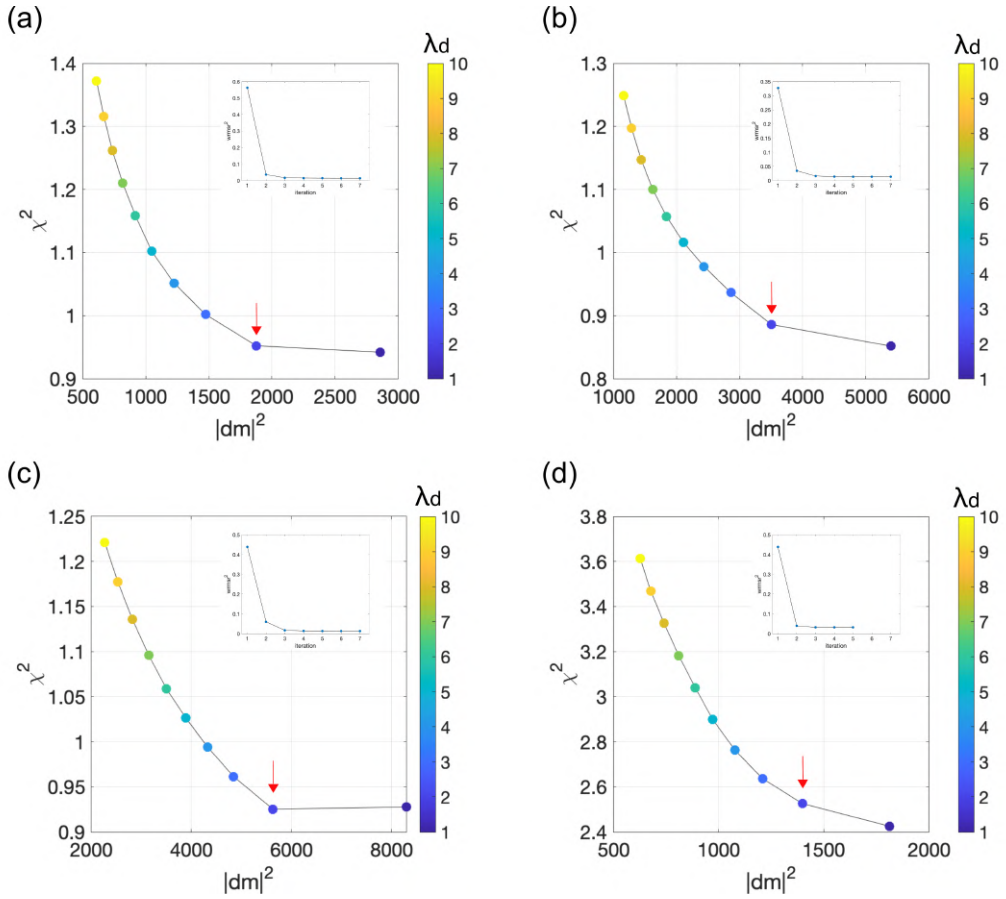

Figure 4.13: *L-curves for model selection. Normalized data residual ($\chi^2 = ddt^2/\epsilon^2$; where ddt is the delay time residual and ϵ is the uncertainty in the time measurements) is plotted as function of the squared of the model norm ($|dm|$). L-curves for (a) Test 2, (b) Test 3, (c) Test 4, and (d) for the purely isotropic Test 5. Curves (a), (b) and (c) are constructed using $\lambda_s/\lambda_d = 100$, while curve (d) using $\lambda_s/\lambda_d = 1000$. Red arrows indicate an ideal solution. Insets at the top-right corner of each panel show the convergence of the preferred solution.*

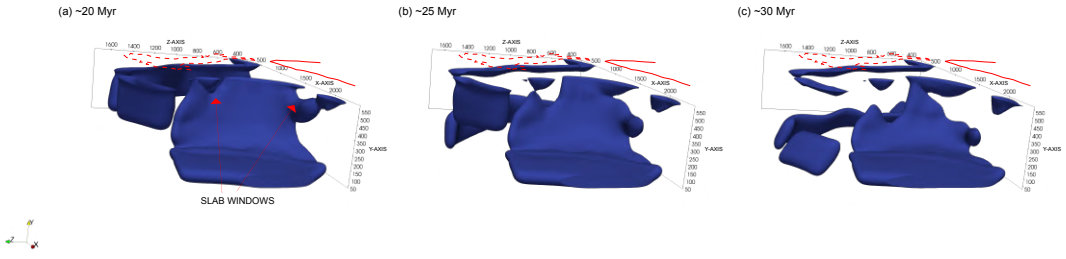

Figure 4.14: *Zoom of the Ionian slab of the Model CWM at (a)∼20 Myr, (b)∼25 Myr and (c)∼30 Myr. The red arrow indicates the slab windows below the Central-Apennines and Africa continental plate. The solid red line indicates the Africa coastlines in the Oligocene-Miocene (Van Hinsbergen et al., 2014), while the dashed red line indicates the present-day coastlines of peninsular Italy.*

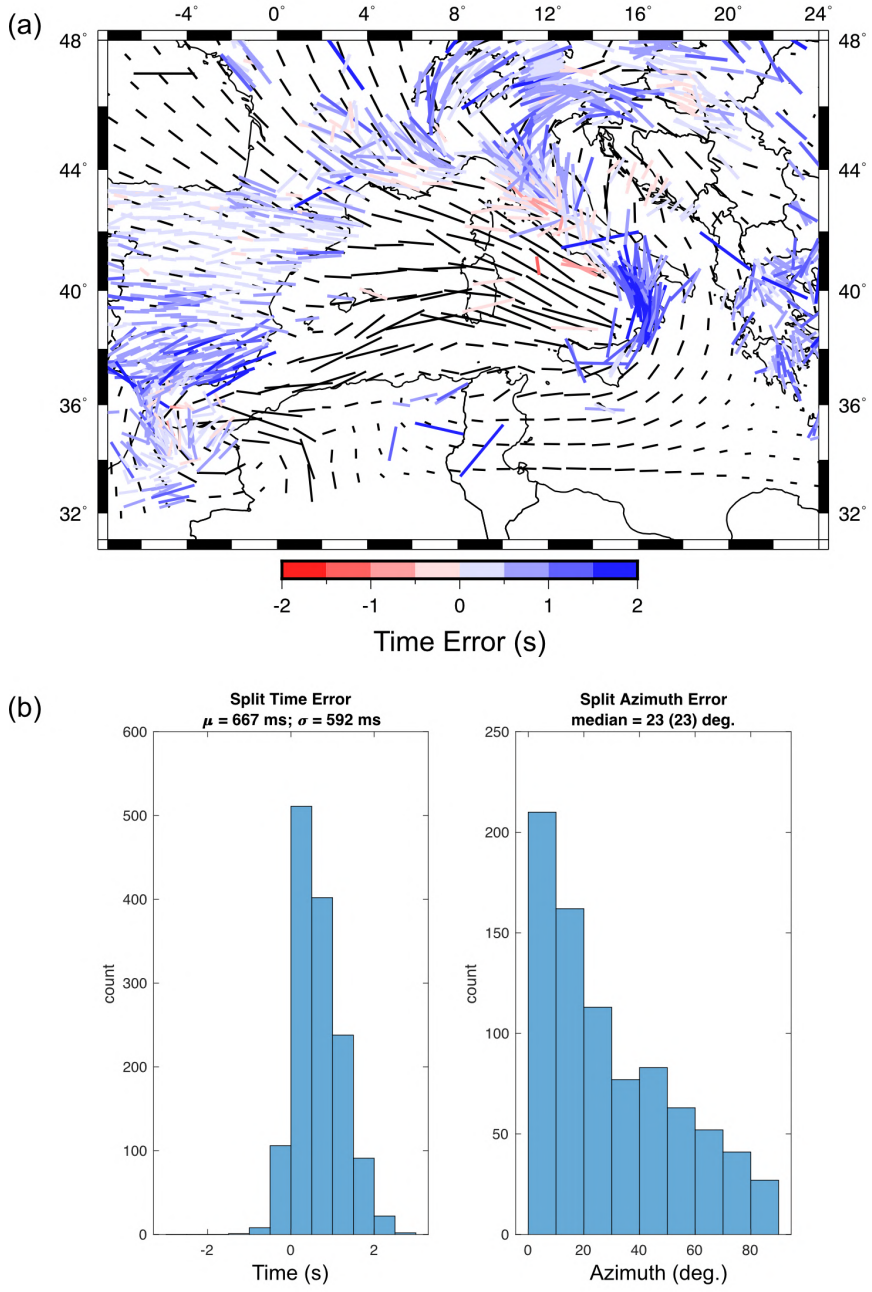

Figure 4.15: *(a) SKS-splitting measurements in the Central-Western Mediterranean (Becker et al., 2012) color-coded by the delay time misfit compared with synthetic SKS splitting measurements for Model CWM at ∼20 Myr (black bars). The EW black bar in the upper left corner indicates 2 s. (b) Split time error and split azimuth error histograms for the Model CWM at ∼20 Myr.*

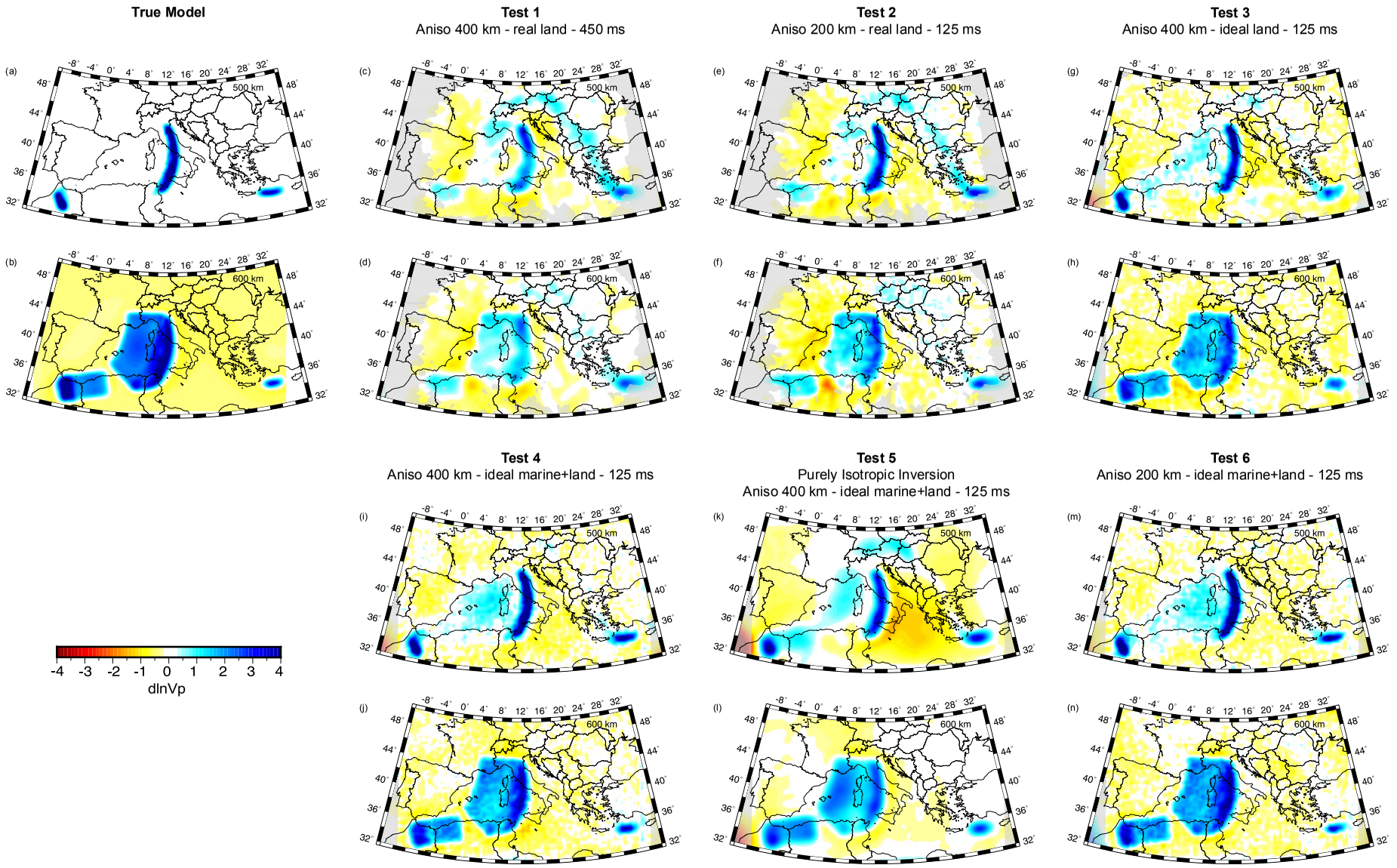

Figure 4.16: *Depth slices at 500 km and 600 km depth for (a-b) the true model, (c-d) Test 1, (e-f) Test 2, (g-h) Test 3, (i-j) Test 4, (k-l) Test 5, and (m-n) Test 6.*

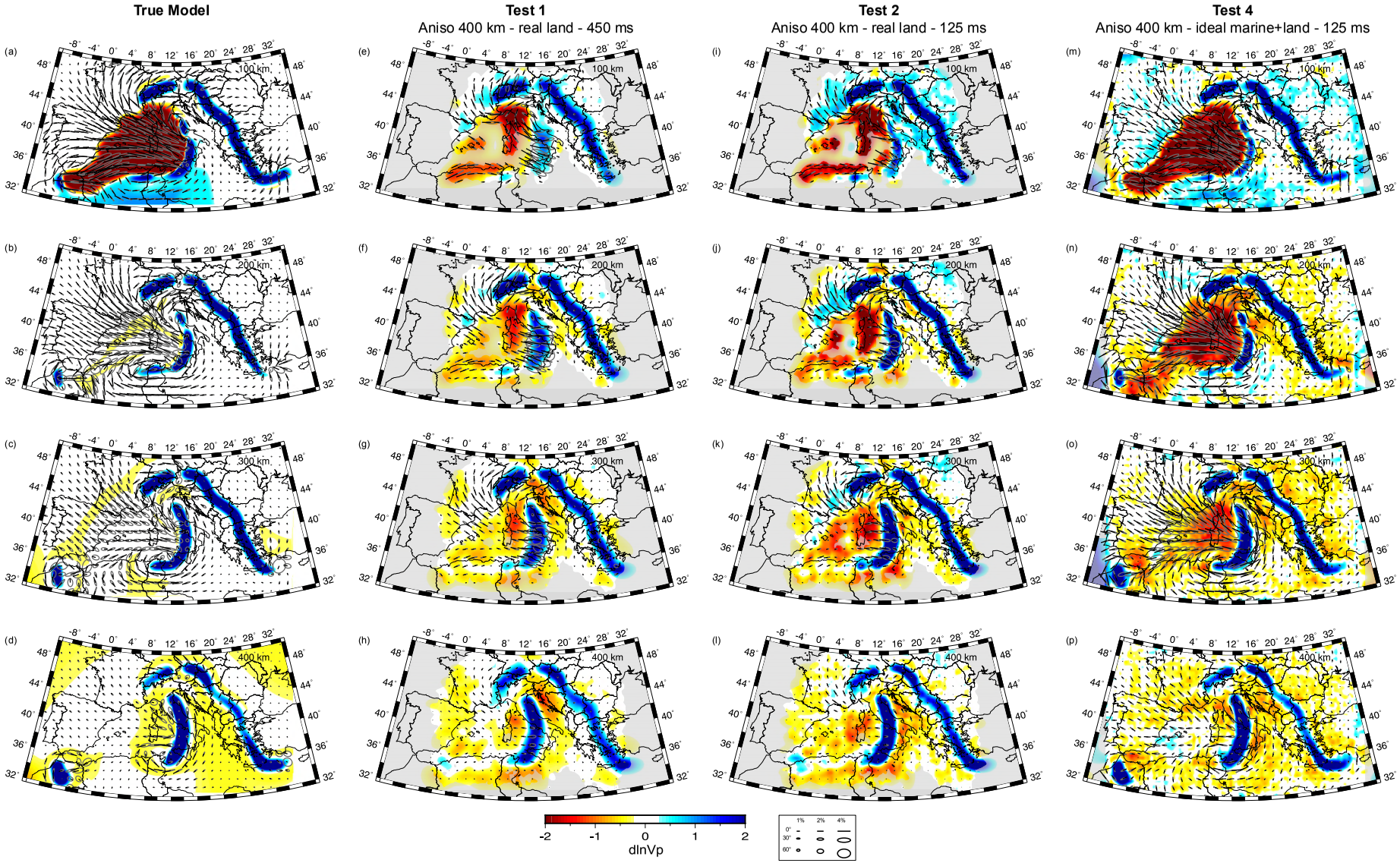

Figure 4.17: *Depth slices as in Figure 4.6 with smaller colorscale limits. Anisotropy is represented by ellipse symbols where the major axis of the ellipse parallels the fast-direction and the minor axis scales linearly with the symmetry axis dip into the view plane such that fabrics parallel and normal to the cross-sections plot as lines and circles, respectively. Anisotropic perturbations were restricted to the upper 400 km. See legend. Areas of poor data coverage are masked in grey.*

Chapter 5

IMAGING UPPER MANTLE ANISOTROPY WITH TELESEISMIC S-WAVE DELAYS: INSIGHTS FROM TOMOGRAPHIC RECONSTRUCTIONS OF SUBDUCTION SIMULATIONS

B. P. Vanderbeek[1], R. Lo Bue[1], F. Rappisi[1], and M. Faccenda[1]

This manuscript is in preparation. BPV and MF designed the study. BPV developed the method. MF created the geodynamic model. FR performed the picking of S-waves and preliminary tomographic models to tune the input parameters. RLB performed all the S-wave tomography inversions. RLB, FR and BPV wrote the first draft of the manuscript. All the co-authors contributed to the final polishing of the manuscript.

[1]Dipartimento di Geoscienze, Università di Padova, Padova, Italy

Abstract

It is well established that flow and deformation in the mantle produces a considerable amount of seismic anisotropy. However, the construction of tomographic models, in particular those derived from body waves, typically relies on the assumption of seismic isotropy. Recent studies have demonstrated that neglecting anisotropy in P-wave tomography can lead to notable imaging artefacts and misinterpretations. Less attention has been given to the effect of anisotropy on S-wave tomography partly because, unlike P-waves, there is not a simple ray-based methodology for modelling S-wave travel-times through anisotropic media. Here, we evaluate the bias introduced when ignoring seismic anisotropy in shear wave tomographic models using a new methodology for the inversion of teleseismic S-wave delays for upper mantle isotropic velocity and hexagonal anisotropy. We model the teleseismic shear wavefield through an elastically anisotropic geodynamic subduction model created via petrologic-thermomechanical modelling. We explore how the chosen coordinates system in which S-wave arrival times are measured (e.g., radial versus transverse) affects the imaging results. We observe that when S-wave travel-times are measured in the direction of polarisation, the apparent anisotropic shear velocity can be approximated using sinusoidal functions of period π and 2π. The sinusoidal approximation allows us to use ray-based methods to predict S-wave travel-times through anisotropic domains and to recover velocity models displaying 3D patterns of mantle fabrics and where the imaging artefacts are substantially reduced.

5.1 Introduction

Since its discovery in the 1960s (e.g., Anderson, 1965; Anderson, 1961; Hess, 1964; McEvilly, 1964), seismic anisotropy has been extensively mapped in many regions of the Earth, from crust to core. In the mantle, anisotropy is mainly caused by the non-random distribution of intrinsically anisotropic minerals (lattice/crystal-preferred orientation - LPO/CPO) as a response to mantle deformation (Kaminski & Ribe, 2001; Karato et al., 2008; Nicolas & Christensen, 1987; Wenk, 2016; Zhang & Karato, 1995) or from the alignment of structures such as faults, tabular intrusions, gas or fluid-filled cracks, and layered media with different elastic properties (shape preferred orientation - SPO). Petrophysical analysis of exhumed and experimentally deformed rock samples, together with micromechanical flow models (Blackman & Kendall, 2002; Faccenda, 2014; Kaminski et al., 2004; Karato et al., 2008; Long & Becker, 2010; Ribe, 1989; Savage, 1999; Skemer & Hansen, 2016) have shown that anisotropic structures of the Earth can create significant directional variations in seismic velocities, which allows to study mantle dynamics exploiting the anisotropic properties of the seismic wavefield.

Despite the well-established anisotropic nature of the Earth's upper mantle, conventional tomographic models, in particular those derived from body waves, are typically constructed based on the assumption of an isotropic Earth. This approximation simplifies the computational problem as taking into account seismic anisotropy involves the introduction of new unknowns in an already underdetermined inverse problem. However, this is a poor assumption considering that (i) body waves exhibit strong sensitivity to anisotropic fabrics and neglecting anisotropy can lead to notable imaging artefacts and misinterpretations (Bezada et al., 2016; Blackman & Kendall, 1997; Blackman et al., 1996; Kendall, 1994; Lloyd & Van Der Lee, 2008; Menke, 2015;

VanderBeek & Faccenda, 2021); (ii) the magnitude of seismic velocity anomalies caused by anisotropy can be even greater than those due to changes in temperature, composition or mineralogy (Anderson, 1989); (iii) tomographic models are used to constrain geodynamic simulations and infer mantle flow and structure (Becker & Boschi, 2002; Faccenna & Becker, 2010; Simmons et al., 2006; Wang & Becker, 2019). It is therefore crucial to include seismic anisotropy when imaging the mantle to advancing our understanding of the physical state and dynamics of the mantle.

A popular and conventional means for detecting upper mantle seismic anisotropy is through the analysis of shear wave splitting (SWS) and surface waves. Several techniques have been proposed to measure SKS splitting (e.g., Chevrot, 2000; Savage, 1999; Sieminski et al., 2007; Silver & Chan, 1988; Vinnik et al., 1989) and this has provided important insights on mantle flow patterns, especially in subduction zone settings (Crampin, 1984; Huang et al., 2011a, 2011b; Long, 2013; Long & Becker, 2010; Long & Silver, 2008, 2009; Savage, 1999; Silver, 1996). However, the SWS measurements have a poor depth resolution and limited sensitivity to the dip of anisotropic fabrics (Beller & Chevrot, 2020; Chevrot, 2006; Chevrot & Van Der Hilst, 2003). Surface waves, on the other hand, are particularly sensitive to variations in depth in both azimuthal and radial anisotropic structures, but they have a poor lateral resolution (hundreds of kilometers). These drawbacks could be overcome by considering seismic anisotropy in the tomographic inversion of teleseismic body wave data.

Recently, VanderBeek and Faccenda (2021) and Wang and Zhao (2021) have independently developed a new inversion strategy that yields accurate reconstructions of the upper mantle isotropic and anisotropic structures.

This new approach simultaneously inverts for P-wave slowness (i.e., the inverse of velocity) and three anisotropic parameters (magnitude of hexagonal anisotropy, azimuth and dip of the symmetry axis respectively). VanderBeek and Faccenda (2021) show that unaccounted for seismic anisotropy (isotropic approximation) or allowing for only azimuthal variations in seismic velocity (i.e., no dipping fabrics) generates strong imaging artifacts in the tomographic results. On the contrary, this new inversion strategy strongly minimizes the artifacts. While anisotropic imaging strategies have been developed for P-wave delay times in an effort to reduce such artifacts, no such ray-based anisotropic imaging strategies exist for S-waves partly because, unlike P-waves, there is not a simple ray-based methodology for modelling S-wave travel-times through anisotropic media. However, the elastic tensor is only partially resolved by knowledge of P-wave anisotropy, and S-wave anisotropy is also necessary to constrain fully the elastic tensor (Mochizuki, 1995; Wu & Lees, 1999). Several studies have successfully been performed using jointly P and S wave arrival times to image anisotropy in the Earth mantle. Liu and Zhao (2016) presented azimuthal anisotropic images of the Japan subduction zone assuming a weak orthorhombic anisotropic medium (i.e. with 3 orthogonal symmetry axes). However, the authors ignored the polarization of S-waves by assuming that all S-waves were polarized in the radial direction. Calò et al. (2016) by jointly inverting the high frequency P-waves, long period surface waves and group dispersion data infer profiles of radial anisotropy, imaging layered structure in the upper mantle beneath North America. More recently, Beller and Chevrot (2020) performed full waveform inversion (FWI) including both P and S phases generating high-resolution images of upper mantle anisotropic fabrics. However, although FWI is capable of solving for the 21 elastic coefficients, thus leading to a more linear imaging problem, it is limited by the computational resources and dense high-quality seismic data. Lloyd and Van Der Lee (2008)

investigate regional S and Rayleigh waves, concluding that anisotropy can be mapped as artifacts in S-wave tomographic images when not accounted for in the inversion process. However, the authors state that the bias introduced in the tomography by the isotropic assumption is small with respect to the magnitude of the velocity anomalies interpreted by seismologists. Furthermore, it is worth noting that Lloyd and Van Der Lee (2008) performed a poor-resolution study and do not consider dipping fast axes. Nevertheless, the nature of anisotropy-induced artifacts has not been largely characterized for only teleseismic shear wave tomography.

Here we present a new methodology to invert teleseismic S-wave delays for upper mantle isotropic velocity and hexagonal anisotropy. By performing waveform modelling through geodynamic subduction simulations, realistic synthetic seismic datasets are created. The geodynamic models include elastic anisotropy predicted from micromechanical flow models of polymineralic aggregates advected through the simulated flow field. We performed isotropic and anisotropic (i.e., azimuthal and fully anisotropic) inversions to show the ability of different imaging strategies in recovering subduction zones structures. The influence on the imaging results of the chosen coordinates system in which S-wave arrival times are measured (e.g., radial or transverse) is addressed. We observe that when S-wave travel-times are measured in the direction of wave polarisation, the apparent anisotropic shear velocity can be approximated using simple sinusoidal functions describing hexagonal anisotropy. The sinusoidal approximation allows us to use ray-based methods to predict S-wave travel-times through anisotropic models. We show that this parameterisation can be used to invert S-wave travel-times for the orientation and strength of anisotropy analogously to the anisotropic P-wave travel-time tomography by VanderBeek and Faccenda (2021), and that artifacts are strongly minimized. Our results highlight that shear wave anisotropy can be accounted for in a ray theoretical framework to constrain

realistic mantle anisotropic fabrics and improve imaging of isotropic features. Future applications of our methodology to real seismic datasets could bring new insights into upper mantle isotropic and anisotropic structures and dynamics.

5.2 Methods

5.2.1 Approximating Shear Wave Anisotropic Velocities

The primary issue preventing anisotropic S-wave travel-time tomography is that no simple strategy exists for modelling such travel-times in a ray-theoretical framework. This is because, unlike P-waves, S-waves may split into two orthogonally polarised quasi-shear waves that propagate at different speeds upon entering a region of elastic anisotropy. Provided that the time delay between the quasi-shear waves is small (i.e. less than the period of the seismic wave), their propagation is coupled and ray theory is not valid for independently tracing the quasi-shear phases (Coates & Chapman, 1990). This is indeed the case for teleseismic S-waves which are typically observed at periods of $\sim$10 s while the delay between fast- and slow-polarised waveforms is generally <2 s. Furthermore, the splitting process will be repeated upon encountering a change in anisotropy or ray geometry and even if ray theory were valid it is not clear which quasi-shear wave should be traced to the observation point. Another complication is that two quasi-shear waves are not produced when the shear wave polarisation parallels a symmetry axis or symmetry plane. The final waveform observed at the surface will generally contain two arrivals within the S-wave observation window that reflect the integrated effects of splitting along the ray path. Which arrival should we measure and can we relate its travel-time to anisotropic properties along the ray path in a manner suitable for a linearised inversion scheme? Here

we propose inverting S-wave travel-times measured in the direction of the initial linear polarisation. We chose this orientation because anisotropy does not significantly perturb the incoming wavelet for small splitting times relative to its period (Chevrot, 2000; Silver & Chan, 1988; Vinnik et al., 1989); this is beneficial for array processing techniques common in teleseismic analyses (e.g., multi-channel cross-correlation; VanDecar & Crosson, 1990).

We posit–and later support this supposition via waveform modelling–that the S-wave observed in the polarisation direction propagates at a velocity between the two quasi-shear wave speeds. We assume that the polarisation of a shear wave entering the imaging volume is approximately linear and remains so as it propagates through the model. In reality, anisotropy will cause elliptical particle motion but provided the splitting time remains small relative to the period of the waveform ($T/\Delta t \lessapprox 5$) the displacement will not deviate significantly from the initial polarisation direction (Rümpker & Silver, 1998). A similar assumption is made in the modelling of splitting intensity (Chevrot, 2000; Chevrot et al., 2004; Sieminski et al., 2007). Given an anisotropic seismic velocity model, we can estimate the velocity of the two quasi-shear waves (v_1 and v_2) from the ray path orientation. We then assume that the propagation velocity varies sinusoidally between v_1 and v_2 and is a function of the angle between the incoming shear wave polarisation and the quasi-shear wave whose displacement is in the plane containing the anisotropic symmetry axis. The details of this approach are provided below.

Numerous studies have demonstrated that elastic anisotropy within the Earth is dominated by hexagonal symmetry (e.g., Becker et al., 2006a; Brownlee et al., 2017; Ismaıl & Mainprice, 1998; Russell et al., 2019). Assuming that the magnitude of anisotropy is relatively weak (<10-20%), the speed at which two orthogonal quasi-shear waves will propagate through an anisotropic layer can be approximated as periodic functions of 2α and 4α where α is the angle between the hexagonal symmetry axis and the S-wave ray path

(Backus, 1965; Thomsen, 1986).

$$v_1 = \overline{v_1}\left[1 \pm g\cos(2\alpha)\right] \tag{5.1}$$

$$v_2 = \overline{v_2}\left[1 \mp h\cos(4\alpha)\right], \tag{5.2}$$

where $\overline{v_1}$ and $\overline{v_2}$ are the mean or isotropic velocities and g and h are the fractional magnitude of the velocity variations associated with the 2α- and 4α-cosines, respectively. The velocities for a ray parallel to the symmetry axis are controlled by the sign of the anisotropic fraction. Note that g and h tend to be of opposite sign with $g > 0$ for mantle anisotropy produced by olivine A-type fabrics. We also note that, $v_1(\alpha = 0) = v_2(\alpha = 0)$ so that $\overline{v_2} = \overline{v_1}[1 \pm g][1 \mp h]^{-1}$ reducing the number of parameters required to describe S-wave anisotropy.

We wish to write the two quasi-shear wave speeds as a function of the symmetry axis azimuth (ψ) and elevation (γ). After some trigonometric manipulation and noting that $\cos(\alpha)$ is given by the dot product between the ray unit vector and the anisotropic symmetry axis unit vector, we can expand Equations 5.1 and 5.2 as,

$$v_1 = \overline{v_1}\left[1 \pm g\left(2\left[\cos(\theta)\cos(\gamma)\cos(\phi-\psi) + \sin(\theta)\sin(\gamma)\right]^2 - 1\right)\right], \tag{5.3}$$

$$\begin{aligned} v_2 = \overline{v_1}\frac{(1 \pm g)}{(1 \mp h)}\Big[1 \mp h\Big(&8\left[\cos(\theta)\cos(\gamma)\cos(\phi-\psi) + \sin(\theta)\sin(\gamma)\right]^4 \\ &-8\left[\cos(\theta)\cos(\gamma)\cos(\phi-\psi) + \sin(\theta)\sin(\gamma)\right]^2 + 1, \end{aligned} \tag{5.4}$$

where θ and ϕ are the ray elevation and azimuth, respectively. We then parameterise the velocity at which the shear wave observed in the direction of polarisation travels as,

$$v = \frac{(v_2 + v_1)}{2}\left[1 + \frac{(v_2 - v_1)}{(v_2 + v_1)}\cos(2\omega - 2\psi')\right], \tag{5.5}$$

where ω is the angle of shear wave polarisation and ψ' is the orientation of the symmetry axis projected into the ray-normal plane. See Figure 5.1 for an illustration of the coordinate system. The frequency-dependent anisotropic shear wave travel-time is given by the volume integral,

$$t = t' + \int_V (u - u')KdV, \tag{5.6}$$

where t' is the travel-time predicted through the 1D reference slowness (i.e. inverse of velocity) model u'; u is the true 3-D slowness model; and K is the approximate Born sensitivity kernel defined in Equations 4 and 5 of VanderBeek and Faccenda (2021). In Equation 5.6, u is defined by $1/v$ and each node in the kernel K maps to a specific ray segment whose orientation is used to define the slowness at that point via Equations 5.3-5.5. See VanderBeek and Faccenda (2021) for further details on the finite-frequency travel-time approximation used here.

5.2.2 Validation of Anisotropic Shear Wave Travel-times

Equations 5.3-5.5 provide a means to estimate the anisotropic propagation velocity and travel-time of a linearly polarised shear wave. To assess the accuracy of this approximation, we measure travel-time delays of teleseismic S-waves propagated through an anisotropic subduction zone model using SPECFEM3D and compare these measured delays to those predicted using Equations 5.3-5.5.

We use the synthetic waveform dataset created by VanderBeek and Faccenda (2021) and briefly summarise its key features below. The teleseismic wavefield is modelled using the spectral element code SPECFEM 3-D (Chen

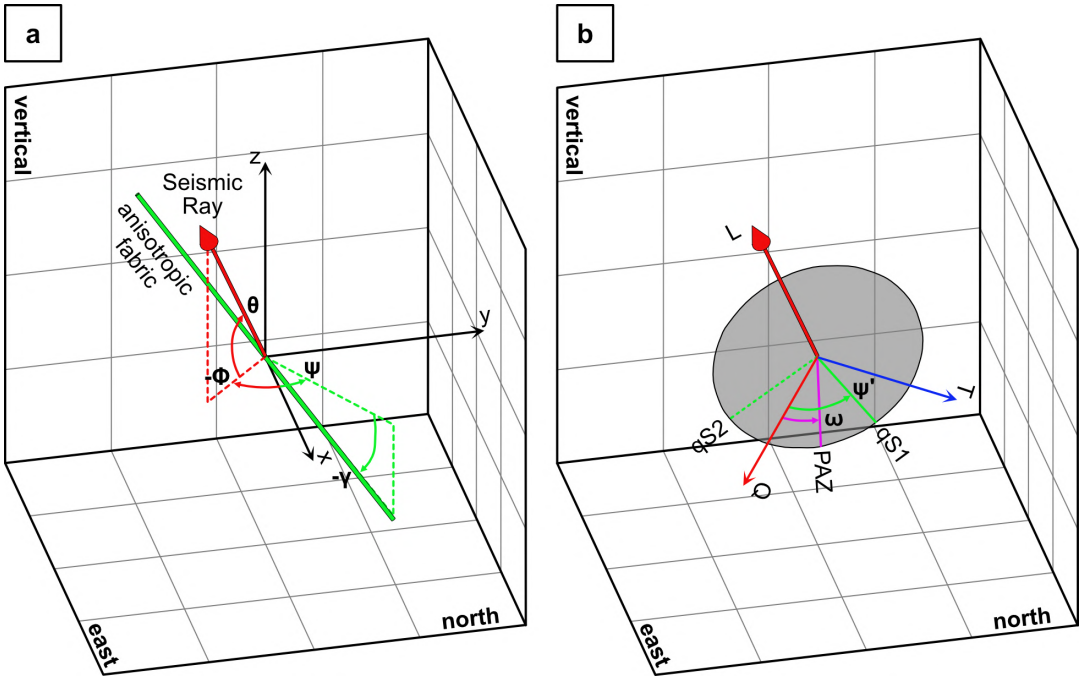

Figure 5.1: *Coordinate system depicting parameters used to model shear wave anisotropy. (a) The S-wave ray path (red arrow) is shown in relation to the orientation of the anisotropic symmetry axis (green bar). The ray and symmetry axis azimuths (ϕ and ψ) are measured positive counter-clockwise from the +x-axis while the ray and symmetry axis elevation are measure positive counter-clockwise from the x,y-plane. (b) The ray-aligned QTL-coordinate system. The shear-wave polarisation direction (ω; pink line labeled PAZ) is shown in the ray-normal plane (grey shaded region) in addition to the two quasi-shear wave polarisations (qS_1 and qS_2). Note that the qS_1 polarisation coincides with the projection of the symmetry axis into the ray-normal plane (ψ'; green line). Angles are measured positive counter-clockwise with respect to the Q-axis in the QT-plane.*

& Tromp, 2007; Komatitsch & Tromp, 1999) with the AxiSEM grid-injection technique (Monteiller et al., 2013; Nissen-Meyer et al., 2014). The anisotropic elastic model used in the waveform modelling is the result of a geodynamic simulation of a slab (1000 km-long half-width) subducting freely in response to its negative buoyancy. Fully anisotropic elastic tensors are predicted via micromechanical modelling of polymineralic aggregates advected through the simulated mantle flow field (see Faccenda, 2014; Faccenda & Capitanio, 2013; Kaminski et al., 2004). The tensors are subsequently simplified by extracting the dominant hexagonally symmetric component. This simplification was also made to maintain focus on the accuracy of the imaging methodology specifically designed to approximate hexagonal anisotropy.

Outside of the local imaging volume the 1D radial Earth model IASP91 (Kennett & Engdahl, 1991) is used to define seismic wave speeds.

The isotropic component of the synthetic subduction zone is shown in Figure 5.2 and contains only one significant anomaly–the seismically fast slab. The anisotropic component of the synthetic model is shown in Figure 5.3 and contains five significant imaging targets that provide insight into the structure and dynamics of the subduction zone. (1) Throughout the upper 300 km, toroidal mantle flow generates a circular pattern in the symmetry axis orientations around the slab edges (Figure 5.3a). (2) At greater depths beneath the incoming plate there is a region of trench-parallel anisotropy (Figure 5.3b). (3) Surrounding the subducting lithosphere, flow entrainment produces anisotropic symmetry axes that follow the trajectory of the descending plate (Figure 5.3c,d). (4) The subducting lithosphere also contains frozen-in anisotropic fabrics characterised by 5% S-wave speed variations oriented east-west. (5) Mantle

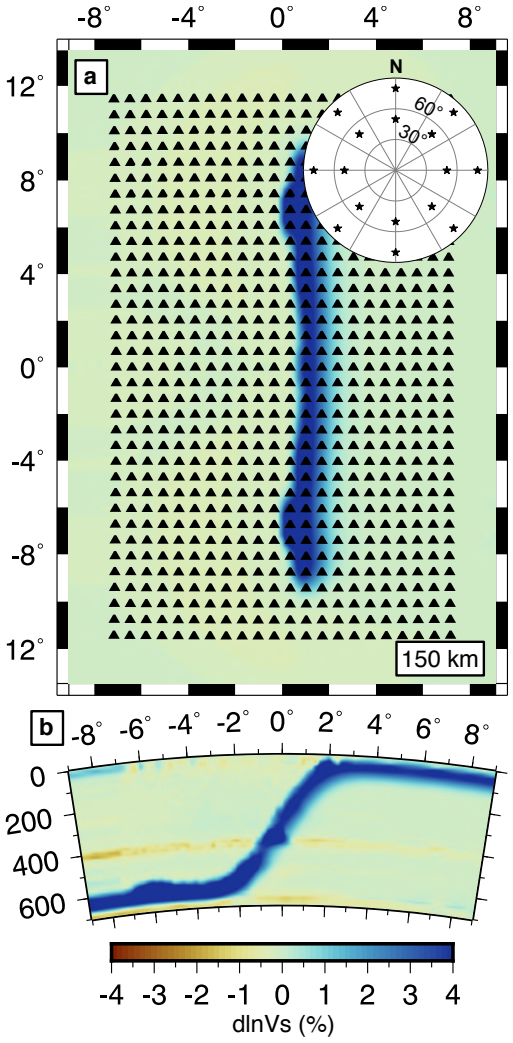

Figure 5.2: *Isotropic structure, array geometry and distribution of teleseismic sources considered in the present study. (a) Seismic stations (black triangles) are uniformly spaced 75 km apart and plotted over isotropic velocity heterogeneity in the true model at 150 km depth. Inset shows location of teleseismic sources (stars) relative to the experiment centre. Sources are located at distances of 50° and 80° and evenly distributed in backazimuth. An east-west cross-section through the centre of the true isotropic model at 0°N is shown in (b). Note that the isotropic structure is symmetric about 0°N.*

circulation within the wedge generates a corner-flow type pattern in anisotropy fabrics near the mid-plate that becomes less evident towards the edges (Figure 5.3c,d).

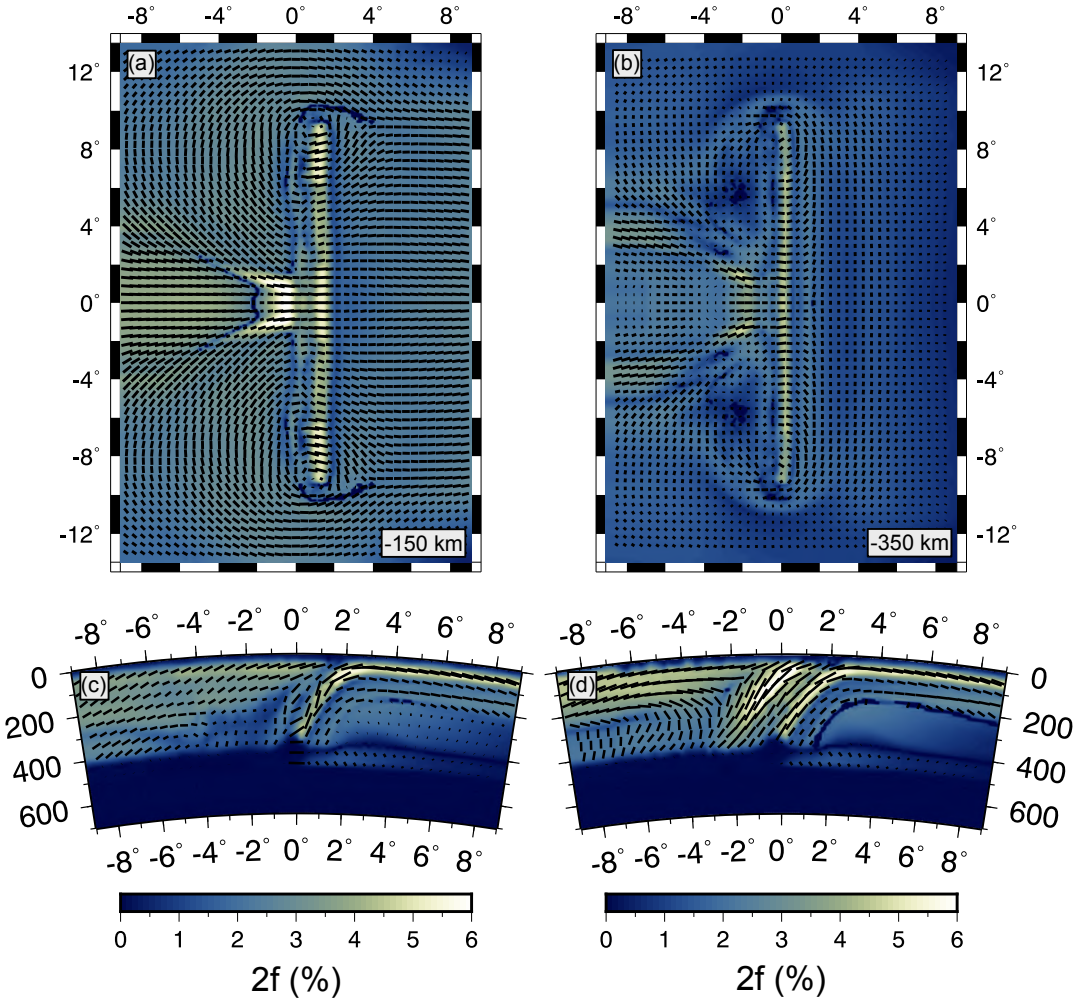

Figure 5.3: *Cross-section through the true anisotropic model. Hexagonal symmetry axis vectors are plotted over the peak-to-peak magnitude of S-wave velocity anisotropy at (a) 150 km and (b) 350 km depth. East-west cross-section are shown at (c) 0°N and (d) 4°30'S. Symmetry axis vectors are scaled by the anisotropic magnitude and projected onto the cross-section plane. Note that the anisotropic structure is symmetric about 0°N.*

The teleseismic wavefield propagated through this model is recorded by an array of 770 receivers equally spaced 75 km apart (Figure 5.2a) yielding a station density comparable to the USArray. In total 16 double-couple sources are modelled; 8 at a range of 50° and another 8 at 80° equally distributed in back-azimuth (Figure 5.2a). The dominant period of the waveforms is 15 s. A second waveform dataset was created in which only the isotropic component

of the elastic tensors are considered and used to derive a reference set of delay times without any anisotropic signal.

We measure relative S-wave travel-time delays following the multi-channel cross-correlation method of VanDecar and Crosson (1990). A second order bandpass filter with corners at 15 s and 40 s is applied to the synthetic seismograms. We measure delays in two coordinate systems. First, we analyse shear waves observed in the transverse direction–a common choice for many teleseismic studies. Second, we measure S-wave delays in the direction of polarisation, or more precisely, parallel to the major axis of the particle motion ellipse. The shear wave polarisation can be determined given the ray orientation and moment tensor. However, in practice moment tensors may be unknown or the polarisation may have been perturbed prior to entering the regional imaging volume. To avoid such issues, we suggest estimating the incoming polarisation for each event using the array-averaged S-waveform. For a given event, we first pick and align S-wave arrivals on the transverse channel. We then stack the aligned traces and perform a polarisation analysis on the stacked three-component signal via an eigendecomposition of the trace covariance matrix (e.g., Flinn, 1965); a 15 s window about the S-waveform is used in this analysis. Each seismogram is then rotated into the principal coordinate system determined by the eigendecomposition and S-wave delays are re-measured in the direction corresponding to the largest eigenvalue. The polarisation angle in the QT-plane (ω; Figure 5.1b) is stored for each event and used for computing travel-times (Equation 5.5). Note that we have assumed ω is constant across the array for a given event which is reasonable for teleseismic phases recorded by regional-scale or smaller arrays. For all sources modelled by VanderBeek and Faccenda (2021), $\omega = 47°$ and the results of the polarisation analysis outlined above agree to within 1°.

By comparing the delay times measured from the SPECFEM generated waveforms to those predicted by our ray-theoretical tomographic method,

we can assess the error in our approximation for S-wave anisotropy. We find that the root-mean-square error (RMSE) between the observed and predicted delays is 241 ms while RMSE for delays predicted without considering anisotropy is 600 ms. The error in our ray-theoretical anisotropic delays is comparable those estimated for modern day S-wave delay time measurements (∼250 ms; Byrnes et al., 2017) and less than the accuracy of most modern tomographic models (∼400 ms). Thus, our approximation appears sufficient for tomographic imaging.

5.2.3 Imaging Method

Having validated equations that relate shear-wave travel-times to mean velocity and the strength and orientation of seismic anisotropy, we formulate an inversion procedure for recovering these anisotropic parameters from the travel-time observations. In constructing our anisotropic model, we seek to minimise the least-squares objective function defined by,

$$\chi^2 = (\Delta\mathbf{t} - \mathbf{J}\Delta\mathbf{m})'\mathbf{C}_t^{-1}(\Delta\mathbf{t} - \mathbf{J}\Delta\mathbf{m}) + \lambda_d\Delta\mathbf{m}'\mathbf{C}_m^{-1}\Delta\mathbf{m} + \lambda_s\Delta\mathbf{m}'\mathbf{C}_s'\mathbf{C}_s\Delta\mathbf{m}, \quad (5.7)$$

where $\Delta\mathbf{t}$ is a (N x 1) vector of travel-time residuals with respect to the current model vector $\mathbf{m}$; $\mathbf{J}$ is the (N x M) Jacobian matrix that relates a change in travel-time to a change in the model parameters; $\Delta\mathbf{m}$ is the model perturbation vector for which we are trying to solve; $\mathbf{C}_t$ is the (N x N) data covariance matrix which we assume to be diagonal and composed of the inverse of the squared data uncertainties (250 ms for our dataset); $\mathbf{C}_m$ is the (M x M) model covariance matrix which we assume to be diagonal and composed of the inverse of the squared parameter uncertainties; $\mathbf{C}_s$ is an (M x M) matrix that defines the model roughness (i.e. the discretised 3D Laplace equation for each parameter); lastly λ_d and λ_s are Lagrangian multipliers that limit the size and roughness of the model perturbation vector. These parameters are

required to regularise the otherwise under-determined and ill-posed inverse problem and their selection is discussed below (section5.2.4). To minimise Equation 5.7, we solve the system of equations defined by,

$$\begin{bmatrix} \mathbf{C}_t^{-1/2}\mathbf{J} \\ \lambda_d \mathbf{C}_m^{-1/2} \\ \lambda_s \mathbf{C}_s \end{bmatrix} \Delta\mathbf{m} = \begin{bmatrix} \mathbf{C}_t^{-1/2}\Delta\mathbf{t} \\ \mathbf{0} \\ \mathbf{0} \end{bmatrix}. \tag{5.8}$$

The solution is obtained via the LSQR algorithm (Paige & Saunders, 1982).

To evaluate Equation 5.8, we must define the linear equations that populate the rows of the Jacobian matrix $\mathbf{J}$ which are obtained by differentiating the travel-time equation (Eq. 5.6) with respect to the anisotropic model parameters. Rather than invert directly for the mean velocity ($\overline{v}$) and the strengths (g, h), azimuth (ψ), and elevation (γ) of anisotropy, we follow VanderBeek and Faccenda (2021) and parameterize the inversion using the mean slowness ($\overline{u} = 1/\overline{v}$) and three anisotropic parameters defined as,

$$A = g\cos(\gamma)\cos(2\psi) \tag{5.9}$$

$$B = g\cos(\gamma)\sin(2\psi) \tag{5.10}$$

$$C = \sqrt{g}\sin(\gamma) \tag{5.11}$$

Under this parameterisation, Equations 5.3 and 5.2.1 become,

$$v_1 = \overline{v_1}\left[1 \pm (Q - G - C^2)\right], \tag{5.12}$$

and

$$v_2 = \overline{v_1}\frac{(1 \pm [G + C^2])}{(1 \mp r_{hg}[G + C^2])}\left[1 \pm r_{hg}\left(2Q^2[G + C^2]^{-1} - 4Q + G + C^2\right)\right]. \tag{5.13}$$

For notational convenience, we have introduced the terms Q and G defined as

$$\begin{aligned} Q = [A\cos(2\phi) + B\sin(2\phi) + G]\cos^2(\theta) + 2C^2\sin^2(\theta) \\ +\sqrt{2}C\left[s_1(G + A)^{1/2}\cos(\phi) + s_2(G - A)^{1/2}\sin(\phi)\right]\sin(2\theta) \end{aligned} \tag{5.14}$$

with $s_1 = \text{sign}(\cos\gamma\cos\psi)$, $s_2 = \text{sign}(\cos\gamma\sin\psi)$ and $G = \sqrt{A^2 + B^2}$. To further limit the number of free parameters, we have also added the term r_{hg} which is the ratio h/g and is assumed constant throughout the inversion. Appropriate values for r_{hg} can be inferred from laboratory measurements of relevant anisotropic fabrics. Here we use $r_{hg} = -0.1746$ which is the average value of the geodynamically modelled elastic tensors. Note also that the sign term ($\pm$) that appears in these equations is selected *a priori* in accordance with the expected symmetry system and is fixed throughout the inversion. Here we use the convention (+,-) for ($\pm, \mp$) corresponding to a seismically fast symmetry axis and slow propagation plane normal to the symmetry axis. Finally, we can write the elements of $\mathbf{J}$ as,

$$J_{ij} = \frac{\partial t_i}{\partial m_j} = -w_{ij}\left(\frac{\partial u_{ij}}{\partial v_{ij}}\right)\left(\frac{\partial v_{ij}}{\partial m_j}\right) \tag{5.15}$$

where w_{ij} expresses the relative influence the model parameter m at the j^{th} location has on the i^{th} travel-time observation in units of km where m_j is one of the anisotropic parameters ($\overline{u}_j$, A_j, B_j, or C_j). For ray theoretical travel-times, w_{ij} is simply the length of the ray segment that is mapped to the j^{th} model node (or $K_{ij}dV_{ij}$ for finite-frequency travel-times). The partial $\partial u_{ij}/\partial v_{ij}$ is given by $-v_{ij}^{-2}$ (i.e. the squared anisotropic slowness for the i^{th} observation

at the j^{th} location) and the partials $\partial v_{ij}/\partial m_j$ can be derived from Equations 5.5 and 5.12-5.14.

Clearly, the partial derivatives in Equation 5.15 are non-linear and depend upon the current model. Therefore, we iteratively solve Equation 5.8. At each iteration, we recompute the Jacobian given the current model, solve Equation 5.8 for new model perturbations, and then update the model (i.e. $\mathbf{m}_{n+1} = \mathbf{m}_n + \Delta\mathbf{m}_n$ for iteration n). Iterations stop once the $||\Delta\mathbf{t}||^2$ converges to a stable value (4-6 iterations for our synthetic tomography problem). Further details regarding the imaging methodology can be found in VanderBeek and Faccenda (2021).

5.2.4 Model Discretisation, Regularisation, and Resolution

The unknown model perturbations are discretised on a regularly spaced 50-km grid with each node being described by the four anisotropic parameters $\overline{u}$, A, B, and C. Appropriate smoothing and damping values were selected via the construction of a series of L-curves in which the squared-residual norm is plotted against the squared-model norm. Solutions near the corner of the L-curve are considered ideal as a further increase in model complexity (i.e. larger model norm) does not substantially improve the data prediction while simpler models rapidly increase the residual norm. To identify an appropriate ratio of λ_s-to-λ_d, we constructed several L-curves at fixed λ_s/λ_d values and systematically varied λ_d. From this analysis, we found $\lambda_s/\lambda_d = 100$ provided good fitting models while less smooth solutions did not improve the datafit and smoother solutions generated larger residuals. For the isotropic inversion, we found $\lambda_d = 5$ corresponded to the corner of the L-curve. Considering that anisotropic structure is likely as heterogeneous as isotropic structure, we adopted the same λ_s-to-λ_d ratio for the anisotropic inversions

and equally damped isotropic and anisotropic perturbations. After performing a series of anisotropic inversions across different λ_d values, we again found that $\lambda_d = 4$ provides an optimal solution for the anisotropic inversions. A selection of L-curves for isotropic and anisotropic inversions are plotted in Figure 5.11.

Assessing model resolution is an important aspect of tomographic reconstructions considering that the solutions are generally non-unique. In this work, we focus on the imaging of a known and geologically-relevant target synthetic structure allowing us to assess model resolution by direct comparison. We refer to VanderBeek and Faccenda (2021) for a more general discussion on the resolution of teleseismic travel-times to anisotropic heterogeneity.

5.3 Results and Discussion

We performed a series of inversions to show the ability of different imaging strategies in recovering subduction zones structures and upper mantle flow patterns using teleseismic S-waves. We started with isotropic inversions and proceeded by gradually adding anisotropy through AB- and ABC-anisotropic inversions, i.e. azimuthal and fully anisotropic, respectively. Using trade-off curves we quantitatively compared the results of the different inversion strategies, evaluating their ability to recover the isotropic and anisotropic structures of the true model.

5.3.1 Isotropic solutions

At the early stages of our work we inverted a dataset of delay times computed from a purely isotropic model (Figure 5.4). Not considering the effect of anisotropy on seismic tomography allows to recover, within the limits of the capabilities of the method (e.g., finite-frequency approximation, imperfect data coverage, manual picking), the geometry of the isotropic structures.

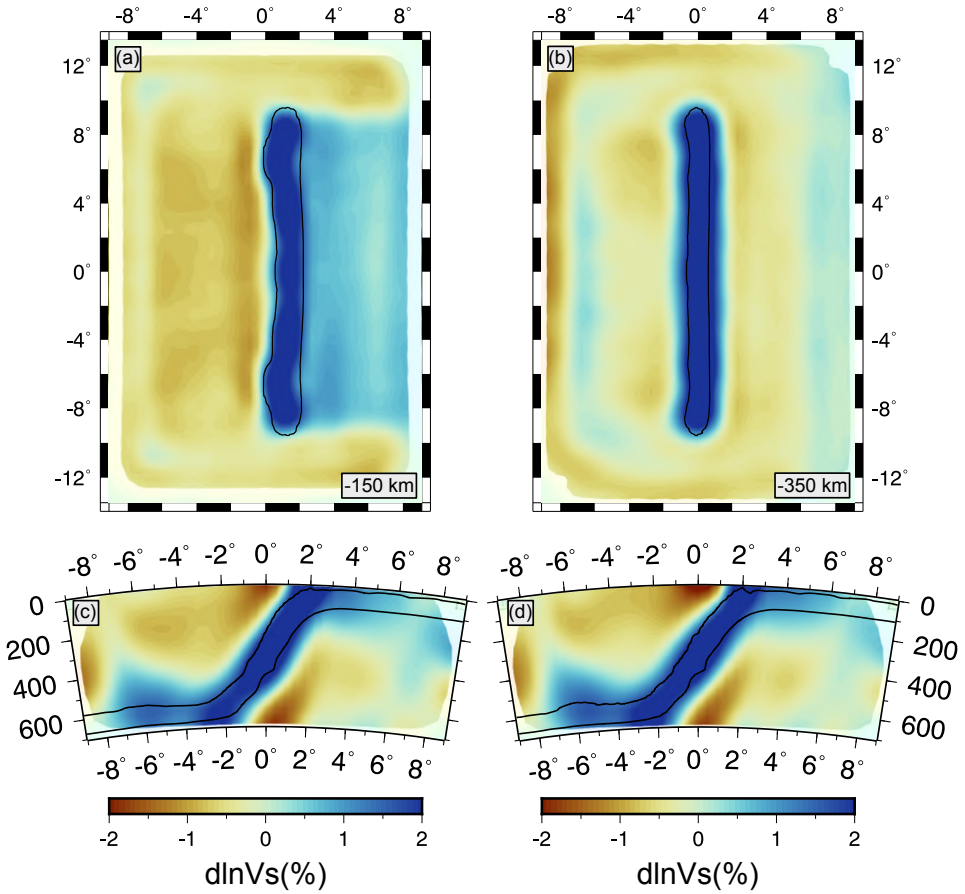

Figure 5.4: *Isotropic inversion of isotropic data. Top view of the velocity perturbations with respect to the 1-D starting velocity model at (a) 150 km and (b) 350 km depth. East-west cross-sections at (c) 4°30′N and (d) 0°N. The black line represents the 1% velocity contour in the true model and outlines the true slab geometry. Areas with poor data coverage are masked.*

This solution will represent the reference model for future comparisons. Figure 5.4 shows a fast anomaly (FA), corresponding to the true slab, extending in the N-S direction at 150 km (Figure 5.4a) and 350 km (Figure 5.4b) depth with no significant imaging artifacts. Weak (∼-1%) slow anomalies (SAs) are imaged all around the slab. Cross sections in Figures 5.4(c,d) present SAs with stronger-magnitude-peaks (i.e. ∼-2%) above and below the slab. The latter sinks into the mantle down to 700 km depth showing a good later symmetry along the latitude plane. However, cross sections exhibit a significant loss of resolution resulting in the smoothing of the FA in the deeper layers.

Successively, we performed isotropic inversions with anisotropic delays

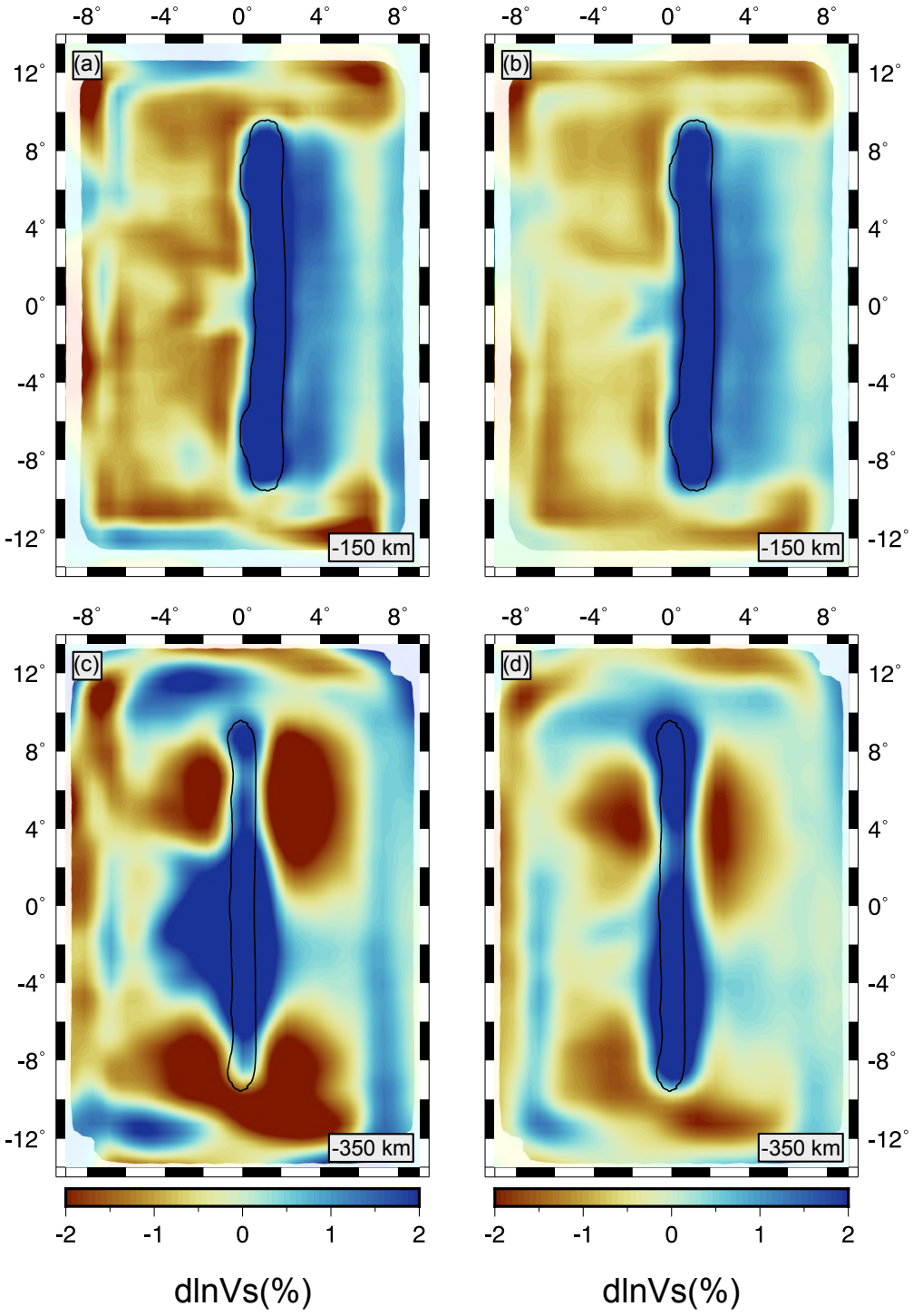

Figure 5.5: *Isotropic inversion of anisotropic delays picked from the transverse component (left column) and the S-wave polarization direction (right column). Velocity perturbations with respect to the 1-D starting velocity model are plotted at (a and b) 150 km and (c and d) 350 km depth. Slab contour and mask as in Fig. 5.4.*

(Figure 5.5 and 5.6) that we first picked from the transverse component (Figure 5.5 and 5.6, left columns). In contrast with the purely isotropic results

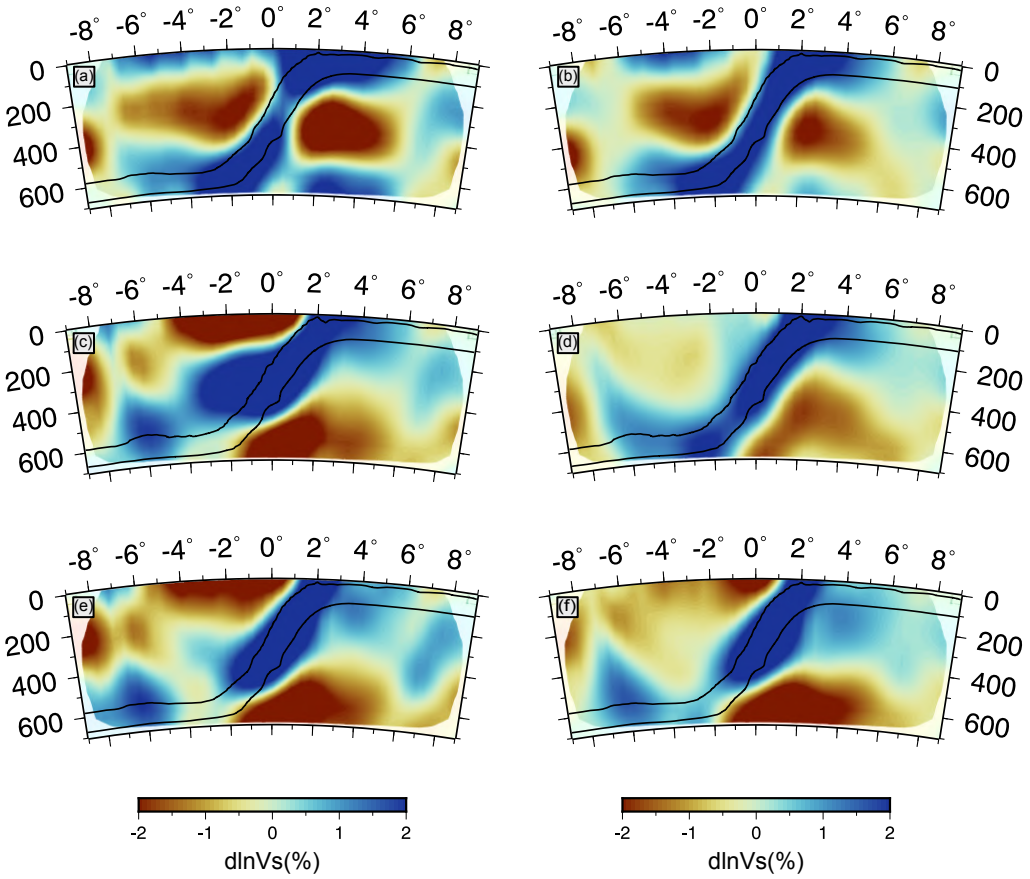

Figure 5.6: *Isotropic inversion of anisotropic delays picked from the transverse component (left column) and the S-wave polarization direction (right column). East-west cross-sections are plotted at (a and b) 4°30′N, (c and d) 0°N and (e and f) 4°30′S. Slab contour and mask as in Fig. 5.4.*

of Figure 5.4, a significant number of artifacts were captured by the new inversion in isotropic approximation (Figure 5.5 and 5.6, left columns). The magnitude of both fast and slow anomalies strongly increased, e.g., this is particularly evident for the SAs in the areas surrounding the slab. This effect is attributable to the presence of strong anisotropy in these regions. Although in the first kilometers of depth the slab geometry is well recovered (Figure 5.5a), significant distortions are found with increasing depth (Figure 5.5c). Cross sections in Figure 5.6a, 5.6c and 5.6e exhibit a deformed slab varying with latitude. E.g., Figure 5.6(a) presents a weakening (i.e. a lower magnitude portion) in the center of the FA at ∼200-250 km depth, which could be interpreted as slab detachment; on the contrary, Figures 5.6(c) exhibits a

wider slab stagnating at ∼400 km depth; Figure 5.6(e) shows instead a ∼500 km slab penetrating into the mantle.

A second set of inversions was performed using delay times picked on the S-wave polarization direction (Figure 5.5 and 5.6, right columns). With respect to the previous case, i.e. with data picked on the transverse component, we observe a general reduction in the amplitude of the slow anomalies and the geometry of the slab is better recovered (Figure 5.5b), although a general worsening with increasing depth (5.5d) still persists. However, Figure 5.5d partly allows to distinguish the N-S elongated shape of the FA which instead was not recovered at this depths (i.e. 350 km depth) when inverting the transverse component (Figure 5.5c). Strong distortions remain on the latitude plane. Cross sections in Figure 5.6b, d and f show the presence of seismic imaging artifacts below and above the slab that, in Figure 5.6b and 5.6d, penetrates down to 700 km stagnating at that depth, while in Figure 5.6f appears detached at ∼500 km depth with some remnants stagnating at the transition zone.

The presence of these artifacts in the tomographic model does not allow to recover the correct geometry of the slab thus potentially leading to wrong interpretations of the seismic images when inverting in isotropic approximation.

5.3.2 AB anisotropic solutions

In this section we show the results of the inversions for the azimuthal anisotropy parameters only (Figure 5.7, 5.8, 5.9 and 5.10, left columns). Considering that among the isotropic tests showed in section 5.3.1 the best results is

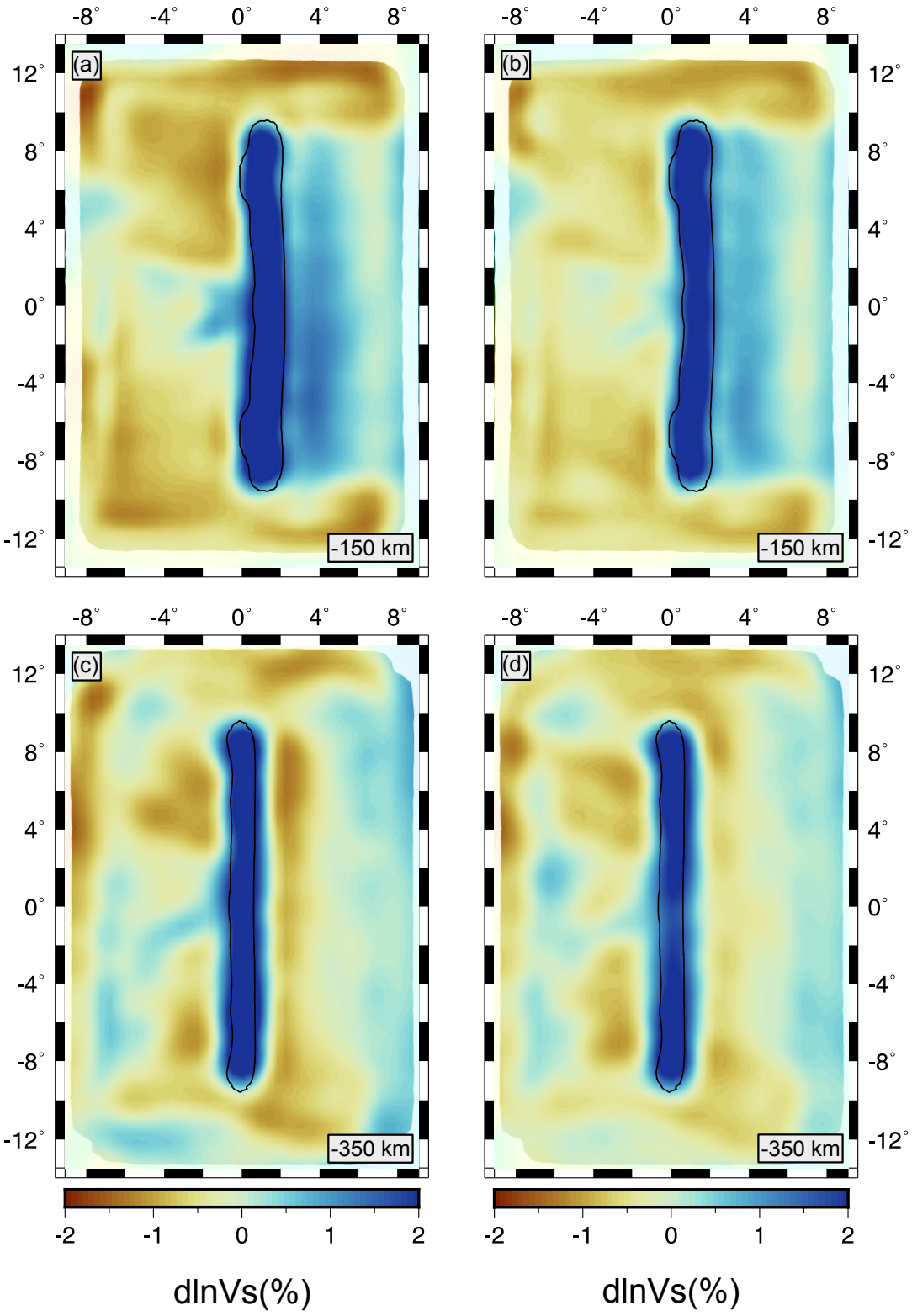

Figure 5.7: *Isotropic structure recovered from azimuthally anisotropic inversion (left column) and from anisotropic inversion that includes symmetry axis azimuth and dip (right column). Velocity perturbations are plotted as in Fig. 5.5. Slab contour and mask as in Fig. 5.4.*

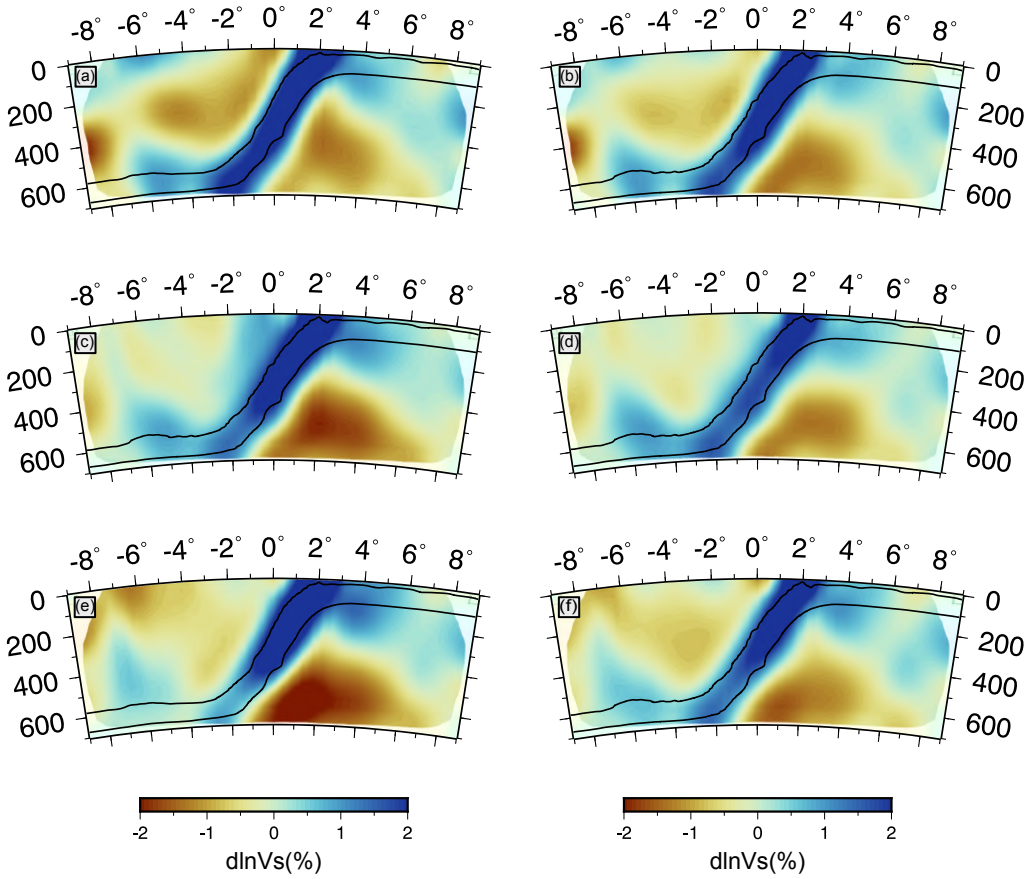

Figure 5.8: *Isotropic structure recovered from azimuthally anisotropic inversion (left column) and from anisotropic inversion that includes symmetry axis azimuth and elevation (right column). Velocity perturbations are plotted as Fig. 5.6. Slab contour and mask as in Fig. 5.4.*

attributable to that performed using delays picked on the polarization direction, we decided to proceed the anisotropic tests using the polarization component only (i.e., not performing inversions with data picked on the transverse component).

Differently from what VanderBeek and Faccenda (2021) observed for P-wave tomography, due to the fact that teleseismic S-waves are more sensitive to azimuthal variations than P-waves are, we note that the first order effect of including only the azimuthal anisotropic parameters (i.e., A and B) in the inversion is to reduce the number and the magnitude of velocities artifacts, consequently to allows for a better recover of the slab geometry (Figure 5.7a,c

and 5.8a,c,e). However, the SAs above and beneath the slab still persists (Figure 5.8a,c,e).

Important insights on mantle dynamics come from the azimuthal anisotropic patterns showed in Figure 5.9 and 5.10 (left columns). The torodial flow, typical of many subduction zones, is retrieved at the edges of the slab (Figure 5.9a) and trench-perpendicular azimuths are observed beneath the incoming plate. With increasing depth the azimuthal assumption introduces several artifacts. Among them, shown in Figure 5.9c, is the presence of apparent isotropic bodies and the not recovering of the toroidal patterns.

Despite including azimuthal anisotropy helps to better recover the isotropic structures with respect to the purely isotropic cases, it is true that neglecting anisotropy dip leads to isotropic and anisotropic imaging artefacts which make the interpretation of the model particularly difficult.

5.3.3 ABC anisotropic solutions

We performed anisotropic inversions for perturbations to S-wave slowness (u) and all the three anisotropic parameters (A, B and C) that define the anisotropic magnitude, azimuth and dip (Figure 5.7, 5.8, 5.9 and 5.10, right columns).

In Figure 5.7(b, d) and 5.8(b, d, f) we observe that the low velocity artifacts are significantly reduced and the solution closely resembles the ideal recovery of the isotropic structure in Figure 5.4. The geometry of the slab is well recovered both at shallower layers and in depth. Vertical sections at the center and at the edges of the model (Figs 5.8b,d and f) show the slab fast anomaly continuously dipping down to 700 km depth. No significant changes in magnitude and geometry are found between the three cross sections, imaging a symmetric slab with respect to the latitudinal plane. The magnitude of the SAs below and above slab is strongly reduced with respect

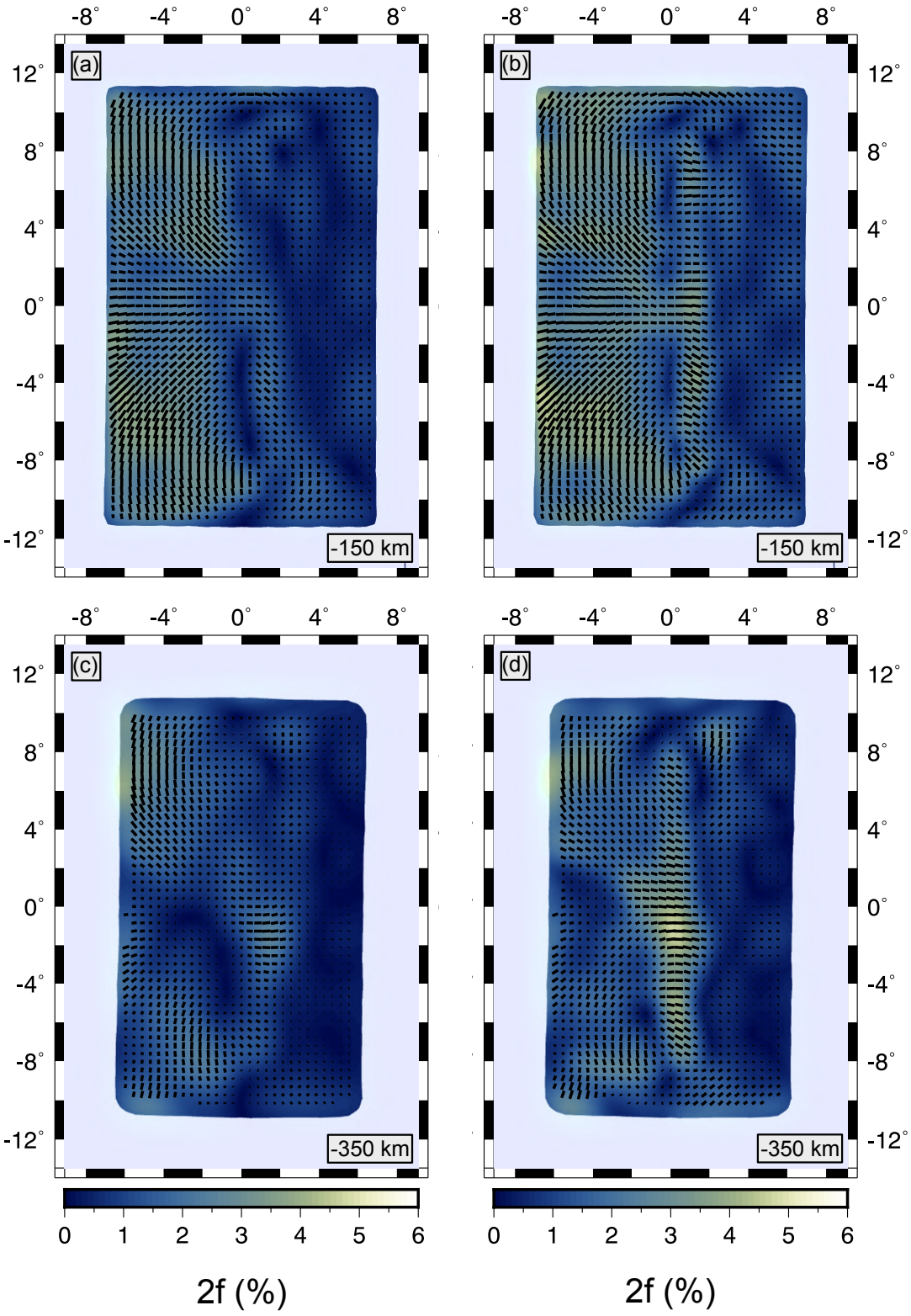

Figure 5.9: *Azimuthal anisotropic structure recovered from inversion for u, A and B terms (left column) and from inversion for u, A, B and C terms (right column). Seismic anisotropy is plotted as in Figure 5.3. Areas with poor directional sampling are masked.*

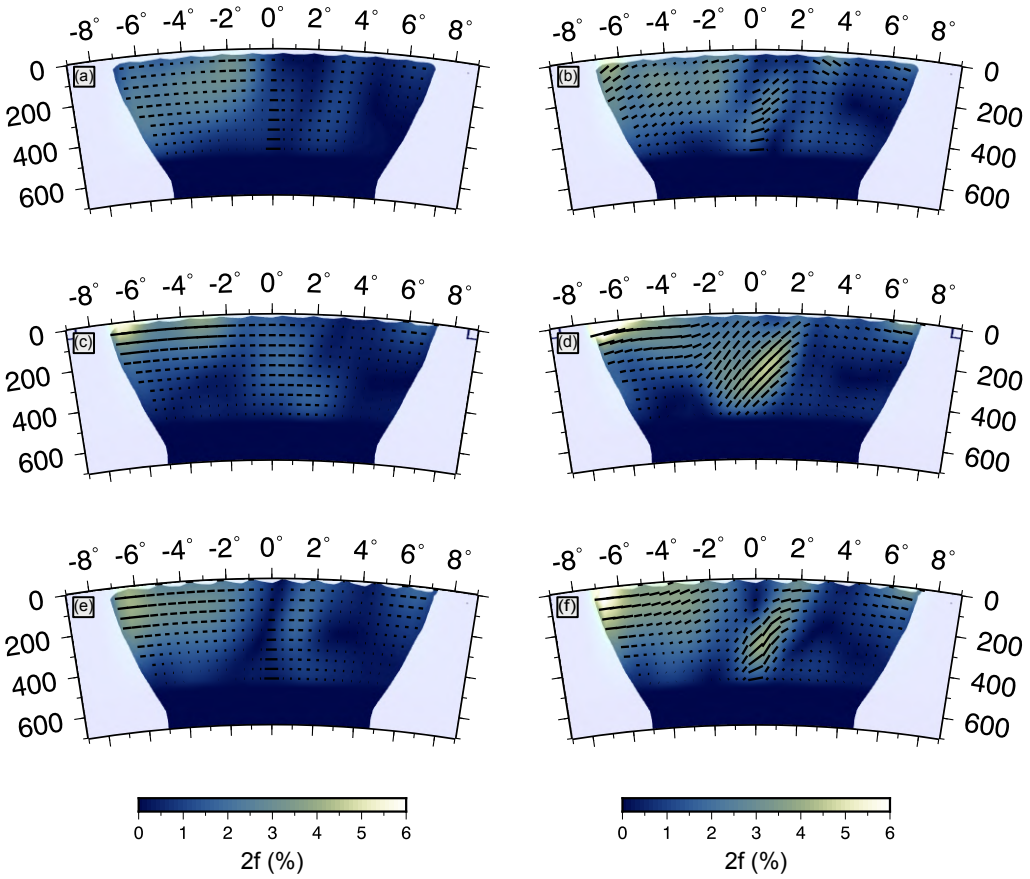

Figure 5.10: *Azimuthal anisotropic structure recovered from inversion for u, A and B terms (left column) and from inversion for u, A, B and C terms (right column).Seismic anisotropy is plotted as in Figure 5.3. Areas with poor directional sampling are masked.*

to the purely isotropic (Figure 5.5 and 5.6) and azimuthal anisotropic (Figure 5.7a, c and 5.8a, c, e) inversions of anisotropic delays.

The recovered anisotropic patterns (Figure 5.9b, d) capture the toroidal flows at the edges of the slab at 150 km and 350 km depth. The trench perpendicular anisotropy in the incoming plate is now well recovered and the number and size of the anisotropic artifacts are strongly reduced. Although the slight overestimation of the anisotropy magnitude observed in the central portion of the slab at 350 km depth (∼5%, Figure 5.9), its geometry is well constrained by the fraction of anisotropy. Anisotropic vertical sections in Figure 5.10b, d, f show the anisotropic patterns and magnitude with depth. We observe that dipping fabrics are found in the slab, and near-horizontal fabrics

beneath the incoming plate.

5.3.4 Comparison between results

From a comparison between our results it emerges that inverting teleseismic S-waves delays simultaneously for perturbation to S-wave slowness and the three anisotropic parameters strongly reduces isotropic artifacts in seismic images, revealing upper mantle structure and dynamics.

Figure 5.11 shows the progressive improvement of the results with respect to the reference model (i.e. isotropic inversion of isotropic data; black curve) in terms of RMS residual values (rms^2) and model norm ($|dlnV|^2 + |df|^2$). The purely isotropic inversion of the delay times picked on the transverse component (orange curve in Figure 5.11) exhibits the highest values of both data fitting and model complexity (rms^2 and $|dlnV|^2 + |df|^2$, respectively). This results in the presence of several isotropic artifacts in the tomographic image as shows in Figure 5.5 and 5.6 (left panels). Notably, improvements are observed when inverting the data picked on the polarization component (red curve in Figure 5.11). We note that, despite the high number of artifacts still present in the seismic images, the trade-off curve exhibits lower values of data misfit and model norm.

Finally, the best results were obtained when the anisotropic parameters are included in the tomographic inversion. It is worth noting that, although the lowest value of rms^2 was obtained for the ABC-anisotropic inversion, the AB- and ABC-anisotropic inversions exhibit similar model complexity, i.e. similar model norm.

As observed in Figure 5.9 and 5.10 and confirmed by the L-curves (Figure 5.11), differently from what VanderBeek and Faccenda (2021) observed for P-wave anisotropic tomography, in the S-wave case analyzed here considering

only azimuthal anisotropy represents a good approximation for recovering the isotropic velocity anomalies without introducing abundant artifacts.

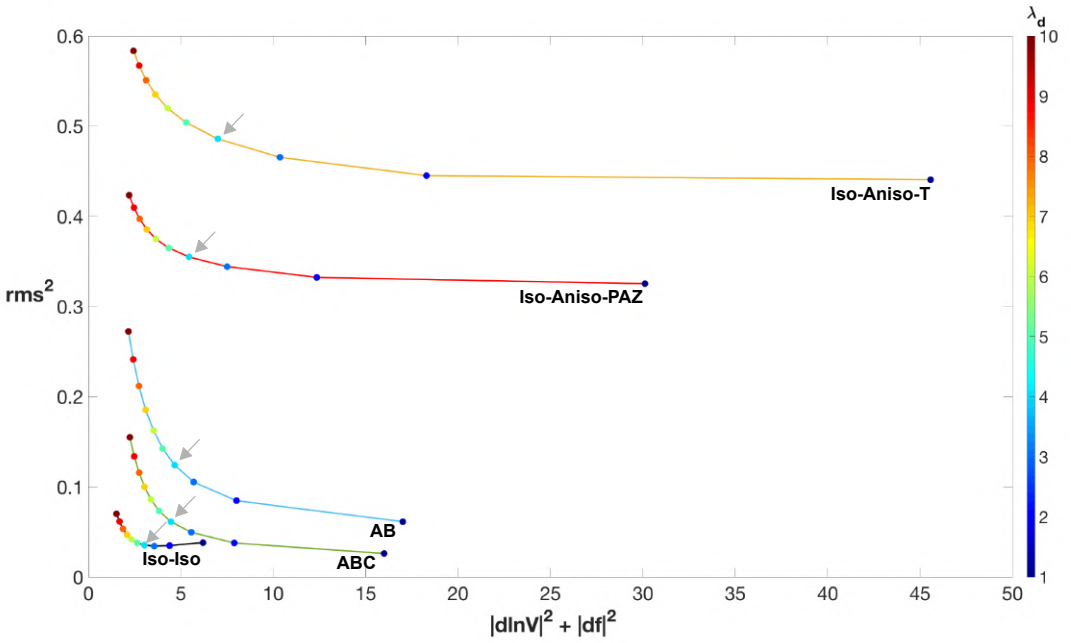

Figure 5.11: *Trade-off curves for damping and smoothing multiplier selection for the isotropic inversion of isotropic data (black line), the isotropic inversion of the anisotropic data picked on the transverse and polarization direction (orange and red lines, respectively) and for the azimuthal (AB, blue line) and fully anisotropic inversion (ABC, green line). The squared RMS is plotted as function of the squared model norm, $|dlnV|^2 + |df|^2$, where $dlnV$ is the fractional velocity perturbation vector and df is the anisotropic magnitude perturbation vector. The values λ_s / λ_d are kept fixed at 100 for both the isotropic and anisotropic cases. Colorbar represents different values of damping factor for slowness. Arrows indicate the preferred solutions, corresponding to $\lambda_d = 4$.*

5.4 Conclusion

We performed a series of isotropic and anisotropic inversions highlighting the ability of each imaging strategy to accurately capture subduction zone structure. Our tomographic results demonstrate that teleseismic S-waves are strikingly sensitive to anisotropy. This sensitivity is well documented by the appearance of several artifacts in the tomographic image when ignoring seismic anisotropy (isotropic assumption).

Unaccounted for anisotropic structure creates significant distortions in slab geometry (changes in dip and appearance of slab gaps) and appearance of several strong low-velocity features. This can significantly corrupt S-wave images of isotropic upper mantle velocities leading to erroneous inferences on subduction dynamics. Severity and geometry of slab distortions and low-velocity artifacts created by anisotropy are dependent on the orientation in which S-wave delays are measured (e.g., radial versus transverse). When measured in the direction of maximum S-wave energy, these artifacts are still present but appear at a generally reduced magnitude.

When anisotropic parameters (i.e., magnitude of hexagonal anisotropy, azimuth and dip of the symmetry axis) are included in the inversion, all major artifacts are strongly minimized. Additionally, major patterns in anisotropic fabrics (e.g., toroidal flow pattern around slab edge, dipping fabrics associated with entrained flow) are well-recovered. These synthetic tests show that teleseismic S-wave alone can constrain 3D upper mantle isotropic and anisotropic structure and modelling anisotropic structure is key to accurately recovering subduction zone shear velocity heterogeneity.

Furthermore, we find that travel-times of shear waves picked in the direction of maximum energy can be approximated by simple sinusoidal functions describing hexagonal anisotropy. This observation allows us to use ray-based methods to predict S-wave travel-times through anisotropic models. This parameterisation can be used to invert S-wave travel-times for the orientation and strength of anisotropy analogously to the anisotropic P-wave travel-time tomography by VanderBeek and Faccenda (2021). Therefore, shear wave anisotropy can be accounted for in a ray theoretical framework to constrain realistic mantle anisotropic fabrics and improve imaging of isotropic features.

We envisage that future studies should carefully assess the role of anisot-

ropy on S-wave teleseismic tomography models to provide more robust interpretations of the upper mantle. Although our synthetic tests demonstrate the utility of teleseismic S-waves in constraining realistic upper mantle anisotropy, the proposed imaging strategy has important limitations that should be overcome. For example, estimating S-wave polarization requires high quality 3-components data or also use of relatively long period data (T > dts).

Ongoing research is aimed at applying our imaging strategy to real data, with a focus on the Cascadia and Central Mediterranean subduction systems. Possible future improvement could aim at jointly invert P-, S-waves and SKS splitting data. The use of both P and S phases and improving ray coverage by including teleseismic and local arrivals will allow for a new and more precise parameterisation of the model. Finally, next studies will extend the current hexagonal symmetry (i.e. with 2 distinct anisotropy axes, 5 independent elastic coefficients) to orthorhombic (i.e. with 3 distinct anisotropy axes, 9 independent elastic coefficients), in order to better resolve the true anisotropy, thus better estimate mantle conditions.

Chapter 6

CONCLUSION AND FUTURE PERSPECTIVES

The main focus of the present Thesis was to investigate the tectonic evolution of the Central-Western Mediterranean convergent margin during the Mid-Late Cenozoic. This goal has been addressed in Chapters 3 and 4 adopting a strategy that combines geodynamic and seismological numerical modelling techniques. The numerical strategy integrated (i) macro-scale geodynamic modelling of the Central-Western Mediterranean subduction system with (ii) micro-scale simulations of strain-induced upper mantle fabrics and (iii) seismological synthetics (isotropic P-wave anomalies, P-wave anisotropy, SKS splitting, Rayleigh wave azimuthal anisotropy and P-wave anisotropic tomography). Furthermore, the geodynamic numerical models were exploited to test the capabilities and limitations of P- and S-waves anisotropic inversions (Chapters 4 and 5, respectively), showing that inverting for seismic anisotropy allows to avoid notable imaging artefacts and improve the reliability of the tomographic result.

In Chapter 3, we attempted to reproduce the tectonic evolution of the Central Mediterranean over the last ∼20–30 Myr by focusing on the role that lithospheric structural heterogeneities within the Adria plate had on its recent dynamics. For this purpose, in some numerical models, calibrated specifically for this region, the Adria plate structure was characterized by the presence of a thin continental lithosphere in the Umbria-Marche region and a stiffer continental promontory in its central portion corresponding to

the Abruzzo-Laziale platform (Calcagnile & Panza, 1980; Geiss, 1987; Lucente et al., 2006; Lucente & Speranza, 2001; Maino et al., 2013; Miller & Piana Agostinetti, 2012; Panza et al., 2003). We have employed a wide range of 3D thermo-mechanical simulations. The modeling results were validated by comparing seismological synthetics (isotropic P-wave anomalies, P-wave anisotropy, SKS splitting, and Rayleigh azimuthal anisotropy) and major tectonic features (i.e., slab and trench geometry) with observations.

This research has clearly shown that lithospheric heterogeneities within the Adria plate profoundly impact on the segmentation of the subducting slab and are fundamental for the development of key tectonic features such as a prolonged eastward retreat of the Ionian plate and the formation of a slab window below the modelled Central Apennines. This suggest that the tectonic history of the Central Mediterranean may have been influenced by the recent dynamics of the Ionian slab and Adria plate. Finally, it should be emphasised that our numerical models can explain the major tectonic events proposed in the literature (e.g., the trench retreat kinematics that lead to the rotation of the Sardinian-Corsican block and to the opening of back-arc basins) and offer valuable constraints on the widely debated break-off of the Ionian slab beneath the Central Apennines, giving a combined geodynamic and seismological reading.

In Chapter 4, we have attempted to take a next step by extending the modelling methodology of Lo Bue et al. (2021) to simulate the geodynamics evolution of the Central-Western Mediterranean subduction systems. This led to the geodynamic model CWM which has been updated by using a more realistic paleo-tectonic configuration of the region characterized by the presence of multiple subducting plates. Although it does not reproduce its exact tectonic structure (e.g., due to the limits of the numerical method, approximations in the initial setup, etc), it seems that using a more complex initial

geometry (i.e. including the Alboran, Alpine and Dinaric-Hellenic slabs) favor a better recover of the mantle flow beneath the region improving the correspondence between the modeled and observed surface and deep isotropic structures, and seismic anisotropy patterns when compared to Model CM of Lo Bue et al. (2021).

The second part of this work involved the application of a tomographic technique recently developed by VanderBeek and Faccenda (2021) for imaging isotropic and anisotropic mantle structure. Using the geodynamic model CWM as benchmark, we evaluate the capabilities of seismic tomography to recover a complex subduction environment (i.e., isotropic seismic velocity and mantle anisotropy) depending on observation network density and data quality. Despite the non-ideal source and receiver distributions, our results show that P-wave anisotropy tomography allows to well recover to a first order isotropic structures and anisotropic patterns. However, we observed that, especially in poorly covered areas, the magnitude of anisotropy appears generally underestimated. In light of this, it is recommended to increase the number of marine and land stations and improve the accuracy of teleseismic arrival time measurements.

Established that anisotropy can produce significant imaging artefacts in telesismic P-wave tomography and that teleseismic P-wave delays can constrain 3D anisotropic structure and reduce imaging artefacts (Bezada et al., 2016; VanderBeek & Faccenda, 2021), in Chapter 5 we wanted to evaluate the nature of anisotropy-induced artefacts in teleseismic S-wave tomography through a new inversion strategy for the inversion of teleseismic S-wave delays for upper mantle isotropic velocity and hexagonal anisotropy. It's found that the isotropic imaging assumption introduces notable artefacts in the recovered velocity models and, consequently, lead to erroneous inferences regarding mantle dynamics. When anisotropic parameters (i.e., magnitude of hexagonal anisotropy, azimuth and dip of the symmetry axis) are

included in the inversion, all major artifacts are strongly minimized. We also demonstrate that shear wave anisotropy can be accounted for in a ray theoretical framework to constrain realistic mantle anisotropic fabrics and improve imaging of isotropic features.

From the research that has been carried out so far, we can conclude that using a combination of geodynamic and seismological numerical modeling techniques can capture to a first order the overall evolution and the present-day geological scenario of the study region, thus representing a powerful tool to investigate mantle dynamics. However, modeling a real subduction evolution is not straightforward and our large-scale geodynamic models are affected by several limitations (e.g., plates geometry fixed at ∼30 Ma, model domain defined in Cartesian coordinates, uncertainties of the paleotectonic reconstructions, etc ...) that could potentially bias the final output. To limit the uncertainties of the models, thus to obtain synthetic geodynamic scenarios more consistent with the observations, future numerical studies should attempt to improve the model geometry by considering the Earth's sphericity and the Africa-Eurasia plates convergence. Our 3D numerical models, and previous studies, have indeed highlighted the importance of considering appropriate plate geometries and lateral buoyancy variations to reproduce the recent dynamics of the study regions (Faccenna & Becker, 2010; Kaus et al., 2020; Lo Bue & Faccenda, 2019; Lo Bue et al., 2021; Magni et al., 2014). With this respect and in order better constrain the initial tectonic configuration, an interesting future development would be to formulate a fluid dynamic inverse problem to reproduce unknown mantle flow back in time from seismic tomographic observations of the mantle and reconstructions of past plate motions using variational data assimilation (Bunge et al., 2003). It is important to note also that the employed geodynamic simulations do not account for compositional variations, presence of fluids/melt

and lithospheric fossil fabrics that can affect the seismic properties of natural tectonic settings. The presence of these further complexities remains to be tested, and it will be considered in future studies. Furthermore, although the aim of the present Thesis was to investigate the Mid-late Cenozoic evolution of the Central-Western Mediterranean, it is worth pointing out that this methodology can potentially be applied to any tectonic environment, e.g., the entire Mediterranean area. This is undoubtedly a major challenge, but it could bring important constraints to the processes that have contributed to shaping one of the most complex tectonic environments on Earth.

At the same time, new anisotropic P- and S-wave tomographic models of the entire Mediterranean area would likely help in better constraining the deep structure and recent dynamics of this region. In general, ongoing research is aimed at applying P- and S-waves imaging strategy to real data (e.g., Cascadia and Central Mediterranean subduction systems).

Despite our synthetic tests demonstrate the utility of teleseismic P- and S-waves in constraining realistic upper mantle anisotropy, the proposed imaging strategies have some limitations that should be overcome. For example, possible future improvement could aim at extending the current hexagonal symmetry to orthorhombic (i.e. with 3 distinct anisotropy axes) and jointly invert P-, S-waves and SKS splitting data. The use of both P and S phases and improving ray coverage by including teleseismic and local arrivals will allow for a new and more precise parameterisation of the model. The retrieved anisotropic fabrics in the hot mantle could then be exploited to improve mantle flow retrodictions given that their strength and orientation is the result of the recent tectonic evolution and accumulated deformation.

In light of what has been observed from our seismological simulations, which confirms what is already known in the literature (Bezada et al., 2016;

VanderBeek & Faccenda, 2021), tomographers should consider seismic anisotropy among the possible causes of velocity anomalies found in the tomographic images, and because it provides more robust and physically-based interpretations of the upper mantle structure and dynamics.

Bibliography

Aki, K., Christoffersson, A., & Husebye, E. S. (1977). Determination of the three-dimensional seismic structure of the lithosphere. *Journal of Geophysical Research*, *82*(2), 277–296.

Amato, A., Alessandrini, B., Cimini, G., Frepoli, A., & Selvaggi, G. (1993). Active and remnant subducted slabs beneath italy: Evidence from seismic tomography and seismicity. *Annals of Geophysics*, *36*(2).

Anderson, D. L. (1965). Recent evidence concerning the structure and composition of the earth's mantle. *Physics and Chemistry of the Earth*, *6*, 1–131.

Anderson, D. L. (1989). *Theory of the earth*. Blackwell scientific publications.

Anderson, J. (1961). Magnetic anisotropy in single-crystal nickel films. *Proceedings of the Physical Society (1958-1967)*, *78*(1), 25.

Antolik, M., Gu, Y. J., Ekström, G., & Dziewonski, A. M. (2003). J362d28: A new joint model of compressional and shear velocity in the earth's mantle. *Geophysical Journal International*, *153*(2), 443–466.

Arab, M., Maherssi, C. E., Granjeon, D., Roure, F., Déverchère, J., Cuilhé, L., Hassaim, M., Mouchot, N., Doublet, S., & Khomsi, S. (2020). On the origin and consequences of crustal-scale extension between africa and sicily since late miocene: Insights from the kaboudia area, western pelagian sea. *Tectonophysics*, *795*, 228565.

Aster, R., Borchers, B., & Thurber, C. (2012). Parameter estimation and inverse problems. *Recherche*, *67*, 02.

Aster, R. C., Borchers, B., & Thurber, C. H. (2018). *Parameter estimation and inverse problems*. Elsevier.

Babuska, V., & Cara, M. (1991). *Seismic anisotropy in the earth* (Vol. 10). Springer Science & Business Media.

Baccheschi, P, Margheriti, L, & Steckler, M. (2007). Seismic anisotropy reveals focused mantle flow around the calabrian slab (southern italy). *Geophysical Research Letters*, *34*(5).

Baccheschi, P, Pastori, M, Margheriti, L, & Piccinini, D. (2016). Shear wave splitting of the 2009 l'aquila seismic sequence: Fluid saturated microcracks and crustal fractures in the abruzzi region (central apennines, italy). *Geophysical Journal International*, *204*(3), 1531—1549.

Backus, G. E. (1965). Possible forms of seismic anisotropy of the uppermost mantle under oceans. *Journal of Geophysical Research*, *70*(14), 3429–3439.

Balling, P., Grützner, C., Tomljenović, B., Spakman, W., & Ustaszewski, K. (2021). Post-collisional mantle delamination in the dinarides implied from staircases of oligo-miocene uplifted marine terraces. *Scientific reports*, *11*(1), 1–11.

Bauville, A., & Baumann, T. S. (2019). Geomio: An open-source matlab toolbox to create the initial configuration of 2-d/3-d thermo-mechanical simulations from 2-d vector drawings. *Geochemistry, Geophysics, Geosystems*, *20*(3), 1665–1675.

Becker, T. W., Lebedev, S, & Long, M. (2012). On the relationship between azimuthal anisotropy from shear wave splitting and surface wave tomography. *Journal of Geophysical Research: Solid Earth*, *117*(B1).

Becker, T. W. (2006). On the effect of temperature and strain-rate dependent viscosity on global mantle flow, net rotation, and plate-driving forces. *Geophysical Journal International*, *167*(2), 943–957.

Becker, T. W., & Boschi, L. (2002). A comparison of tomographic and geodynamic mantle models. *Geochemistry, Geophysics, Geosystems*, *3*(1).

Becker, T. W., Chevrot, S., Schulte-Pelkum, V., & Blackman, D. K. (2006a). Statistical properties of seismic anisotropy predicted by upper mantle geodynamic models. *Journal of Geophysical Research: Solid Earth*, *111*(B8).

Becker, T. W., & Faccenna, C. (2009). A review of the role of subduction dynamics for regional and global plate motions. *Subduction zone geodynamics*, 3–34.

Becker, T. W., Kellogg, J. B., Ekström, G., & O'Connell, R. J. (2003). Comparison of azimuthal seismic anisotropy from surface waves and finite strain from global mantle-circulation models. *Geophysical Journal International*, *155*(2), 696–714.

Becker, T. W., Kustowski, B., & Ekström, G. (2008). Radial seismic anisotropy as a constraint for upper mantle rheology. *Earth and Planetary Science Letters*, *267*(1-2), 213–227.

Becker, T. W., Schulte-Pelkum, V., Blackman, D. K., Kellogg, J. B., & O'Connell, R. J. (2006b). Mantle flow under the western united states from shear wave splitting. *Earth and Planetary Science Letters*, *247*(3-4), 235–251.

Beller, S., & Chevrot, S. (2020). Probing depth and lateral variations of upper-mantle seismic anisotropy from full-waveform inversion of teleseismic body-waves. *Geophysical Journal International*, *222*(1), 352–387.

Benoit, M. H., Torpey, M., Liszewski, K., Levin, V., & Park, J. (2011). P and s wave upper mantle seismic velocity structure beneath the northern apennines: New evidence for the end of subduction. *Geochemistry, Geophysics, Geosystems*, *12*(6).

Bernard, R. E., Behr, W. M., Becker, T. W., & Young, D. J. (2019). Relationships between olivine cpo and deformation parameters in naturally deformed rocks and implications for mantle seismic anisotropy. *Geochemistry, Geophysics, Geosystems*, *20*(7), 3469–3494.

Bezada, M., Faccenda, M, & Toomey, D. (2016). Representing anisotropic subduction zones with isotropic velocity models: A characterization of the problem and some steps on a possible path forward. *Geochemistry, Geophysics, Geosystems*, *17*(8), 3164–3189.

Bezada, M., Humphreys, E., Toomey, D., Harnafi, M, Dávila, J., & Gallart, J. (2013). Evidence for slab rollback in westernmost mediterranean from improved upper mantle imaging. *Earth Planet. Sci. Lett*, *368*, 51–60.

Bijwaard, H., Spakman, W., & Engdahl, E. R. (1998). Closing the gap between regional and global travel time tomography. *Journal of Geophysical Research: Solid Earth*, *103*(B12), 30055–30078.

Billen, M. I. (2008). Modeling the dynamics of subducting slabs. *Annu. Rev. Earth Planet. Sci.*, *36*, 325–356.

Blackman, D. K., & Kendall, J.-M. (1997). Sensitivity of teleseismic body waves to mineral texture and melt in the mantle beneath a mid–ocean ridge. *Philosophical Transactions of the Royal Society of London. Series A: Mathematical, Physical and Engineering Sciences*, *355*(1723), 217–231.

Blackman, D. K., & Kendall, J.-M. (2002). Seismic anisotropy in the upper mantle 2. predictions for current plate boundary flow models. *Geochemistry, Geophysics, Geosystems*, *3*(9), 1–of.

Blackman, D. K., Kendall, J.-M., Dawson, P. R., Wenk, H.-R., Boyce, D., & Morgan, J. P. (1996). Teleseismic imaging of subaxial flow at mid-ocean ridges: Traveltime effects of anisotropic mineral texture in the mantle. *Geophysical Journal International*, *127*(2), 415–426.

Boneh, Y., Morales, L. F., Kaminski, E., & Skemer, P. (2015). Modeling olivine cpo evolution with complex deformation histories: Implications for the interpretation of seismic anisotropy in the mantle. *Geochemistry, Geophysics, Geosystems*, *16*(10), 3436–3455.

Booth, D. C., & Crampin, S. (1983). The anisotropic reflectivity technique: Theory. *Geophysical Journal International*, *72*(3), 755–766.

Boschi, L., & Dziewonski, A. M. (1999). High-and low-resolution images of the earth's mantle: Implications of different approaches to tomographic modeling. *Journal of Geophysical Research: Solid Earth*, *104*(B11), 25567–25594.

Bowman, J. R., & Ando, M. (1987). Shear-wave splitting in the upper-mantle wedge above the tonga subduction zone. *Geophysical Journal International*, *88*(1), 25–41.

Bozdağ, E., Peter, D., Lefebvre, M., Komatitsch, D., Tromp, J., Hill, J., Podhorszki, N., & Pugmire, D. (2016). Global adjoint tomography: First-generation model. *Geophysical Journal International*, *207*(3), 1739–1766.

Browaeys, J. T., & Chevrot, S. (2004). Decomposition of the elastic tensor and geophysical applications. *Geophysical Journal International*, *159*(2), 667–678.

Brownlee, S. J., Schulte-Pelkum, V., Raju, A., Mahan, K., Condit, C., & Orlandini, O. F. (2017). Characteristics of deep crustal seismic anisotropy from a compilation of rock elasticity tensors and their expression in receiver functions. *Tectonics*, *36*(9), 1835–1857.

Buland, R., & Chapman, C. (1983). The computation of seismic travel times. *Bulletin of the Seismological Society of America*, *73*(5), 1271–1302.

Bunge, H.-P., Hagelberg, C., & Travis, B. (2003). Mantle circulation models with variational data assimilation: Inferring past mantle flow and structure from plate motion histories and seismic tomography. *Geophysical Journal International*, *152*(2), 280–301.

Buontempo, L, Bokelmann, G., Barruol, G., & Morales, J. (2008). Seismic anisotropy beneath southern iberia from sks splitting. *Earth and Planetary Science Letters*, *273*(3-4), 237–250.

Burgos, G., Montagner, J.-P., Beucler, E, Capdeville, Y., Mocquet, A, & Drilleau, M. (2014). Oceanic lithosphere-asthenosphere boundary from surface wave dispersion data. *Journal of Geophysical Research: Solid Earth*, *119*(2), 1079–1093.

Byrnes, J. S., Toomey, D. R., Hooft, E. E., Nábělek, J., & Braunmiller, J. (2017). Mantle dynamics beneath the discrete and diffuse plate boundaries of the j uan de f uca plate: Results from c ascadia i nitiative body wave tomography. *Geochemistry, Geophysics, Geosystems*, *18*(8), 2906–2929.

Bystricky, M, Kunze, K, Burlini, L, & Burg, J.-P. (2000). High shear strain of olivine aggregates: Rheological and seismic consequences. *Science*, *290*(5496), 1564–1567.

Calcagnile, G, & Panza, G. (1980). The main characteristics of the lithosphere-asthenosphere system in italy and surrounding regions. *Pure and Applied Geophysics*, *119*(4), 865–879.

Calò, M, Bodin, T., & Romanowicz, B. (2016). Layered structure in the upper mantle across north america from joint inversion of long and short period seismic data. *Earth and Planetary Science Letters*, *449*, 164–175.

Capitanio, F., Faccenna, C., Zlotnik, S., & Stegman, D. (2011). Subduction dynamics and the origin of andean orogeny and the bolivian orocline. *Nature*, *480*(7375), 83–86.

Capitanio, F. A., & Faccenda, M. (2012). Complex mantle flow around heterogeneous subducting oceanic plates. *Earth and Planetary Science Letters*, *353*, 29–37.

Carminati, E, Wortel, M., Spakman, W, & Sabadini, R. (1998). The role of slab detachment processes in the opening of the western–central mediterranean basins: Some geological and geophysical evidence. *Earth and Planetary Science Letters*, *160*(3-4), 651–665.

Carminati, E., Lustrino, M., & Doglioni, C. (2012). Geodynamic evolution of the central and western mediterranean: Tectonics vs. igneous petrology constraints. *Tectonophysics*, *579*, 173–192.

Chapman, C., & Shearer, P. (1989). Ray tracing in azimuthally anisotropic media—ii. quasi-shear wave coupling. *Geophysical Journal International*, *96*(1), 65–83.

Chastel, Y. B., Dawson, P. R., Wenk, H.-R., & Bennett, K. (1993). Anisotropic convection with implications for the upper mantle. *Journal of Geophysical Research: Solid Earth*, *98*(B10), 17757–17771.

Chen, M., & Tromp, J. (2007). Theoretical and numerical investigations of global and regional seismic wave propagation in weakly anisotropic earth models. *Geophysical Journal International*, *168*(3), 1130–1152.

Chertova, M., Spakman, W, Geenen, T, Van Den Berg, A., & Van Hinsbergen, D. (2014). Underpinning tectonic reconstructions of the western mediterranean region with dynamic slab evolution from 3-d numerical modeling. *Journal of Geophysical Research: Solid Earth*, *119*(7), 5876–5902.

Chevrot, S. (2000). Multichannel analysis of shear wave splitting. *Journal of Geophysical Research: Solid Earth*, *105*(B9), 21579–21590.

Chevrot, S. (2006). Finite-frequency vectorial tomography: A new method for high-resolution imaging of upper mantle anisotropy. *Geophysical Journal International*, *165*(2), 641–657.

Chevrot, S., Favier, N., & Komatitsch, D. (2004). Shear wave splitting in three-dimensional anisotropic media. *Geophysical Journal International*, *159*(2), 711–720.

Chevrot, S., & Van Der Hilst, R. D. (2003). On the effects of a dipping axis of symmetry on shear wave splitting measurements in a transversely isotropic medium. *Geophysical Journal International*, *152*(2), 497–505.

Chiarabba, C, Jovane, L, & DiStefano, R. (2005). A new view of italian seismicity using 20 years of instrumental recordings. *Tectonophysics*, *395*(3-4), 251–268.

Christensen, U., & Yuen, D. (1985). Layered convection induced by phase transitions. *Journal of Geophysical Research A: Space Physics*, *90*(B12), 10,291–10,300. https://doi.org/10.1029/jb090ib12p10291

Christensen, U. (1982). Phase boundaries in finite amplitude mantle convection. *Geophysical Journal International*, *68*(2), 487–497.

Christensen, U. R. (1987). Some geodynamical effects of anisotropic viscosity. *Geophysical Journal International*, *91*(3), 711–736.

Civello, S., & Margheriti, L. (2004). Toroidal mantle flow around the calabrian slab (italy) from sks splitting. *Geophysical Research Letters*, *31*(10).

Coates, R., & Chapman, C. (1990). Quasi-shear wave coupling in weakly anisotropic 3-d media. *Geophysical Journal International*, *103*(2), 301–320.

Confal, J. M., Faccenda, M., Eken, T., & Taymaz, T. (2018). Numerical simulation of 3-d mantle flow evolution in subduction zone environments in relation to seismic anisotropy beneath the eastern mediterranean region. *Earth and Planetary Science Letters*, *497*, 50–61.

Connolly, J., & Kerrick, D. (1987). An algorithm and computer program for calculating composition phase diagrams. *Calphad*, *11*(1), 1–55.

Connolly, J. A. (2005). Computation of phase equilibria by linear programming: A tool for geodynamic modeling and its application to subduction zone decarbonation. *Earth and Planetary Science Letters*, *236*(1-2), 524–541.

Crameri, F. (2018a). Geodynamic diagnostics, scientific visualisation and staglab 3.0. *Geoscientific Model Development*, *11*(6), 2541–2562.

Crameri, F. (2018b). Scientific colour-maps. *Zenodo. doi*, *10*.

Crampin, S. (1981). A review of wave motion in anisotropic and cracked elastic-media. *Wave motion*, *3*(4), 343–391.

Crampin, S. (1984). Effective anisotropic elastic constants for wave propagation through cracked solids. *Geophysical Journal International*, *76*(1), 135–145.

Crotwell, H. P., Owens, T. J., & Ritsema, J. (1999). The taup toolkit: Flexible seismic travel-time and ray-path utilities. *Seismological Research Letters*, *70*(2), 154–160.

Dalton, C. A., & Ekström, G. (2006). Global models of surface wave attenuation. *Journal of Geophysical Research: Solid Earth*, *111*(B5).

Dawson, P. R., & Wenk, H.-R. (2000). Texturing of the upper mantle during convection. *Philosophical Magazine A*, *80*(3), 573–598.

de Montserrat, A., Faccenda, M., & Pennacchioni, G. (2021). Extrinsic anisotropy of two-phase newtonian aggregates: Fabric characterization and parameterization. *Journal of Geophysical Research: Solid Earth*, *126*(11), e2021JB022232.

De Capitani, C., & Brown, T. H. (1987). The computation of chemical equilibrium in complex systems containing non-ideal solutions. *Geochimica et Cosmochimica Acta*, *51*(10), 2639–2652.

Dewey, J., Helman, M., Knott, S., Turco, E, & Hutton, D. (1989). Kinematics of the western mediterranean. *Geological Society, London, Special Publications*, *45*(1), 265–283.

Di Giuseppe, E, Van Hunen, J, Funiciello, F, Faccenna, C, & Giardini, D. (2008). Slab stiffness control of trench motion: Insights from numerical models. *Geochemistry, Geophysics, Geosystems*, *9*(2).

Dorogokupets, P., Karpov, I., & Lashkevich, V. (1988). Thermodynamics of silica polymorphs. *International Geology Review*, *30*(12), 1278–1287.

Dziewonski, A. M., Hager, B. H., & O'Connell, R. J. (1977). Large-scale heterogeneities in the lower mantle. *Journal of Geophysical Research*, *82*(2), 239–255.

El-Sharkawy, A., Meier, T., Lebedev, S., Behrmann, J. H., Hamada, M., Cristiano, L., Weidle, C., & Köhn, D. (2020). The slab puzzle of the alpine-mediterranean region: Insights from a new, high-resolution, shear wave velocity model of the upper mantle. *Geochemistry, Geophysics, Geosystems*, *21*(8), e2020GC008993.

Escher, A., & Beaumont, C. (1997). Formation, burial and exhumation of basement nappes at crustal scale: A geometric model based on the western swiss-italian alps. *Journal of structural Geology*, *19*(7), 955–974.

Faccenda, M, Minelli, G, & Gerya, T. (2009). Coupled and decoupled regimes of continental collision: Numerical modeling. *Earth and Planetary Science Letters*, *278*(3-4), 337–349.

Faccenda, M. (2014). Mid mantle seismic anisotropy around subduction zones. *Physics of the Earth and Planetary Interiors*, *227*, 1–19.

Faccenda, M., & Capitanio, F. A. (2012). Development of mantle seismic anisotropy during subduction-induced 3-d flow. *Geophysical Research Letters*, *39*(11).

Faccenda, M., & Capitanio, F. A. (2013). Seismic anisotropy around subduction zones: Insights from three-dimensional modeling of upper mantle deformation and sks splitting calculations. *Geochemistry, Geophysics, Geosystems*, *14*(1), 243–262.

Faccenda, M., & Dal Zilio, L. (2017). The role of solid–solid phase transitions in mantle convection. *Lithos*, *268*, 198–224.

Faccenda, M., Ferreira, A. M., Tisato, N., Lithgow-Bertelloni, C., Stixrude, L., & Pennacchioni, G. (2019). Extrinsic elastic anisotropy in a compositionally heterogeneous earth's mantle. *Journal of Geophysical Research: Solid Earth*, *124*(2), 1671–1687.

Faccenda, M., Gerya, T. V., & Chakraborty, S. (2008). Styles of post-subduction collisional orogeny: Influence of convergence velocity, crustal rheology and radiogenic heat production. *Lithos*, *103*(1-2), 257–287.

Faccenna, C., & Becker, T. W. (2010). Shaping mobile belts by small-scale convection. *Nature*, *465*(7298), 602–605.

Faccenna, C., Becker, T. W., Auer, L., Billi, A., Boschi, L., Brun, J. P., Capitanio, F. A., Funiciello, F., Horvàth, F., Jolivet, L., et al. (2014). Mantle dynamics in the mediterranean. *Reviews of Geophysics*, *52*(3), 283–332.

Faccenna, C., Becker, T. W., Jolivet, L., & Keskin, M. (2013). Mantle convection in the middle east: Reconciling afar upwelling, arabia indentation and aegean trench rollback. *Earth and Planetary Science Letters*, *375*, 254–269.

Faccenna, C., Becker, T. W., Lucente, F. P., Jolivet, L., & Rossetti, F. (2001). History of subduction and back arc extension in the central mediterranean. *Geophysical Journal International*, *145*(3), 809–820.

Faccenna, C., Funiciello, F., Civetta, L., D Antonio, M., Moroni, M., & Piromallo, C. (2007). Slab disruption, mantle circulation, and the opening of the tyrrhenian basins. *Special Papers-Geological Society of America*, *418*, 153.

Faccenna, C., Mattei, M., Funiciello, R., & Jolivet, L. (1997). Styles of back-arc extension in the central mediterranean. *Terra Nova*, *9*(3), 126–130.

Faccenna, C., Piromallo, C., Crespo-Blanc, A., Jolivet, L., & Rossetti, F. (2004). Lateral slab deformation and the origin of the western mediterranean arcs. *Tectonics*, *23*(1).

Fedorenko, R. P. (1964). The speed of convergence of one iterative process. *USSR Computational Mathematics and Mathematical Physics*, *4*(3), 227–235.

Flinn, E. (1965). Signal analysis using rectilinearity and direction of particle motion. *Proceedings of the IEEE*, *53*(12), 1874–1876.

Fox, M., Herman, F., Willett, S. D., & Schmid, S. M. (2016). The exhumation history of the european alps inferred from linear inversion of thermochronometric data. *American Journal of Science*, *316*(6), 505–541.

Fukao, Y., & Obayashi, M. (2013). Subducted slabs stagnant above, penetrating through, and trapped below the 660 km discontinuity. *Journal of Geophysical Research: Solid Earth*, *118*(11), 5920–5938.

Fukao, Y., Obayashi, M., Inoue, H., & Nenbai, M. (1992). Subducting slabs stagnant in the mantle transition zone. *Journal of Geophysical Research: Solid Earth*, *97*(B4), 4809–4822.

Fukao, Y., Widiyantoro, S., & Obayashi, M. (2001). Stagnant slabs in the upper and lower mantle transition region. *Reviews of Geophysics*, *39*(3), 291–323.

Funiciello, F., & Faccenna, C. (2010). Unraveling the geodynamics of the central mediterranean in a tank. *Journal of the Virtual Explorer*, *36*. https://doi.org/10.3809/jvirtex.2010.00231

Gassmöller, R., Dannberg, J., Bangerth, W., Heister, T., & Myhill, R. (2020). On formulations of compressible mantle convection. *Geophysical Journal International*, *221*(2), 1264–1280.

Gattacceca, J., & Speranza, F. (2002). Paleomagnetism of jurassic to miocene sediments from the apenninic carbonate platform (southern apennines, italy): Evidence for a 60 counterclockwise miocene rotation. *Earth and Planetary Science Letters*, *201*(1), 19–34.

Geiss, E. A new compilation of crustal thickness data for the mediterranean area. In: *Annales geophysicae. series b. terrestrial and planetary physics*. 1987.

Gerya, T. (2019). *Introduction to numerical geodynamic modelling*. Cambridge University Press.

Gerya, T., Connolly, J. A., & Yuen, D. A. (2008). Why is terrestrial subduction one-sided? *Geology*, *36*(1), 43–46.

Gerya, T. V., Connolly, J. A., Yuen, D. A., Gorczyk, W., & Capel, A. M. (2006). Seismic implications of mantle wedge plumes. *Physics of the Earth and Planetary Interiors*, *156*(1-2), 59–74.

Gerya, T. V., Perchuk, L. L., Maresch, W. V., & Willner, A. P. (2004). Inherent gravitational instability of hot continental crust: Implications for doming and diapirism in granulite facies terrains. *SPECIAL PAPERS-GEOLOGICAL SOCIETY OF AMERICA*, 97–116.

Giacomuzzi, G, Civalleri, M, De Gori, P, & Chiarabba, C. (2012). A 3d vs model of the upper mantle beneath italy: Insight on the geodynamics of central mediterranean. *Earth and Planetary Science Letters*, *335*, 105–120.

Grand, S. P., Van der Hilst, R. D., & Widiyantoro, S. (1997). High resolution global tomography: A snapshot of convection in the earth. *Geological Society of America Today*, *7*(4).

Gueguen, E., Doglioni, C., & Fernandez, M. (1998). On the post-25 ma geodynamic evolution of the western mediterranean. *Tectonophysics*, *298*(1-3), 259–269.

Guillaume, B., Funiciello, F., Faccenna, C., Martinod, J., & Olivetti, V. (2010). Spreading pulses of the tyrrhenian sea during the narrowing of the calabrian slab. *Geology*, *38*(9), 819–822.

Guillaume, B., Husson, L., Funiciello, F., & Faccenna, C. (2013). The dynamics of laterally variable subductions: Laboratory models applied to the hellenides. *Solid Earth*, *4*(2), 179–200.

Gutscher, M.-A., Malod, J, Rehault, J.-P., Contrucci, I, Klingelhoefer, F, Mendes-Victor, L, & Spakman, W. (2002). Evidence for active subduction beneath gibraltar. *Geology*, *30*(12), 1071–1074.

Hansen, L. N., Faccenda, M., & Warren, J. M. (2021). A review of mechanisms generating seismic anisotropy in the upper mantle. *Physics of the Earth and Planetary Interiors*, 106662.

Hansen, L. N., Zhao, Y.-H., Zimmerman, M. E., & Kohlstedt, D. L. (2014). Protracted fabric evolution in olivine: Implications for the relationship among strain, crystallographic fabric, and seismic anisotropy. *Earth and Planetary Science Letters*, *387*, 157–168.

Hess, H. (1964). Seismic anisotropy of the uppermost mantle under oceans. *Nature*, *203*(4945), 629–631.

Heuret, A., & Lallemand, S. (2005). Plate motions, slab dynamics and back-arc deformation. *Physics of the Earth and Planetary Interiors*, *149*(1-2), 31–51.

Holt, A. F., Royden, L. H., Becker, T. W., & Faccenna, C. (2018). Slab interactions in 3-d subduction settings: The philippine sea plate region. *Earth and Planetary Science Letters*, *489*, 72–83.

Holt, A., Becker, T., & Buffett, B. (2015). Trench migration and overriding plate stress in dynamic subduction models. *Geophysical Journal International*, *201*(1), 172–192.

Holt, A., Royden, L., & Becker, T. (2017). The dynamics of double slab subduction. *Geophysical Journal International*, *209*(1), 250–265.

Hu, J., Faccenda, M., & Liu, L. (2017). Subduction-controlled mantle flow and seismic anisotropy in south america. *Earth and Planetary Science Letters*, *470*, 13–24.

Hua, Y., Zhao, D., & Xu, Y. (2017). P wave anisotropic tomography of the alps. *Journal of Geophysical Research: Solid Earth*, *122*(6), 4509–4528.

Huang, Z., Zhao, D., & Wang, L. (2011a). Frequency-dependent shear-wave splitting and multilayer anisotropy in northeast japan. *Geophysical Research Letters*, *38*(8).

Huang, Z., Zhao, D., & Wang, L. (2011b). Shear wave anisotropy in the crust, mantle wedge, and subducting pacific slab under northeast japan. *Geochemistry, Geophysics, Geosystems*, *12*(1).

Ismaıl, W. B., & Mainprice, D. (1998). An olivine fabric database: An overview of upper mantle fabrics and seismic anisotropy. *Tectonophysics*, *296*(1-2), 145–157.

Ismail-Zadeh, A., & Tackley, P. (2010). *Computational methods for geodynamics*. Cambridge University Press.

Jadamec, M., & Billen, M. I. (2012). The role of rheology and slab shape on rapid mantle flow: Three-dimensional numerical models of the alaska slab edge. *Journal of Geophysical Research: Solid Earth*, *117*(B2).

Jadamec, M. A. (2016). Insights on slab-driven mantle flow from advances in three-dimensional modelling. *Journal of Geodynamics*, *100*, 51–70.

Jadamec, M. A., & Billen, M. I. (2010). Reconciling surface plate motions with rapid three-dimensional mantle flow around a slab edge. *Nature*, *465*(7296), 338–341.

Jagoutz, O., Royden, L., Holt, A. F., & Becker, T. W. (2015). Anomalously fast convergence of india and eurasia caused by double subduction. *Nature Geoscience*, *8*(6), 475–478.

Jolivet, L., Augier, R., Faccenna, C., Negro, F., Rimmele, G., Agard, P., Robin, C., Rossetti, F., & Crespo-Blanc, A. (2008). Subduction, convergence and the mode of backarc extension in the mediterranean region. *Bulletin de la Société Géologique de France*, *179*(6), 525–550.

Jolivet, L., Augier, R., Robin, C., Suc, J.-P., & Rouchy, J. M. (2006). Lithospheric-scale geodynamic context of the messinian salinity crisis. *Sedimentary geology*, *188*, 9–33.

Jolivet, L., & Faccenna, C. (2000). Mediterranean extension and the africa-eurasia collision. *Tectonics*, *19*(6), 1095–1106.

Jolivet, L., Faccenna, C., & Piromallo, C. (2009). From mantle to crust: Stretching the mediterranean. *Earth and Planetary Science Letters*, *285*(1-2), 198–209.

Jung, H. (2017). Crystal preferred orientations of olivine, orthopyroxene, serpentine, chlorite, and amphibole, and implications for seismic anisotropy in subduction zones: A review. *Geosciences Journal*, *21*(6), 985–1011.

Jung, H., & Karato, S.-i. (2001). Water-induced fabric transitions in olivine. *Science*, *293*(5534), 1460–1463.

Jung, H., Katayama, I, Jiang, Z, Hiraga, T, & Karato, S.-I. (2006). Effect of water and stress on the lattice-preferred orientation of olivine. *Tectonophysics*, *421*(1-2), 1–22.

Kaminski, E, & Ribe, N. (2001). A kinematic model for recrystallization and texture development in olivine polycrystals. *Earth and Planetary Science Letters*, *189*(3-4), 253–267.

Kaminski, E., & Ribe, N. M. (2002). Timescales for the evolution of seismic anisotropy in mantle flow. *Geochemistry, Geophysics, Geosystems*, *3*(8), 1–17.

Kaminski, E., Ribe, N. M., & Browaeys, J. T. (2004). D-rex, a program for calculation of seismic anisotropy due to crystal lattice preferred orientation in the convective upper mantle. *Geophysical Journal International*, *158*(2), 744–752.

Karato, S.-i. (2008). Deformation of earth materials. *An Introduction to the Rheology of Solid Earth*, *463*.

Karato, S.-i., Jung, H., Katayama, I., & Skemer, P. (2008). Geodynamic significance of seismic anisotropy of the upper mantle: New insights from laboratory studies. *Annu. Rev. Earth Planet. Sci.*, *36*, 59–95.

Karato, S.-i., & Wu, P. (1993). Rheology of the upper mantle: A synthesis. *Science*, *260*(5109), 771–778.

Karpov, I., Kiselev, A., & Letnikov, F. (1976). Computer modeling of natural mineral formation. *Nedra, Moscow*.

Kästle, E. D., El-Sharkawy, A, Boschi, L, Meier, T, Rosenberg, C, Bellahsen, N, Cristiano, L, & Weidle, C. (2018). Surface wave tomography of the alps using ambient-noise and

earthquake phase velocity measurements. *Journal of Geophysical Research: Solid Earth*, *123*(2), 1770–1792.

Kästle, E. D., Rosenberg, C., Boschi, L., Bellahsen, N., Meier, T., & El-Sharkawy, A. (2020). Slab break-offs in the alpine subduction zone. *International Journal of Earth Sciences*, *109*(2), 587–603.

Katayama, I., Jung, H., & Karato, S.-i. (2004). New type of olivine fabric from deformation experiments at modest water content and low stress. *Geology*, *32*(12), 1045–1048.

Katayama, I., & Karato, S.-i. (2006). Effect of temperature on the b-to c-type olivine fabric transition and implication for flow pattern in subduction zones. *Physics of the Earth and Planetary Interiors*, *157*(1-2), 33–45.

Katayama, I., & Karato, S.-i. (2008). Low-temperature, high-stress deformation of olivine under water-saturated conditions. *Physics of the Earth and Planetary Interiors*, *168*, 125–133.

Kaus, B., Le Breton, E., Reuber, G., & Schuler, C. Using geodynamic modeling to test plate tectonic scenarios of the mediterranean-alpine area. In: *Egu general assembly conference abstracts*. 2020, 11134.

Kendall, J.-M. (1994). Teleseismic arrivals at a mid-ocean ridge: Effects of mantle melt and anisotropy. *Geophysical Research Letters*, *21*(4), 301–304.

Kennett, B., & Engdahl, E. (1991). Traveltimes for global earthquake location and phase identification. *Geophysical Journal International*, *105*(2), 429–465.

Kennett, B. (2009). *Seismic wave propagation in stratified media*. ANU Press.

Kennett, B. L., Engdahl, E., & Buland, R. (1995). Constraints on seismic velocities in the earth from traveltimes. *Geophysical Journal International*, *122*(1), 108–124.

Király, Á, Conrad, C. P., & Hansen, L. N. (2020). Evolving viscous anisotropy in the upper mantle and its geodynamic implications. *Geochemistry, Geophysics, Geosystems*, *21*(10), e2020GC009159.

Király, Á., Faccenna, C., & Funiciello, F. (2018). Subduction zones interaction around the adria microplate and the origin of the apenninic arc. *Tectonics*, *37*(10), 3941–3953.

Kocks, U. F., AS, A., & MF, A. (1975). Thermodynamics and kinetics of slip.

Komatitsch, D., & Tromp, J. (1999). Introduction to the spectral element method for three-dimensional seismic wave propagation. *Geophysical journal international*, *139*(3), 806–822.

Koulakov, I, Kaban, M., Tesauro, M., & Cloetingh, S. (2009). P-and s-velocity anomalies in the upper mantle beneath europe from tomographic inversion of isc data. *Geophysical Journal International*, *179*(1), 345–366.

Kuhlemann, J. (2007). Paleogeographic and paleotopographic evolution of the swiss and eastern alps since the oligocene. *Global and Planetary Change*, *58*(1-4), 224–236.

Lassak, T. M., Fouch, M. J., Hall, C. E., & Kaminski, É. (2006). Seismic characterization of mantle flow in subduction systems: Can we resolve a hydrated mantle wedge? *Earth and Planetary Science Letters*, *243*(3-4), 632–649.

Lee, K.-H., Jiang, Z., & Karato, S.-i. (2002). A scanning electron microscope study of the effects of dynamic recrystallization on lattice preferred orientation in olivine. *Tectonophysics*, *351*(4), 331–341.

Lévěque, J.-J., Rivera, L., & Wittlinger, G. (1993). On the use of the checker-board test to assess the resolution of tomographic inversions. *Geophysical Journal International*, *115*(1), 313–318.

Liu, L., & Stegman, D. R. (2012). Origin of columbia river flood basalt controlled by propagating rupture of the farallon slab. *Nature*, *482*(7385), 386–389.

Liu, Q, & Gu, Y. (2012). Seismic imaging: From classical to adjoint tomography. *Tectonophysics*, *566*, 31–66.

Liu, X., & Zhao, D. (2016). Seismic velocity azimuthal anisotropy of the japan subduction zone: Constraints from p and s wave traveltimes. *Journal of Geophysical Research: Solid Earth*, *121*(7), 5086–5115.

Lloyd, S., & Van Der Lee, S. (2008). Influence of observed mantle anisotropy on isotropic tomographic models. *Geochemistry, Geophysics, Geosystems*, *9*(7).

Lo Bue, R, & Faccenda, M. Three-dimensional modelling of the recent evolution of the mediterranean convergent margin. In: *Agu fall meeting abstracts*. *2019*. 2019, DI21B–0032.

Lo Bue, R., Faccenda, M., & Yang, J. (2021). The role of adria plate lithospheric structures on the recent dynamics of the central mediterranean region. *Journal of Geophysical Research: Solid Earth*, e2021JB022377. https://doi.org/https://doi.org/10.1029/2021JB022377

Lonergan, L., & White, N. (1997). Origin of the betic-rif mountain belt. *Tectonics*, *16*(3), 504–522.

Long, M. D. (2013). Constraints on subduction geodynamics from seismic anisotropy. *Reviews of Geophysics*, *51*(1), 76–112.

Long, M. D., & Becker, T. W. (2010). Mantle dynamics and seismic anisotropy. *Earth and Planetary Science Letters*, *297*(3-4), 341–354.

Long, M. D., Hager, B. H., De Hoop, M. V., & Van Der Hilst, R. D. (2007). Two-dimensional modelling of subduction zone anisotropy with application to southwestern japan. *Geophysical Journal International*, *170*(2), 839–856.

Long, M. D., & Silver, P. G. (2008). The subduction zone flow field from seismic anisotropy: A global view. *science*, *319*(5861), 315–318.

Long, M. D., & Silver, P. G. (2009). Shear wave splitting and mantle anisotropy: Measurements, interpretations, and new directions. *Surveys in Geophysics*, *30*(4), 407–461.

Lucente, F. P., Chiarabba, C., Cimini, G. B., & Giardini, D. (1999). Tomographic constraints on the geodynamic evolution of the italian region. *Journal of Geophysical Research: Solid Earth*, *104*(B9), 20307–20327.

Lucente, F. P., & Margheriti, L. (2008). Subduction rollback, slab breakoff, and induced strain in the uppermost mantle beneath italy. *Geology*, *36*(5), 375–378.

Lucente, F. P., Margheriti, L., Piromallo, C., & Barruol, G. (2006). Seismic anisotropy reveals the long route of the slab through the western-central mediterranean mantle. *Earth and Planetary Science Letters*, *241*(3-4), 517–529.

Lucente, F. P., & Speranza, F. (2001). Belt bending driven by lateral bending of subducting lithospheric slab: Geophysical evidences from the northern apennines (italy). *Tectonophysics*, *337*(1-2), 53–64.

Luth, S., Willingshofer, E., Sokoutis, D., & Cloetingh, S. (2013). Does subduction polarity changes below the alps? inferences from analogue modelling. *Tectonophysics*, *582*, 140–161.

Magni, V., Faccenna, C., Van Hunen, J., & Funiciello, F. (2014). How collision triggers backarc extension: Insight into mediterranean style of extension from 3-d numerical models. *Geology*, *42*(6), 511–514.

Maino, M., Decarlis, A., Felletti, F., & Seno, S. (2013). Tectono-sedimentary evolution of the tertiary piedmont basin (nw italy) within the oligo–miocene central mediterranean geodynamics. *Tectonics*, *32*(3), 593–619.

Mainprice, D., Le Page, Y., Rodgers, J., & Jouanna, P. (2007). Predicted elastic properties of the hydrous d phase at mantle pressures: Implications for the anisotropy of subducted

slabs near 670-km discontinuity and in the lower mantle. *Earth and Planetary Science Letters*, *259*(3-4), 283–296.

Malinverno, A., & Ryan, W. B. (1986). Extension in the tyrrhenian sea and shortening in the apennines as result of arc migration driven by sinking of the lithosphere. *Tectonics*, *5*(2), 227–245.

Margheriti, L, Lucente, F., & Pondrelli, S. (2003). Sks splitting measurements in the apenninic-tyrrhenian domain (italy) and their relation with lithospheric subduction and mantle convection. *Journal of Geophysical Research: Solid Earth*, *108*(B4).

Masalu, D. C. (2007). Mapping absolute migration of global mid-ocean ridges since 80 ma to present. *Earth, planets and space*, *59*(9), 1061–1066.

Mason, W., Moresi, L, Betts, P., & Miller, M. (2010). Three-dimensional numerical models of the influence of a buoyant oceanic plateau on subduction zones. *Tectonophysics*, *483*(1-2), 71–79.

Masters, T. G., Johnson, S., Laske, G., & Bolton, H. (1996). A shear-velocity model of the mantle. *Philosophical Transactions of the Royal Society of London. Series A: Mathematical, Physical and Engineering Sciences*, *354*(1711), 1385–1411.

Mauffret, A, Frizon de Lamotte, D, Lallemant, S., Gorini, C., & Maillard, A. (2004). E–w opening of the algerian basin (western mediterranean). *Terra Nova*, *16*(5), 257–264.

Maupin, V, & Park, J. (2015). 1.09—theory and observations—seismic anisotropy. *Treatise on Geophysics*, *20*, 277–305.

McEvilly, T. (1964). Central us crust—upper mantle structure from love and rayleigh wave phase velocity inversion. *Bulletin of the Seismological Society of America*, *54*(6A), 1997–2015.

McKenzie, D. P., Roberts, J. M., & Weiss, N. O. (1974). Convection in the earth's mantle: Towards a numerical simulation. *Journal of Fluid Mechanics*, *62*(3), 465–538.

Menant, A., Sternai, P., Jolivet, L., Guillou-Frottier, L., & Gerya, T. (2016). 3d numerical modeling of mantle flow, crustal dynamics and magma genesis associated with slab roll-back and tearing: The eastern mediterranean case. *Earth and Planetary Science Letters*, *442*, 93–107.

Menke, W. (2015). Equivalent heterogeneity analysis as a tool for understanding the resolving power of anisotropic travel-time tomography. *Bulletin of the Seismological Society of America*, *105*(2A), 719–733.

Menke, W., & Levin, V. (2003). The cross-convolution method for interpreting sks splitting observations, with application to one and two-layer anisotropic earth models. *Geophysical Journal International*, *154*(2), 379–392.

Miller, M. S., & Becker, T. W. (2012). Mantle flow deflected by interactions between subducted slabs and cratonic keels. *Nature Geoscience*, *5*(10), 726–730.

Miller, M., & Piana Agostinetti, N. (2012). Insights into the evolution of the italian lithospheric structure from s receiver function analysis. *Earth Science Planetary Letters*, *345-348*, 49–59.

Mishin, Y. A., Gerya, T. V., Burg, J.-P., & Connolly, J. A. (2008). Dynamics of double subduction: Numerical modeling. *Physics of the Earth and Planetary Interiors*, *171*(1-4), 280–295.

Mochizuki, E. (1995). Anisotropic tomography of p-wave traveltimes. *Geophysical Journal International*, *123*(1), 297–300.

Monteiller, V., & Chevrot, S. (2011). High-resolution imaging of the deep anisotropic structure of the san andreas fault system beneath southern california. *Geophysical Journal International*, *186*(2), 418–446.

Monteiller, V., Chevrot, S., Komatitsch, D., & Fuji, N. (2013). A hybrid method to compute short-period synthetic seismograms of teleseismic body waves in a 3-d regional model. *Geophysical Journal International*, *192*(1), 230–247.

Moser, T. (1991). Shortest path calculation of seismic rays. *Geophysics*, *56*(1), 59–67.

Müller, G. (1971). Approximate treatment of elastic body waves in media with spherical symmetry. *Geophysical Journal International*, *23*(4), 435–449.

Munzarová, H., Plomerová, J., & Kissling, E. (2018). Novel anisotropic teleseismic body-wave tomography code anitomo to illuminate heterogeneous anisotropic upper mantle: Part i—theory and inversion tuning with realistic synthetic data. *Geophysical Journal International*, *215*(1), 524–545.

Nakagawa, T., Tackley, P. J., Deschamps, F., & Connolly, J. A. (2009). Incorporating self-consistently calculated mineral physics into thermochemical mantle convection simulations in a 3-d spherical shell and its influence on seismic anomalies in earth's mantle. *Geochemistry, Geophysics, Geosystems*, *10*(3).

Neri, G, Marotta, A., Orecchio, B., Presti, D, Totaro, C., Barzaghi, R., & Borghi, A. (2012). How lithospheric subduction changes along the calabrian arc in southern italy: Geophysical evidences. *International Journal of Earth Sciences*, *101*(7), 1949–1969.

Neri, G., Orecchio, B., Totaro, C., Falcone, G., & Presti, D. (2009). Subduction beneath southern italy close the ending: Results from seismic tomography. *Seismological Research Letters*, *80*(1), 63–70.

Nicolas, A., & Christensen, N. I. (1987). Formation of anisotropy in upper mantle peridotites-a review. *Composition, structure and dynamics of the lithosphere-asthenosphere system*, *16*, 111–123.

Nissen-Meyer, T., Van Driel, M., Stähler, S. C., Hosseini, K., Hempel, S., Auer, L., Colombi, A., & Fournier, A. (2014). Axisem: Broadband 3-d seismic wavefields in axisymmetric media. *Solid Earth*, *5*(1), 425–445.

Nocquet, J.-M., Sue, C., Walpersdorf, A, Tran, T, Lenôtre, N, Vernant, P, Cushing, M, Jouanne, F, Masson, F, Baize, S, et al. (2016). Present-day uplift of the western alps. *Scientific reports*, *6*(1), 1–6.

Obayashi, M., & Fukao, Y. (1997). P and pcp travel time tomography for the core-mantle boundary. *Journal of Geophysical Research: Solid Earth*, *102*(B8), 17825–17841.

Orowan, E. (1934). Zur kristallplastizität. i. *Zeitschrift für Physik*, *89*(9), 605–613.

Paczkowski, K., Thissen, C. J., Long, M. D., & Montési, L. G. (2014). Deflection of mantle flow beneath subducting slabs and the origin of subslab anisotropy. *Geophysical Research Letters*, *41*(19), 6734–6742.

Paige, C. C., & Saunders, M. A. (1982). Lsqr: An algorithm for sparse linear equations and sparse least squares. *ACM Transactions on Mathematical Software (TOMS)*, *8*(1), 43–71.

Panza, G., Pontevivo, A, Chimera, G, Raykova, R, & Aoudia, A. (2003). The lithosphere-asthenosphere: Italy and surroundings. *Episodes*, *26*(3), 169–174.

Park, J., & Levin, V. (2002). Seismic anisotropy: Tracing plate dynamics in the mantle. *Science*, *296*(5567), 485–489.

Patacca, E., Sartori, R, & Scandone, P. (1990). Tyrrhenian basin and apenninic arcs: Kinematic relations since late tortonian times. *Memorie della Società Geologica Italiana*, *45*, 425–451.

Patankar, S. V. (2018). *Numerical heat transfer and fluid flow*. CRC press.

Peral, M., Ruh, J., Zlotnik, S., Funiciello, F., Fernàndez, M., Vergés, J., & Gerya, T. (2020). Analog and numerical experiments of double subduction systems with opposite polarity in adjacent segments. *Geochemistry, Geophysics, Geosystems*, *21*(6), e2020GC009035.

Petrescu, L., Pondrelli, S., Salimbeni, S., Faccenda, M., Group, A. W., et al. (2020). Mantle flow below the central and greater alpine region: Insights from sks anisotropy analysis at alparray and permanent stations. *Solid Earth*, *11*(4), 1275–1290.

Piromallo, C, Becker, T., Funiciello, F, & Faccenna, C. (2006). Three-dimensional instantaneous mantle flow induced by subduction. *Geophysical Research Letters*, *33*(8).

Piromallo, C., & Morelli, A. (1997). Imaging the mediterranean upper mantle by p-wave travel time tomography. *Annals of Geophysics*, *40*(4).

Piromallo, C., & Morelli, A. (2003). P wave tomography of the mantle under the alpine-mediterranean area. *Journal of Geophysical Research: Solid Earth*, *108*(B2).

Platt, J., & Vissers, R. (1989). Extensional collapse of thickened continental lithosphere: A working hypothesis for the alboran sea and gibraltar arc. *Geology*, *17*(6), 540–543.

Plomerová, J, Margheriti, L, Park, J, Babuška, V, Pondrelli, S, Vecsey, L, Piccinini, D, Levin, V, Baccheschi, P, & Salimbeni, S. (2006). Seismic anisotropy beneath the northern apennines (italy): Mantle flow or lithosphere fabric? *Earth and Planetary Science Letters*, *247*(1-2), 157–170.

Polanyi, M. (1934). Über eine art gitterstörung, die einen kristall plastisch machen könnte. *Zeitschrift für Physik*, *89*(9), 660–664.

Presti, D., Totaro, C., Neri, G., & Orecchio, B. (2019). New earthquake data in the calabrian subduction zone, italy, suggest revision of the presumed dynamics in the upper part of the subducting slab. *Seismological Research Letters*, *90*(5), 1994–2004.

Ranalli, G. (1995). *Rheology of the earth*. Springer Science & Business Media.

Rappisi, F., & Faccenda, M. (2019). Geodynamic and seismological numerical modelling for seismic anisotropy studies. *AGUFM*, *2019*, DI21B–0038.

Rappisi, F., VanderBeek, B., Faccenda, M, Morelli, A, & Molinari, I. (2022). Slab geometry and upper mantle flow patterns in the central mediterranean from 3d anisotropic p-wave tomography. *Journal of Geophysical Research: Solid Earth*, e2021JB023488.

Rawlinson, N, & Spakman, W. (2016). On the use of sensitivity tests in seismic tomography. *Geophysical Journal International*, *205*(2), 1221–1243.

Rawlinson, N., Fichtner, A., Sambridge, M., & Young, M. K. (2014). Seismic tomography and the assessment of uncertainty. *Advances in geophysics*, *55*, 1–76.

Reuber, G. S., & Simons, F. J. (2020). Multi-physics adjoint modeling of earth structure: Combining gravimetric, seismic, and geodynamic inversions. *GEM-International Journal on Geomathematics*, *11*(1), 1–38.

Ribe, N. M. (1989). Seismic anisotropy and mantle flow. *Journal of Geophysical Research: Solid Earth*, *94*(B4), 4213–4223.

Ribe, N. M. (1992). On the relation between seismic anisotropy and finite strain. *Journal of Geophysical Research: Solid Earth*, *97*(B6), 8737–8747.

Richter, F. M. (1973). Finite amplitude convection through a phase boundary. *Geophysical Journal International*, *35*(1-3), 265–276.

Rodríguez-González, J., Billen, M. I., & Negredo, A. M. (2014). Non-steady-state subduction and trench-parallel flow induced by overriding plate structure. *Earth and Planetary Science Letters*, *401*, 227–235.

Rollet, N., Déverchere, J., Beslier, M.-O., Guennoc, P., Réhault, J.-P., Sosson, M., & Truffert, C. (2002). Back arc extension, tectonic inheritance, and volcanism in the ligurian sea, western mediterranean. *Tectonics*, *21*(3), 6–1.

Romagny, A., Jolivet, L., Menant, A., Bessière, E., Maillard, A., Canva, A., Gorini, C., & Augier, R. (2020). Detailed tectonic reconstructions of the western mediterranean region for the last 35 ma, insights on driving mechanisms. *BSGF-Earth Sciences Bulletin*, *191*(1), 37.

Romanowicz, B. A. Seismic tomography of the earth's mantle (D. Alderton & S. A. Elias, Eds.; Second Edition). In: In *Encyclopedia of geology (second edition)* (D. Alderton & S. A. Elias, Eds.; Second Edition). Ed. by Alderton, D., & Elias, S. A. Second Edition. Oxford: Academic Press, 2021, pp. 587–609. ISBN: 978-0-08-102909-1. https://doi.org/https://doi.org/10.1016/B978-0-08-102908-4.00169-7.

Rosenbaum, G., Gasparon, M., Lucente, F. P., Peccerillo, A., & Miller, M. S. (2008). Kinematics of slab tear faults during subduction segmentation and implications for italian magmatism. *Tectonics*, *27*(2).

Rosenbaum, G., Lister, G. S., & Duboz, C. (2002a). Relative motions of africa, iberia and europe during alpine orogeny. *Tectonophysics*, *359*(1-2), 117–129.

Rosenbaum, G., Lister, G. S., Duboz, C., et al. (2002b). Reconstruction of the tectonic evolution of the western mediterranean since the oligocene. *Journal of the Virtual Explorer*, *8*(January).

Ruan, Y., Lei, W., Modrak, R., Örsvuran, R., Bozdağ, E., & Tromp, J. (2019). Balancing unevenly distributed data in seismic tomography: A global adjoint tomography example. *Geophysical Journal International*, *219*(2), 1225–1236.

Rümpker, G., & Silver, P. G. (1998). Apparent shear-wave splitting parameters in the presence of vertically varying anisotropy. *Geophysical Journal International*, *135*(3), 790–800.

Russell, J. B., Gaherty, J. B., Lin, P.-Y. P., Lizarralde, D., Collins, J. A., Hirth, G., & Evans, R. L. (2019). High-resolution constraints on pacific upper mantle petrofabric inferred from surface-wave anisotropy. *Journal of Geophysical Research: Solid Earth*, *124*(1), 631–657.

Salimbeni, S., Pondrelli, S., & Margheriti, L. (2013). Hints on the deformation penetration induced by subductions and collision processes: Seismic anisotropy beneath the adria region (central mediterranean). *Journal of Geophysical Research: Solid Earth*, *118*(11), 5814–5826.

Savage, M. (1999). Seismic anisotropy and mantle deformation: What have we learned from shear wave splitting? *Reviews of Geophysics*, *37*(1), 65–106.

Scarfì, L., Barberi, G., Barreca, G., Cannavò, F., Koulakov, I., & Patanè, D. (2018). Slab narrowing in the central mediterranean: The calabro-ionian subduction zone as imaged by high resolution seismic tomography. *Scientific reports*, *8*(1), 1–12.

Schmeling, H. (1987). On the relation between initial conditions and late stages of rayleigh-taylor instabilities. *Tectonophysics*, *133*(1-2), 65–80.

Schmid, C., Van Der Lee, S., & Giardini, D. (2004). Delay times and shear wave splitting in the mediterranean region. *Geophysical Journal International*, *159*(1), 275–290.

Schubert, G., Turcotte, D. L., & Olson, P. (2001). *Mantle convection in the earth and planets*. Cambridge University Press.

Schubert, G., Yuen, D. A., & Turcotte, D. L. (1975). Role of phase transitions in a dynamic mantle. *Geophysical Journal International*, *42*(2), 705–735.

Selvaggi, G, & Chiarabba, C. (1995). Seismicity and p-wave velocity image of the southern tyrrhenian subduction zone. *Geophysical Journal International*, *121*(3), 818–826.

Sharples, W, Jadamec, M., Moresi, L.-N., & Capitanio, F. A. (2014). Overriding plate controls on subduction evolution. *Journal of Geophysical Research: Solid Earth*, *119*(8), 6684–6704.

Sieminski, A., Liu, Q., Trampert, J., & Tromp, J. (2007). Finite-frequency sensitivity of surface waves to anisotropy based upon adjoint methods. *Geophysical Journal International*, *168*(3), 1153–1174.

Sieminski, A., Paulssen, H., Trampert, J., & Tromp, J. (2008). Finite-frequency sks splitting: Measurement and sensitivity kernels. *Bulletin of the Seismological Society of America*, *98*(4), 1797–1810.

Silver, P. G. (1996). Seismic anisotropy beneath the continents: Probing the depths of geology. *Annual review of earth and planetary sciences*, *24*(1), 385–432.

Silver, P. G., & Chan, W. W. (1988). Implications for continental structure and evolution from seismic anisotropy. *Nature*, *335*(6185), 34–39.

Silver, P. G., & Chan, W. W. (1991). Shear wave splitting and subcontinental mantle deformation. *Journal of Geophysical Research: Solid Earth*, *96*(B10), 16429–16454.

Simmons, N. A., Forte, A. M., Boschi, L., & Grand, S. P. (2010). Gypsum: A joint tomographic model of mantle density and seismic wave speeds. *Journal of Geophysical Research: Solid Earth*, *115*(B12).

Simmons, N. A., Forte, A. M., & Grand, S. P. (2006). Constraining mantle flow with seismic and geodynamic data: A joint approach. *Earth and Planetary Science Letters*, *246*(1-2), 109–124.

Skemer, P., & Hansen, L. N. (2016). Inferring upper-mantle flow from seismic anisotropy: An experimental perspective. *Tectonophysics*, *668*, 1–14.

Smith, G. P., Wiens, D. A., Fischer, K. M., Dorman, L. M., Webb, S. C., & Hildebrand, J. A. (2001). A complex pattern of mantle flow in the lau backarc. *Science*, *292*(5517), 713–716.

Sobolev, S. V., Grésillaud, A., & Cara, M. (1999). How robust is isotropic delay time tomography for anisotropic mantle? *Geophysical research letters*, *26*(4), 509–512.

Spakman, W, & Nolet, G. Imaging algorithms, accuracy and resolution in delay time tomography. In: *Mathematical geophysics*. Springer, 1988, pp. 155–187.

Spakman, W, Wortel, M., & Vlaar, N. (1988). The hellenic subduction zone: A tomographic image and its geodynamic implications. *Geophysical research letters*, *15*(1), 60–63.

Spakman, W. (1990). Tomographic images of the upper mantle below central europe and the mediterranean. *Terra Nova*, *2*(6), 542–553.

Spakman, W. (1991). Delay-time tomography of the upper mantle below europe, the mediterranean, and asia minor. *Geophysical Journal International*, *107*(2), 309–332.

Spakman, W., Van der Lee, S., & Van der Hilst, R. (1993). Travel-time tomography of the european-mediterranean mantle down to 1400 km. *Physics of the Earth and Planetary Interiors*, *79*(1-2), 3–74.

Spakman, W., & Wortel, R. A tomographic view on western mediterranean geodynamics. In: *The transmed atlas. the mediterranean region from crust to mantle*. Springer, 2004, pp. 31–52.

Stegman, D. R., Freeman, J., Schellart, W. P., Moresi, L, & May, D. (2006). Influence of trench width on subduction hinge retreat rates in 3-d models of slab rollback. *Geochemistry, Geophysics, Geosystems*, *7*(3).

Tackley, P. J. (1993). Effects of strongly temperature-dependent viscosity on time-dependent, three-dimensional models of mantle convection. *Geophysical Research Letters*, *20*(20), 2187–2190.

Tackley, P. J. (2000). Self-consistent generation of tectonic plates in time-dependent, three-dimensional mantle convection simulations. *Geochemistry, Geophysics, Geosystems*, *1*(8).

Tackley, P. J. (2008). Modelling compressible mantle convection with large viscosity contrasts in a three-dimensional spherical shell using the yin-yang grid. *Physics of the Earth and Planetary Interiors*, *171*(1-4), 7–18.

Taylor, G. I. (1934). The mechanism of plastic deformation of crystals. part i.—theoretical. *Proceedings of the Royal Society of London. Series A, Containing Papers of a Mathematical and Physical Character*, *145*(855), 362–387.

Thomsen, L. (1986). Weak elastic anisotropy. *Geophysics*, *51*(10), 1954–1966.

Tommasi, A. (1998). Forward modeling of the development of seismic anisotropy in the upper mantle. *Earth and Planetary Science Letters*, *160*(1-2), 1–13.

Tommasi, A., & Vauchez, A. (2015). Heterogeneity and anisotropy in the lithospheric mantle. *Tectonophysics*, *661*, 11–37.

Toomey, D. R., Solomon, S. C., & Purdy, G. (1994). Tomographic imaging of the shallow crustal structure of the east pacific rise at 9° 30 n. *Journal of Geophysical Research: Solid Earth*, *99*(B12), 24135–24157.

Turcotte, D, & Schubert, G. (2014). Geodynamics, 160–228, 263–334, 425–463.

Van der Hilst, R. D., Widiyantoro, S., & Engdahl, E. (1997). Evidence for deep mantle circulation from global tomography. *Nature*, *386*(6625), 578–584.

Van der Hist, R., Engdahl, R., Spakman, W., & Nolet, G. (1991). Tomographic imaging of subducted lithosphere below northwest pacific island arcs. *Nature*, *353*(6339), 37–43.

Van der Meer, D. G., Van Hinsbergen, D. J., & Spakman, W. (2018). Atlas of the underworld: Slab remnants in the mantle, their sinking history, and a new outlook on lower mantle viscosity. *Tectonophysics*, *723*, 309–448.

Van Dinther, Y., Morra, G., Funiciello, F., & Faccenna, C. (2010). Role of the overriding plate in the subduction process: Insights from numerical models. *Tectonophysics*, *484*(1-4), 74–86.

Van Hinsbergen, D. J., Torsvik, T. H., Schmid, S. M., Maţenco, L. C., Maffione, M., Vissers, R. L., Gürer, D., & Spakman, W. (2020). Orogenic architecture of the mediterranean region and kinematic reconstruction of its tectonic evolution since the triassic. *Gondwana Research*, *81*, 79–229.

Van Hinsbergen, D. J., Vissers, R. L., & Spakman, W. (2014). Origin and consequences of western mediterranean subduction, rollback, and slab segmentation. *Tectonics*, *33*(4), 393–419.

Van Zelst, I., Crameri, F., Pusok, A. E., Glerum, A., Dannberg, J., & Thieulot, C. (2021). 101 geodynamic modelling: How to design, carry out, and interpret numerical studies. *Solid Earth Discussions*, 1–80.

VanDecar, J., & Crosson, R. (1990). Determination of teleseismic relative phase arrival times using multi-channel cross-correlation and least squares. *Bulletin of the Seismological Society of America*, *80*(1), 150–169.

VanderBeek, B., & Faccenda, M. (2021). Imaging upper mantle anisotropy with teleseismic p-wave delays: Insights from tomographic reconstructions of subduction simulations. *Geophysical Journal International*, *225*(3), 2097–2119.

Vignaroli, G., Faccenna, C., Jolivet, L., Piromallo, C., & Rossetti, F. (2008). Subduction polarity reversal at the junction between the western alps and the northern apennines, italy. *Tectonophysics*, *450*(1-4), 34–50.

Vinnik, L., Kind, R, Kosarev, G., & Makeyeva, L. (1989). Azimuthal anisotropy in the lithosphere from observations of long-period s-waves. *Geophysical Journal International*, *99*(3), 549–559.

Wang, W., & Becker, T. W. (2019). Upper mantle seismic anisotropy as a constraint for mantle flow and continental dynamics of the north american plate. *Earth and Planetary Science Letters*, *514*, 143–155.

Wang, Z., & Zhao, D. (2021). 3d anisotropic structure of the japan subduction zone. *Science advances*, *7*(4), eabc9620.

Ward, S. N. (1994). Constraints on the seismotectonics of the central mediterranean from very long baseline interferometry. *Geophysical Journal International*, *117*(2), 441–452.

Weinberg, R. F., & Schmeling, H. (1992). Polydiapirs: Multiwavelength gravity structures. *Journal of Structural Geology*, *14*(4), 425–436.

Wenk, H.-R., & Tomé, C. (1999). Modeling dynamic recrystallization of olivine aggregates deformed in simple shear. *Journal of Geophysical Research: Solid Earth*, *104*(B11), 25513–25527.

Wenk, H. R. (2016). *Preferred orientation in deformed metal and rocks: An introduction to modern texture analysis*. Elsevier.

Wessel, P, Luis, J., Uieda, L, Scharroo, R, Wobbe, F, Smith, W., & Tian, D. (2019). The generic mapping tools version 6. *Geochemistry, Geophysics, Geosystems*, *20*(11), 5556–5564.

Wesseling, P. (1995). *Introduction to multigrid methods* (tech. rep.).

Woidt, W.-D. (1978). Finite element calculations applied to salt dome analysis. *Tectonophysics*, *50*(2-3), 369–386.

Wortel, M., & Spakman, W. (2000). Subduction and slab detachment in the mediterranean-carpathian region. *Science*, *290*(5498), 1910–1917.

Wortel, R., Govers, R., & Spakman, W. Continental collision and the step-wise evolution of convergent plate boundaries: From structure to dynamics. In: *Subduction zone geodynamics*. Springer, 2009, pp. 47–59.

Wu, H., & Lees, J. M. (1999). Cartesian parametrization of anisotropic traveltime tomography. *Geophysical Journal International*, *137*(1), 64–80.

Zhang, S., & Karato, S.-i. (1995). Lattice preferred orientation of olivine aggregates deformed in simple shear. *Nature*, *375*(6534), 774–777.

Zhang, S., Karato, S.-i., Gerald, J. F., Faul, U. H., & Zhou, Y. (2000). Simple shear deformation of olivine aggregates. *Tectonophysics*, *316*(1-2), 133–152.

Zhao, C., Hobbs, B. E., & Ord, A. (2009). *Fundamentals of computational geoscience: Numerical methods and algorithms* (Vol. 122). Springer Science & Business Media.

Zhao, D., Hasegawa, A., & Horiuchi, S. (1992). Tomographic imaging of p and s wave velocity structure beneath northeastern japan. *Journal of Geophysical Research: Solid Earth*, *97*(B13), 19909–19928.

Zhao, L., Paul, A., Malusà, M. G., Xu, X., Zheng, T., Solarino, S., Guillot, S., Schwartz, S., Dumont, T., Salimbeni, S., et al. (2016). Continuity of the alpine slab unraveled by high-resolution p wave tomography. *Journal of Geophysical Research: Solid Earth*, *121*(12), 8720–8737.

Zhong, S., & Gurnis, M. (1994). Role of plates and temperature-dependent viscosity in phase change dynamics. *Journal of Geophysical Research: Solid Earth*, *99*(B8), 15903–15917.

Zhong, S., & Gurnis, M. (1996). Interaction ouniciello weak faults and non-newtonian rheology produces plate tectonics in a 3d model of mantle flow. *Nature*, *383*(6597), 245–247.

Zhong, S., Yuen, D. A., Moresi, L. N., & Schubert, G. (2007). Numerical methods for mantle convection. *Treatise on geophysics*, *7*, 227–252.

Zhou, Q., Hu, J., Liu, L., Chaparro, T., Stegman, D. R., & Faccenda, M. (2018). Western us seismic anisotropy revealing complex mantle dynamics. *Earth and Planetary Science Letters*, *500*, 156–167.

Zhu, H., & Tromp, J. (2013). Mapping tectonic deformation in the crust and upper mantle beneath europe and the north atlantic ocean. *Science*, *341*(6148), 871–875.

Acknowledgements

First, and most of all, I thank my supervisor, Manuele Faccenda, for giving me the opportunity to get to know and deepen the world of numerical modeling that has become the heart of this PhD project. His knowledge and experience in the field and his constant guidance have helped to create a stimulating environment for my work.

I would like to express gratitude to my co-supervisor, and most importantly friend, Dr. Brandon Vanderbeek for his valuable support in academia and beyond. Thanks to you, the world of seismology and "spritz" is less mysterious!

I am deeply grateful to Dr. Jianfeng Yang, for the clear explanations he gave me early in my PhD which were really valuable for starting my studies in geodynamic numerical modeling.

I would like to express my deepest gratitude to the reviewers of this thesis Professors Claudio Faccenna and Fabio Capitanio for their valuable and constructive feedback.

I wish to thank my loving and supportive partner and colleague Francesco, for encouraging and above all for having "endured me" in these years of life together.

I would like to thank my ex officemate Albert, for his friendship, precious advice and all the good time spent together in the Paduan evenings!

Thanks to the newcomer Jun, who was immediately a dear office colleague.

My gratitude extends to the Department of Geosciences of the University of Padua for the funding opportunity that allowed me to undertake my studies in a multicultural, positive, and growth environment.

In addition, I am particularly grateful to Manuele for giving me the opportunity to be part of the NEWTON project. Working with the Newtonians has been an honor and above all a pleasure. Albert, Brandon, Francesco, Manuele thank you for being colleagues and above all friends, these years would not have been like this without you. With your advice, our ungrammatical Italian-Spanish-American-Venetian chatter and our evenings at "Civico 4" made these years in Padua unforgettable. Grazie sai!

Finally, I would like to thank my family, my parents and my brothers, for providing me with unfailing support and continuous encouragement throughout my years of study.

My heartfelt thanks go to my father: I hope I made you proud of me, wherever you are.